ISSN 0912-1803

PHOTON FACTORY ACTIVITY REPORT

1996

#14

High Energy Accelerator Research Organization, KEK

Photon Factory Activity Report 1996

Staff members and visitors of the Photon Factory gathered in front of the PF building.

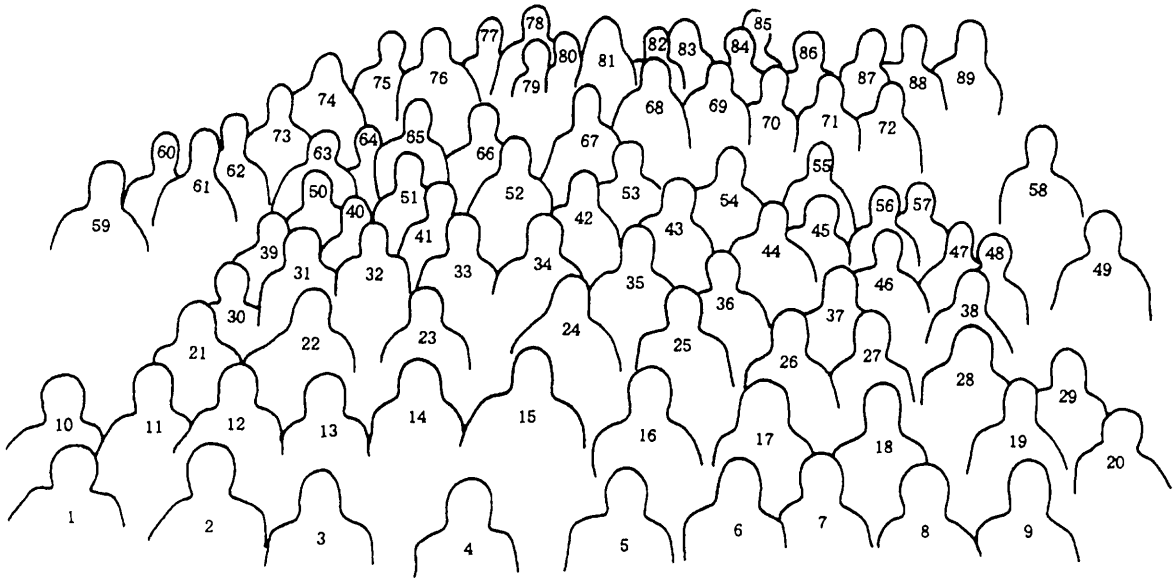

1. T. Urano
2. S. Kamada
3. A. Mikuni
4. H. Kobayakawa
5. M. Kihara
6. O. Shimomura
7. H. Kitamura
8. K. Ohmi
9. K. Furukawa
10. M. Isawa
11. M. Kobayashi
12. K. Nasu
13. H. Kobayashi
14. K. Kobayashi
15. H. Kawata
16. M. Suzuki
17. T. Kosuge
18. M. Tanaka
19. T. Honda
20. T. Kurihara
21. Y. Hori
22. M. Katoh
23. S. Sakanaka
24. A. Ueda
25. I. Abe
26. K. Haga
27. T. Kasuga
28. T. Mitsuhashi
29. M. Nomura
30. Y. Kobayashi
31. T. Nogami
32. S. Tokumoto
33. K. Hirano
34. K. Tsuchiya
35. S. Ohsawa
36. H. Hanaki
37. T. Oogoe
38. Y. Saitoh
39. T. Osaka
40. S. Kuroda
41. S. Kishimoto
42. A. Enomoto
43. Y. Ogawa
44. K. Kakihara
45. A. Mochihashi
46. K. Ito
47. M. Ikeda
48. A. Iida
49. S. Anami
50. E. Shigemasa
51. Y. Murakami
52. M. Watanabe
53. C. O. Pak
54. N. Watanabe
55. S. Asaoka
56. H. Sugiyama
57. N. Tomita
58. H. Honma
59. Y. Takiyama
60. T. Yokoo
61. Y. Sato
62. T. Kamitani
63. T. Suwada
64. A. Shirakawa
65. D. Cookson
66. G. Foran
67. T. Kikegawa
68. A. Koyama
69. Y. Uchida
70. T. Kikuchi
71. T. Mori
72. S. Michizono
73. H. Katagiri
74. A. Toyoshima
75. H. Iijima
76. H. Maezawa
77. H. Kawada
78. K. Ohsumi
79. N. Usami
80. H. Toyama
81. M. Kimura
82. S. Takano
83. A. Kikuchi
84. F. Mori
85. A. Mishina
86. M. Noji
87. K. Nakahara
88. T. Shidara
89. Y. Kitajima

PREFACE

It is my pleasure to present the Photon Factory Activity Report No. 14, which covers the period from October 1995 to March 1997. This was a crucial period for the facility, leading to a major re-organization of the administrative structure of the laboratory which became effective on April 1st, 1997. The Photon Factory "facility" has been re-organized and upgraded into an independent research institute with the addition of neutron and muon based research sections. This new "Institute of Materials Structure Science", belonging to the "High Energy Accelerator Research Organization", will continue to operate and develop the Photon Factory further in the future. The current volume is the last yearly activity report published under the previous administration.

In its 14th year of operation, the PF 2.5 GeV ring was routinely filled up to 400 mA during normal multi-bunch operation, and a record of 773 mA was set during machine study operation. The "High Brilliance Project" aiming at reducing the emittance by a factor of five, has made considerable progress and promises to keep the Photon Factory competitive with the third-generation rings. Beamline "Scrap-and-Build" projects were continued successfully with the construction of four new state-of-the-art beam-lines, and more coming up. User's research was active as ever with 332 proposals approved during fiscal year 1996. High-lights of the activities in various fields are summarized in this volume.

Further facility development projects in progress include the PF-AR (Advanced Ring for pulsed X-rays) project. This involves the up-grade of the parasitic operation at the TRISTAN Accumulation Ring (AR) into a new dedicated ring for single bunch and high flux synchrotron radiation in the X-ray region. During a three months period towards the end of 1995, the experimental operation of the TRISTAN Main Ring for super-brilliant synchrotron radiation was conducted successfully.

I am very pleased that the new research institute is going to inherit this facility and the users community in an extremely good shape. I look forward to seeing research with synchrotron radiation flourish even more under the new administration.

Motohiro Kihara
Director, Photon Factory

Acknowledgments

The editors would like to thank Ms. Miyako Kimura and Mrs. Sumie Imai for their help in editing this issue.

KEK Progress Report 97-2 A/M

KEK Reports are available from:

Technical Information & Library
High Energy Accelerator Research Organization.
1-1 Oho, Tsukuba-shi
Ibaraki-ken, 305
JAPAN

Phone: +81-298-64-5137
Fax: +81-298-64-4604
e-mail: LIBRARY@KEKVAX.KEK.JP
URL. (Internet): http://www.kek.jp
Cable: KEKOHO

CONTENTS

INTRODUCTION

The Photon Factory (PF) has been a synchrotron radiation research facility belonging to the National Laboratory for High Energy Physics (KEK) operated by the Ministry of Education, Science, Sports, and Culture. It consists of a 2.5-GeV electron/positron linear accelerator, a 2.5-GeV electron/positron storage ring as a dedicated light source, parasitic operation at the TRISTAN Accumulation Ring (AR) and many beamlines and experimental stations associated with them. Proposals for research utilizing the facilities are accepted from scientists at universities, government laboratories, public organizations, private corporations and also from foreign countries.

This Activity Report covers the period from October 1995 to March 1997, which marked the 14th year of successful operation. The 2.5 GeV ring has become an extremely reliable light source, normally filling up to 400 mA ring current with an average current of 300 mA and a life time of longer than 60 hours. Almost 99% of scheduled operation was successfully made supplying users with 3536 hours of beam time. As is described in more detail in section B of the ACCELERATOR OPERATIONS, RESEARCHES AND DEVELOPMENTS section, the 2.5 GeV ring will be modified to realize a smaller emittance of 27 nm.rad, so that the brilliance of the bending magnet and insertion device sources will be enhanced by a factor of 5 to10. The autumn run of 1996 was the last operation of the ring with the lattice originally commissioned in 1982. A nine-months shut-down of the ring is taking place from December, 1996 to September, 1997. The light source group conducted a special machine-study for high ring-current on December 16, 1996 just before the long shutdown. They attained a ring current of 773 mA, which set a new record of stored current for the 2.5 GeV storage-ring. The TRISTAN AR was parasitically used for synchrotron radiation research for 2934 hours during the period from September, 1995 to June, 1996. The AR has been used for machine study for accelerator development for the B-Factory project after June, 1996.

Machine study of the 2.5 GeV ring logged approximately 750 hours during the reported period. The most notable achievement was the test of the high current operation as mentioned above. This was made possible mainly by the development of new damped cavities. A number of other machine studies accomplishments that contributed to supplying stable photon beams to users are also reported.

Right after the end of the autumn run, the reconstruction of the 2.5 GeV storage ring started in December, 1996. This includes removal of old vacuum chambers, installation of new quadrupole and sextupole magnets, new beam monitor system, new injection system, new control system of the ring and insertion devices. Further efforts will be made to re-commission the ring in October, 1997.

Along with the work to improve the brilliance of the sources, significant efforts were also made to build new beamlines that make best use of the brilliant source characteristics. A good example is BL-2C which covers an energy range from 250 eV to 1400 eV. The optics of this beamline uses varied space plane grating and is able to attain a resolution of 5,000 - 10,000 over the entire energy range even with the present source parameters. With improved source parameters expected to become available with the new lower emittance operation, a resolution of better than 10,000 is expected with a reasonable photon flux. We are also continuing our efforts to rebuild several old beamlines with insufficient performance to meet the requirements of recent advanced experiments. Beamline BL-11A (80-1200eV) was build to replace an old grass-hopper monochromator beamline and aims to support XAFS studies of light elements. The beamline BL-12A (100-1200eV) was rejuvenated for the characterization of VUV and soft X-ray optical elements. Beamline BL-6B was converted into a macromolecular crystallography station in collaboration with the Tsukuba Advanced Research Alliance of the University of Tsukuba which includes 14 pharmaceutical companies as collaborators. We expect that this beamline will help activities of structure-based drug design. The old monochromator and mirror systems of BL-10C (small angle X-ray scattering) that have been used for 15 years were replaced by new ones in order to realize better focal spot, higher intensity and stable operation. A new XAFS beamline is being constructed on BL-9A which was formerly used as an X-ray lithography beamline by the NEC Corporation. The optics of this beamline utilizes two paraboloid mirrors and a double crystal monochromator.

Instrumental developments for diffraction,

scattering and spectroscopic experiments were also actively pursued. A spectrometer for polarized soft X-ray scattering was built and commissioned, which will make best use of the high resolution soft X-ray undulator beamline BL-2C. A photon-electron coincidence spectrometer was developed for Compton scattering experiments, which will be used for three dimensional determination of electron momentum density in solids. A fast detector using stacked avalanche photo-diodes was developed and used in x-ray diffraction experiments. This detector is capable of counting up to 10^9 photons/sec. Five more new developments that promises to contribute to users' activities are also reported in the section B, of the EXPERIMENTAL FACILITIES section.

Many users worked harder and more intensively on their experiments before the nine months long shutdown for the emittance upgrade, resulting in the production of many new scientific outputs. Some of highlights of the experiments are reported in the SCIENTIFIC DISCIPLINES section. Many reports on achievements of individual experimental proposals are presented in the USERS' REPORTS section.

In order to encourage users and in-house staff scientists to conduct extended or big-project-type research, a special category "S" is included in our proposal review system. The S-category proposals are active for 3 years and have priority beam time, up to 25 % of the beamtime of relevant experimental stations. Three S-category proposals were active through the period covered by this activity report: 94-S001 (high resolution photoelectron spectroscopy: Prof. Suga of Osaka University), 96-S001 (nuclear resonant scattering: Prof. Kikuta of the University of Tokyo) and 96-S002 (structural study under high pressure and high temperature: Prof. Yagi of the University of Tokyo). Reports by Suga (page S-1), Zhang (S-9) and Yagi (S-14) give some of the results obtained under those S-category proposals, respectively.

To compensate for the lack of in-house man-power for user support, the commitment of users in operating beamlines and experimental stations is encouraged. The small angle X-ray scattering station is a typical example of such stations. High-lights of structural biology experiments carried out on those stations are described on pages S-22 to S-26. The beam-time demands for the protein crystallography stations has been heavily exceeding supply. Despite this shortage of beam-time, many protein crystal structures have been solved using diffraction data accumulated at the Photon Factory as high-lighted on S-26 - S-29.

The first intravenous coronary angiography examination on a human subject in Japan was carried out on BL-NE1A at the AR in May, 1996. This was also the first time in the world that a two dimensional imaging system was used on a synchrotron beamline for such purposes. Clinically useful information was extracted from the images obtained and medical community praised the method as very promising.

The direct observation of charge and orbital ordering in perovskite-type manganite was made for the first time utilizing anomalous scattering of Mn and the ATS (Anisotropy of the Tensor of Susceptibility) technique. It should be noted that the first direct experimental evidence for the orbital ordering was obtained by measuring an intensity dependence on an azimuthal scanning of a super-lattice reflection. This experiment was carried out by the initiative of an in-house staff group and such contributions of in-house staff scientists are now encouraged.

Use of circularly or elliptically polarized synchrotron radiation has been continuously carried out. An example is the measurement of non-resonant magnetic scattering from ferromagnetic iron crystal described on pages S-5 - S-7. Especially, the use of X-ray phase plate to control the degree of linear and circular polarization was very effective in obtaining an enhancement of a flipping ratio of diffracted intensities between one magnetized direction and the reversed direction. In addition to the many projects with solid state samples, some gas phase experiments were also done. An example is the Xe double photoionization measurement which succeded in measuring the angular correlation pattern of the ejected two electrons for right and left circular polarization. The result reflects the electron-electron correlation in Xe atom. Several other remarkable scientific results are also given in the SCIENTIFIC DISCIPLINES section.

In the PROJECTS section, some results of the feasibility studies to convert the 6.5 GeV AR ring into a

dedicated single bunch X-ray machine are described. This proposal focusses on the use of intense pulse X-rays for time-resolved diffraction, scattering and spectroscopic experiments. Another major project was the operation of the TRISTAN Main Ring at 8 to 10 GeV for synchrotron radiation experiments during October to December, 1995. Despite the time limitations, tune-up of the ring, commissioning of the insertion device and the beamline went smoothly. We gained experiences in operating a ring having an emittance of several nm rad and handling super-brilliant X-ray beams. Several interesting results were obtained such as high resolution muscle diffraction (P-14) and two photon correlation in the X-ray region (P-20).

The present activity report is the last one to be published under the name "National Laboratory for High Energy Physics". In December, 1996, a decision was reached to establish a new organization, "High Energy Accelerator Research Organization" as a result of a merger of the National Laboratory for High Energy Physics, the Institute of Nuclear Studies, the University of Tokyo and the Meson Science Laboratory of the University of Tokyo. The new organization was established on April 1, 1997 and consists of four research institutes (Institute of Particle and Nuclear Studies, Institute of Materials Structure Science, Accelerator Laboratory, and Applied Science Laboratory). The Photon Factory became a part of the Institute of Materials Structure Science, along with two other user oriented facilities, the Neutron Science Laboratory (KENS) and the Meson Science Laboratory.

T. Matsushita, PF

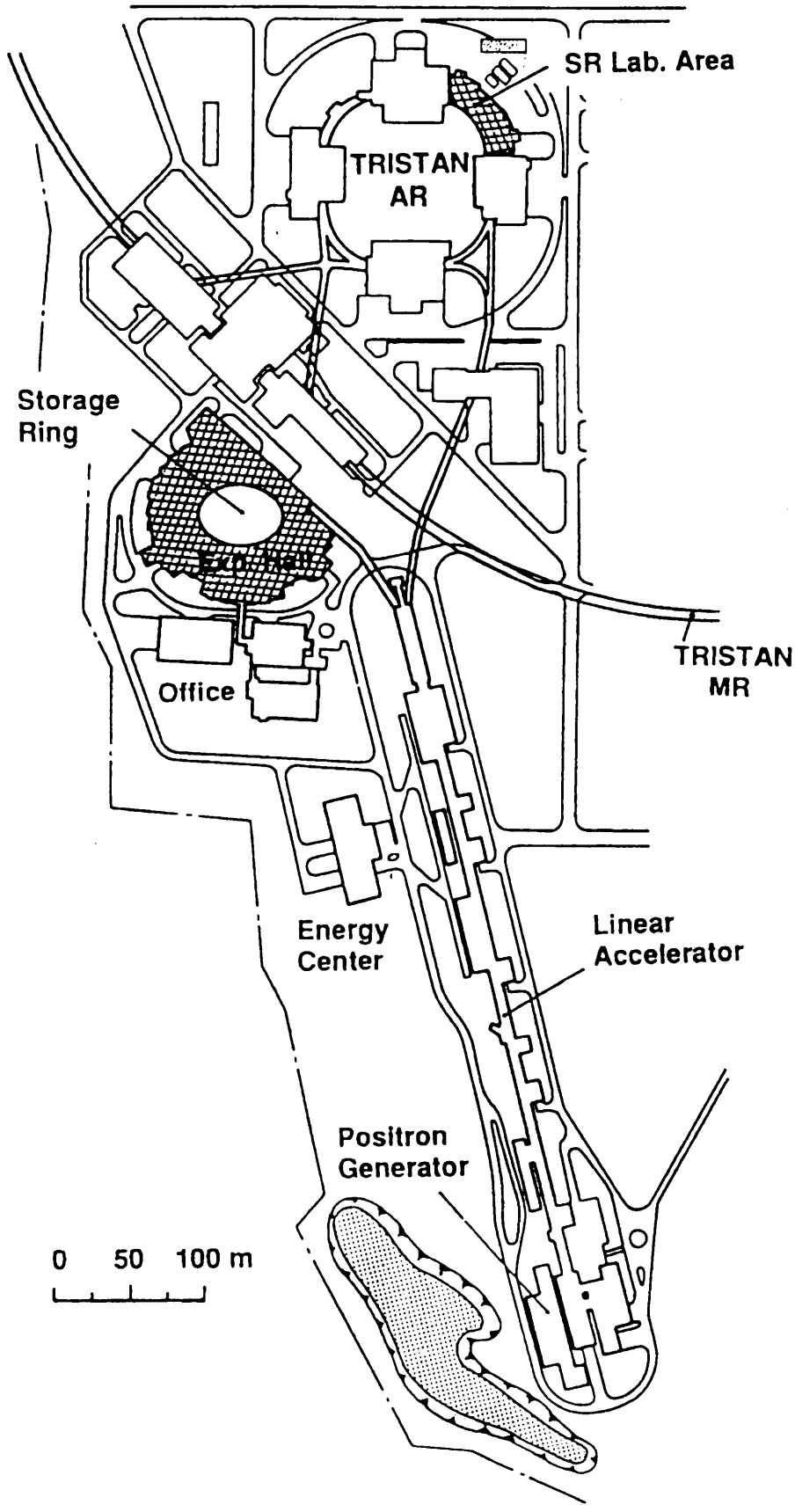

Fig. 1 Plan view of the Photon Factory

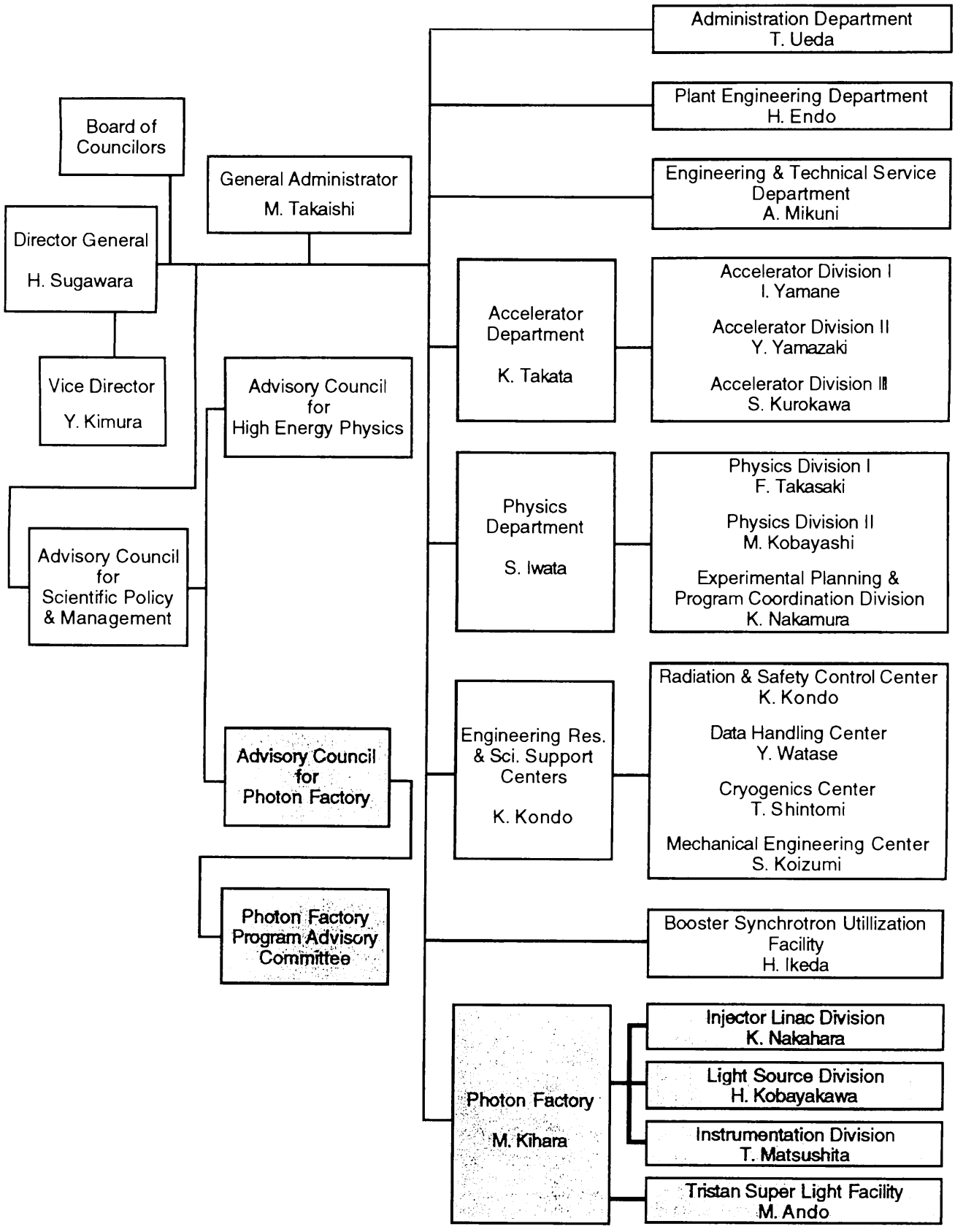

Fig. 2 Organization of KEK

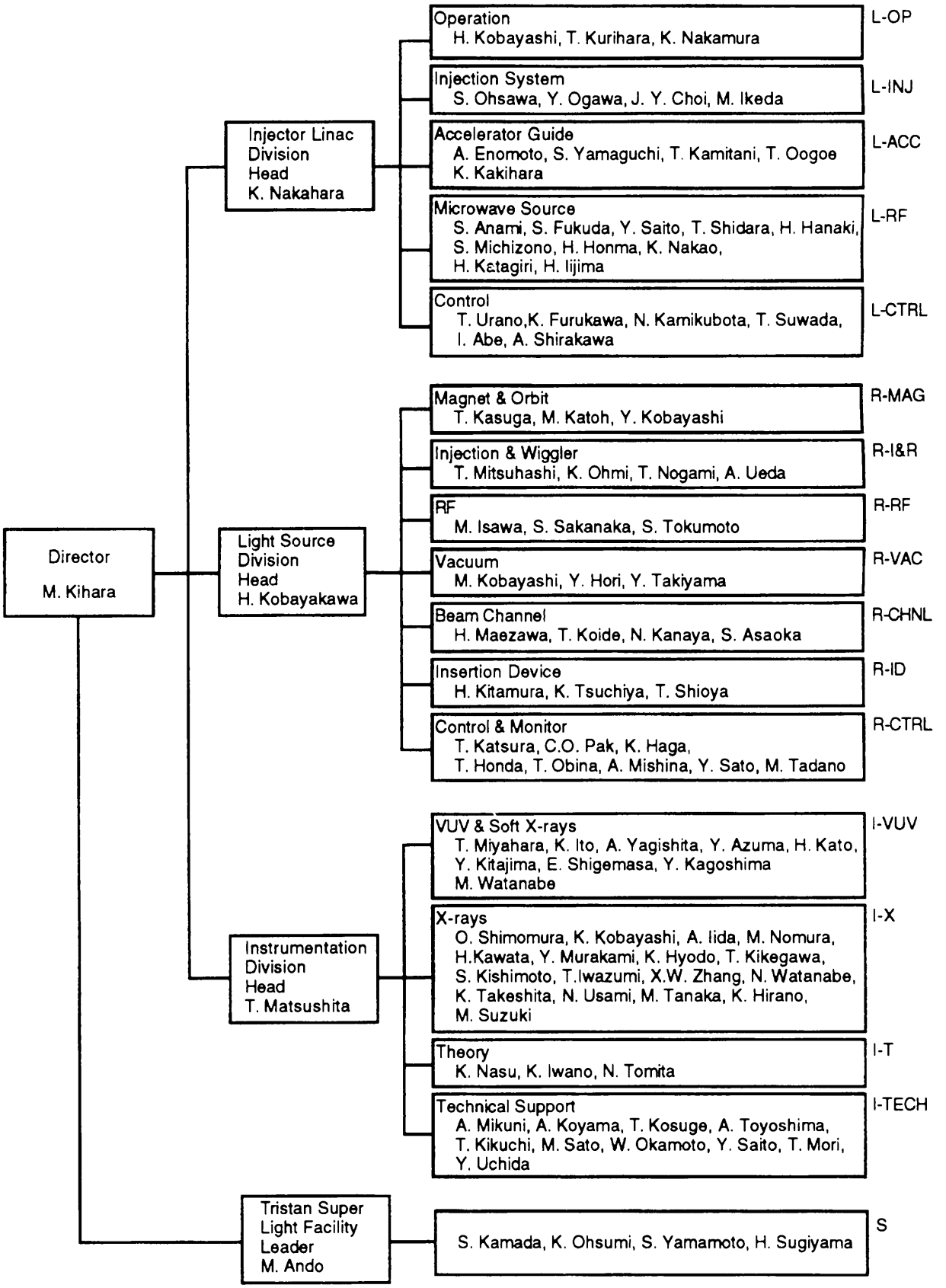

Fig. 3 Organization of the Photon Factory

Table 1a Members of Advisory Council; April '94 ~ March '96

** Chairman * Vice-Chairman

ANAMI, Shozo	Injector Linac Division, PF, KEK
ANDO, Masami	Tristan Super Light Facility, PF, KEK
FUJII, Yasuhiko	Institute for Solid State Physics, University of Tokyo
HIEDA, Kotaro	Faculty of Science, Rikkyo University
ISHII, Takehiko*	Institute for Solid State Physics, University of Tokyo
ITO, Kenji	Instrumentation Division, PF, KEK
KIKUTA, Seishi	Faculty of Engineering, University of Tokyo
KOBAYAKAWA, Hisashi	Light Source Division, PF, KEK
KOBAYASHI, Masanori	Light Source Division, PF, KEK
MAEZAWA, Hideki	Light Source Division, PF, KEK
MATSUSHITA, Tadashi	Instrumentation Division, PF, KEK
MITSUI, Yukio	Department of Bio Engineering, Nagaoka University of Technology
NAKAHARA, Kazuo	Injector Linac Division, PF, KEK
NAKAJIMA, Tetsuo	Instrumentation Division, PF, KEK
NITTONO, Osamu	Faculty of Engineering, Tokyo Institute of Technology
OHTA, Toshiaki	Faculty of Science, University of Tokyo
SATO, Isamu**	Injector Linac Division, PF, KEK
SHIMOMURA, Osamu	Instrumentation Division, PF, KEK
SHIOTANI, Nobuhiro	Tokyo University of Fisheries
SUGA, Shigemasa	Faculty of Engineering Science, Osaka University
SUZUKI, Kenji	Institute for Materials Research, Tohoku University

Table 1b Members of Advisory Council; April '96 ~ March '97

** Chairman * Vice-Chairman

ANAMI, Shozo	Injector Linac Division, PF, KEK
FUJII, Yasuhiko*	Institute for Solid State Physics, University of Tokyo
HIEDA, Kotaro	Faculty of Science, Rikkyo University
IIDA, Atsuo	Instrumentation Division, PF, KEK
ITO, Kenji	Instrumentation Division, PF, KEK
KASUGA, Toshio	Light Source Division, PF, KEK
KIKUTA, Seishi	Faculty of Engineering, University of Tokyo
KOBAYAKAWA, Hisashi	Light Source Division, PF, KEK
KOBAYASHI, Hitoshi	Injector Linac Division, PF, KEK
KOBAYASHI, Masanori	Light Source Division, PF, KEK
MAEZAWA, Hideki	Light Source Division, PF, KEK
MATSUSHITA, Tadashi**	Instrumentation Division, PF, KEK
MITSUI, Yukio	Department of Bio Engineering, Nagaoka University of Technology
NAKAHARA, Kazuo	Injector Linac Division, PF, KEK
OHTA, Toshiaki	Faculty of Science, University of Tokyo
OSHIMA, Masaharu	Faculty of Engineering, University of Tokyo
SATO, Shigeru	Faculty of Scinece, Tohoku University
SHIMOMURA, Osamu	Instrumentation Division, PF, KEK
SHIOTANI, Nobuhiro	Tokyo University of Fisheries
SUGA, Shigemasa	Faculty of Engineering Science, Osaka Univ.
WAKABAYASHI, Katsuzo	Faculty of Engineering Science, Osaka Univ.

Table 2a Members of Program Advisory Committee; Fiscal Year '95

* Chairman

ASHIDA, Tamaichi	School of Engineering, Nagoya University
JO, Takeo	Faculty of Science, Hiroshima University
KAKIZAKI, Akito	Institute for Solid State Physics, University of Tokyo
KATAOKA, Mikio	Faculty of Science, Osaka University
KOBAYAKAWA, Hisashi	Light Source Division, PF, KEK
MATSUSHITA, Tadashi*	Instrumentation Division, PF, KEK
OHSUMI, Kazumasa	Instrumentation Division, PF, KEK
OYANAGI, Hiroyuki	Electrotechnical Laboratory
SAKAI, Nobuhiko	Faculty of Science, Himeji Institute of Technology
SATO, Isamu	Injector Linac Division, PF, KEK
SATO, Yukinori	Research Institute for Scientific Measurements, Tohoku University
TSUJI, Kazuhiko	Faculty of Science and Technology, Keio University
TSUKIHARA, Tomitake	Institute for Protein Research, Osaka University
YAMAGUCHI, Toshio	Faculty of Science, Fukuoka University
WAKABAYASHI, Katsuzo	Faculty of Engineering Science, Osaka University

Table 2b Members of Program Advisory Committee; Fiscal Year '96

* Chairman

HAMAYA, Nozomu	Faculty of Science, Ochanomizu University
JO, Takeo	Faculty of Science, Hiroshima University
KAKIZAKI, Akito	Institute for Solid State Physics, University of Tokyo
KATAOKA, Mikio	Graduate School of Science, Osaka University
KOBAYAKAWA, Hisashi	Light Source Division, PF, KEK
MATSUSHITA, Tadashi*	Instrumentation Division, PF, KEK
MIKI, Kunio	Graduate School of Science, Kyoto University
NAKAHARA, Kazuo	Injector Linac Division, PF, KEK
OHSUMI, Kazumasa	Instrumentation Division, PF, KEK
TAKAHASHI, Toshio	Institute for Solid State Physics, University of Tokyo
TSUKIHARA, Tomitake	Institute for Protein Research, Osaka University
UDAGAWA, Yasuo	Research Institute for Scientific Measurements, Tohoku University
YAGI, Naoto	School of Medicine, Tohoku University
YAGISHITA, Akira	Instrumentation Division, PF, KEK
YAMAGUCHI, Toshio	Faculty of Science, Fukuoka University

Table 3 Staff members of the Photon Factory

Name		Responsibility*	e-mail address
Research Staff			
KIHARA, Motohiro		Director	KIHARAM@KEKVAX.KEK.JP
ANAMI, Shozo		L-RF	ANAMI@KEKVAX.KEK.JP
CHOI, Jae-Young	Aug. 31, 96 L	L-INJ	CHOIJ@KEKVAX.KEK.JP
ENOMOTO, Atsushi		L-ACC	ENOMOTOA@KEKVAX.KEK.JP
FUKUDA, Shigeki		L-RF	SFUKUDA@KEKVAX.KEK.JP
FURUKAWA, Kazuro		L-CTRL	FURUKAWA@MAPLE.KEK.JP
HANAKI, Hirofumi		L-RF	HANAKI@KEKVAX.KEK.JP
KAMIKUBOTA, Norihiko		L-CTRL	KAMI@KEKVAX.KEK.JP
KAMITANI, Takuya		L-ACC	KAMITANI@MAPLE.KEK.JP
KOBAYASHI, Hitoshi		L-OP	HITOSHIK@KEKVAX.KEK.JP
KURIHARA, Toshikazu		L-OP	TKURIHAR@KEKVAX.KEK.JP
MICHIZONO, Shin'ichiro		L-RF	MICHIZON@MAPLE.KEK.JP
NAKAHARA, Kazuo		L-Head	NAKAHAR@KEKVAX.KEK.JP
OGAWA, Yujiro		L-INJ	OGAWAYJ@KEKVAX.KEK.JP
OHSAWA, Satoshi		L-INJ	OHSAWA@KEKVAX.KEK.JP
SAITO, Yoshio	Sep. 16, 96 L	L-RF	
SHIDARA, Tetsuo		L-RF	SHIDARA@KEKVAX.KEK.JP
SUWADA, Tsuyoshi		L-CTRL	SUWADA@MAIL.KEK.JP
URANO, Takao		L-CTRL	URANO@MAPLE.KEK.JP
YAMAGUCHI, Seiya		L-RF	SYAMA@MAPLE.KEK.JP
HAGA, Kaiichi		R-CTRL	HAGA@KEKVAX.KEK.JP
HONDA, Tohru		R-CTRL	HONDAT@CCPFMAIL.KEK.JP
HORI, Yoichiro		R-VAC	HORI@KEKVAX.KEK.JP
ISAWA, Masaaki		R-RF	ISAWA@KEKVAX.KEK.JP
KANAYA, Noriichi		R-CHNL	KANAYA@KEKVAX.KEK.JP
KASUGA, Toshio		R-MAG	KASUGAT@KEKVAX.KEK.JP
KATOH, Masahiro		R-MAG	KATOHM@KEKVAX.KEK.JP
KATSURA, Tomotaro		R-CTRL	KATSURA@KEKVAX.KEK.JP
KITAMURA, Hideo	Mar. 31, 97 L	R-ID	
KOBAYAKAWA, Hisashi	Mar. 31, 97 L	R-Head	KOBAYAKA@KEKVAX.KEK.JP
KOBAYASHI, Masanori		R-VAC	KOBYSIMR@KEKVAX.KEK.JP
KOBAYASHI, Yukinori		R-MAG	YUKINORI@KEKVAX.KEK.JP
KOIDE, Tsuneharu	Jan. 31, 97 L	R-CHNL	TKOIDE@KEKVAX.KEK.JP
MAEZAWA, Hideki		R-CHNL	MAEZAWAH@KEKVAX.KEK.JP
MITSUHASHI, Toshiyuki		R-I&W	MITSUHAS@KEKVAX.KEK.JP
OBINA, Takashi	Jul. 1, 96 J	R-CTRL	OBINA@KEKVAX.KEK.JP
OHMI, Kazuhito		R-I&W	OHMI@PINECONE.KEK.JP
PAK, Cheol On		R-CTRL	PAK@KEKVAX.KEK.JP
SAKANAKA, Shyogo		R-RF	SAKANAKA@MAIL.KEK.JP
TSUCHIYA, Kimichika		R-ID	TSUCHIYA@KEKVAX.KEK.JP
AZUMA, Yoshiro		I-VUV	AZUMA@KEKVAX.KEK.JP
HIRANO, Keiichi		I-X	HIRANO@CCPFMAIL.KEK.JP
HYODO, Kazuyuki		I-X	HYODO@KEKVAX.KEK.JP
IIDA, Atsuo		I-X	AIIDA@CCPFMAIL.KEK.JP
ITO, Kenji		I-VUV	ITO@KEKVAX.KEK.JP
IWANO, Kaoru		I-T	IWANO@NASUWS1.KEK.JP
IWAZUMI, Toshiaki		I-X	IWAZUMI@KEKVAX.KEK.JP
KAGOSHIMA, Yasushi	Sep. 30, 96 L	I-VUV	KAGOSIMA@KEKVAX.KEK.JP
KATO, Hiroo		I-VUV	HIROO@KEKVAX.KEK.JP
KAWATA, Hiroshi		I-X	KAWATA@KEKVAX.KEK.JP
KIKEGAWA, Takumi		I-X	KIKEGAWA@KEKVAX.KEK.JP
KISHIMOTO, Shunji		I-X	KISIMOTO@KEKVAX.KEK.JP
KITAJIMA, Yoshinori		I-VUV	KITAJIMA@KEKVAX.KEK.JP

(to be continued)

Name		Responsibility*	e-mail address
KOBAYASHI, Katsumi		I-X	KOBAYASK@KEKVAX.KEK.JP
KOIDE, Tsuneharu	Feb. 1, 97 J	I-VUV	TKOIDE@KEKVAX.KEK.JP
MATSUSHITA, Tadashi		I-Head	MATSUS@KEKVAX.KEK.JP
MIYAHARA, Tsuneaki	Sep. 30, 96 L	I-VUV	MIYAHARA@KEKVAX.KEK.JP
MURAKAMI, Youichi		I-X	MYOUICHI@KEKVAX.KEK.JP
NASU, Keiichiro		I-T	KNASU@NASUWS1.KEK.JP
NOMURA, Masaharu		I-X	NOMURAM@CCPFMAIL.KEK.JP
SHIGEMASA, Eiji		I-VUV	SIGEMASA@CCPFMAIL.KEK.JP
SHIMOMURA, Osamu	Mar. 31, 97 L	I-X	SHIMOMURA@KEKVAX.KEK.JP
SUZUKI, Mamoru		I-X	SUZUKI@PFWEIS.KEK.JP
TAKESHITA, Kunikazu	Sep. 30, 96 L	I-X	TAKESHIT@KEKVAX.KEK.JP
TANAKA, Masahiko		I-X	MASAHIKO@KEKVAX.KEK.JP
TOMITA, Norikazu		I-T	TOMITA@NASUWS4.KEK.JP
USAMI, Noriko		I-X	USAMI@CCPFMAIL.KEK.JP
WATANABE, Masamitsu	Sep. 16, 96 J	I-VUV	MASAMITU@KEKVAX.KEK.JP
WATANABE, Nobuhisa		I-X	NOBUHISA@CCPFMAIL.KEK.JP
YAGISHITA, Akira		I-VUV	YAGISITA@KEKVAX.KEK.JP
ZHANG, Xiaowei		I-X	XIAOWEI@KEKVAX.KEK.JP
ANDO, Masami		S-Leader	ANDO@MAIL.KEK.JP
KAMADA, Susumu		S	KAMADA@KEKVAX.KEK.JP
OHSUMI, Kazumasa		S	OHSUMIK@KEKVAX.KEK.JP
SUGIYAMA, Hiroshi		S	HIROSHIS@MAIL.KEK.JP
YAMAMOTO, Shigeru		S	SHIGERU@KEKVAX.KEK.JP
Supporting Staff			
ABE, Isamu		L-CTRL	ABEI@KEKUX1.KEK.JP
HONMA, Hiroyuki		L-RF	HONMA@MAPLE.KEK.JP
IIJIMA, Hitoshi		L-RF	
IKEDA, Mitsuo	May 1, 96 J	L-INJ	IKEDAM@MAPLE.KEK.JP
KAKIHARA, Kazuhisa		L-ACC	KAKIHARA@KEKVAX.KEK.JP
KATAGIRI, Hiroaki		L-RF	KATAGIRI@KEKVAX.KEK.JP
NAKAMURA, Kie		L-OP	KIE@KEKVAX.KEK.JP
NAKAO, Katsumi		L-RF	NAKAOK@KEKVAX.KEK.JP
OOGOE, Takao		L-ACC	OOGOE@KEKVAX.KEK.JP
SHIRAKAWA, Akihiro		L-CTRL	SIRAKAWA@KEKVAX.KEK.JP
ASAOKA, Seiji		R-CHNL	
MISHINA, Atsushi		R-CTRL	MISHINA@KEKVAX.KEK.JP
NOGAMI, Takashi		R-I&W	NOGAMI@MAIL.KEK.JP
SATO, Yoshihiro		R-CTRL	YOSHIHIR@KEKVAX.KEK.JP
SHIOYA, Tatsuro		R-ID	SHIOYA@MAIL.KEK.JP
TADANO, Mikito		R-CTRL	TADANO@CCCEMAIL.KEK.JP
TAKIYAMA, Youichi	Mar. 31, 97 L	R-VAC	TAKIYAMA@KEKVAX.KEK.JP
TOKUMOTO, Shuichi		R-RF	TOKUMOTO@KEKVAX.KEK.JP
UEDA, Akira		R-I&W	UEDA@PINECONE.KEK.JP
KIKUCHI, Takashi		I-TECH	KIKUCHI@KEKVAX.KEK.JP
KOSUGE, Takashi		I-TECH	KOSUGE@PFIQST.KEK.JP
KOYAMA, Atsushi		I-TECH	KOYAMA@KEKVAX.KEK.JP
MIKUNI, Akira		I-TECH	MIKUNI@KEKVAX.KEK.JP
MORI, Takeharu		I-TECH	MORIT@KEKVAX.KEK.JP
OKAMOTO, Wataru		I-TECH	OKAMOTOW@KEKVAX.KEK.JP
SAITO, Yuuki		I-TECH	YSAITO@CCPF1.KEK.JP
SATO, Masato		I-TECH	SATOM@KEKVAX.KEK.JP
TOYOSHIMA, Akio		I-TECH	TOYOSIMA@CCPFMAIL.KEK.JP
UCHIDA, Yoshinori		I-TECH	UCHIDA@KEKVAX.KEK.JP

*: Refer to Fig. 3 for abbreviations.
J: Date when he/she joinded the PF.
L:Date when he/she left the PF.
R:Date when he/she retired from the PF.

Table 4 Annual number of staff & visiting scientists

Position	Department	1986	1987	1988	1989	1990	1991	1992	1993	1994	1995	1996
Chief Director		1	1	1	1	1	1	1	1	1	1	1
Professor	Injector Linac	4	4	4	3	3	4	3	3	3	4	4
	Light Source	4	4	4	4	5	5	4	5	5	5	6
	Instrumentation	3	4	5	5	5	6	8	9	8	8	7
Associate Professor	Injector Linac	1	2	3	5	7	6	7	7	7	6	4
	Light Source	3	3	3	5	4	3	3	3	3	3	3
	Instrumentation	7	9	7	10	9	8	10	10	11	10	8
Research Associate	Injector Linac	11	10	10	9	8	9	9	9	10	10	9
	Light Source	9	12	12	9	11	11	12	12	12	12	12
	Instrumentation	13	13	14	11	15	15	15	18	18	17	17
Technical Staff	Injector Linac	7	8	9	10	11	11	11	11	11	10	10
	Light Source	7	7	8	10	10	10	10	10	9	9	9
	Instrumentation	8	9	11	10	9	10	10	10	10	10	10
Visiting Scientist	Injector Linac	2	2	2	2	2	2	2	1	0	1	2
	Light Source	4	4	4	4	4	4	4	3	3	4	4
	Instrumentation	6	6	6	6	6	7	6	6	3	6	6
Total		90	98	103	104	110	112	115	118	114	116	112

Table 5 Budget in earch fiscal year

(in million yen)

Item	1986	1987	1988	1989	1990	1991	1992	1993	1994	1995	1996
Salary	561	561	642	757	764	859	898	939	1,029	1,163	1,097
PF Storage (channel, insertion device, etc.)	131	647	0	0	196	103	0	0	0	428	0
PF Experiments	190	196	237	341	367	399	375	366	366	366	328
PF Operation & Maintenance	820	907	962	1,078	1,107	1,107	1,042	1,015	1,096	1,096	984
Computer Rentals	136	136	141	145	145	145	145	145	140	145	144
Positron Source & Electric Plant Operation	138	208	258	300	308	300	253	224	175	157	84
Cooling System & Electric Operation	211	214	217	231	235	240	218	212	218	217	281
Electricity	381	331	355	425	423	423	423	418	431	431	905
PF-Industrial Cooperative Experiments	185	166	302	219	171	174	154	132	86	81	83
AR Construction and Experiments		398	267	387	250	260	148	145	145	145	130
AR Operation & Maintenance											835
B Factory (Linac Upgrade)									400	1,567	658
Miscellaneous	162	120	301	243	287	388	564	877	567	609	345
Total	2,915	3,884	3,682	4,126	4,253	4,398	4,220	4,473	4,653	6,405	5,874

Table 6 Summary of operation in FY 1995 (April 1995 - March 1996)

(hours)

Cycle	Linac	PF Ring	User's time*	AR	Dedicated to SR at AR
1	2856	2808	2376	2448	1536
2	1512	1464	1160	960	0
Total	4368	4272	3536	3408	1536

*Bonus time not included

Table 7 Timetable of the Machine Operation in FY 1996.
PF: PF ring AR: TRISTAN accumulation ring
MR: TRISTAN main ring

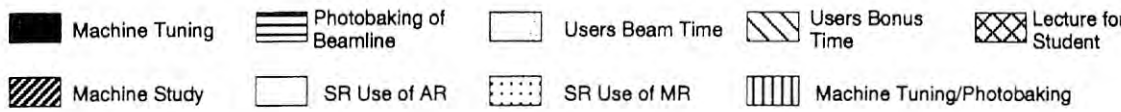

cycle																									
	Time	MON 9 17	TUE 9 17	WED 9 17	THU 9 17	FRI 9 17	SAT 9 17	SUN 9 17	MON 9 17	TUE 9 17	WED 9 17	THU 9 17	FRI 9 17	SAT 9 17	SUN 9 17	MON 9 17	TUE 9 17	WED 9 17	THU 9 17	FRI 9 17	SAT 9 17	SUN 9 17			
1	Date	3/25	26	27	28	29	30	31	4/1	2	3	4	5	6	7	8	9	10	11	12	13	14			
	Linac																								
	PF																								
	AR																								
	MR																								
1	Date	15	16	17	18	19	20	21	22	23	24	25	26	27	28	29	30	5/1	2	3	4	5			
	Linac																								
	PF																								
	AR																								
	MR																								
1	Date	6	7	8	9	10	11	12	13	14	15	16	17	18	19	20	21	22	23	24	25	26			
	Linac																								
	PF																								
	AR																								
	MR																								
1	Date	27	28	29	30	31	6/1	2	3	4	5	6	7	8	9	10	11	12	13	14	15	16			
	Linac																								
	PF																								
	AR																								
	MR																								
1	Date	17	18	19	20	21	22	23	24	25	26	27	28	29	30	7/1	2	3	4	5	6	7			
	Linac																								
	PF																								
	AR																								
	MR																								
1	Date	8	9	10	11	12	13	14	15	16	17	18	19	20	21	22	23	24	25	26	27	28			
	Linac																								
	PF																								
	AR																								
	MR																								
2	Date	10/14	15	16	17	18	19	20	21	22	23	24	25	26	27	28	29	30	31	11/1	2	3			
	Linac																								
	PF																								
	AR																								
	MR																								
2	Date	4	5	6	7	8	9	10	11	12	13	14	15	16	17	18	19	20	21	22	23	24			
	Linac																								
	PF																								
	AR																								
	MR																								
2	Date	25	26	27	28	29	30	12/1	2	3	4	5	6	7	8	9	10	11	12	13	14	15			
	Linac																								
	PF																								
	AR																								
	MR																								
2	Date	16	17	18	19	20	21	22	23	24	25	26	27	28	29	30	31	1/1	2	3	4	5			
	Linac																								
	PF																								
	AR																								
	MR																								

SEMINARS, MEETINGS AND WORKSHOPS

Thirty three seminars were given by in-house staff and visiting scientists during the period from Octorber 1995 to March 1997. Thirteen users' meetings and workshops were held during the same period, including the annual PF symposium.

PF Seminars

Ukai, M. (Department of Applied Physics, Tokyo University of Agriculture and Technology)
Spectroscopy of Superexcited Molecules in the Region of Valence Shell Absorption — October 20, 1995

Lablanquie, P. (LURE)
Investigation of Double Photoionisation Processes Using Electron-Electron Coincidence Techniques — October 24, 1995

Tischer, M. (Freie Universität Berlin)
Investigation of Co and Ni Monolayers by Means of Magnetic Circular X-Ray Dichroism and Element Specific Magnetic Susceptibility — October 30, 1995

Dmitrienko, V. E. (A.V. Shubnikov Institute of Crystallography, Russian Academy of Sciences)
X-Ray Diffraction Optics, Forbidden Reflections, Polarization Phenomena, Coherence, etc. — November 7, 1995

Wulff, M. (ESRF)
The Realisation of Ultra Fast Diffraction Methods for Protein Crystallography at ESRF — November 8, 1995

Akahama, Y. (Faculty of Science, Himeji Institute of Technology)
Pressure-Induced Structural Transition and Metallization of Solid Oxygen — November 24, 1995

Michael, B. D. (Cancer Research Trust Gray Laboratory)
Studies on the Energetics and Reaction Kinetics of Radiation Damege to DNA — December 19, 1995

Takahashi, T. (Institute for Solid State Physics, University of Tokyo)
Surface and Interface Structures by X-Ray Diffraction — December 22, 1995

Ivanov, S. (Moscow State University)
Optical Design of Undulator Beamlines and Monochromators at the Kurchatov Synchrotron Radiation Source (project) — February 1, 1996

Smolyakov, N. (Kurchatov Synchrotron Radiation Source)
VUV-Undulator with Low Heat Load for High Energy Electron Storage Rings — February 1, 1996

Wakabayashi, K. (Faculty of Engineering Science, Osaka University)
X-Ray Diffraction Studies on the Molecular Mechanism of Muscular Contraction: Recent Topics — February 2, 1996

Fandrich, F. (Max-Planck-Gesellschaft)
High-Resolution X-Ray Sensitive CCD Camera Systems for X-Ray Topography and Diffractometry — February 16, 1996

Kotani, A. (Institute for Solid State Physics, University of Tokyo)
Theory of X-Ray Emission Spectra — February 23, 1996

Eichler, J. (Institute of Applied Physics, Tsukuba University)
Radiative Electron Capture in Relativistic Atomic Collisions — March 14, 1996

Okudaira, K. (Faculty of Engineering, Chiba University)
Studies of Molecular Orientation, Electronic Structure and Energy-Selective Photochemical Reaction in Organic Ultrathin Films — March 15, 1996

Enomoto, R. (Physics Department, KEK)
Detector Technology and its Application in High Energy Physics Experiment — March 22, 1996

Noelle, D. (Dortmund University)
DELTA and VUV-FEL; Status and Prospects — April 23, 1996

Oyanagi, H. (Electrotechnical Laboratory)
Dynamic Processes in Solids: Probed by X-Ray Absorption Fine Structure — April 26, 1996

Fukai, Y. (Department of Physics, Chuo University)
Metals and Alloys under High Hydrogen Pressures — May 31, 1996

Hieda, K. (Faculty of Science, Rikkyo University)
DNA Damage Induced by Monochromatic Vacuum-UV and Soft X-Ray Photons — July 5, 1996

Altun, Z. (Department of Physics, Marmara University)
Photoionization of Complex Atoms — July 9, 1996

Martensson, N. (Department of Physics, Uppsala University)
Resonant Photoemission and Resonant Auger Raman Investigations of Adsorbates and Solids:Dynamics of Core – Hole Decay and Competing (femtosecond processes) – Coherent vs. Incoherent Processes — July 17, 1996

Yanagihara, M. (Research Institute for Scientific Measurements, Tohoku University)
Effects of the Core Hole on Soft-X-Ray Emissions : B 1s Emission in h-BN — July 26, 1996

Takenaka, H. (NTT Interdisciplinary Research Laboratory)
Technology and Application on Multi-Layer X-Ray Optics — September 18, 1996

Seki, K. (Graduate School of Science, Nagoya University)
Molecular Orientation and Electronic Structures of Organic Ultrathin Films and Interfaces Studied by Synchrotron Radiation — September 27, 1996

Watanabe, M. (Photon Factory, KEK)
Research on Many Electron Effects and Line Shapes of Photoelectron and Photo-Luminescence Spectra of Alkali Metals, Mg, and Al — October 25, 1996

Polack, F. (Optics Group, LURE)
X-UV and X-Ray Beamline Optics at LURE Super-ACO — November 15, 1996

Tokunaga, F. (Graduate School of Science, Osaka University)
Light-Induced Structural Change of Photo-Energy Conversion Membrane "Purple E Membrane" — November 29, 1996

Dietz, K. (Universität Bonn)
A Theoretical Description of Molecules and Atoms Interacting with Short, Intense Laser Pulses — December 12, 1996

Cherepkov, N. A. (State Academy of Aerospace Instrumentation)
Photoionization of Polarized Atoms: Applications of Free Atoms and Ferromagnets — December 20, 1996

Ikeda, S. (Booster Synchrotron Utilization Facility, KEK)
Visualizing the Hydrogen Wave Function – Isotope Effects in Hydrogen Bond Dielectrics — January 24, 1997

Ikeda, H. (Booster Synchrotron Utilization Facility, KEK)
Neutron Scattering from Percolating Magnets with Fractal Geometry — February 28, 1997

Doyama, M. (Teikyo University of Science Technology)
Development and Applications of Positron Microscopes — March 19, 1997

Meetings and Workshops

School on the New Powder Diffractometer with a Multiple-Detector System at the BL-4B Experimental Station	December 12-13, 1995
International Workshop on the Generation and Application of Coherent X-rays	January 10-11, 1996
Future Prospects of Studies in the VUV and Soft-Xray Regions at the Photon Factory	March 4-5, 1996
Meeting on the MR Light Source Experiments	March 6-7, 1996
Workshop on Triply Photoexcited Hollow Lithium	March 8, 1996
Kick-off Meeting of the Advanced PF-AR	April 25, 1996
Workshop on XAFS at the Advanced PF-AR	May 13, 1996
Workshop on the Monochromator for the MR Light Source	July 12, 1996
PF–SPring-8 Joint Workshop on the Control System	September 24-25, 1996
The First User's Meeting for Atomic and Molecular Science	November 8, 1996
The Workshop on the Future of Single-Bunch Operation at the Photon Factory	November 26, 1996
Theoretial X-ray Spectroscopy Workshop	December 5-6, 1996
The 14th Photon Factory Symposium	December 16-17, 1996

Awards

Tsukuba Prize, 1996

Masami ANDO, Kazuyuki HYODO (KEK), Yasuro SUGISHITA, Yuji ITAI, Sadanori OHTSUKA, Tohru TAKEDA (Univ. of Tsukuba)
"Development of a two-dimensional imaging susyem for intravenose coronary angiography using synchrotron radiation"

Young Scientests Award of the Crystallographic Society of Japan, 1996

Mamoru SUZUKI (KEK)
"Structure Analysis of MIF by Multi-wavelength Dispersion Method using Genetic Engineering"

Publications

PHOTON FACTORY NEWS ISSN 0916-0604 Vol.14, No.1-4

GRADUATE UNIVERSITY FOR ADVANCED STUDIES

The Graduate University for Advanced Studies was established in 1988. It has the following three schools:

School of Cultural Studies
School of Mathematical and Physical Sciences
School of Life Sciences

KEK has participated in the Graduate University to form the Department of Synchrotron Radiation Science and the Department of Accelerator Science, both of which belong to the School of Mathematical and Physical Sciences.

Students in the Department of Synchrotron Radiation Science are expected to study the basic theory of generation of synchrotron radiation, its characteristics, interaction of radiation with matter, and then engage in research by utilizing various facilities at the PF. Areas of thesis research include the development of radiation sources, optical elements, and instruments for diffraction, scattering, spectroscopy, and irradiation experiments as well as exploration of new areas of application of synchrotron radiation to science and technology.

DOCTORAL DEGREE RECIPIENTS IN 1996 AND 1997.

CHOWDHURY, Ali Zafor, Ph.D. (March 21, 1996)
"Generalized Hubbard Model for Electronic States of Potassium Doped Zeolite and Barium Bismuthate."
Thesis Advisor: K. Nasu
Committee Chair: T. Miyahara

UCHIDA, Masaya, Ph.D. (March 21, 1996)
"Crystallographic Study of Olivine in Thin Sections by the Micro-area Diffraction Method."
Thesis Advisor: M. Ohsumi
Committee Chair: O. Shimomura

ZHAO, Jiyong, Ph.D. (March 21, 1996)
"Study of Nuclear Resonant Bragg Scattering from Synthetic 2.2% and 95% ^{57}Fe Hematitie Single Crystals."
Thesis Advisor: M. Ando
Committee Chair: T. Miyahara

ADACHI, Takafumi, Ph.D. (March 24, 1997)
"Structual Phase Transition and Charge Fluctuations in NaCl-type Rare Earth Compounds under High Pressure."
Thesis Advisor: O. Shimomura
Committee Chair: K. Ohsumi

OKITSU, Kohei Ph.D. (March 24, 1997)
"Dielectric Anisotropy of Cobalt Crystals near K-Absorption Edge Measured by Using an Energy Tunable X-ray Polarimeter with a Phase Retarder."
Thesis Advisor: T. Matsushita
Committee Chair: A. Iida

PROPOSAL GUIDELINES FOR EXPERIMENTERS AT PHOTON FACTORY

1. HOW TO SUBMIT A PROPOSAL

Photon Factory is open to everybody in scientific research. A proposal should be filed on a new application form which is available on request from the Research Cooperation Section of the Administration Department of KEK. Proposals with the old form will not be accepted. An applicant should carefully read the guide before filing an application. A spokesperson should get the agreement of the members to join the team.

An overseas applicant is requested to find an appropriate "contact person in Japan (CPJ)", who will mediate between the applicant and KEK*. Please contact the person in charge of the experimental station you want to use, if you do not know any appropriate CPJ. He/she will suggest the persons appropriate for the applicant's research plan. A list of the people in charge of the experimental stations can be found in this report.

All experimental proposals are subject to approval of the Photon Factory Program Advisory Committee (PF-PAC). In Table 8, we have shown the total number of proposals approved by this PAC. The CPJ will be informed about the decision.

*The contact person in Japan will help you translate Japanese and English, assist with visa applications and your experiments. In order to assure his/her agreement the signature or seal imprint of the CPJ is required.

2. CATEGORY OF PROPOSALS

2.1 for university researchers etc.

There are four categories of application; G(General), S1, S2(Special), P(Preliminary) and U(Urgent). The character, process of approval and terms of validity are different among those categories.

G is the category for general experiments using synchrotron radiation. Deadlines of application and valid terms are as follows:

Deadlines:
November 7, 1997 (a) and May 1, 1998 (b)
Valid terms:
from April, 1998 to March, 2000 for (a)
from October, 1998 to September, 2000 for (b)

P is the category for preliminary experiments in order to determine the feasibility of proposals for categories G or S2 and for the new comers in this field. There are some limitations as listed below.

1) The maximum beamtime for one project is less than about 120 hours.
2) One spokesperson can have only one project at a time.
3) More than three proposals of this category cannot be approved for an experimental station at a PF-PAC.

Deadlines:
November 7, 1997 (a) and May 1, 1998 (b)
Valid terms:
from April, 1998 to March, 1999 for (a)
from October, 1998 to September, 1999 for (b)

S1 is the category for those projects that require major apparatus developments. Please contact the Research Cooperation Section regarding details about the S1 category.

S2 is the special category for those experiments that may have extremely high scientific value and may need much machine time. Among those could be experiments for the development of a difficult technique or those requiring special operation of the storage ring. Photon Factory supports the projects of this category financially within certain limits; the funds cannot be used for travel expenses or salary. At least one Japanese scientist should be included in a team. The process of judgement is different from other categories. An applicant has to present his/her proposal orally before the PF-PAC. Deadline and valid term are as follows:

Deadlines:
September 19, 1997 (a) and March 20, 1998 (b)
Valid term:
from April, 1998 to March, 2001 for (a)
from October, 1998 to September, 2001 for (b)

The progress report should be presented at the "Photon Factory Symposium" which takes place every year.

U is the category for urgent proposals which cannot be postponed until the next deadline, and which are of extremely high scientific value. Once approved, these projects may exclude already assigned beamtime for other projects. Applicants can apply at any time but the valid terms are limited as follows:

a project approved between October and March: until end of March,
a project approved between April and September: until end of September.

2.2 for researchers in private companies etc.

Photon Factory is also open for scientists working in private corporations within certain limits. However, a fee is charged for beamtime.

3. ACCOMMODATION

KEK provides guest houses at a low cost for visiting scientists. In the case of domestic experimenters, please contact the person in charge of your experimental station. Overseas experimenters should ask the CPJ to book rooms. KEK supports travel and living expenses for domestic experimenters within certain limits but does not do so for overseas experimenters.

4. OTHERS

(1) Experimenters must obey the safety rules at KEK and PF.
(2) Further procedure may be requested in order to carry out an experiment.
(3) If there are questions regarding the procedures, please contact
Research Cooperation Section,
Administration Department,
High Energy Accelerator Research Organization,
FAX: +81-298-64-4602

Table 8 Number of proposals approved by the PAC

Research Field	1983	1984	1985	1986	1987	1988	1989	1990	1991	1992	1993	1994	1995	1996
(A) EXAFS	42	26	35	40	61	66	57	71	69	67	81	75	85	50
(B) Biology	18	18	28	28	32	38	57	61	75	89	92	121	121	96
(C) X-Ray	24	29	75	54	73	65	61	80	92	109	111	134	127	90
(D) VUV & Soft X-Ray	19	12	27	26	28	28	36	27	45	44	55	52	66	37
Total	103	85	165	148	194	197	211	239	281	309	339	382	399	273

List of proposals accepted in FY 1996

Proposal Number	Spokesperson	Title
96-G001	T. Hattori School of Engineering, Nagoya Univ.	XAFS analysis of the support-effects on noble metal catalysts
96-G002	T. Hattori School of Engineering, Nagoya Univ.	Structural analysis of Ga species in Ga-silicate by means of XAFS
96-G003	T. Usuki Faculty of Science, Yamagata Univ.	Short-range order of chalco-bromide glasses
96-G004	S. Funahashi School of Science, Nagoya Univ.	Solvation structure of copper(I) ion in non-aqueous solvents
96-G006	M. Ichikawa Catalysis Research Center, Hokkaido Univ.	EXAFS studies of the lattice relaxation of metal clusters entrapped in micro/meso pore zeolite and their size effects
96-G007	Y. Okamoto Faculty of Engineering Science, Osaka Univ.	Structure and catalysis of composite metal sulfide clusters confined in zeolite
96-G009	Y. Yoshimura National Institute of Materials and Chemical Research	XAFS study on the local structure of noble-metal sulfide catalysts
96-G010	H. Sakane Faculty of Engineering, Yamanashi Univ.	Analysis of local structure of exchanged-ion in ion-exchanged hydroxyapatite
96-G011	H. Nasu Faculty of Engineering, Mie Univ.	Study of the structure of the glasses with large optical nonlinearity
96-G012	G. Parkinson School of Applied Chemistry, Curtin Univ. of Technology	XAFS investigations of the precipitation of gibbsite from synthetic Bayer liquors
96-G013	R. J. Kennedy National High Magnetic Field Laboratory, Florida A&M Univ.	XAFS of ferrite thin films
96-G014	Y. Kubozono Faculty of Science, Okayama Univ.	EXAFS study on metallofullerene $Ca@C_{60}$
96-G015	S. Tsunashima School of Engineering, Nagoya Univ.	The correlation of local structure with the GMR effect in magnetic multilayers
96-G017	H. Ishida Faculty of Science, Okayama Univ.	EXAFS stuties on the structural phase transitions in $(CH_3NH_3)_2MX_6$ (M=Sn, Pt; X=Cl, Br, I)
96-G019	T. Ohta Graduate School of Science, Univ. of Tokyo	EXAFS studies of atomic adsorbed structures on Au and Pt electrodes

Proposal Number	Spokesperson	Title
96-G020	M. Nomura Photon Factory, KEK	XAFS studies of copper-metallothionein accumulated in LEC rat liver
96-G021	M. Nomura Photon Factory, KEK	XAFS studies of mercury and tin compounds in fish-eating birds
96-G023	H. Kageyama Osaka National Research Institute, AIST	Structure of implanted Ni and Mn ions in silica
96-G024	M. Yao Graduate School of Science, Kyoto Univ.	X-ray absorption fine structures of selenium cluster beam
96-G025	Y. Katayama Faculty of Science and Technology, Keio Univ.	EXAFS study on liquid selenium under high-pressure and high-temperature
96-G026	T. Ogawa Advanced Science Research Center, Japan Atomic Energy Research Institute	XAFS of uranium solid and liquid solutions
96-G027	M. Cygler Biotechnology Research Institute	High resolution study of lipases and cysteine protease proenzymes
96-G028	M. C. Lawrence Biomolecular Research Institute	Sialic acid binding proteins
96-G029	T. Nonaka Faculty of Engineering, Nagaoka Univ. of Technology	Dynamic structure analysis of bovine pancreatic ribonuclease by time-resolved Laue method
96-G030	T. Nonaka Faculty of Engineering, Nagaoka Univ. of Technology	High-resolution X-ray structure analysis of *Rana catesbeiana* egg lectin
96-G031	T. Nonaka Faculty of Engineering, Nagaoka Univ. of Technology	Dynamic X-ray structure analysis of 7α-hydroxysteroid dehydrogenase from *Escherichia coli*
96-G032	T. Senda Faculty of Engineering, Nagaoka Univ. of Technology	X-ray structure analysis of the PheB enzyme from *Bacillus stearothermophilus*
96-G033	T. Senda Faculty of Engineering, Nagaoka Univ. of Technology	X-ray structure analysis of Calmoduline complexed with antipsychotic drugs
96-G034	T. Senda Faculty of Engineering, Nagaoka Univ. of Technology	X-ray structure analysis of Imidazole glycerol phosphate dehydrates (IGPD)
96-G035	F. Frolow The Weizmann Institute of Science	High resolution structure of bacterioferritin
96-G036	W. Saenger Inst. für Kristallogr., Freie Univ. Berlin	Crystal structure determination of photosystem I

Proposal Number	Spokesperson	Title
96-G037	M. Tanokura Biotechnology Research Center, Univ. of Tokyo	Activation and catalytic mechanisms of acid proteinases studied by time-resolved Laue method
96-G038	H. Sasaki Biotechnology Research Center, Univ. of Tokyo	X-ray crystallography of the major flavin reductase from *Vibrio fischeri*
96-G039	A. Suzuki School of Engineering, Nagoya Univ.	X-ray crystal analysis of reaction mechanism of *Escherichia coli* glycerol kinase
96-G040	K. Fukuyama Faculty of Science, Osaka Univ.	High resolution X-ray crystallographic analyses of spherical viruses
96-G041	B. Mikami Research Institute for Food Science, Kyoto Univ.	X-ray structural analysis of soybean storage proteins
96-G042	N. Yasuoka Faculty of Science, Himeji Institute of Technology	Synchrotron radiation study of diol dehydrase
96-G043	T. Matsumoto National Inst. of Agrobiological Resources	X-ray crystal analysis of tulip arylacylamidase
96-G044	H. Mizuno National Inst. of Agrobiological Resources	X-ray studies of snake venom anticoagulant proteins
96-G045	K. Itoh Faculty of Science, Himeji Institute of Technology	High resolution X-ray diffraction experiments for bovine heart cytochrome *c* oxidase
96-G046	S. Yoshikawa Faculty of Science, Himeji Institute of Technology	X-ray diffraction experiments for cytochrome bc_1 complex and NADH-ubiquinone reductase
96-G047	A. Takenaka Faculty of Bioscience and Biotechnology, Tokyo Institute of Technology	X-ray analyses of the basic structures of functional nudleic acids
96-G048	A. Takenaka Faculty of Bioscience and Biotechnology, Tokyo Institute of Technology	X-ray analyses of 2-oxoacid dehydrogenase complexes
96-G049	Y. Shirakihara National Institute of Genetics	X-ray crystal analysis of nucleotide bound form of $\alpha 3\beta 3$ complex of F1-ATPase
96-G050	T. Fujii Institute for Chemical Research, Kyoto Univ.	Crystallographic analysis of archaeal ferredoxin
96-G051	Y. Hata Institute for Chemical Research, Kyoto Univ.	Structural study on reaction mechanism of dehalogenases by X-ray methods
96-G052	T. Sato Faculty of Engineering, Tokushima Univ.	X-ray structures of prolylendopeptidase and pepase-inhibiting peptides complex

Proposal Number	Spokesperson	Title
96-G053	H. Kumagai Faculty of Agriculture, Kyoto Univ.	X-ray structure analysis of monoamine oxidase from *Escherichia coli*
96-G054	N. Kato School of Medicine, Nagoya Univ.	Structural analysis of crystals of bacterial lipopolysaccharides (LPS)
96-G055	N. Watanabe Photon Factory, KEK	Preparation of heavy-atom derivatives using high-pressure noble gas
96-G056	K. Miki Graduate School of Science, Kyoto Univ.	X-ray crystallographic studies of θ-toxin
96-G057	T. Hakoshima Division of Structural Biology, Nara Institute of Science and Technology	Structural study of protein DNA interaction
96-G058	J. W. Lee Donner Lab. LBNL	Structural determination of the bovine heart mitochondrial cytochrome bc_1 complex
96-G059	M. Redinbo Biomolecular Structure Center, Univ. of Washington	Crystallographic studies of human topoisomerase I complexed to DNA
96-G060	T. Izard Biomolecular Structure Center, Univ. Washington	Crystallographic studies on the icosahedral core of the pyruvate dehydrogenase multienzyme complex
96-G061	R. Lancaster Max-Planck-Institut für Biophysik	X-ray structure analysis of the membrane protein complex fumarate reductase from *Wollinella succinogenes*
96-G062	S. Iwata Max-Planck-Institutfür Biophysik	X-ray crystallographic analysis of the cytochrome c oxidase from *Paracoccus denitrificans*
96-G063	Z.-Y. Wang Faculty of Engineering, Tohoku Univ.	A SAXS study on the aggregated structures of pigments from Photosynthetic bacteria
96-G064	K. Tashiro Faculty of Science, Osaka Univ.	Synchrotron X-ray study on crystallization kinetics of polyethylene blends
96-G065	Y. Tajima Faculty of Science, Tokyo Metropolitan Univ.	Rearrangement of thin and thick filaments in isometrically contracting smooth muscle
96-G066	F. Tokunaga Faculty of Science, Osaka Univ.	Molecular mechanism of light-driven ion pump
96-G068	I. Hatta School of Engineering, Nagoya Univ.	Study on phospholipid-phospholipid hydrolysis mixtures using simultaneous X-ray diffraction and calorimetry

Proposal Number	Spokesperson	Title
96-G069	P. J. Quinn Department of Biochemistry, King's College London	Dynamic phase behaviour of mixed aqueous dispersions of phospholipids and diacylglycerol
96-G070	H. Iwamoto School of Medicine, Teikyo Univ.	X-ray diffraction study of the molecular mechanism of resistance to stretch of muscle
96-G071	S. Matsuoka School of Medicine, Sapporo Medical Univ.	Kinetics of formation of the ripple phase and the HII phase in lipids
96-G072	K. Hieda College of Science, Rikkyo Univ.	Action spectra of wet biological samples in the ultrasoft X-ray region
96-G073	R. Yokoya Japan Atomic Energy Research Instiurte	X-ray energy dependence of the size distribution of the fragments produced from the irradiated polynucleotide
96-G074	K. Takakura Dept. of Physics, International Christian Univ.	The study of the mechanism in irradiation effect on nucleic acids by using polarized soft X-rays
96-G076	T. Megumi Research Inst. for Advanced Sci. and Tech., Univ. of Osaka Prefecture	Phosphorylation of adenosine with photons of K-shell absorption edge of phosphorus
96-G077	K. Kobayashi Photon Factory, KEK	X-ray energy dependence of radiolysis of biomolecules in concentrated aqueous solution
96-G078	K. Kobayashi Photon Factory, KEK	Absorption spectra of biological molecules in aqueous solution
96-G079	K. Kobayashi Photon Factory, KEK	Energy dependence of lethal effect on yeast in soft X-ray region
96-G080	I. Nakai Faculty of Science, Science Univ. of Tokyo	X-ray fluorescence imaging and total reflection analysis of aluminum in biological samples
96-G081	N. Shimojo Institute of Community Medicine, Univ. of Tsukuba	Development of a combination analysis of SR-XRF imaging and TUNEL staining and its medical application
96-G082	Y. Ikeda Dept. of Aquatic Bioscicences, Tokyo Univ. of Fisheries	Assessment of environmental chemical pollutants over fish by scale change
96-G083	K. Okoshi School of Science and Engineering, Ishinomaki Senshu Univ.	Ontogenetic study of vanadium accumulation in the fan worm *Pseudopotamilla occelata*
96-G085	S. Sasaki Materials and Structures Laboratory, Tokyo Institute of Technology	Structure analysis of a-SiO_x thin film by X-ray diffraction

Proposal Number	Spokesperson	Title
96-G086	S. Sasaki Materials and Structures Laboratory, Tokyo Institute of Technology	Magnetic anisotropy of YIG and ferrite by circularly polarized X-rays
96-G087	M. Yashima Materials and Structures Laboratory, Tokyo Institute of Technology	Lattice constant and oxygen displacement of zirconia- and hafnia-solid solutions
96-G089	M. Ohmasa Faculty of Science, Himeji Institute of Technology	Studies on textures and their orientation in feldspar crystals
96-G090	M. Miyamoto Graduate School of Science, Univ. of Tokyo	Identification of fine exsolved mineral in olivine of Martian meteorite
96-G091	H. Toraya Ceramics Research Laboratory, Nagoya Institute of Technology	Optimization of operating system for high-resolution powder diffractometer with multiple-detector system
96-G092	K. Ishida Faculty of Science and Technology, Science Univ. of Tokyo	Study of high-Tc compounds by X-ray powder diffraction near the absorption edges
96-G093	Y. Takanishi Faculty of Engineering, Tokyo Institute of Technology	Precise analysis of layer structure in ferroelectric and antiferroelectric smectic liquid crystals
96-G094	T. Enoki Faculty of Science, Tokyo Institute of Technology	Magnetism of BEDT-TTF-based charge transfer complexes
96-G096	S. Morimoto Faculty of Engineering Science, Osaka Univ.	Magnetic scattering of charge disproportionate perovskite iron oxide
96-G096	M. K. Sanyal Saha Institute of Nuclear Physics	X-ray magnetic scattering studies of multilayers
96-G097	T. Shimura Graduate School of Engineering, Osaka Univ.	The structural change of the crystalline phase in the thermal oxide layer on Si (001) substrate by preoxidation and post-oxidation anneal
96-G098	I. Takahashi School of Engineering, Nagoya Univ.	X-ray diffraction study on surface structure of dissolving crystals
96-G099	K. Tsuji Faculty of Science and Technology, Keio Univ.	Amorphization from the quenched high pressure phase in III-V and II-VI compounds
96-G100	Y. Waseda Institute for Advanced Materials Processing, Tohoku Univ.	Structural study of complex liquids by the anomalous X-ray scattering method
96-G101	M. Tanaka Photon Factory, KEK	Crystallographic studies on the relationship between morphology and structure of brookite (TiO_2)

Proposal Number	Spokesperson	Title
96-G102	S. Morimoto Faculty of Engineering Science, Osaka Univ.	Precise structure analysis of charge disproportionate perovskite oxide $CaFeO_3$
96-G103	M. Mori Nagoya Univ.	Quasiperiodicity of Al-Pd-Mn icosahedral phase perfect quasicrystals
96-G104	Y. Soejima Faculty of science, Kyushu Univ.	An application of super lattice FRED for structure determination
96-G105	O. Urakawa Kyoto Institute of Technology	Morphology control of polymer/ metal-salt composite by an electric field
96-G106	T. Yamaguchi Faculty of Science, Fukuoka Univ.	Small-angle X-ray scattering from aqueous solutions of long chain polyoxyethylene n-hexadecyl ethers
96-G108	J. G. Thompson Research School of Chemistry, Australian National University	Metal atom and oxygen vacancy ordering in anion excess and anion deficient fluorite-related compounds
96-G109	E. N. Maslen Dept. of Physics, Univ. of Western Australia	Synchrotron radiation imaging of the electron density in and beyond the bonds: Materials' properties from diffraction images
96-G110	S. Kishimoto Photon Factory, KEK	Development of time-spectroscopy method for electrons emitted from excited nuclei by using an APD detector
96-G112	O. Sakata Materials and Structures Laboratory, Tokyo Institute of Technology	Structure of monolayer Ga atoms on Si(100):As 2×1 using grazing-angle X-ray standing waves and surface diffraction
96-G113	H. Hashizume Materials and Structures Laboratory, Tokyo Institute of Technology	Surface structures of strontium titanates at high temperatures and structures of growing oxide surfaces
96-G114	K. Tsuji Faculty of Science and Technology, Keio Univ.	Structure of liquid alkali metals and liquid iodine under pressure
96-G115	Y. Katayama Faculty of Science and Technology, Keio Univ.	Density of liquid Te and Te compounds under high-pressure and high-temperature
96-G116	S. Urakawa Faculty of Science, Okayama Univ.	X-ray diffraction analysis of molten NaCl and NaBr under high pressure
96-G117	A. Onodera Faculty of Engineering Science, Osaka Univ.	Observation of elementary process in the diamond formation from organic compounds under high pressure
96-G118	Y. Fukai Dept. of Physics, Chuo Univ.	Formation of superabundant vacancies in metal hydrides
96-G119	Y. Amemiya Faculty of Engineering, Univ. of Tokyo	Development of the TV-type X-ray detectors for diffraction studies and its application

Proposal Number	Spokesperson	Title
96-G121	H. Yokoyama Electrotechnical Laboratory	Structures of liquid crystalline phase and solid-like phase in Langmuir monolayers of amphiphilic azobenzene derivatives
96-G122	K. Uosaki Graduate School of Science, Hokkaido Univ.	In situ study of GaAs single crystal electrode/solution interface by surface X-ray scattering
96-G123	K. Itaya Graduate School of Engineering, Tohoku Univ.	Structural analysis of electrodeposited monolayers on metal and semiconductor electrode surfaces in electrolyte solutions
96-G124	A. Iida Photon Factory, KEK	High sensitivity total reflection X-ray fluorescence analysis of Si wafers
96-G125	K. Akimoto School of Engineering, Nagoya Univ.	Semiconductor interfaces studied by anomalous X-ray diffraction
96-G126	A. Onodera Faculty of Engineering Science, Osaka Univ.	Search for high-temperature phase(s) of the high-pressure metallic state of <IV> compounds
96-G127	I. Shirotani Faculty of Engineering, Muroran Institute of Technology	X-ray diffraction of metal complexes at high pressure
96-G128	S. Minomura Faculty of Science, Okayama Univ. of Science	Atomic position of the chalcopylrite structure under high pressure
96-G129	Y. Kubozono Faculty of Science, Okayama Univ.	Temperature dependence of lattice constant and Debye-Waller factor in fullerene superconductors
96-G130	S. Sasaki Materials and Structures Laboratory, Tokyo Institute of Technology	Measurement of compressibility for iodine-intercalated Bi superconductor
96-G131	M. Imai National Research Institute for Metals	Pressure effect on structure of NiO
96-G132	S. C. Moss Dept. of Physics, Univ. of Houston	Synchrotron studies of interfacial structure and epitaxy in magnetic metallic multilayer films
96-G133	H. Hashizume Materials and Structures Laboratory, Tokyo Institute of Technology	Surface roughness of carbonates during deposition and etching from liquid: X-ray scattering study
96-G134	H. Maeda Japan Atomic Energy Research Institute	X-ray diffuse scattering of heavy ion irradiated materials
96-G135	R. Garrett ANSTO	Hard X-ray phase contrast imaging
96-G136	G. Kutluk Photon Factory, KEK	3d resonance Auger electron spectroscopy of rare earth atoms

Proposal Number	Spokesperson	Title
96-G137	Y. Azuma Photon Factory, KEK	Multi-electron photoexcitation of laser-excited atoms with synchrotron radiation
96-G138	M. Oshima Graduate School of Engineering, Univ. of Tokyo	A study on quantum dots formation by semiconductor surface control
96-G139	M. Oshima Graduate School of Engineering, Univ. of Tokyo	A study on electronic properties of extremely small area with very high energy resolution
96-G140	M. Yoshikawa Plasma Research Center, Univ. of Tsukuba	Calibration of VUV spectrometer for plasma diagnostics
96-G141	H. Kobayasi Faculty of Engineering Science, Osaka Univ.	Chemical composition of silicon oxide layers and the interface states
96-G142	P. L. Smith Harvard College Observatory, Harvard Univ.	VUV photoabsorption cross sections for astronomy
96-G143	K.-P. Huber SIMS, National Research Council of Canada	High-resolution absorption cross section measurements on H_2O and N_2 at temperatures of 300 and 20 K
96-G144	K. Furuya Faculty of Science, Science Univ. of Tokyo	Surface oxidation of TiN and $Ti_xAl_{1-x}N$ studied by XAS and XPS
96-G145	K. Kameta Faculty of Science, Tokyo Institute of Technology	Neutral decay processes of molecular superexcited states produced by VUV photon impact——VUV fluorescence measurement
96-G146	Y. Tezuka Institute for Solid State Physics, Univ. of Tokyo	High-resolution photoemission studies of $CePd_3$ and $CePd_2$
96-G147	S. Shin Institute for Solid State Physics, Univ. of Tokyo	Preliminary experiment of coincidence spectroscopy between soft-X-ray emission and photoelectron
96-G149	S. Tohno Institute of Atomic Energy, Kyoto Univ.	Chemical state analysis of sulfur in atmospheric aerosols and rain water
96-G150	T. Ohta Graduate School of Science, Univ. of Tokyo	C and O-K NEXAFS and UPS studies of furan adsorbed on Cu and Ni metal surfaces
96-G151	T. Ohta Graduate School of Science, Univ. of Tokyo	S K-edge XAFS studies on sulfur dioxide adsorbed on Pd and Pt single crystal surfaces
96G152	M. Yanagihara Research Inst. for Scientific Measurements, Tohoku Univ.	Studies on the buried interfaces using soft-X-ray fluorescence spectroscopy

Proposal Number	Spokesperson	Title
96-C030	S. Komiya Fujitsu Laboratories Ltd.	Structure analysis of thin film interface
96-C031	M. Ito Central Research Laboratory, Hitach Ltd.	X-ray imaging studies
96-C034	K. Tani Power Reactor and Nuclear Fuel Development Corporation	Development of a high power CW linear electron accelerator system
96-C043	S. Okude NKK Corp.	Chemical state determination with synchrotron radiation
96-C044	M. Ohsawa Fuji Electric Corporate Reserach and Development, Ltd.	Highly sensitive structure analysis of thin films by synchrotron radiation
96-C045	T. Kiyokura Interdisciplinary Research Laboratory, NTT	Studies of the electronic properties of nano-structures with undulator synchrotron radiation
96-C047	D. Amano Sumitomo Heavy Industries, Ltd.	Basic research on the design study of insertion devices
96-C049	A. Komura Hitachi Zosen Corp.	Development of monochromator for high brilliance synchrotron radiation

G: General
U: Urgent
S: Special
P: Preliminary
Y: Approved for charged beam time.
C: Collaborations between the Photon Factory and institutes of private companies.

Proposal Number	Spokesperson	Title
96-G154	H. Daimon Faculty of Engineering Science, Osaka Univ.	Photoelectron holography and 2-dimensional photoelectron angular distribution
96-G155	H. Daimon Faculty of Engineering Science, Osaka Univ.	ARUPS studies of metal atom adsorbed semiconductor surfaces, TiS_2 and M_xTiS_2 at low temperatures
96-G156	S. Suga Faculty of Engineering Science, Osaka Univ.	Spin-resolved photoemission of ferromagnetic epitaxial films and superlattices
96-G157	M. Hirai Faculty of Engineering, Gunma Univ.	Structural stability of acidic phospholipid dispersion system
96-G158	J. N. Varghese Biomolecular Research Institute	Studies of barley glucanase enzymes with inhibitor/substrate complexes
96-G160	H. Schmidt Böcking Institut für Kernphysik, Univ. Frankfurt	He double photoionization/excitation measurements with the COLTRIMS method
96-G161	K. Asakura Research Center for Spectrochemistry, Faculty of Science, Univ. of Tokyo	Development of in-situ quantitative characterization method of adsorbed hydrogen on metal particles by $L_{2,3}$ XANES spectra
96-G162	N. Ichikuni Chiba Univ.	Studies on the active site structures of the 2-dimensionally dispersed Mo oxide catalysts
96-G163	K. Ebitani Faculty of Engineering, Tokyo Institute of Technology	Study on interactions between Rh and rare-earth elements in supported rhodium catalyst
96-G164	T. Miyanaga Faculty of Science, Hirosaki Univ.	Supercooling and glass transition in the droplets
96-G165	K. Kawasaki Niihama National College of Technology	XAFS analysis on supported palladium catalysts for asymmetric hydrogenation
96-G166	Y. Nakamura Graduate School of Science, Hokkaido Univ.	EXAFS studies about the growth of metal particles in Na_2O-B_2O_3 glasses
96-G167	T. Tanase Faculty of Science, Toho Univ.	An XAFS study on Biorelevant dinuclear complexes involving Mn, Co, Zn, Fe, and Ru ions
96-G169	H. Kanai Faculty of Science, Kyoto Prefectural Univ.	XAFS analysis for hyperfine interaction between noble metal-ceria
96-G170	Y. Ono Faculty of Engineering, Tokyo Institue of Technology	Structure of rubidium amide supported on alumina as a superbase
96-G171	V. A. Shuvaeva School of Science, Kwansei Gakuin Univ.	Polarized XAFS study of phase transitions in perovskite-type compounds

Proposal Number	Spokesperson	Title
96-G172	J.-C. Park Dept. of Chemistry, Pusan Women's Univ.	XAFS studies on the anion intercalation of K_2NiF_4 - type metal oxides, $La_{2-x}A_xMO_4$, (A=Nd, Sr; M=Co, Ni, Cu)
96-G173	T. Murata Kyoto Univ. of Education	XAFS studies of the local structure of monobromonaphthalene dissolved in supercritical Xe
96-G174	J.-H. Choy College of Natural Sciences, Seoul National Univ.	X-ray absorption spectroscopic investigation for the electronic and geometric structures of the superconducting and insulating layer-by-layer nanocomposites
96-G175	S. Funahasi Graduate School of Science, Nagoya Univ.	Structure determination of the precursor complex for electron transfer reactions by the time-resolved XAFS method
96-G176	H. Uwe Institute of Applied Physics, Univ. of Tsukuba	Local structure of Li-Mn spinel complex oxide studied by EXAFS
96-G177	H. Takechi Faculty of Engineering, Fukuoka Institute of Technology	Structural analysis on soft ferrite treated by mechanical alloying
96-G179	K. Asakura Research Center for Spectrochemistry, Faculty of Science, Univ. of Tokyo	Dynamic study on structures of Mo, W-carbonyls entrapped in Zeolite pore by photo-exidation reaction
96-G181	I. Watanabe Graduate School of Science, Osaka Univ.	XAFS study on the gas/liquid interface
96G182	I. Nakai Faculty of Science, Science Univ. of Tokyo	In situ XAFS analyses of the charge-discharge processes in the Li secondary battery materials
96-G183	C. Numako Faculty of Integrated Arts and Sciences, Tokushima Univ.	Characterization of metallic elements highly accumulated in animal tissues
96-G184	J.-H. Choy College of Natural Sciences, Seoul National Univ.	XAFS studies on the local structure of nanosized semiconductor particles stabilized in layered matrix
96-G185	M. Matsuura Miyagi National College of Technology	Roll of small additives in the formation of textured microcrystallines by HDDR for NdFeB
96-G186	H. Takebe Interdisciplinary Graduate School of Engineering Sciences, Kyushu Univ.	Local structure around Nd^{3+} ions with small concentration in oxide glasses
96-G188	H. Ohno Japan Atomic Energy Research Institute	EAXFS of irradiated non-crystal solids
96-G189	J.-H. Choy College of Natural Sciences, Seoul National University	X-ray absorption spectroscopic study on the metal-oxygen bonding nature in 4d transition metal oxide
96-G190	M. Tanokura Biotechnology Research Center, Univ. of Tokyo	X-ray crystallography of some mutants of malate dehydrogenase from *Thermus flavus*

Proposal Number	Spokesperson	Title
96-G191	M. Tanokura Biotechnology Research Center, Univ. of Tokyo	X-ray crystallography of Glu58-carboxymethylated RNase T1
96-G192	H. Sasaki Biotechnology Research Center, Univ. of Tokyoo	X-ray crystallography of brazzein, a sweet protein
96-G193	O. Nureki Graduate School of Science, Univ. of Tokyo	X-ray crystallography of aminoacyl-tRNA synthetases and the complex with its substrates
96-G194	T. Tada Research Inst. for Advanced Sci. and Tech., Univ. of Osaka Prefecture	X-ray structure analyses of enzymes in the TCA cycle of *Euglena gracilis*
96-G196	H. Matsuzawa Faculty of Agriculture, Univ. of Tokyo	Crystallographic analysis of extended-spectrum b-lactamase Toho-1 from *E.coli* TUH12191
96-G197	H. Matsuzawa Faculty of Agriculture, Univ. of Tokyo	Crystallographic analysis of acid stable xylanase from *Aspergillus kawachii*
96-G198	P. D. Carr Research School of Chemistry, Australian National Univ.	Crystallographic studies of the extracellular domain of the beta subunit of the interleukin-5 receptor
96-G200	J. Martin Center for Drug Design and Development, Univ. of Queensland	X-ray crystallographic stuides on protein folding factors
96-G201	S. W. Shu College of Natural Sciences, Seoul National Univ.	Synchrotron high-resolution data collection of nucleic acid-acting enzymes
96-G202	K. Scott Garvan Institute of Medical Research	Single crystal X-ray diffraction data for complexes of phospholipase A2 and inhibitors
96-G203	D. I. Stuart Laboratory of Molecular Biophysics, Univ. of Oxford	Crystallography of biomedically important proteins
96-G204	S. Ikemizu Institute of Applied Biochemistry Univ. of Tsukuba	Crystallographic studies on cell adhesion molecule CD31
96-G206	M. Kusunoki Institute of Protein Research, Osaka Univ.	X-ray analysis of the catalytic mechanism of UDP-glucose pyrophosphorylase
96-G207	Y. Hata Institute for Chemical Research, Kyoto Univ.	Structural study of reaction mechanism of *P. aeruginosa* alkaline protease
96-G208	A. Kita Graduate School of Science, Kyoto Univ.	X-ray crystallographic studies of metapyrocatechase

Proposal Number	Spokesperson	Title
96-G209	K. Kitadokoro Faculty of Science, Kyoto Univ.	X-ray crystallographic studies of photolyase (DNA photoreactivating enzyme)
96-G210	H. Yamaguchi Institute for Protein Research, Osaka Univ.	Structural study of copper-containing monoamine oxidase
96-G211	M. Guss Department of Biochemistry, Univ. of Sydney	Protein crystallography: Metalloproteins and glycosaminoglycan degrading enzymes
96-G212	N. Tanaka Faculty of Bioscience and Biotechnology, Tokyo Institute of Technology	Structure analysis of cytochrome *c* 554
96-G213	N. Tanaka Faculty of Bioscience and Biotechnology, Tokyo Institute of Technology	Structure analysis on thermophilic IPMDH complexed with IPM
96-G214	H. Moriyama Faculty of Bioscience and Biotechnology, Tokyo Institute of Technology	Structure analysis of IPMDH with the T-jump Laue method
96-G215	S. Harada Faculty of Pharmaceutical Science, Univ. of Tokyo	Dynamical crystal structure analysis of proteases
96-G216	H. Kato Institute for Chemical Research, Kyoto Univ.	Time-resolved crystallography of CN bond ligases by Laue diffraction
96-G217	N. Kamiya Institute of Physical and Chemical Research	Crystal structure analysis of *Aleuria aurantia* lectin
96-G218	Y. Kawano Institute of Physical and Chemical Research	X-ray crystal structure analysis of bleomycin-binding protein and its complex
96-G219	Y. Hiragi Institute for Chemical Research, Kyoto Univ.	Pressure effect on the association-dissociation of hydrophobic protein
96-G220	Y. Hiragi Institute for Chemical Research, Kyoto Univ.	Structure and kinetics of GroEL oligomer formation by temperature-jump
96-G221	M. Tanokura Biotechnology Research Center, Univ. of Tokyo	Analysis of the folding intermediate of *Aspergillus niger* acid proteinase A
96-G222	K. Kuwajima Graduate School of Science, Univ. of Tokyo	Dynamic structural change of chaperonin GroEL in its functional states
96-G223	S. Ueno Faculty of Applied Biological Science, Hiroshima Univ.	Dynamics of polymorphic transformations in triacylglycerols
96-G226	S. Doniach Ginzton Laboratory, Stanford Univ.	Time-resolved solution X-ray scattering studies of protein folding using the CCD X-ray detector

Proposal Number	Spokesperson	Title
96-G227	H. Maezawa School of Medicine, Tokai Univ.	Effects on the enzyme activity of the innershell photoionization in the target atoms induced by X-rays
96-G228	K. Takakura International Christian Univ.	Enhancement effect of strand breaks in DNA induced by soft X-ray irradiation through platinum atomic target
96-G229	H. Mori School of Medicine, Tokai Univ.	Determination of selenium in situ by monochromatic synchrotron radiation excited-X-ray fluorescence spectrometry (Total reflection method)
96-G230	T. Saito Jichi Medical School	Cytochemical study of the metabolism in the retina with zooming tube
96-G231	M. Tanaka Photon Factory, KEK	Perovskite-type $REAlO_3$: phase transition studies at elevated temperatures
96-G232	K. Kawasaki Niihama National College of Technology	Observation of recrystallization process of metallic materials by grain projection method
96-G233	A. Iida Photon Factory, KEK	Characterization of local layer structure of smectic liquid crystal by X-ray
96-G234	M. Wakatsuki Institute of Materials Science, Univ. of Tsukuba	Characterization of metallic impurities (Ti, Zr, and Cu) in high purity synthetic diamond
96-G235	K. Sakurai National Research Institute for Metals	Chemical characterization of trace metals in small liquid drop
96-G236	H. Horiuchi Graduate School of Science, Univ. of Tokyo	Perovskit-type $RAlO_3$: Analyses of lattice deformation and structure change
96-G237	A. Nukui National Institute for Research in Inorganic Materials	Structural study of photo-conductive glasses by RDF
96-G238	Y. Kubota Osaka Women's Univ.	Structure analysis at the electron level of the Laves phases
96-G239	H. Ishibashi College of Integrated Arts and Sciences, Univ. of Osaka Prefecture	Electron density distribution of triangular lattice VX_2 (X=Cl, Br and I)
96-G240	K. Koto Faculty of Integrated Arts and Sciences, Tokushima Univ.	Structure refinement of metastable alumina microcrystal
96-G241	Y. Fujii Institute for Solid State Physics, Univ. of Tokyo	Lattice dimerization of spin-Peierls transition in NaV_2O_5
96-G242	I. Takahashi School of Science, Kwansei Gakuin Univ.	X-ray diffraction study on microcrystallinity on Si(001) and its electronic properites

Proposal Number	Spokesperson	Title
96-G243	K. Sakaue School of Science, Kwansei Gakuin Univ.	Synthesis and characterization of gradient monochromators
96-G244	H. Maeda Japan Atomic Energy Research Institute	A study of low temperature irradiation induced small defects by X-ray diffuse scattering at low temperature
96-G245	M. Takata School of Engineering, Nagoya Univ.	Studies on structure and quantum size effects of nanocrystals embedded in glass
96-G246	E. Matsubara Graduate School of Engineering, Kyoto Univ.	Structural study of Si-O, Si-N, Si-O-N amorphous thin films by grazing incidence X-ray scattering method
96-G247	J. Mizuki Japan Atomic Energy Research Institute	XAFS and DAFS studies on high e thin film of $SrTiO_3$ and $(SrBa)TiO_3$
96-G248	M. Sakata School of Engineering, Nagoya Univ.	A study of isotopic effects in KDP by imaging of hydrogen bond
96-G249	N. Ikeda Advancet Research Inst. for Sci. and Eng., Waseda Univ.	Charge ordering structure in $LuFe_2O_4$
96-G250	H. Horiuchi Graduate School of Science, Univ. of Tokyo	Structure studies on $CeAlO_3$ and $CeGaO_3$
96-G251	E. Ohtani Graduate School of Science, Tohoku Univ.	Determination of the phase boundaries and the rate of transformation of Mg_2SiO_4
96-G252	S. Endo Research Center for Extreme Materials, Osaka Univ.	High pressure phase transition in antiferroelectric $PbZrO_3$
96-G253	S. Nanao Institute of Industrial Science, Univ. of Tokyo	The behavior of quasicrystals under high pressure and high temperatures
96-G254	Y. Kondo Faculty of Engineering, Tohoku Univ.	Defect production by Br- and I-1s core excitation in KBr, KI and RbI single crystals
96-G255	K. Akimoto Graduate School of Engineering, Nagoya Univ.	Lattice strains at the semiconductor surface
96-G256	K. Sakaue School of Science, Kwansei Gakuin Univ.	Characterization of extremly thin $BaTiO_3$ films
96--G257	N. Wada Faculty of Engineering, Toyo Univ.	Structural analysis of alkali-metal intercalated layered silicate
96-G258	T. Nanba Faculty of Science, Kobe Univ.	Pressure induced structural phase transition in CuBr microcrystals

Proposal Number	Spokesperson	Title
96-G259	K. Kobayashi Photon Factory KEK	Spin polarized states in perovskite Mn oxides by means of magnetic circular dichroism (MCD)
96-G260	H. Hashizume Materials and Structures Laboratory, Tokyo Institute of Technology	Magnetic roughness of multilayer interfaces probed by X-ray scattering
96-G261	J. Chaboy ICMA, CSIC	Relationship between hydrogen uptake and manganese magnetic moment instability in R-Mn compounds: XCMD investigation
96-G262	F. Itoh Faculty of Engineering, Gunma Univ.	A study of X-ray circular magnetic dichroism and magnetic compton scattering of actinide compounds
96-G263	H. Sakurai Faculty of Engineering, Gunma Univ.	Magnetic structure of Co/Ag multilayers
96-G264	T. Kato Univ. of Tsukuba	Determination of garnet-perovskite transition in Mg silicate system
96-G265	A. Kakizaki Institute for Solid State Physics, Univ. of Tokyo	Heat-load tests of a water cooled absorber for high brilliant synchrotron light source
96-G266	Y. Horikoshi School of Science and Engineering, Waseda Univ.	A study of surface electronic states of metastable alloy semiconductor crystals
96-G268	T. Koizumi College of Science, Rikkyo Univ.	Photoionization of 4d electrons in singly-charged ions
96-G269	T. Nagata Faculty of science and Technology, Meisei Univ.	Measurement in the 4d region of absolute photoionization cross sections for rare-earth atoms
96-G270	K. Nakagawa Faculty of Education, Kobe Univ.	Fundamental processes of radiation effect in aromatic molecular crystal
96-G271	K. Edamoto Faculty of Science, Tokyo Institute of Technology	Angle-resolved photoemission study of ZrC (100) and (111) surfaces
96-G272	K. Akimoto Institute of Applied Science, Univ. of Tsukuba	Angle-resolved photoemission studies of phthalocyanine thin films
96-G273	J. Kawai Graduate School of Engineering, Kyoto Univ.	Photoelectron spectroscopy of insulators
96-G274	Y. Nihei Institute of Industrial Science, Univ. of Tokyo	Study on interface defects on heteroepitaxial layers by scanned energy photoelectron diffraction

Proposal Number	Spokesperson	Title
96-G275	K. Furuya Faculty of Science, Science Univ. of Tokyo	Study on dissociative adsorption of NO by XAS and XPS
96-G276	H. Shimada National Institute of Materials and Chemical Research	Resonant photoemission study on electronic structure of binary sulfide catalysts
96-G277	Y. Fukuda Research Institute of Electronics, Shizuoka Univ.	Photoelectron diffraction study of InP(001)-(4×2) surface and sulfur-treated surfaces
96-G278	K. Ono Graduate School of Engineering, Univ. of Tokyo	Electronic structure of surface nano-structures
96-G279	J. Kawai Graduate School of Engineering, Kyoto Univ.	Spin state analysis by X-ray fluorescence yield X-ray absorption spectroscopy
96-G280	M. Oshima Graduate School of Engineering, Univ. of Tokyo	Soft X-ray electron spectroscopy of atomic scale semiconductor interlayer
96-G281	A. Enomoto Photon Factory, KEK	Vibration and alignment issues on linac beam characteristics
96-G282	A. Mondragon Molecular Biology and Cell Biology, Northwestern Univ.	Structural studies of type I DNA topoisomerases
96-G283	N. Hiramatsu Faculty of Engineering, Fukuoka Univ.	Transformation behavior of bio-related materials among gel-glass-crystalline states
96-G284	M. Hidaka Faculty of Science, Kyushu Univ.	Correlation between local structure distortions and spin-Peierls transition of $CuGeO_3$
96-U002	Y. Noh Dept. of Materials Science and Engineering, Kwangju Inst. of Science and Technology	Synchrotron X-ray study on crystallization process of amorphous BST and PZT films
96-S001	S. Kikuta Graduate School of Engineering, Univ. of Tokyo	Fundamental studies and applications of nuclear resonant scattering
96-S002	T. Yagi Institute for Solid State Physics, Univ. of Tokyo	Structure of the lower mantle based on the high pressure and high temperature *in situ* X-ray diffraction study
96-P001	N. Shimojo Institute of Community Medicine, Univ. of Tsukuba	Studies on interaction between mercury compounds and Cu, Zn-SOD by EXAFS
96-P002	Y. Aso Kyushu Univ.	Small-angle X-ray scattering studies on the stability of lipoate acetyltransferase core

Proposal Number	Spokesperson	Title
96-P003	H. Tsubakino Faculty of Engineering, Himeji Institute of Technology	Effects of addition of third elements on precipitation of δ' phase in Al-Li ternary alloys
96-P004	H. Masuda Faculty of Engineering, Tokyo Metropolitan Univ.	Measurement of optical properties of metal nanohole-array membrane
96-P005	M. Shiono Faculty of Science, Kyushu Univ.	Structure determination of $Ni(NH_3)_6Cl_2$ in low temperature phase
96-P006	M. Yamamoto Institute of Atomic Energy, Kyoto Univ.	ARUPS studies on the change in the electronic structure of Ti and Hf(0001) by oxygen adsorption
96-P007	K. Sayama National Institute of Materials and Chemical Research	Effect of Li on CO_2 hydrogenation over zeolite supported Rh catalysts
96-P009	S. Imamura Facutly of Engineering and Design, Kyoto Institute of Technology	Local structures of composite metal oxides prepared by rapid hydrolysis
96-P010	H. Wada Graduate School of Engineering, Kyoto Univ.	XAFS measurements of the field induced valence transition systems based on Eu
96-P011	T. Tanimori Faculty of Science, Tokyo Institute of Technology	The test for X-ray realtime analysis and polarization measurements with MSGC
96-P012	M. Terasawa Faculty of Enigneering, Himeji Institute of Technology	Study of radiation damage in nuclear reactor material by topographic observation
96-P014	S. Tsuneta Faculty of Science, Univ. of Tokyo	Calibration of XUV multilayer telescope aboard sounding rocket
96-Y001	K. Kubodera Interdisciplinary Research Lab. NTT	Materials analysis using synchrotron radiation
96-Y002	M. Sagara Mitsubishi Chemical Corp.	The structural analysis of Ru-Sn catalysis by XAFS
96-Y003	K. Iinuma NEC Corp.	Photo-chemical reaction experiments and X-ray optics
96-Y004	S. Sato Fujitsu Laboratories Ltd.	Exposure tests by synchrotron radiation in BL-17A, BL-17B, and BL-17C
96-Y005	K. Kuroda Central Research Laboratory, Hitachi Ltd.	BL-8A; soft X-ray diffractometry, X-ray absorption spectroscopy, soft X-ray microprobe. B; EXAFS experiments, total reflection measurement. C; lithography, microprobe experiments, micro X-ray diffractometry
96-Y006	O. Kaida Matsushita Technoresearch Inc.	XAFS Study of Nickel hydroxide

Proposal Number	Spokesperson	Title
96-Y007	K. Suzuki Central Research Laboratory, Hitachi Ltd.	BL-8A; soft X-ray diffractometry, X-ray absorption spectroscopy, soft X-ray microprobe. B; EXAFS experiments, total reflection measurement. C; lithography, michoprobe experiments, micro X-ray diffractometry
96-Y008	K. Yoshimi NEC Corp.	Soft X-ray lithography, photo-chemical reaction experiments and X-ray optics
96-Y009	S. Sato Fujitsu Laboratories Ltd.	Exposure tests by synchrotron radiation in BL-17A, BL-17B, and BL-17C
96-Y010	T. Yamazaki SAN Analysis & Consulting Service	EXAFS studies on the structure of Ni supported catalysis
96-C001	Y. Ohishi Tsukuba Research Laboraty, Sumitomo Chemicals, Inc.	Small angle X-ray scattering study for dynamical strucutre change of polymers
96-C002	S. Kimura Microelectronics Research Laboratories, NEC. Corp.	Evaluation of semi-conductor crystals with ultra-precise X-ray optics
96-C003	M. Imafuku Advanced Materials & Technology Research Laboratories, Nippon Steel Corporation	The dynamics of materials processing studied by synchrotron radiation
96C-004	S. Kawado Research Center, Sony Corp.	Developement of precise characterizaion techniques for semiconductor
96-C005	S. Nakagawa Kawasaki Heavy Industries, Ltd.	Basic study of diagnostic applications of SR monochromatic X-rays to medicine
96-C006	S. Yasuami ULSI Reserach Center, Toshiba Corp.	Analysis of microscopic structures using synchrotron radiation
96-C011	H. Hashimoto Toray Research Center	Studies of melts by means of XAFS
96-C012	K. Ogawa Fuji Photo Film Co., Ltd.	Local structure analysis of photographic silver halides
96-C017	N. Ishikawa Petroleum Energy Center	Studies of catalysts for crude oil processing with synchrotron radiation EXAFS
96-C020	Y. Iketaki Research Development Corporation of Japan	Measurement and analysis of soft X-ray absorption cross sections of atoms and molecules irradiated with ultraviolet light
96-C022	T. Akai Mitsubishi Chemical Corp.	Strucural studies on complexes used for liquified phase autoxidation by XAFS
96-C025	K. Sudo Mitsui Toasu Chemicals, Inc.	XAFS studies of metal catalysts for polymer resin synthesis
96-C027	K. Murakami Nicon Corp.	Characterization of X-ray multilayer reflecting mirrors using synchrotron radiation

Proposal Number	Spokesperson	Title
96-C030	S. Komiya Fujitsu Laboratories Ltd.	Structure analysis of thin film interface
96-C031	M. Ito Central Research Laboratory, Hitach Ltd.	X-ray imaging studies
96-C034	K. Tani Power Reactor and Nuclear Fuel Development Corporation	Development of a high power CW linear electron accelerator system
96-C043	S. Okude NKK Corp.	Chemical state determination with synchrotron radiation
96-C044	M. Ohsawa Fuji Electric Corporate Reserach and Development, Ltd.	Highly sensitive structure analysis of thin films by synchrotron radiation
96-C045	T. Kiyokura Interdisciplinary Research Laboratory, NTT	Studies of the electronic properties of nano-structures with undulator synchrotron radiation
96-C047	D. Amano Sumitomo Heavy Industries, Ltd.	Basic research on the design study of insertion devices
96-C049	A. Komura Hitachi Zosen Corp.	Development of monochromator for high brilliance synchrotron radiation

G: General
U: Urgent
S: Special
P: Preliminary
Y: Approved for charged beam time.
C: Collaborations between the Photon Factory and institutes of private companies.

Scientific Disciplines

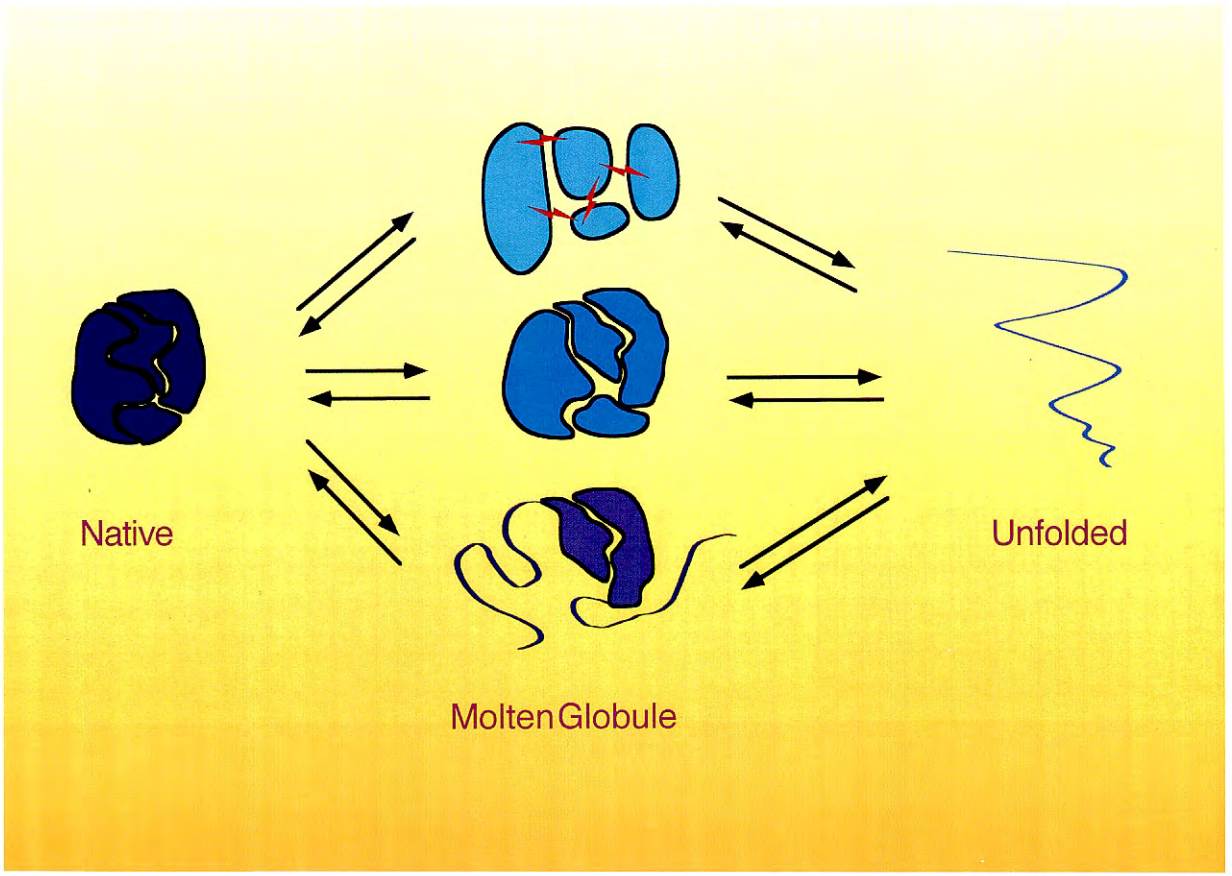

Schematic description of various types of molten globules derived from the results of solution X-ray scattering.

You can jump to the article by clicking its title.

CONTENTS

A. ELECTRONIC PROPERTIES OF CONDENSED MATTER (SOFT X-RAY REGION)

1 HIGH-RESOLUTION PHOTOEMISSION SPECTROSCOPY

High-resolution photoemission spectroscopy is now a standard tool to probe the electronic structures of various materials, such as correlated electron systems. A photoemission system with high energy resolution was constructed in the 92S002 project. The instrument comprises of a SCIENTA SES200 analyzer and a liquid-He cryostat. The project was run by a collaboration of outside users' groups and the Photon Factory internal staff. Low temperatures down to 11 K could be achieved with temperature regulation. The resolution of the analyzer is better than 30 meV. The total resolution mostly depends upon the resolution of the monochromator. In the 125 eV region, for example, the total resolution could be better than 40 meV. The whole system is open to all outside users who have active proposals accepted by the program assessing committee.

By using this system intensive studies have been made for Yb and Ce compounds, which have strong electron correlations. Figure 1 shows a typical result of the Kondo resonance peak of a Kondo insulator, YbB_{12}, resolved by this high-resolution photoemission instrument. The Kondo resonance peak was observed at about 25 meV below the Fermi level, in agreement with the Kondo temperature of about 220 K. The gap as a Kondo insulator is resolved in the B 2*p* valence band at low photon energies. The coexistence of the Kondo peak and the transport gap can be understood using a renormalized band picture.

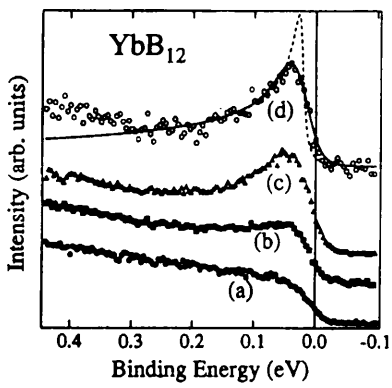

Fig. 1 Kondo resonance peak of YbB12 revealed by high-resolution photoemission at 30 K. The photon energies are a) 21.2, b) 40.8 and c) 125 eV.

Another example is on Yb_4As_3, which shows a heavy fermion behavior at low temperatures in spite of an extremely low carrier concentration. This material shows a structural phase transition at Tt = 288 K from a valence fluctuating state with a cubic crystal structure to charge ordered state with a trigonal structure. It is about 231 K for x = 0.12, the charge ordering and phase transition are strongly suppressed for x = 0.29. The electronic properties are found to drastically change in $Yb_4(As_{1-x}Sb_x)_3$ mixed crystals. The result for x = 0.12 is shown in Fig. 2, where the stabilization of the Yb^{2+} state on 3 long <111> chains and stabilization of the Yb^{3+} state on a <111> short chain is clarified. The narrowing mechanism of the Yb 4*f* state is also clarified. It has been confirmed that the spin degree of freedom is decoupled from the charge degree of freedom at low temperatures.

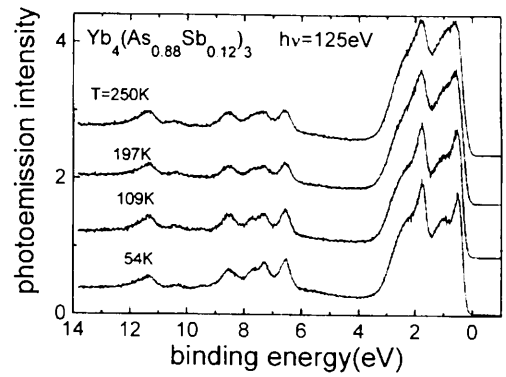

Fig. 2 Temperature dependence of the Yb^{2+} and Yb^{3+} photoemission spectra of a heavy fermion system $Yb_4(As_{0.88}Sb_{0.12})_3$.

It is known that resonance photoemission is a powerful technique for revealing details about the electronic structures. The 4*d* core resonance excitation provides much information about the 4*f* electronic states in Ce compounds. The 4*f* components are definitely resolved, as shown in Fig. 3, by taking the difference between the resonance maximum (122 eV) and minimum (114 eV). The temperature dependence of these spectra clarifies that the tail of the Kondo peak above the Fermi level is observed in the photoemission spectra. A theoretical analysis is performed based on the NCA calculation in the impurity Anderson model.

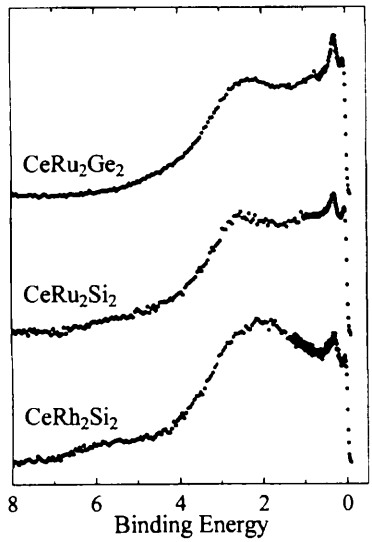

Fig. 3 Ce 4*f* photoemission spectra of typical Ce compounds.

Such studies should be extended to higher photon energies with very high resolution in the near future.

S. Suga, KEK and Department of Material Physics, Osaka University

2 SOFT X-RAY EMISSION SPECTROSCOPY

Soft x-ray emission spectroscopy (SXES) has recently been carried out by using synchrotron radiation; it has been found that SXES gives important information about the interaction of matter and light. SXES has a clear selection rule about the angular momentum, because it is a dipole transition. It is caused mainly within the same atomic species, because the core hole is strongly localized. Thus, the partial components of the density of states localized at an atom can be studied by SXES. It is especially evident for light element, such as B, C, N, and O. Furthermore, the inelastic-light-scattering process by various excitation photon energies corresponding to the resonance state of the electronic structure has been found in the soft x-ray region for several materials as well as for the fluorescence process.

Experiments were carried out at undulator beamlines BL2B and C, BL16B, and BL19B and a bend-magnet beamline (BL3B) installed at PF. A SXES spectrometer uses the Rowland circle geometry in which the input slit, spherical grating, and multichannel detector lie on the focal circle, whose radii are 5 m, 7 m, and 10 m; their line densities are 600, 1200, and 2400 lines/mm, respectively.

The SXES spectra of YNi_2B_2C, as an example of multiternary compounds, were measured. A comparison of the convoluted C- and B-projected DOS curves with the observed CK- and BK-SXES spectra shows that both spectra coincide with each other. We thus conclude that the SXES spectra and the valence-band photoelectron EDC of YNi_2B_2C can be interpreted in terms of the energy-band picture. Furthermore, it is found that the fractional DOS at the Fermi edge is higher in superconducting YNi_2B_2C than in non-superconducting $LaNi_2B_2C$. This is consistent with the prediction of the energy band calculation.

The transition-metal (TM)-2*p*-SXES of several transition metal compounds, such as Sc, Ti, V, Cr, and Mn compounds, has also been carried out. Strong inelastic scattering was found. The inelastic scattering in transition metal compounds can be elucidated by the *d-d* transition and the charge-transfer transition, though the coincidence with theory is not very good.

Several SXES studies about semiconductors, such as Si, BN, P, AlAs, and BP, have been carried out. Strong inelastic scattering as well as the fluorescence spectra was found. Compared with a band calculation,

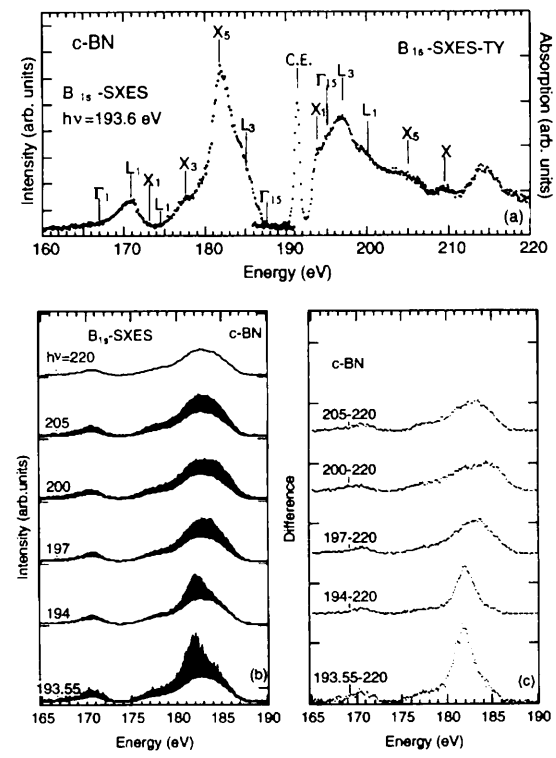

Fig. 4 (a) B1s-Total-yield spectrum of cBN. (b)Dots show B1s-SXES spectra and (c)their difference spectra from hn = 220 eV spectrum.

the momentum conservation between an excited electron and a valence hole was found.

S. Shin, Synchrotron Radiation Laboratory, Institute for Solid State Physics, University of Tokyo

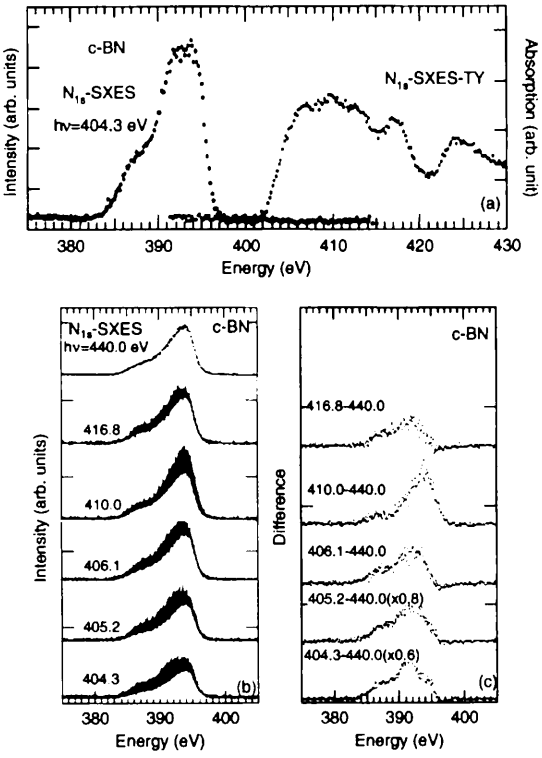

Fig. 5 (a) N1s-total-yield spectrum of cBN. (b)Dots show N1s-SXES spectra and (c)their difference spectra from hn = 440 eV spectrum.

3 SPIN-RESOLVED PHOTOEMISSION SPECTROSCOPY

Spin-resolved photoelectron spectroscopy is utilized to investigate the spin-dependent electronic structures of magnetic materials, such as ferromagnets, magnetic compounds, magnetic thin films, multilayers, and atoms and molecules, adsorbed on magnetic and non-magnetic solid surfaces. It is also used as a unique experimental method to investigate the roles of the electron spin, which appears in many electron effects in photoexcitation and its decay processes, which are observed as magnetic linear and circular dichroism, spin polarized photoelectron diffraction, spin-resolved valence band and core level photoelectron spectra, spin polarization of Auger electron spectra and so on. At the Photon Factory, spin-resolved photoemission experiments were performed at the Revolver undulator beamline (BL19A) using a 100-keV Mott scattering-type electron-spin polarimeter.

In Figs. 6(a) and 6(b) we show a set of majority and minority spin spectra of the Ni(110) valence bands observed in normal emission for excitation energies of between 20 and 90 eV. The binding-energy difference between each corresponding peak in the majority and minority spin spectra is due to exchange splitting. The spectral features of the majority and minority spin spectra consist of two major peaks and satellites, and show a photon-energy dependence, which corresponds to the dispersion along the Γ-K-X direction. By a

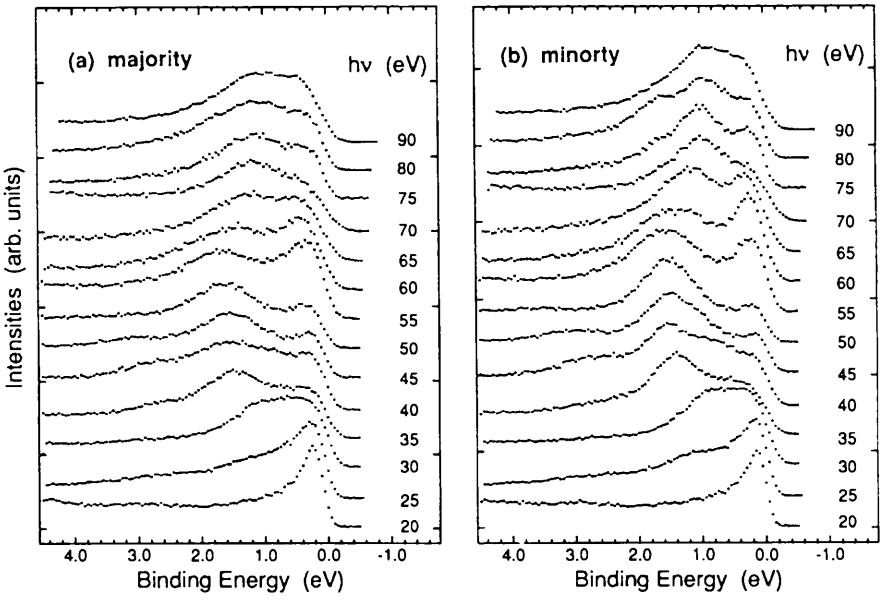

Fig. 6 Majority (a) and minority (b) spin spectra of Ni(110) valence band observed at excitation energies of from 20 eV to 90 eV, which correspond to the band dispersion along the Γ-K-X direction in the Brillouin zone.

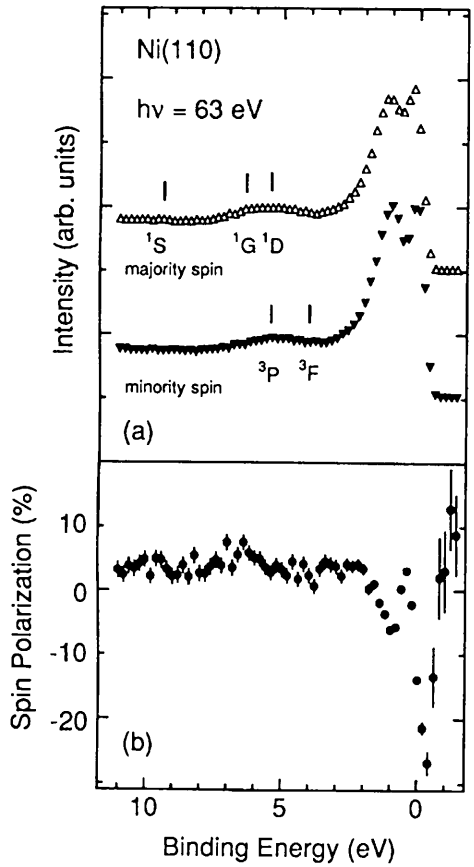

Fig. 7 Majority and minority spin spectra of the Ni(110) valence band. The vertical bars indicate the positions of the $3d^8$ final states expected by an atomic model.

quantitative analysis of the spectra we found that the binding-energy difference between different Ni $3d$ bands in the majority spin spectrum is smaller than that in the minority spin spectrum. This implies that the correlation of Ni $3d$ electrons in the majority spin bands is larger than that in the minority spin bands.

In the valence band photoemission of Ni, satellite structures have been observed up to 30 eV below the Fermi level, which have attracted attention for many years. The strong electron correlation enables us to understand satellites qualitatively by theories based on an atomic model. Figure 7 shows the majority and minority spin spectra of valence band satellites of ferromagnetic Ni. In the figure, distinct features in both the majority and minority spin spectra are observed in the 6 eV satellite. In the majority spin spectrum a broad feature with weak peaks at 6.4 and 5.5 eV is observed. In the minority spin spectrum, a broad feature has a weak peak at 5.6 eV. If we adopt an atomic model where the $3d^8$ final state is localized at a Ni atom, the intense peak at 6.4 eV in the majority spin satellite corresponds to the ^1G final state, which dominantly contributes to the positive spin polarization of the 6 eV satellite. The weak peaks around 5.5 eV in both majority and minority spin spectra correspond to the ^1D and ^3P final states, respectively. In this figure, the spectral feature corresponding to the ^3F spectrum in the minority spin state is not clearly resolved. This might be due to the broad and weak features of the ^3F state.

A. Kakizaki, Synchrotron Radiation Laboratory, Institute for Solid State Physics, University of Tokyo

B. ELECTRONIC PROPERTIES OF CONDENSED MATTER (X-RAY SCATTERING)

This section covers topics on the electronic properties of condensed matter by using X-ray scattering. Many excellent experiments were carried out this year. Among these experiments, we selected the following four topics because they include new techniques so that applications to many other field can be expected: the observation of charge- and orbital-ordering, non-resonant magnetic diffraction, inelastic scattering, and nuclear resonant scattering.

1 DIRECT OBSERVATION OF CHARGE- AND ORBITAL-ORDERING IN $La_{0.5}Sr_{1.5}MnO_4$

Recently, it has been recognized that the charge, spin, and orbital degrees of freedom play important roles in the electric and magnetic properties of the transition-metal-oxides. Especially, in perovskite-type manganites, the discovery of a wide variety of phenomena has stimulated people into activity in this field.[1] Here, we present a direct observation of an alternating Mn^{3+}/Mn^{4+} pattern and an orbital ordering pattern of an e_g-electron of Mn^{3+} in a layered perovskite-type manganite, $La_{0.5}Sr_{1.5}MnO_4$. Synchrotron X-ray diffraction measurements were performed at BL - 4C by using the anomalous dispersion of Mn^{3+}, Mn^{4+} and ATS (Anisotropy of the Tensor of Susceptibility) reflection techniques.

A. Charge ordering (CO): The proposed CO model is shown in Fig. 8.[2] The resulting CO unit cell has dimensions of $\sqrt{2}$ a $\times\sqrt{2}$a $\times$ c relative to the high-

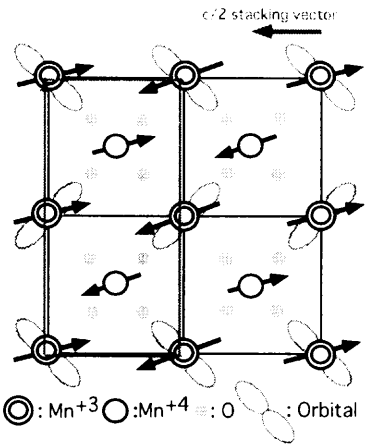

Fig. 8 Schematic of charge, spin, and orbital ordering in a layered perovskite manganite, $La_{0.5}Sr_{1.5}Mn_{O4}$.

temperature structure. The atomic-scattering factor near to the absorption-edge (E_A) is represented by f(E) = f_0 + f'(E) + i f''(E) as a sum of the Thomson-scattering factor and the anomalous-scattering factor. Since the E_A of Mn^{3+} will be a slightly shifted from E_A of Mn^{4+}, we can expect an enhancement of the CO superlattice peaks near to E_A. We really observed an anomaly of the superlattice peak (3/2,3/2,0) near to E_A at T = 29.6 K. The energy dependence of the superlattice intensity agreed well with the theoretical curve, which was calculated from the experimentally obtained f'(E) and f''(E) of Mn^{3+} and Mn^{4+}. This is direct evidence that the alternating Mn^{3+}/Mn^{4+} pattern is formed in the CO state.

B. Orbital ordering (OO): we supposed the OO pattern of e_g electrons in Mn^{3+} based on the spin configuration, as shown in Fig. 8, because the spins will be parallel in the direction of the spread of the orbitals by a double-exchange-like mechanism. The unit cell of this OO model is $\sqrt{2}a \times \sqrt{2}a \times c$. We used the ATS reflection technique in order to observe such a OO.[3] The ATS reflection means that "forbidden" reflections are caused by the anisotropy of the X-ray susceptibility of atoms, i.e. the atomic-scattering factor, due to the asphericity of the atomic-electron density and so on. This anisotropy is very small in the X-ray region, and in conventional X-ray diffraction theories the tensor of susceptibility is supposed to be isotropic, namely, the atomic-scattering factor is treated as a scalar. However, near to the X-ray absorption edges the anisotropy is largely enhanced through resonant scattering, so that the ATS reflections become measurable. Since the tensor of susceptibility of $Mn^{3+}(1)$ is not equivalent to that of $Mn^{3+}(2)$ in the OO state, as shown in Fig. 8, the ATS reflections should be observed. We really observed a very large enhancement of the OO superlattice reflection (3/4,3/4,0) at E = 6.552 keV, which is slightly higher than the absorption edge of Mn^{3+}. We also observed the typical oscillation of the ATS reflection around the scattering vector (azimuthal scan). The calculated curve can well fit the experimental data with only one parameter of the magnifying factor of the intensity axis. This is the first strong evidence of OO in this system.

The temperature dependence of the intensity of the CO and OO superlattice peaks indicate that the spin-ordering transition and configuration is based on the CO and OO state. Moreover, the CO may follow the OO. It is considered that this OO is caused by a reduction of the Coulomb energy. Namely, the anisotropy of charge motion due to the OO avoids an increase in the Coulomb energy: if the orbital of Mn^{3+} on a diagonal is extended in the direction of the same Mn^{4+}, the Coulomb energy will be increased on the Mn^{4+} site by the charge transfer. As a result of this OO, the CO will be caused. Thus, the OO in this system should be distinguished from the OO, which is stabilized by a cooperative Jahn-Teller distortion.

Y. Murakami, PF

References

1) e.g. Y. Tokura et al., J. Phys. Soc. Jpn. **63**, 3931 (1994).
2) Y. Moritomo et al., Phys. Rev. B **51**, 3297 (1995). B.J. Sternlieb et al., Phys. Rev. Lett. **76**, 2169 (1996).
3) T. Nagano et al., J. Phys. Soc. Jpn. 65, 3060 (1996).

2 NON-RESONANT X-RAY MAGNETIC DIFFRACTION STUDIES OF FERROMAGNETS

Non-resonant X-ray magnetic diffraction is known to be a unique tool by which a magnetic form factor can be separated into the orbital and spin parts (LS separation).[1] The white-beam method[2] of X-ray non-resonant magnetic diffraction, developed early in the 1990's, proved to be a powerful tool for measuring accurate magnetic form factors of ferromagnets comparable to those of neutron-diffraction experiments.

Here, we present the latest two results of non-resonant X-ray magnetic diffraction experiments made at BL-3C1. One is the LS separation experiment of hcp-Tb by the white-beam method. The other is the first application of a phase plate to a non-resonant X-ray magnetic diffraction experiment. In the latter, not only the phase plate was successfully applied to the X-ray magnetic diffraction, but also the magnetic effect could be enhanced by nearly an order of magnitude by combining a linear polarizer with the phase plate.

Firstly, the LS separation measurement of Tb is presented. We measured the flipping ratio of the diffraction intensity of the (103) plane of ferromagnetic hcp-Tb at 80K. The flipping ratio (R) is defined as, $(I_+ - I_-)/(I_+ + I_-)$, where I_+ is the diffraction intensity of the one magnetization direction and I_- is that of the reversed magnetization direction. From the X-ray magnetic-scattering theory,[1] R is represented as

$R(\alpha)=(\hbar\omega/mc^2)fp\{L(k)(\cos(\alpha)+\sin(\alpha))+2S(k)\sin(\alpha)\}/n(k)$,

where $\hbar\omega$ and mc^2 are the energies of the X-rays and the electron rest mass, respectively, f_P is the polarization factor, defined as $P_c/(1-P_l)$, where P_l and P_c are the degree of linear and circular polarization of the incident X-rays on the specimen, respectively, L(k), S(k) and n(k) are the form factors of the orbital magnetic moment, the spin magnetic moment and the electron charge, respectively, and α is the angle between the directions of the incident X-rays and the magnetization of the specimen. From measurement of R for two different α's, the L(k)/n(k) and S(k)/n(k) were obtained.

In this experiment the magnetization direction was along its easy axis of [010]. We measured the flipping ratio (R) for the reciprocal-lattice points of (h 0 3h) (h=2,4,5,6) and for those of the crystallographically equivalent (-h 0 3h) (h=2,4,5,6). The angle α was 76.3° for the (h 0 3h) and 13.7° for (-h 0 3h). From the observed R(76.3°) and R(13.7°), L(k)/n(k) and S(k)/n(k) were obtained, and are shown in Fig. 9. This result would be the first explicit separation of the total magnetic form factor into the orbital and spin parts. The solid and dashed lines in Fig. 9 are the calculated L(k)/n(k) and S(k)/n(k) for the Tb^{+3} ($4f^8$) ion under the dipole approximation and Hund's rule. The experimental data well reproduce the characteristic feature of the calculated curves.

Secondly, an enhancement of the magnetic effect of the non-resonant X-ray magnetic diffraction is shown by using a linear polarizer and a phase plate for

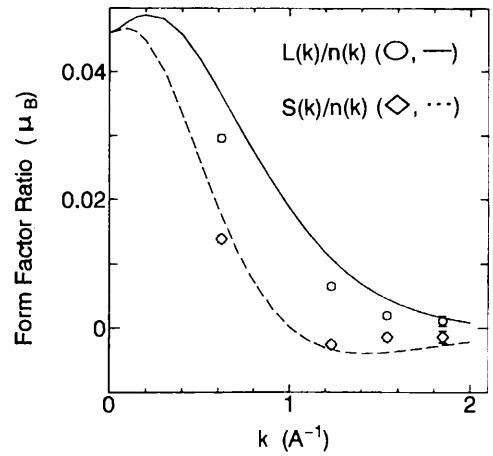

Fig. 9 Experimental and calculated form factor ratios, L(k)/n(k) and S(k)/n(k), for pure metalic Tb.

the first time. A phase plate of the transparent type was recently developed.[3] Synchrotron radiation ejected from a bending magnet was monochromatized by a Si(111) double-crystal monochromator. Then, the X-rays were passed through the phase plate of a diamond single crystal, where the incident linear polarization was transformed to another polarization state of P_l and P_c. The values of P_l and P_c, and hence f_P, were controlled through an offset angle of $\Delta\theta$ from the diffraction condition at the phase-plate crystal. The monochromatized and polarized X-rays were incident on a pure iron single crystal, which was set so that the (220) diffraction would take place in the horizontal plane with a scattering angle of 90°. We used the (333) reflection at the monochromator for Bragg scattering, which was 43.2°, close to 45°; then, the monochromator functioned as a linear polarizer due to a large extinction ratio of 520. We measured the flipping ratio (R) of the Fe (220) diffraction for various $\Delta\theta$'s. The observed R values are plotted in Fig. 10. The maximum R amounts

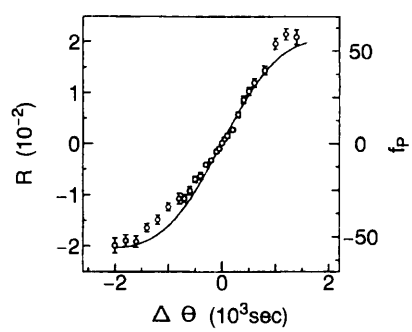

Fig.10 Experimental and calculated flipping ratio, R, of the Fe(220) diffraction intensity for various offset angles, $\Delta\theta$'s, of the phase plate crystal.

to 2×10^{-2}, which is nearly an order of magnitude larger than that measured by the white-beam method previously,[4] and is the largest among those ever measured in the non-resonant X-ray magnetic diffraction of ferromagnets. The corresponding fp is 55. This enhancement is due to an increase in the degree of linear polarization by the linear polarizer and precise control of the polarization by the phase plate. In Fig. 10 the calculated curve of R is shown as a solid line, and the experiment and calculation agree well.

M. Ito, Himeji Institute of Technology

References

1) M. Blume and D. Gibbs, Phys. Rev. B 37 (1988) 1779.
2) S. P. Collins et al, Philos. Mag. B 65 (1992) 37.
3) K. Hirano et al, Jpn. J. Appl. Phys. 30 (1991) L407.
4) M. Ito et al, PF Act. Rep. #12 (1995) 40.

3 INELASTIC X-RAY SCATTERING SPECTROSCOPY

3.1 Introduction

Since both the energy and momentum transferred can be parameters, the inelastic X-ray scattering (IXS) spectra possess various information which is largely unexploited. The reason for the paucity of the IXSS studies lies in its weak intensity. Recent developments of insertion devices, however, are making it possible to obtain quality IXS spectra within a reasonable span of time.

The differential cross section of IXSS is expressed in terms of the dynamic structure factor (S(q,E)) as follows:

$$\frac{\partial^2\sigma}{\partial\Omega\partial E} = (e_0 \cdot e_1)\left\{\frac{e^2}{mc^2}\right\}^2\left\{\frac{E_1}{E_0}\right\}S(q,E), \qquad (1)$$

where E and q are the energy and momentum transferred, and S(q,E) is related to the wavefunctions of the initial and final states of the system by

$$S(q,E) = \sum_f \left|\left\langle f\left|\sum_{j=1}^{N}\exp(iq\cdot r_j)\right|i\right\rangle\right|^2 \cdot \delta(E - E_{fi}). \qquad (2)$$

IXSS can be classified according to the magnitudes of q and E. Figure 11 shows the inelastic scattering spectra from liquid benzene taken at scattering angles of 60° and 90°. To the lower energy side of the exciting line, a broad Compton-like

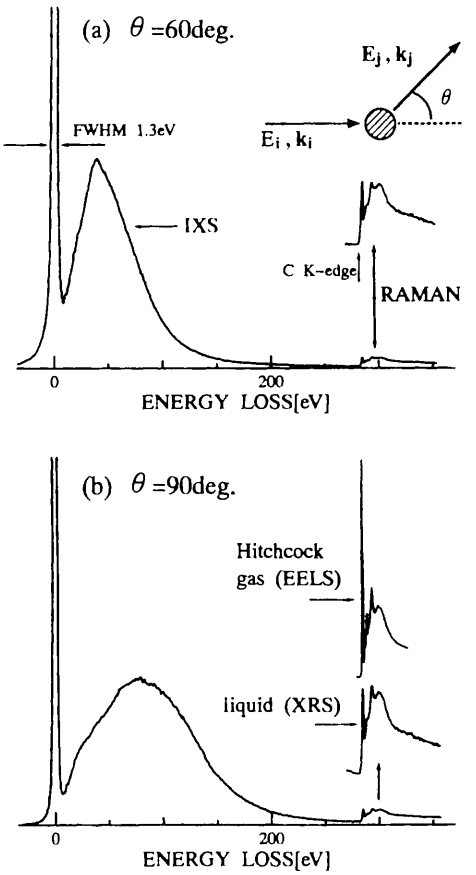

Fig. 11 Inelastic scattering spectra of liquid benzene at scattering angles of 60° (a) and 90° (b). Inserted in (b) is an electron energy loss spectrum of gas phase benzene.

scattering spectrum which depends on the scattering angle is observed. Then, at an energy loss of 284 eV, which is the K-absorption energy of carbon, there is an onset of an X-ray Raman spectrum followed by XANES-like features, which do not change with the scattering angle. The implication of these inelastic scattering spectra is described in detail in the following.

3.2 IXS by core electrons : X-ray Raman Spectroscopy (XRS)

The X-ray Raman scattering is a special case of IXS, where qr in eq.2 is small enough that the exponential term can be approximated as 1+iqr. The condition qr<<1 is satisfied if the spatial spread of the wavefunction involved is small as those of core electrons. Then, the dipole approximation is justified

and the matrix element in the dynamic structure factor is reduced to <f|qr|i>, which is in principle the same as that for absorption and emission. Hence, XRS gives essentially the same spectra as the soft X-ray absorption, but has several experimental advantages. Because X-rays are used, XRS is free from the various problems that plague soft X-ray spectroscopy, eg., surface contamination, a charge-up phenomenon, stray light, and the need of a vacuum. A wide energy range can be easily surveyed without changing the experimental conditions. In particular, as can be understood from the insert of Fig. 12, the crystal axis can be precisely aligned parallel or perpendicular to q, allowing a perfect separation of σ (in the plane) and π(perpendicular to the plane) transitions for layered compounds, like graphite and hexagonal boron nitride (h-BN).

Figure 12 shows the scattering spectra of a h-BN single crystal taken with the scattering angle either parallel or perpendicular to the crystal c-axis. The measurement was performed at BL-16A, a multipole wiggler beam line. Scattered X-rays were analyzed with a polychromator equipped with a cylindrically bent 50 × 50mm^2 Ge(440) crystal having a 550mm radius of curvature. As is evident from the form of the matrix element, q in XRS plays the same role as the polarization vector in absorption spectroscopy. Since the c-axis of h-BN is perpendicular to the layer or the ring plane, in-plane transitions ($1s\rightarrow\sigma^*$ states) are forbidden in the q||c configuration, while those perpendicular to the plane ($1s\rightarrow\pi^*$ states) are forbidden in q$\perp$c. It is unambiguously concluded from Fig.12 that the first band at 192 eV, which has been employed for the determination of the orientation of h-BN by XANES, consists entirely of the transition to π^* states. Although not shown here, XRS of the N edge that start at 402 eV can also be obtained by just changing the energy of the exciting X-rays.

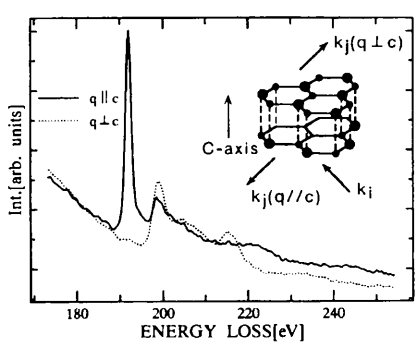

Fig. 12 XRS spectra of h-BN single crystal near to the B K absorption edge. Solid line: q|| c, dots: q$\perp$c.

3.3 IXS by valence electrons

Eqs. 1 and 2 are quite general, and should be used when qr<<1 does not hold, eg. for inelastic scattering from valence electrons. The thus-obtained S(q,E) has broad physical implications. The generalized oscillator strength (GOS) , df(q,E)/dE, is an example. GOS is defined by

$$\frac{df(q,E)}{dE}=\frac{E}{R(qa_0)^2}\sum_f\left|\left\langle f\left|\sum_{j=1}^{N}\exp(iq\cdot r_j)\right|i\right\rangle\right|^2\cdot\delta(E-E_{fi}). \quad (3)$$

Here, a_0 is the Bohr radius and R the Rydberg constant. GOS is a normalized quantity and can be made absolute by applying the Bethe sum rule,

$$\int_0^\infty\frac{df(q,E)}{dE}dE=N. \quad (4)$$

From GOS, various properties of matter can be extracted: the dielectric response function, the stopping power, the polarizability and so on (M. Inokuti, Rev. Mod. Phys. 43, 297 (1971)). In particular, GOS can be used to derive the absolute values of the static structure factor (S(q)), which is related to the electron-pair correlation function, and is a very correlation-sensitive quantity, as is evident from

$$S(q)=\int_0^\infty S(q,E)dE \quad (5)$$
$$=\left\langle\iint\Gamma(r_1,r_2)\exp[iq\cdot(r_1-r_2)]dr_1dr_2-|F(q)|^2\right\rangle_\Omega+N.$$

Here, $\Gamma(r_1,r_2)$ is the two-electron density, F(q) the elastic-scattering factor, N the number of electrons in the system, and $<\text{---}>_\Omega$ the spherical average.

The global variation of a GOS over extended ranges of energy and momentum transferred is best illustrated in a form called the Bethe surface, which contains all information about the interactions between matter and electrons or phonons. Although the significance of the Bethe surface is often stressed, few experimental determinations have been reported so far.

Figure 13 shows the Bethe surface of liquid water viewed from two different directions. The measurements were carried out at BL-16A with the

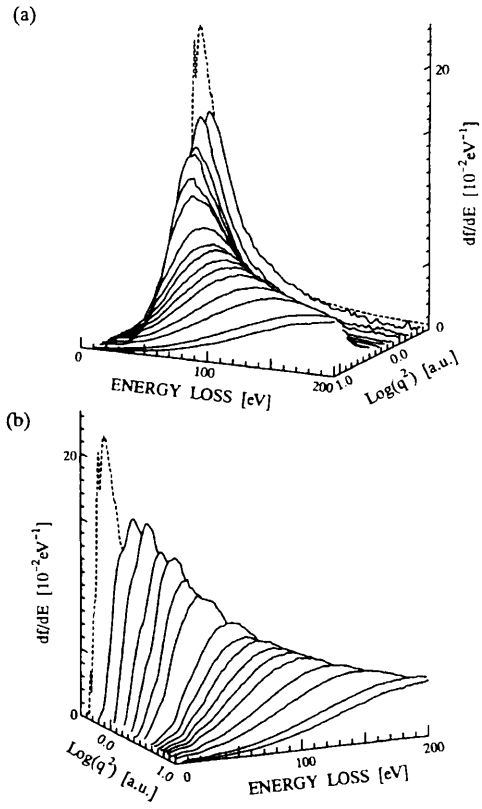

Fig.13 Bethe surface of liquid water viewed from two different directions. The dots are for gas phase water at q=0.

same experimental setup as that for the X-ray Raman scattering studies. From GOS the imaginary as well as the real part of the dielectric response function can be calculated as a functions of both q and E, and S(q) can also be determined by the use of eq. 5.

Figure 14 shows a comparison of the observed S(q) with calculated ones by using wavefunctions of various sophistication. An independent atom model (IAM) with a Hartree-Fock approximation (IAM-HF) does not take electron correlation as well as molecular

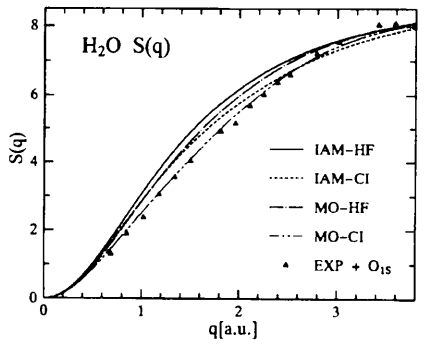

Fig.14 Comparison of the observed S(q) of water with various calculations.

bond formation effects into consideration. As a result, the S(q) calculated by IAM deviates significantly from the observed one. On the other hand, the S(q) calculated by MO-CI, which take both correlation and bond formation into account, almost coincides with the observed one. It should be stressed that the total energy which is usually used to qualify wavefunctions is not sensitive to electron correlation effects. Thus, S(q) makes a crucial test to judge the quality of wavefunctions from the viewpoint of correlation. Measurements of S(q) and comparisons with calculations are in progress on more complicated molecules.

Y. Udagawa, Tohoku University

4 NUCLEAR RESONANT EXCITATION OF ^{161}Dy AND ^{151}Eu

Since the success of Synchrotron Radiation (SR)-excited ^{57}Fe nuclear resonance excitation, several Mössbauer isotopes were reported to be excited by a SR pulse, such as ^{119}Sn, ^{169}Tm, ^{83}Kr and ^{181}Ta. The first nuclear excitation of ^{161}Dy and ^{151}Eu was observed this year, which were added to the SR-excited Mössbauer elements list.[1] One difficulty in this experiment was the poor detection efficiency of the avalanche photodiode detector (APD). Because both the resonance energies of ^{161}Dy and ^{151}Eu are over than 20keV, the APD has only 1% detection efficiency for these energies. Instead of detecting the resonance photons, we detected the nuclear resonant L-X rays fluorescence, for which energies the APD detection efficiency is a few ten percent.

The experiment was carried out at the X-ray undulator beamline AR-NE3. The experimental arrangement is shown in Fig.15. The excitation X-ray was monochromated by a water-cooled Si 111 double-crystal monochromator and by a high-resolution one comprising of two Si 660 channel-cut crystals with a dispersive setting. The time-delayed fluorescence components were observed as a function of the incident X-ray energy; the results are shown in Fig. 16. The time decay of nuclear resonant fluorescence of ^{161}Dy and ^{151}Eu from 30ns to 90 ns are shown in Fig. 17. The half-time of ^{161}Dy and ^{151}Eu are 29.4±1.9 ns in Fig. 17 and 9.3 ± 0.3ns, respectively, consistent with the values in the literature.[2]

Furthermore, the nuclear-resonant energies of ^{161}Dy and ^{151}Eu were determined based on a silicon

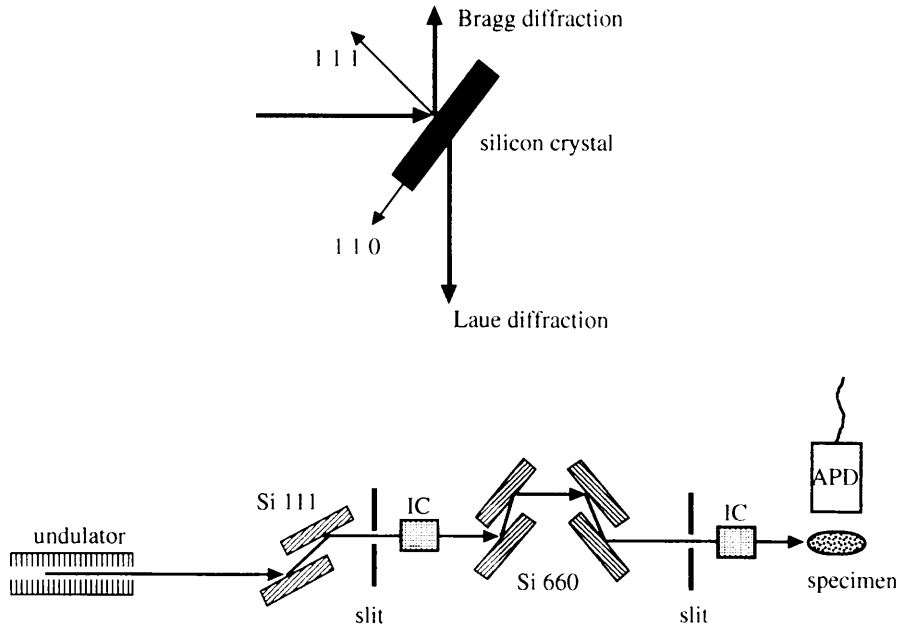

Fig.15 Side view of the experimental arrangement.

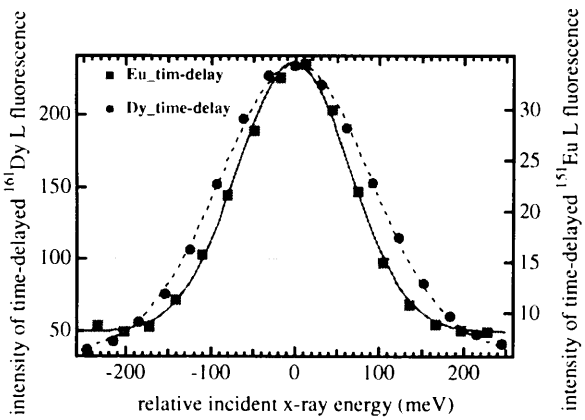

Fig.16 Intensities of the time-delayed L fluorescence from ^{161}Dy and ^{151}Eu versus incident X-ray energies.

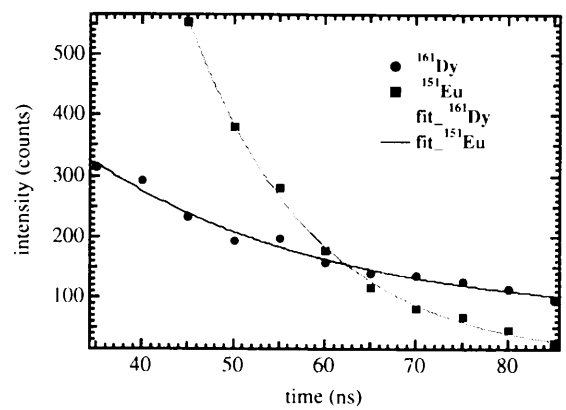

Fig.17 Time-decay profiles of ^{161}Dy and ^{151}Eu. The time starting point is the SR pulse; the noise events are negligible after 30 ns.

crystal lattice constant (0.5431018nm, at 22.5 °C and 1atm.). For the 25.65keV ^{161}Dy resonance energy; Laue-diffraction conditions of Si (12 12 0) ($\theta_B \approx 38.1°$) and its crossed lattice plane (8 8 8) Bragg diffraction ($\theta_B \approx 49°$) were selected; for 21.54keV ^{151}Eu, (10 10 0) ($\theta_B \approx 48.6°$) and (7 7 7) ($\theta_B \approx 40°$) of the same crystal was used. These two diffraction pairs occur in turn when the crystal is rotated within a small angle range of 3 degrees, which can be realized by a tangent-bar-driven high-resolution goniometer equipped with a rotary encoder. Diffraction profiles of Si (12 12 0) and (8 8 8) are shown in Fig. 18. Systematical errors could be considered as follows: (i) the crystal-lattice constant part, which is due to room-temperature fluctuations and the accuracy of its measurement; (ii) the diffraction angle part, which includes the miss alignment, crystal tilt, index of refraction, diffraction profiles, precision of the rotation table, accuracy of the angular encoder and so on. During the measurement, the temperature fluctuation was 0.2K, and the accuracy of the thermosencer was 0.1K. Therefore, the contribution of first part was estimated to be within 0.8ppm. It is small in comparison to that of part (ii). The incidence x-ray beam was 0.2(H) × 1.0(V)mm^2, which is close to the crystal rotation axis, within 0.3 mrad; the tilt angles of the two lattice planes were adjusted to within 1.7 mrad.

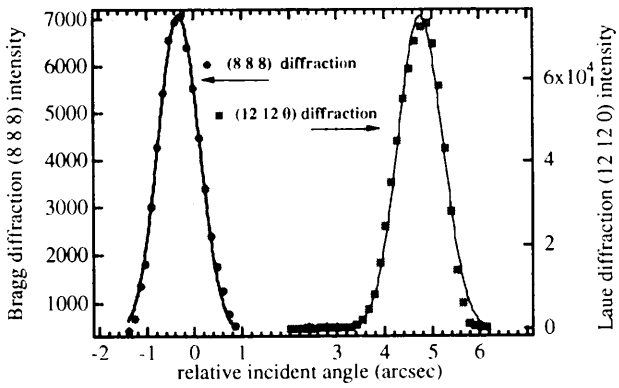

Fig.18 Diffractions of Si (12 12 0) and (8 8 8) for a resonance energy of ^{161}Dy. The abscissa is the relative incident angle for the Laue (12 12 0) and Bragg (888) diffractions. The angle between two diffraction peaks was observed to be 2.89334°.

These two terms interfere with the accuracy of the diffraction angles by about 1.4 μrad and 0.7 μrad, respectively. The rotary encoder (Canon X-1M) has an angular resolution of 0.00001°, and the accuracy is better than 1 arcsec for around. Since the measurement rotated the goniometer within 3 degrees, this error could be considered to be within 0.2 μrad. The total error described above is estimated to be less than 6ppm.

From the experimental results, the resonance energy of ^{161}Dy was determined to be 25.65130 ± 0.00016 keV. This value agrees fairly well with that in the literature (^{161}Tb 25.65135 ± 0.00003 keV).[2] The resonance energy of ^{151}Eu was measured as 21.54150 ± 0.00014 keV under the same experimental situation as ^{161}Dy, which is 440 ppm larger than that in the literature (21.532 ± 0.008 keV)[3] and in excess of the standard deviation there.

X. Zhang, PF

Reference

1) Ichiro Koyama, Yoshitaka Yoda, Xiaowei Zhang, Masami Ando and Seishi Kikuta: Jpn.J. Appl. Phys. **35** (1996) 6297
2) Richard B. Firestone et al. Ed. "Table of Isotopes" eight edition. 1996, John Wiley &Sons. INC. A Wiley-Interscience Publication. Appendix C. Nuclear specroscopy Standards.
3) ibid. Page 1555

C. STRUCTURAL PROPERTIES OF CONDENSED MATTERS

1. REFINEMENT OF COMPOSIT MODULATED STRUCTURES USING HIGH-QUALITY SINGLE-MICROCRYSTAL DATA FROM BL14A

Composite modulated structures are a subset of modulated or higher dimensional structures which can be understood as two substructures of different periodicities intergrown on the atomic level. The atoms in one substructure interact with the atoms in the other to optimise their chemical environments, i.e. their coordination polyhedra, bond lengths and non-bonding interactions. Consequently, each substructure modulates the other to mutually satisfy their chemistry.

The Ta_2O_5-WO_3 pseudo-binary system contains an extensive solid-solution with a composite modulated structure.This solid solution, $(1-x)Ta_2O_5 \times WO_3$, $0 \leq x \leq 0.267$, can be considered as having an anion-deficient α-UO_3-type structure. The elegance of a composite modulated structural description of such phases is that the same structural description applies across the entire solid solution.

To understand in crystal chemical terms why these structures are able to adapt continuously across such wide composition ranges it is necessary to have very accurately determined structural parameters both in terms of the atomic positions and compositional ordering across their respective composition ranges.

Collecting single microcrystal X-ray diffraction data using a high-flux synchrotron source on BL-14A allows for the attainment of good-quality data which are relatively free of systematic errors associated with absorption and secondary extinction. Other advantages are the low background and, particularly relevant for the subject systems, the ability to enhance scattering contrast between neighbouring elements by tuning the energy to just below an absorption edge for the lighter of two elements.

In this system, structures have been successfully refined at two different compositions from within a solid solution. Data were collected from microcrystals of $(1-x)Ta_2O_5 \times WO_3$, $0 \leq x \leq 0.267$, a solid solution at $x = 0.267$[1] and 0.14.[2] The refined structures[3,4] both showed a gradual evolution of the Ta/W coordination polyhedron from distorted octahedral (4 + 2) to pentagonal bipyramidal (5 + 2) (see Fig.19) with the W

atoms tending to occupy the former.

When the displacements of the metal and oxygen atoms were presented in their 4-dimensional form as atomic-modulation functions it became clear that the displacive Fourier coefficients for each of the structures were identical within 3σ, the only difference between the two structures being the magnitude of the modulation wave-vector. In other words, when described as a composite modulated structure, the one set of displacement parameters applies across the solid solution.

The chemical driving force underlying the W atom's preference for the distorted octahedral sites is illustrated by plotting the bond-valence sum[6] of the metal atom site as a function of q·T modulo, an integer (Fig. 20). Despite the gradual evolution of the coordination polyhedron (Fig.19) the metal and oxygen atom substructures perturb each other in such a way to as generate an almost bimodal distribution of chemical environments, i.e. sites which can accommodate W and sites which can not. A direct observation of the Ta/W compositional modulation was achievable since it was possible to enhance the scattering contrast between Ta and W using anomalous scattering, by collecting data just below the Ta L_{III} absorption edge.

The fine detail contained in the refinement results of this composite modulated structure demonstrates the unique advantages of obtaining high-quality single microcrystal diffraction data using a high-flux synchrotron source.

J. G. Thompson, Australian National Univ.

References

1) J.G. Thompson, N.Ishizawa, S. Schmid, B. Butler, S. Kishimoto, A.D. Rae, and R.L. Withers:Photon Factory Activity Report 1992, 10, 329.

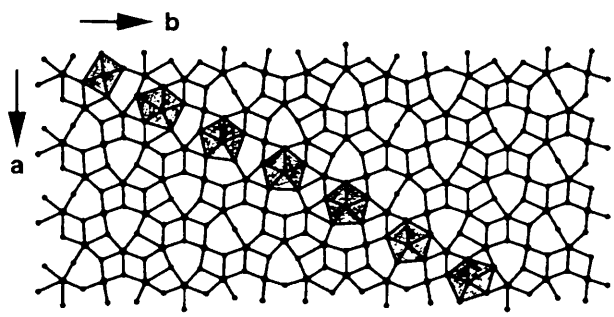

Fig.19 Portion of the final refined x =0.14 structure projected down the c axis direction with equatorial oxygens (O) and metals (M) represented by small and large circles, respectively.

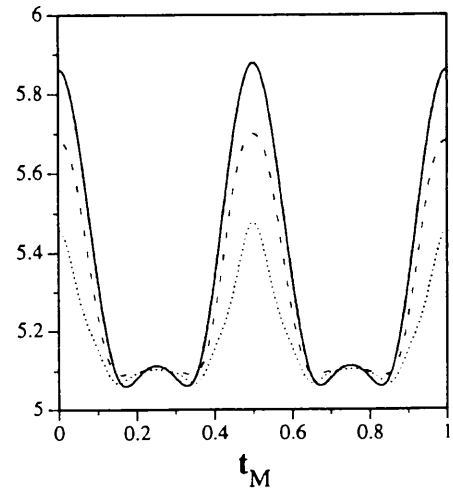

Fig. 20 Plot of the bond valence sums for the Ta/W site as a function of t_M (= **q**· T) for (1-x)Ta_2O_5 × WO_3, x = 0.1 (solid curve), x = 0.14 (dashed curve) and x = 0.267 (dotted curve).

2) J.G. Thompson, N. Ishizawa, S. Schmid, B. Butler, S. Kishimoto, A.D.Rae, and R.L. Withers: Photon Factory Activity Report 1993, 11,304.
3) S. Schmid, J.G. Thompson, A.D. Rae, B. Butler, N. Ishizawa, S.Kishimoto, and R.L. Withers: Acta Crystallogr., Sect. B, 51,(1995) 698.
4) A.D. Rae, S. Schmid, J.G. Thompson, R.L. Withers, and N. Ishizawa: Acta Crystallogr., Sect. B, 51, (1995) 709.
5) S. Schmid, K. Füterer, and J.G. Thompson: Acta Crystallogr.,Sect. B, 52, (1996) 223.
6) N.E. Brese and M. O'Keeffe: Acta Crystallogr., Sect. B, 47, (1991) 192.

2. OPTICAL PROPERTIES OF Er IMPURITY IN InP DIRECTLY RELATED TO LOCAL STRUCTURES AROUND Er ATOMS

Er emits light at 1.5 μm, which is the wavelength at the minimum transmission loss of the silica-based fiber and is stable at ambient temperature. The use for optical devices in the optical communication systems has been attracting much attention. However, the intensity of the luminescence is greatly dependent on the growth conditions. Figure 21 shows an example. The peak intensity at 1.54 μm changes by almost one order of magnitude when the growth temperature change from 550°C to 610°C. This dependence was

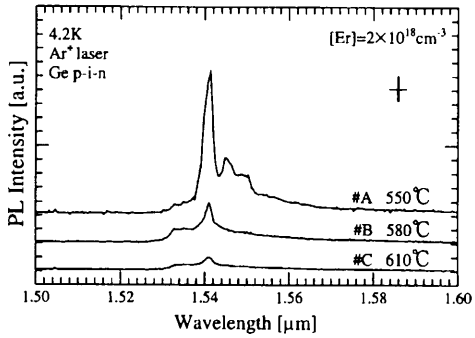

Fig. 21 Photoluminescence spectra from Er in InP. The intensity depends strongly on the growth temperature.

the same for an Er concentration of $2 \times 10^{18}cm^{-3}$. Since the 1.5 μm luminescence is due to an intra-shell transition in Er^{+3}, it is perturbed by only the near-neighbor atoms arrangement. Therefore, XAFS measurement at the Er edge should be the best-suited method to reveal the local structures around the Er atoms. The fluorescence XAFS measurement was conducted at beam line BL-12C, which was newly constructed for XAFS measurements on dilute and ultra-low quantity elements.

Figure 22 shows XAFS oscillations for several samples. Even at these low Er concentrations (uniformly doped in 1 mm-thick InP) high-quality signals were obtained. In the figure it is observed that the periods and amplitudes are different among those grown at higher temperatures (≥580°C, indicted by

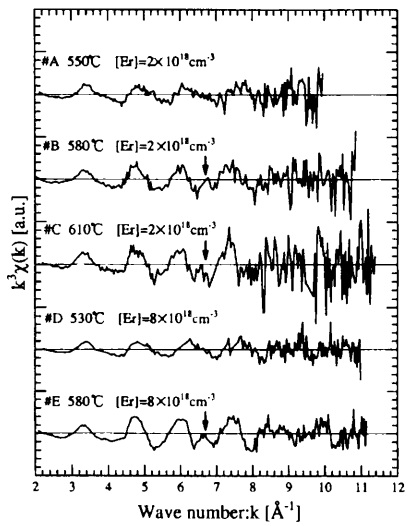

Fig. 22 XAFS oscillations for several samples grown at different temperatures and doped at different concentrations.

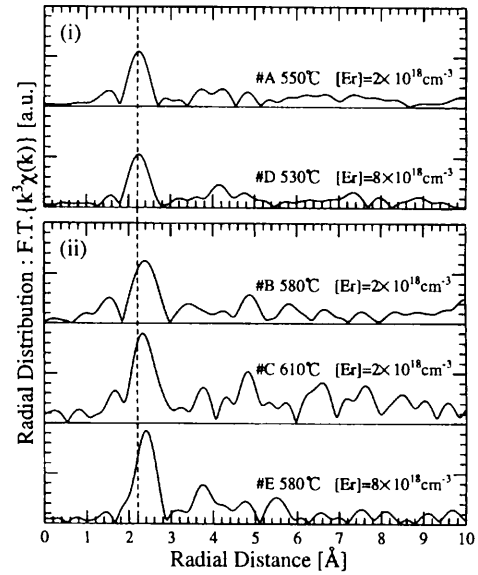

Fig. 23 Fourier transform of XAFS oscillations in Fig.22. They are clearly classified into two groups.

arrows) and at lower temperatures (≤550°C). It is much clearer in Fig. 23 where the Fourier transform of XAFS oscillations in Fig. 22 is shown. The location and peak height of the first peaks are classified into two groups. Those peaks were compared with the theoretically generated spectra, assuming several possible atom arrangements of Er, itself, and its near neighbors. Group (i) was found to correspond to Er substituted at the In-site (zincblende structure. Denoted as Er_{In}) and group (ii) to the rocksalt ErP (denoted as ErP). A further analysis revealed that the bond lengths in Er_{In} and ErP are 2.67±0.02Å and 2.77±0.03Å, respectively; 2.67Å is equal to the sum of the Er and P tetrahedral radii (1.57Å+ 1.10Å) and 2.77Å is quite close to 2.803Å of the Er-P bond length in rocksalt ErP. The coordination numbers for Er_{In} and ErP were 3.8~3.95 and 6.1~7.3, respectively. Though the accuracy of the coordination number is not high, it is close to 4 for the zincblende structure and 6 for the rocksalt structure.

The rocksalt structure ErP is semimetal. Er in a semimetal may have no chance to emit light, and has a very low excitation efficiency, since there is no energy gap wide enough for these processes. Er_{In} is an isolated impurity in InP with a sufficiently wide energy gap. Those are the reasons for the low and high emission efficiency. At higher growth temperatures Er may have sufficient thermal energy to form ErP microcrystals in the InP matrix.

Y. Takeda, Nagoya Univ.

3. A NEW UNQUENCHABLE HIGH-PRESSURE MINERAL IN THE LOWER MANTLE

The major components of the Earth's upper mantle are believed to be olivine, pyroxene, and garnet. In order to clarify the constitution and structure of the lower mantle, intensive studies have been made on the high-pressure phase transformations of these minerals above 26 GPa, a pressure corresponding to the Earth's lower mantle. It became clear that pyroxene transforms into very dense silicate with a perovskite structure, while olivine breaks down into an assemblage of silicate perovskite plus magnesiowustite, which has a rock salt structure. Both of these silicate perovskites have orthorhombic symmetry and are quenchable to ambient condition upon the release of pressure. These studies have clarified that the orthorhombic perovskite phase would be the most abundant mineral in the lower mantle. Compaired to studies on olivine and pyroxene, only very limited studies have been made on the behavior of garnet, because both the transition pressure and temperature are higher compared to olivine or pyroxene. A recent high-pressure *in situ* X-ray diffraction study on garnet clarified the formation of a new high-pressure mineral with an orthorhombic perovskite structure, but is unquenchable and transforms into the $LiNbO_3$ structure upon the release of pressure (Funamori et al., 1997).

Experiments were made at BL-13B2 using a diamond-anvil-type high-pressure apparatus coupled with an Imaging Plate (IP) detector. A natural garnet sample was squeezed and then heated above 1000 ℃ by a YAG laser at two different pressures. The X-ray diffraction profile obtained at 52.8 GPa is shown in Fig. 24A. The pressure decreased from 67.5 GPa during a high-temperature transformation. Most of the intense lines are well indexed as orthorhombic perovskite. The intensities of these lines are similar to those of $MgSiO_3$ perovskite. The other lines can be assigned to Ca-rich perovskite, stishovite, and garnet. The orthorhombic perovskite phase was observed even at 9.7 GPa, though splitting of the characteristic triplet 020+112+200 became unclear with decreasing pressure (Fig. 24B, 24C). Figure 24D shows the profile obtained after complete decompression. Diffraction from the orthorhombic perovskite can not be observed in this figure. The main peaks can be indexed on the basis of the $LiNbO_3$ structure, which has rhombohedral

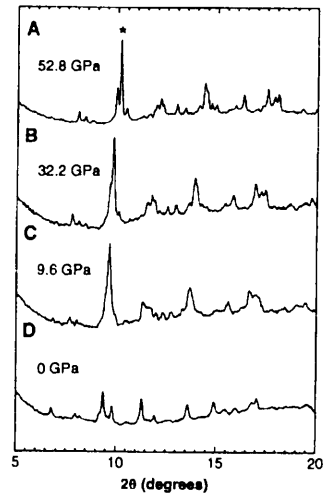

Fig. 24 X-ray diffraction profiles of the sample heated at ~60 GPa obtained during decompression. The star (★) indicates the characteristic triplet 020+112+200 of orthorhombic perovskite.

symmetry. The unit-cell parameters are a=4.837(1) A, c=12.733(7) Å, and V=258.0(2) Å3. The low intensities of the peaks of the rhombohedral phase might indicate the partial amorphization of orthorhombic perovskite, in addition to amorphization of Ca-rich perovskite. On the other hand, diffractions from orthorhombic perovskite was observed after complete decompression for a sample heated at 39.5 GPa (the pressure after heating was 30.2 GPa).

From the present experiments, it is clear that natural garnet of Py49Alm29Gro21Sp1 composition transforms to an assemblage of orthorhombic perovskite, Ca-rich perovskite, and an Al-rich phase with an unknown structure at ~35 GPa. At ~60 GPa, it transforms to an assemblage of orthorhombic perovskite plus Ca-rich perovskite. The orthorhombic perovskite phase synthesized at ~60 GPa converts to the rhombohedral phase upon the release of pressure. The perovskite might partially amorphize during decompression.

The present study clarified that garnet transforms into perovskite under a lower mantle condition, but is unquenchable and transforms into the $LiNbO_3$ structure upon the release of pressure. This unquenchable behavior can be explained by the dissolution of aluminum, which was contained in the starting garnet, into the perovskite structure. The increase in the aluminum content of the perovskite phase with pressure reduces the tolerance factor of the perovskite structure

and causes a transformation to the $LiNbO_3$ phase.

Our results show that the capacity of orthorhombic perovskite to accommodate aluminum increases with pressure. As the orthorhombic perovskite accommodates the mantle inventory of aluminum, even under the conditions of the uppermost part of the lower mantle, this phase seems to be the host mineral of aluminum to a deep part of the lower mantle.

T. Yagi, Univ. of Tokyo

Reference

1) N. Funamori, T. Yagi, N. Miyajima, and K. Fujino, Science, 275, 513 (1997)

4. SUPERABUNDANT VACANCIES AND DIFFUSION ENHANCEMENT IN METAL-HYDROGEN ALLOYS

X-ray diffraction measurements at high temperatures(≤ 1200°C) and high hydrogen pressures (≤ 8 GPa) revealed new features of metal-atom vacancies (superabundant vacancies) and an enhancement of the metal-atom diffusion.

Figure 25 shows an example of the process of superabundant vacancy formation in Ni, observed by using a cubic anvil press (MAX 80 or MAX 90) at a synchrotron radiation source at KEK. After the initial lattice expansion caused by hydrogenation, a gradual lattice contraction took place over a period of several hours as vacancies were introduced from the surface into the interior of the sample. The concentration of the vacancies, determined by density measurements after recovery to the ambient conditions, amounted to 20 at.%, ca. 10^7 times the thermal equilibrium value in pure Ni under the corresponding p, T conditions.

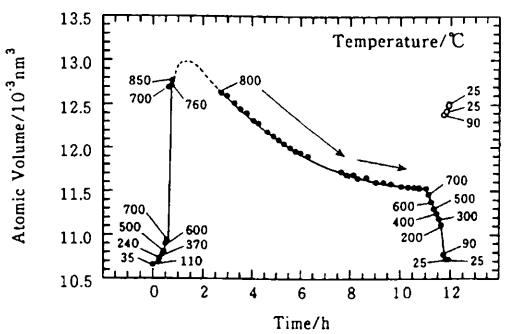

Fig. 25 Temporal variation of the atomic volume (unit-cell volume/4) of NiH_X in the course of a heat treatment under a hydrogen pressure of 5 GPa.

Similar superabundant vacancy formation was observed in a number of other metal -hydrogen systems,[1-3] and is now understood as being a general property of interstitial alloys.[4,5]

One of the most important consequences of superabundant vacancy formation is the enhancement of metal-atom diffusion. Fugures 26a and b compare the concentration profiles observed in Cu-Ni diffusion couples after a diffusion heat treatment; Fig.26a shows the situation under 5 GPa of hydrogen pressure and Fig. 26b under the same value of mechanical pressure. The interdiffusion coefficient is enhanced by ~10^4 on the Ni end and only ≤ 10 on the Cu end. This is clearly the effect of interstitial hydrogen; the solubility of hydrogen is [H]/[Ni] ~0.6 and [H]/[Cu] ~0.05 under these conditions. A similar enhancement of the interdiffusion was also observed in the phase-separation process of Pd-Rh alloys.[6]

The discovery of these phenomena, made possible by in situ X-ray diffraction at high temperatures and high hydrogen pressures, has opened a new field of research having profound implications in both fundamental and technological aspects of metal science.

Y. Fukai, Chuo Univ.

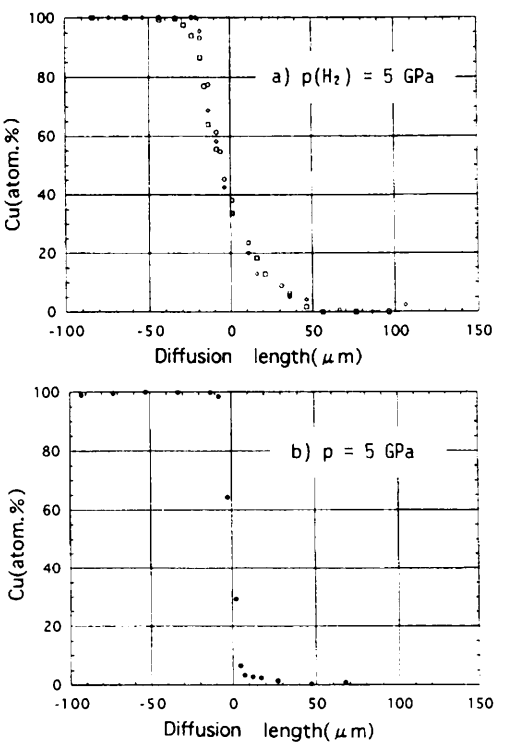

Fig. 26 Concentration profiles across the interface of Cu-Ni diffusion couples after a heat treatment at 800°C for 30 min; a) under a hydrogen pressure of 5 GPa, b) under a mechanical pressure of 5 GPa.

References
1) Y.Fukai and N.Okuma: Jpn. J. Appl.Phys., 32,L1256(1993)
2) Y.Fukai and N.Okuma: Phy. Rev. Lett., 73,1640(1994)
3) K.Nakamura and Y.Fukai: J. Alloys Compounds, 231,46(1995)
4) Y.Fukai: J. Alloys Compounds, 231,35(1995)
5) Y.Fukai, Y.Kurokawa and H.Hiraoka: J. Japan Inst. Metals, in press
6) K.Watanabe, N.Okuma, Y.Fukai, Y.Sakamoto and Y.Hayashi: Scripta Materialia, 34,551(1996)

D. STRUCTURAL PROPERTIES OF SOLID SURFACES AND ADSORBATES

As mentioned in the last volume, many studies are progressing concerning surface and interface structures using synchrotron radiation at the Photon Factory. The X-ray diffraction (XRD) method is a powerful tool for systems with long-range orders, such as metal/Si(111) - $\sqrt{3} \times \sqrt{3}$ structures.[1,2] Thus, we have decided to construct a new experimental station (BL-15B2) dedicated to surface-diffraction studies, which will be reported in the next volume.

On the other hand, Extended X-ray Absorption Fine Structure (EXAFS) is now well known as a suitable technique to study local structures using synchrotron radiation. Fluorescent-yield detection under the total-reflection condition is utilized to measure the EXAFS spectra of the surface adsorbates of sub-monolayer amounts, not only in the hard X-ray region,[3] but also in the soft X-ray region.[4] Thanks to the good performance of a new grazing-incidence monochromator station at BL-11A, the first surface EXAFS measurement at the Photon Factory on the oxygen *K*-edge has been conducted.[5]

I would like to introduce here two recent topical studies at the Photon Factory. One is the study on an electrode surface (liquid-solid interface); the other is on a study of surface local vibration.

Y. Kitajima, PF

References
1) S. Nakatani, Y. Kuwahara, T. Takahashi, and M. Aono, in this volume.
2) Y. Matsumoto, K. Akimoto, and A. Ichimiya, in this volume.
3) W.-J. Chun, S. Kishimoto, K. Asakura, and Y. Iwasawa, in this volume.
4) S. Terada, T. Yokoyama, M. Sakano, A. Imanishi, Y. Kitajima, M. Kiguchi, Y. Okamoto, and T. Ohta, in this volume.
5) K. Amemiya, Y. Kitajima, Y. Yonamoto, S. Terada, T. Yokoyama, and T. Ohta, in this volume.

1. *IN SITU* STUDIES OF A SEMICONDUCTOR ELECTRODE / ELECTROLYTE SOLUTION INTERFACE

The in situ study of an electrode/solution interface represents a problem of great relevance to surface science and other interfacial disciplines. Recently, these studies need direct experiments at the atomic level. The STM and AFM techniques provide very useful information concerning the electrode surface. The accuracy for the determination of the atomic distance, however, is rather limited. The application of surface X-ray techniques, which give much information at the atomic level concerning the electrode/electrolyte interface, have been expected. Only a few reports on studies using surface X-ray scattering (SXS), surface-extended X-ray absorption fine structure (SEXAFS) and X-ray standing wave (XSW) techniques[1-3] have been available.

The observation and control of electrochemical and photoelectrochemical reactions of semiconductor electrodes are very important for establishing etching processes and stable photoelectrochemical cells. No papers concerning the application of surface X-ray techniques to a semiconductor/electrolyte interface, however, have been published. Thus, SXS and EXAFS techniques in BL-16A and BL-13B, respectively, were employed for the first time to investigate the anodic dissolution process of a *p*-GaAs(100) surface[4] and the local structure of electrochemically deposited Cu on *p*-GaAs(100),[5] respectively.

SXS results: When an anodic potential was applied to the *p*-GaAs electrode, a dissolution current flowed and the intensity of the diffracted peaks corresponding to the (11) direction decreased with time. Figure 27 shows the time course of the diffraction peak intensity after the application of +0.5 V, where a steady current of 30 $\mu A \cdot cm^{-2}$ flowed. Although a very large current (several $mA \cdot cm^{-2}$) was observed at +0.5 V in a

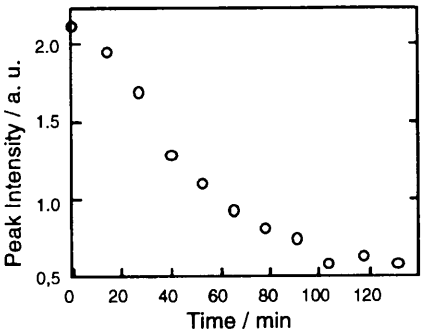

Fig. 27 Diffraction intensity for the (11) direction of *p*-GaAs(001) recorded as a function of time at +0.5 V in 0.1 M HCl solution.

conventional electrochemical cell, only a small current flowed in the present SXS measurement due to the very thin solution layer. The intensity of the diffraction peak decreased, and then became constant. This decrease in the diffraction intensity indicates that the *p*-GaAs(001) surface became rough. This result is in good agreement with our AFM results[6] concerning the anodic dissolution process.

EXAFS results: EXAFS parameters obtained for the Cu overlayers on the *p*-GaAs(001) electrode of four different coverages, θ, of 0.05, 0.25, 1, and 6 monolayers are summarized in Table 1. When θ were 1 and 6, only an interaction with the nearest neighbor Cu was obtained. The distances, (R), in these cases are very close to that of Cu with an fcc structure, 2.56 Å. Coordination numbers, N, (10.5 for θ=6 and 9.6 for θ=1) are, however, less than that for the fcc structure, 12. These results indicate that Cu clusters were formed on the GaAs surface when θ was more than one monolayer. Two new interactions with O (R=1.83 Å and N=1.5) and Cu of different distance (R=2.09 Å and N=0.8) were observed in addition to that with the fcc Cu (R=2.56 Å and N=1.5) when θ=0.25. When θ was 0.05, only these two interactions were observed. The interaction with O suggests that Cu was coordinated by a water molecule and/or sulfate anion. The small Cu-Cu distance observed for lower θ suggests the formation of Cu nano-clusters consisting of a small number of Cu atoms.

Table 1 EXAFS parameters.

θ		R / Å	N
0.05	Cu-O	1.84	1.3
	Cu-Cu	2.13	1.5
0.25	Cu-O	1.83	1.2
	Cu-Cu	2.09	0.8
	Cu-Cu	2.56	1.5
1	Cu-Cu	2.53	9.6
6	Cu-Cu	2.52	10.5

K. Uosaki and T. Kondo, Univ. Hokkaido

References

1) H. D. Abruña, "*Electrochemical Interfaces*", VCH Publishers, New York (1991).
2) M. F. Toney and J. McBreen, *Interface*, The Electrochemical Society, Spring (1991) 22.
3) T. Kondo and K. Uosaki, Hyomen, **33** (1995) 580.
4) K. Uosaki, M. Koinuma, T. Kondo, S. Ye, I. Yagi, H. Noguchi, K. Tamura, K. Takeshita, and T. Matsushita, *J. Electroanal. Chem.*, in press (1997).
5) T. Kondo, K. Tamura, M. Koinuma, H. Oyanagi, and K. Uosaki, *Chem. Lett.*, in press (1997).
6) M. Koinuma and K. Uosaki, *Surf. Sci.*, **311** (1994) L737.

2. COVERAGE DEPENDENCE OF THE Cl-METAL BOND STRENGTHS ON Ni (100) AND Cu (100) SURFACES

Extended X-ray-absorption fine structure (EXAFS) spectroscopy is a powerful technique not only for the determination of local surface strcutures, but also for investigations of surface vibrational properties, including anharmonicity. The coverage dependence of the adsorbate-substrate bond strengths has been studied by means of polarization- and temperature-dependent EXAFS measurements for Cl on Ni (100) and Cu (100) surfaces. The experiments were carried out at BL-11B. The Cl coverages were estimated to be 0.25 and 0.50 ML for Cl/Ni(100) and 0.12 and 0.50 ML for Cl/Cu(100), where 0.50 ML implies saturation coverage, which provided clear c(2×2) LEED patterns for both surfaces. The EXAFS spectra were taken at the X-ray incidence angles of 90° (normal incidence) and 15° at temperatures of 100 and 300 K using the Cl-K fluorescence yield mode. Figure 28 shows the filtered EXAFS oscillation functions for the first-nearest neighbor Cl-metal shells. In the case of Cu(100), one can find that the Cl-Cu distance is shorter in 0.50 ML than in 0.12 ML when one compares the phase delay between the low-temperature data. The fitting analysis gave the distances of 2.39Å and 2.42Å, respectively. On the other hand, in Cl/Ni(100) the reverse is true; namely 2.35Å for 0.50 ML and 2.31Å

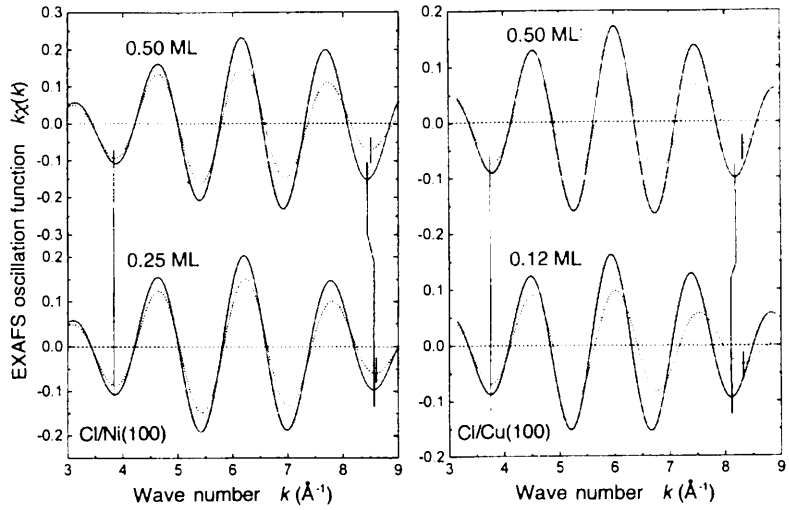

Fig. 28 Filtered Cl K-edge EXAFS oscillation functions $\chi(k)$ (k is the photoelectron wave number) for the first-nearest neighbor Cl-metal shells on Ni(100) and Cu(100) taken at temperatures of 100 K (solid lines) and 300 K (dotted lines). Some vertical lines are added for easier understanding of the phase delays.

for 0.25 ML. Figure 28 also provides information on the temperature dependence of the amplitude and phase, which is derived from the vibrational amplitude (Debye-Waller factor) and anharmonicity, respectively. In Cl/Cu(100) both quantities were found to be smaller at 0.50 ML, while in Cl/Ni(100) they are greater at 0.50 ML. All of the present findings conclusively suggest that the Cl-Cu bond is strengthened while the Cl-Ni one is weakened when the coverage increases. Density-functional calculations of surface clusters were performed in order to understand the different properties between Ni and Cu. The calculations excellently reproduced the experimental results, and indicate that the Cl charge behaves in a different manner with the coverage, leading to a dissimilar coverage dependence of the Cl-metal bond strengths. This originates from different Cl-metal bonding natures ascribed to the Cl $3p$ - Ni $3d$ and Cl $3p$ - Cu $4s$ interactions.

T. Yokoyama, The Univ. of Tokyo

References

1) T. Yokoyama, S. Terada, Y. Okamoto, M. Sakano, T. Ohta, Y. Kitajima, M. Tischer and K. Baberschke, Surf. Sci. **374** (1997) 243.
2) M. Kiguchi, T. Yokoyama, S. Terada, M. Sakano, Y. Okamoto, T. Ohta, Y. Kitajima and H. Kuroda, Phys. Rev. B **56** (1997) 1561.

E. ATOMIC AND MOLECULAR SCIENCE

1. ATOMIC SPECTROSCOPY

Electron correlations play an important role in atomic photo-ionization processes. From among the recent activities of atomic-photoionization research, two examples, electron manifesting correlation effects, are introduced. One of them is a show-case, demonstrating inter-shell and intra-shell interactions; the other is a direct probe for examining electron correlations in the continuum.

To study f-orbital collapse induced by inter-shell and intra-shell interactions, the $4d$ photoabsorption spectra of the Xe^{+}, Xe^{2+}, and Xe^{3+} sequence have been measured by a merging-beam technique at BL-3B. In Fig. 29, the radical redistribution of the 4d oscillator strength is observed in the sequence; in Xe^{+} most of the $4d$ oscillator strength is in the continuum, but in Xe^{3+} a very strong discrete transition is observed. The $4d$-$5p$ transitions are open for the ion-species of Xe. Those transitions are observed at around 55 eV in each spectrum. An interpretation for the radical oscillator strength redistribution, may be given in terms of a partial collapse of the nf bound states in Xe^{2+} and Xe^{3+}. Although calculations by the Multi-Configuration Dirac-Fock code have been tried to reproduce the experimental spectra, it failed for the Xe^{2+} and Xe^{3+} spectra. The failure implies that bound-continuum

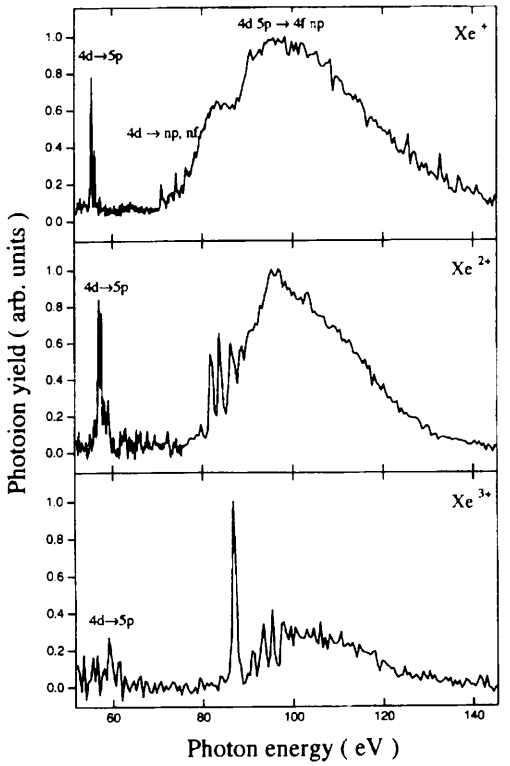

Fig. 29 4d photoabsorption spectra of Xe^{+}, Xe^{2+}, and Xe^{3+} ions. M. Sano, Y. Itoh, T. Koizumi, T.M. Kojima, S.D. Kravis, M. Oura, T. Sekioka, N. Watanabe, Y. Awaya, and F. Koike.

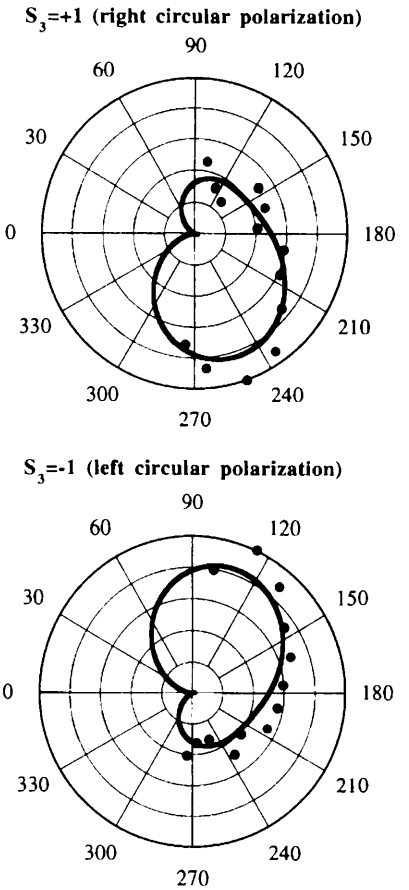

Fig. 30 Angular correlation patterns of two electrons ejected from Xe atoms. K. Soejima, K. Okuno, M. Shimbo, A. Danjo, E. Shigemasa, and A. Yagishita.

interactions should be taken into account. The theoretical treatment for strong bound-continuum interactions remains as an unresolved problem, since the observation of the striking 4*d* photoabsorption behavior in the Ba, Ba^{+}, and Ba^{2+} sequence.

A complete and exact description of the forces in the atom follows from quantum electrodynamics, which is already a well-established theory. Therefore, electron-electron correlation studies in atomic double photoionization, as compared to other systems (nuclear elementary particles), have the advantage that forces are known exactly. Recently, electron-electron coincidence measurements have been performed at BL-28A for the direct double photoionization process,

$$Xe + h\nu\ (44.75\ eV) \rightarrow Xe^{2+}(5p^4\ ^1D^e) + e_1(1\ eV) + e_2(8.35\ eV). \quad (1)$$

The angular correlation patterns between two outgoing electrons of e_1(1 eV) and e_2 (8.35 eV) in the perpendicular reaction plane to the propagation direction of circularly polarized synchrotron radiation are shown in Fig. 30. The circular dichroism in the angular correlation patterns is clearly observed in Fig. 30. Because of the electron-electron correlation, it is not allowed to assume that each electron is in a one-electron angular-momentum eigenstate. Instead, many pairs of angular momenta (l_1, l_2) will contribute to the two-electron continuum state, such that (l_1+l_2) is either even or odd. If one assumes the simplest angular-momentum pairs of (l_1, l_2)=(s, p) for the outgoing electron pairs, the angular correlation pattern may be expressed by

$$N_{true}(\phi_1 = 0^0, \phi_2 = variable) = A_0 + A_1 \cos\phi_2 + A_2 \cos 2\phi_2$$

$$\pm \frac{1}{2}(B_1 \sin\phi_2 + B_2 \sin 2\phi_2) \quad (2)$$

for 100% circularly polarized radiation. The coefficients depend on the fixed emission direction selected for the low-energy photoelectron (e_1) and the dipole matrix elements (magnitude and relative phases) for double photoionization. The solid curves in Fig. 30

show least-square fits of Eq. (2) to the experimental data points. From the reasonable fitting results, one can say that the (s, p) angular-momentum pairs dominate in the double photoionization expressed by Eq. (1). To examine the electron-electron correlations, one must calculate the dipole matrix elements using the initial- and final-sate wavefunctions, in which the electron-electron correlations are properly described. This theoretical work is under way in collaboration with theoreticians.

2. MOLECULAR SPECTROSCOPY

2.1 Valence Electronic Excitation

The penetration of solar radiation into the atmosphere in the wavelength region 250-130 nm is controlled by the O_2 absorption cross sections in the Herzberg bands, the Herzberg continuum, the Schumann-Runge(S-R) bands and the S-R continuum. For accurate modeling of these important processes, computations involving O_2 and minor species must be performed on a line-by-line basis. Photoabsorption cross sections with a resolution sufficient to yield the absolute cross sections are required for the molecules of interest. The minimum instrumental width of the existing grating spectrometers in the VUV region is 0.4 cm^{-1}. However, the linewidths of some molecular bands of interest in atmospheric science, particularly the S-R bands of O_2 for v'>12, are close to the Doppler width, i.e., ~0.12 cm^{-1} at 295 K. This situation motivated us to use the newly developed Fourier Transform (FT) spectrometer at Imperial College (IC), which can be operated with ~0.025 cm^{-1}, with intense synchrotron radiation as a background light source. In the IC VUV FT spectrometer, all of optical elements are installed in a tank of $l \times w \times h$ ~1.5 m × 0.3m × 0.3m so that it can be pumped out easily. A specially designed beam splitter of MgF_2 was used for wavelengths shorter than 150 nm. Synchrotron radiation was passed through a predisperser system, which enabled us to obtain a strong continuum with bandwidths limited to 2-4 nm, to have an ideal condition for FT spectroscopy. The band-head area of the (14,0) band of the S-R system is shown in Fig. 31, where the effects of different resolution, (0.06, 0.12, 0.20, and 0.30 cm^{-1}), are clearly shown. We deduced the predissociation widths for several hundred spectral lines, since the present lineshape can be described by a Voigt profile, which is a convolution of the Gaussian Doppler lineshape and the Lorentzian predissociation lineshape. The predissociation widths depend on the vibrational levels as well as the rotational levels. This gives us important information to elucidate the mechanism of the predissociation of the O_2 B $^3\Sigma_u^-$ state produced through S-R absorption.

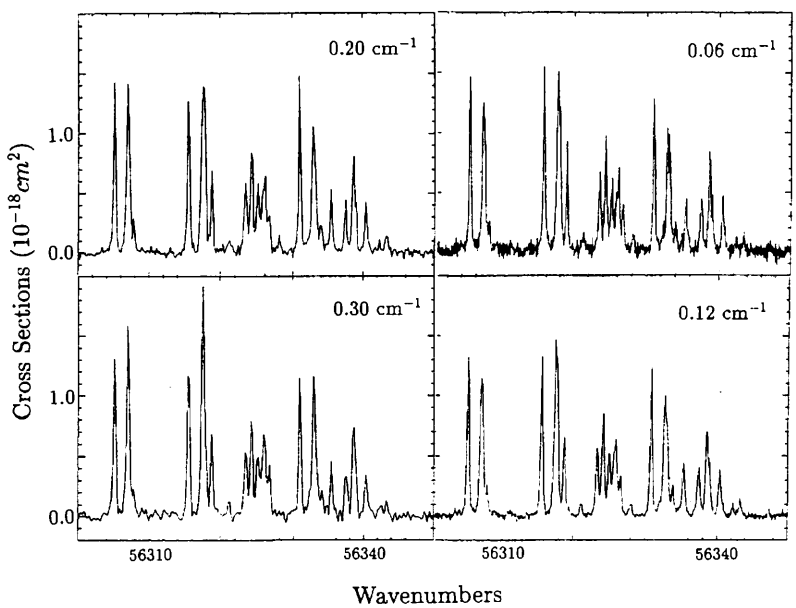

Fig. 31 The cross sections of the (14, 0) band of the Schumann-Runge system of O_2 with four values of resolution. K. Yoshino, A.P. Thorne and K. Ito.

2.2 Core Electronic Excitation

In the molecular core-level photoionization and photoexcitation processes, investigations on the influence of the anisotropic molecular potential on the emitted photo- and Auger electrons, and of the nuclear motion within the core-hole lifetime upon the dissociation dynamics are intriguing subjects. It has been shown that the angle-resolved photoelectron spectroscopy of fixed-in-space molecules gives detailed information about the photoionization processes, and high-resolution angle-resolved photoion spectroscopy provides an opportunity to examine the vibronic coupling for the core-level discrete resonances. These spectroscopic techniques have been developed at the Photon Factory.

The first example is a measurement of the angular distribution of $1s\sigma_{g,u}$ photoelectrons from CO_2, oriented parallel to the electric vector of incident light in the photon energy region of the σ^*_g and σ^*_u shape resonances. In Fig. 32 the measured angular distributions are shown by filled circles for photon energies 542 eV(σ^*_g resonance), 550 eV, 559 eV(σ^*_u resonance) and 579 eV. In these polar plots, the angle is measured from the molecular axis. It is quite interesting to point out that the photoelectrons are ejected preferentially along molecular axis at the σ^*_u shape resonance, while perpendicular to the axis at the σ^*_g shape resonance. Analyses of the experimental results indicate that the observed angular-distribution patterns at the shape resonances reflect the mixing of multiple partial waves and the interferences among them, instead of a single dominant partial wave component. This is in contrast to the N_2 case, where the angular distribution at the σ^*_u shape resonance is characterized by the l=3 partial wave. Quasi-atomic model calculations have reproduced the observed distribution fairly well. In this model, the angular distribution for CO_2 can be described as the coherent sum of the photoelectron current emitted from the two equivalent oxygen atoms. It is concluded in this model that the intra-molecular interference and the *spd*-hybridization in the photoelectron wave function play an important role to characterize the emission directions of the photoelectrons.

The second investigation concerns the nature of the C1s $\rightarrow \pi^*$ resonance of carbon-containing triatomic molecules. Figure 33 shows the high-resolution (ΔE_{photon}=0.08 eV) angle resolved ion-yield spectra for

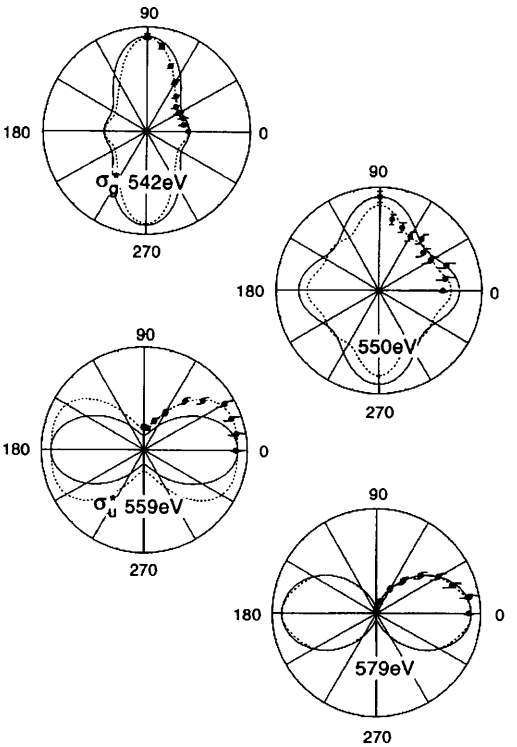

Fig. 32 Polar plots of the angular distributions of photoelectrons from CO_2 molecules oriented parallel to the polarization vector, which is directed to the 0°-180° line. The filled circles with error bars represent the experimental data points, and the broken curves show the fits to the experimental data. The theoretical results are drawn by the solid curves, which are normalized at the maximum points. N. Watanabe, J. Adachi, K. Soejima, E. Shigemasa, A. Yagishita, N.G. Fominykh and A.A. Pavychev.

CS_2 (a), OCS (b) and CO_2 (c); the solid line shows the ion yield measured at 90° and the dotted line at 0° with respect to the electric vector of the incident radiation, together with the anisotropy parameter β. The spectral profiles of the π^* resonance peaks for these three molecules show strong differences: 1) the symmetric and sharp π^* peak of CS_2 indicates that the Renner-Teller splitting between the $\pi^*_{in\text{-}plane}$ excited state with a bent equilibrium geometry and the $\pi^*_{out\text{-}of\text{-}plane}$ excited state with a linear equilibrium geometry is less than 0.1 eV, and that only the zero-point stretching and bending vibrational levels are involved in the peak, 2) the Renner-Teller splitting is very large for CO_2 and a great number of unresolved vibrational levels of bending and symmetric stretching modes are coupled in the $\pi^*_{in\text{-}plane}$ and $\pi^*_{out\text{-}of\text{-}plane}$ excited states, 3) the three fine structures

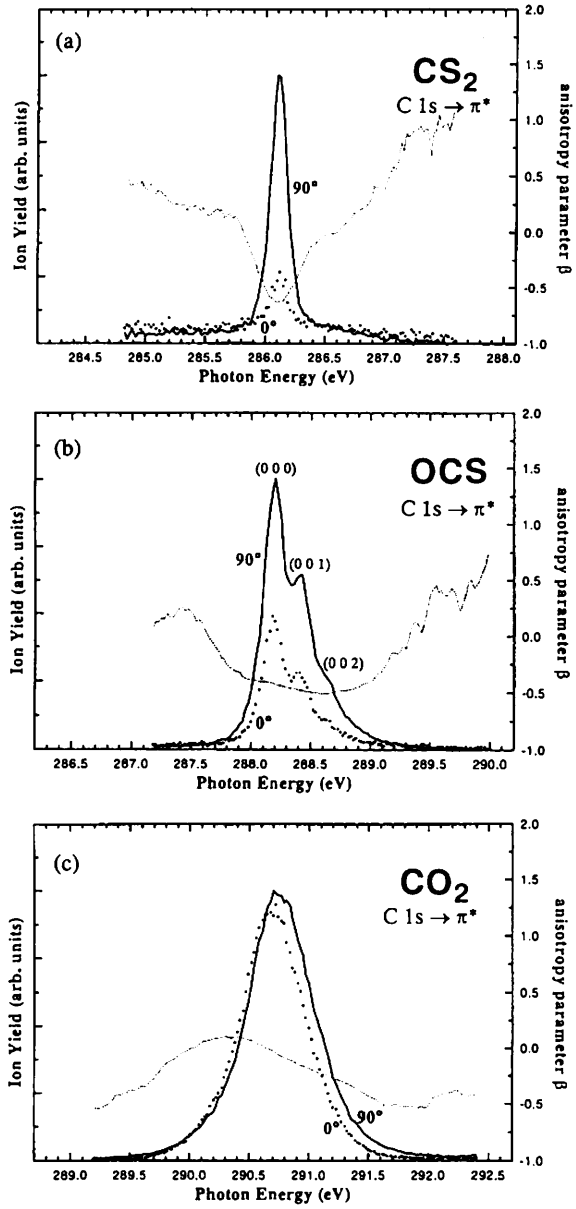

Fig. 33 Angle-resolved ion yield spectra for the excited state of CS_2 (a), OCS (b) and CO_2 (c) measured with a bandpass of 0.08 eV. The solid lines show the ion yields measured at 90° and the dotted lines at 0° together with the anisotropy parameter b. J. Adachi, N. Kosugi, E. Shigemasa and A. Yagishita.

with separations of 0.21 eV for OCS are assigned to the v=0, 1 and 2 of the ν_3 C-O stretching mode involving some bending vibrations in the $\pi^*_{\text{in-plane}}$ excited state. It should be emphasized that fragment ions are energetically emitted not only in the 90° direction, but also in the 0° in the C1s → π* excitation. Especially for CO_2, the 0° ion yield is comparable to the 90° ion yield. This is related to a strong vibrational coupling of

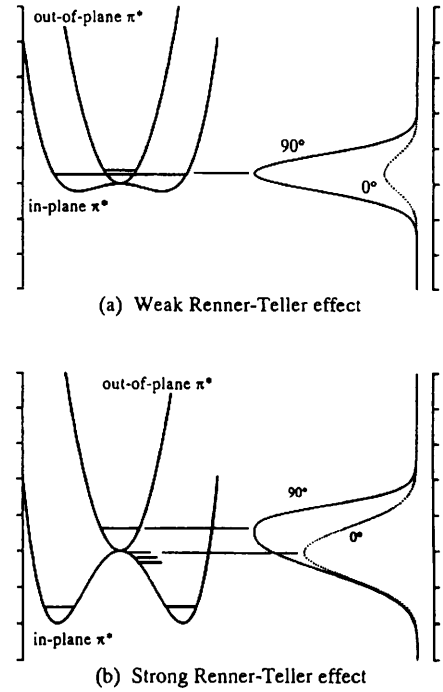

Fig. 34 Schematic potential energy curves of the C1s → in-plane π* ($\pi^*_{\text{in-plane}}$) and out-of-plane π* ($\pi^*_{\text{out-of-plane}}$) excited states for (a) weak and (b) strong Renner-Teller effects. J. Adachi, N. Kosugi, E. Shigemasa and A. Yagishita.

the $\pi^*_{\text{in-plane}}$ excited state with bending vibrations through the Renner-Teller effect. Such situations are schematically represented in Fig. 34, as the dependence of the fragment ion yield curves at 0° and 90° upon the strengths of the Renner-Teller effects.

A. Yagishita, PF

F. SOLUTION STRUCTURE AND STRUCTURE FORMATION OF PROTEINS

Small angle X-ray scattering (SAXS) using synchrotron radiation has been a widely utilized technique in structural biology as well as protein crystallography. SAXS is a much lower resolution technique than X-ray crystallography. A major advantage, in addition to the ability to measure proteins in solution, is that samples can be studied under near-physiological conditions or under extreme conditions where proteins take non-native conformations, which are frequently impossible for protein crystals. We have two types of SAXS camera at the Photon Factory: one

is the so-called MUSCLE diffractometer installed at BL-15A; the other is the so-called SAXES camera installed at BL-10C. The MUSCLE diffractometer, designed to study the contraction mechanism of muscles, utilizes a focused beam with a bent mirror and a bent monochromator. The SAXES also gives a focused beam with a bent cylindrical mirror, which is monochromatized by a doube crystal monochromator. The following are the most typical and important examples of SAXS studies on protein solutions.

1. STRUCTURE AND FUNCTION OF CALMODULIN

The principal means by which cells respond to increases in the intracellular free calcium ion concentration produced by primary stimuli is through calcium receptor proteins. These proteins act as "molecular switches" in various biochemical pathways by binding calcium ions reversibly and by altering their interaction with target proteins. Such interactions activate the protein targets, stimulating physiological processes in response to the calcium signal. Calmodulin is the most extensively studied intracellular calcium-binding protein, both in terms of its structure and with respect to its role in modulating a variety of cell functions through its interactions with many different enzymes.

Because of the importance of calmodulin, much work has focused on the molecular mechanisms underlying the protein-protein interaction and the ensuing enzyme activation. SAXS studies play central roles in a better understanding of such problems. Many excellent studies have been published with the data taken at the Photon Factory. In fact, a calcium-dependent dumbbell to the globular transition of calmodulin upon the binding of target peptides has been revealed by SAXS, which led to a structural analysis of the calmodulin-peptide complex to atomic resolution by X-ray crystallography and NMR.

The Izumi and Yoshino group, one of the pioneers in this special field, extended their SAXS work to yeast calmodulin.[1] Although the primary structure of calmodulin is extremely conservative among vertebrates and invertebrates, for the primary structure of yeast calmodulin, the homology is exceptionally low, only 60%. Vertebrate calmodulin contains 4 calcium binding sites. However, yeast calmodulin cannot bind calcium at the fourth site. Yeast calmodulin is a poor activator of vertebrate enzymes. The solution structure of yeast calmodulin has been studied in order to elucidate such functional differences.

Table 2 Radius of gyration of calmodulins

CAMs	-Ca^{2+}	5Ca^{2+}	5Ca^{2+}+MLCK-22
bovine brain	20.9	21.5	17.9
yeast	21.1	19.9	18.3
C4Y	20.6	19.5	18.0
C4Y140E	20.5	20.2	18.2

The radius of gyration of yeast calmodulin decreased from 21.1 Å to 19.9 Å when excess Ca^{2+} was added (Table 2). This is the opposite change found in bovine brain calmodulin. An increase in the radius of gyration is usually observed upon the binding of Ca^{2+} for a typical vertebrate calmodulin (Table 2). The profiles of the pair-distribution function suggested that yeast calmodulin without Ca^{2+} has a dumbbell-like shape which changes toward a rather asymmetric globular shape from its dumbbell shape by binding Ca^{2+}. In the presence of a calmodulin binding peptide, such as MLCK-22, a synthetic peptide corresponding to residues 577-598 of skeletal myosin light chain kinase, the radius of gyration of yeast calmodulin decreased by 1.6 Å, and the molecular its shape, estimated from the profile of the pair-distribution function, was globular, but less compact than that of vertebrate calmodulin.

In order to explore the functional role of Ca^{2+} binding to the fourth site, they produced chimeric proteins of chicken and yeast calmodulin. C4Y consists of Ala-1 to Ile-130 for chicken (including Ca^{2+} binding site I, II and III) and Asp-131 to Lys-148 of yeast calmodulin (including site IV). C4Y140E is produced by a single substitution of Glu for Gln-140 in the C4Y. The decrease in the radius of gyration upon binding of Ca^{2+} is observed for both chimeric calmodulins (Table 2). The fact suggests that the difference in the structural behavior upon binding of Ca^{2+} between vertebrate and yeast calmodulin is attributable to the difference in the ability of Ca^{2+} to the binding site IV. The shape change for C4Y is almost identical to that of yeast calmodulin, while C4Y140E retains a dumbbell-like structure upon the binding of Ca^{2+}.

These results suggests that the functional differences between yeast vertebrate calmodulin could be interpreted on the basis of the structural differences between them, and that Ca^{2+} binding at site IV is essential to form the full active dumbbell structure,

which is characteristic of vertebrate-type calmodulin.[1]

SAXS studies have suggested that the solution structure of calmodulin is not necessarily identical to the crystal structure. Using a deletion mutant of calmodulin, Kataoka et al. reported further evidence for the structural difference between in solution and in crystal.[2] The crystal structure of mutant calmodulin lacking Glu-84 (des84) shows interesting and significant deviations from the structure of native calmodulin. The linker region of the central helix in des84 is bent by approx. 30° at Lys-75 and approx. 90° at Ile-85. Thus, the overall shape looks rather more globular than dumbbell.

The solution scattering profile of des84 was completely identical to that of wild-type calmodulin, indicating that the solution structure of des84 is indistinguishable from that of the wild type. The radius of gyration and the maximum dimension of des84 in the presence of Ca^{2+} are 20.8 Å and 62.5 Å, respectively. These values are larger than those expected from the crystal structure of des84, 18.5 Å and 55.0 Å, and smaller than those expected from the crystal structure of the wild type, 22.8 Å and 67.5 Å.

The distance distribution function (Fig. 35) indicates that it assumes an elongated, dumbbell shape in solution. The observed differences between the averaged solution structure and the crystal structures of des84 and the wild type suggests that an ensemble of structures is available to calmodulin in solution, and that the linker region of the central helix of calmodulin functions as a flexible tether. Only one component would be selected for crystallization.[2]

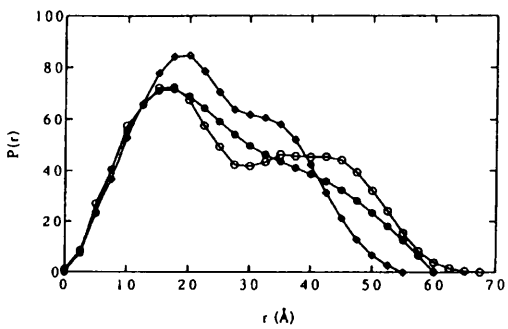

Fig. 35 Comparison of the distance distribution functions. The solid circle indicates the observed P(r) for Ca^{2+}-des84; the open circle, the calculated P(r) for the crystal structure of Ca^{2+}-wild type calmodulin; the open square, the calculated P(r) for the crystal structure of Ca^{2+}-des84.

2. X-RAY SOLUTION SCATTERING STUDIES OF PROTEIN FOLDING

Protein folding is a reaction in which an extended polypeptide chain acquires maximal packing through the formation of the secondary and tertiary structures. Therefore, the compactness and shape are the critical properties characterizing the process of protein folding. Because the stability of the native state is determined by the subtle free energy balance between the native and denatured states, the characterization of the denatured state is also essential to understand the conformational stability of the native state. Kataoka and coworkers have shown that solution X-ray scattering is the best technique available today in order to address these problems.[3] Although the structural resolution of the unfolded or compact denatured states elucidated from solution X-ray scattering is low, it provides a variety of information complementary to those obtained by NMR or X-ray crystallography.

2.1 Structural characterization of various denatured states

An ideal model for an unfolded protein is that of a "random coil". Since classical experiments demonstrated that proteins denatured by guanidine hydrochloride (GuHCl) are random coils, it is misconstrued that the denatured state is a random coil under all conditions. However, there is evidence that proteins can have significant amounts of residual structure, even in 4M GuHCl. Solution X-ray scattering data can give information on the extent of the randomness of a chain-like conformation. In this context, Akasaka and coworkers[4] investigated the methanol-induced denatured state of cytochrome c intensively. They revealed that at an intermediate methanol concentration (25%) cytochrome c takes a compact denatured conformer (I_M). A further addition of methanol transformed this I_M state into an expanded and highly helical denatured state (H). The H state has a chain-like conformation. The radius of gyration of the H state is similar to that of the acid denatured state (D), which has almost no helical content. The determined phase diagram of cytochrome c is given in Fig. 36.[4]

2.2 Structural characterization of molten globule

Much attention has been paid for characterizing a

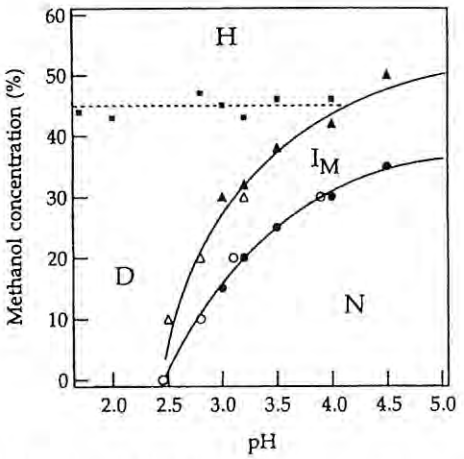

Fig. 36 Experimentally determined phase diagram of cytochrome c involving four conformational states, native (N), I_M, D and H.

unique pathway of protein folding and its discrete intermediate states. The most popular equilibrium intermediate state is the molten globule state. According to the original definition, the molten globule state has a native-like secondary structure and compactness, but a disordered tertiary structure. The conformational state with properties similar to the molten globule state was detected for various proteins under mild-denaturing conditions, such as low concentrations of denaturant or acid pH. It was subsequently proposed to be similar to the kinetic intermediate accumulated during the refolding process of several proteins.

Kataoka and coworkers have investigated the typical molten globule state of globular proteins, and revealed that the molten globule can be classified into two categories[3,5]: one gives a monophasic P(r) function, like molten globules of cytochrome c and a-lactalbumin; the other gives a biphasic P(r) function, like molten globules of apomyoglobin and Staphylococcal nuclease. A monophasic P(r) is a characteristic to a spherical structure like the native state. We also demonstrated that a molten globule having a monophasic P(r) shows a significant amount of tertiary fold. However, the molten globule having a biphasic P(r) shows a little amount of tertiary fold. We interpret that the biphasic P(r) of a molten globule represents a hydrophobic core with flaring tail(s). Thus, solution X-ray scattering has revealed the structural varieties in the molten globule. The proposed general and global structural images for various molten globules are shown in Fig. 37 based on our solution X-ray scattering data combined with thermodynamic

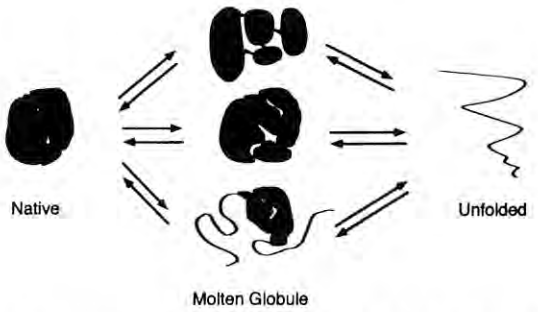

Fig. 37 Schematic description of various types of molten globules derived from the results of solution X-ray scattering.

studies of these proteins.[5]

2.3 Protein globularization during folding

The important questions that cannot be accessed through the equilibrium measurements described above are whether the kinetic folding intermediate is identical to the equilibrium intermediate, and whether compaction is preceded by secondary structure formation. Kinetic measurements using various spectroscopic techniques lead to the conclusion that some of the structural properties of the kinetic intermediate are close to those of the equilibrium intermediate. A stopped-flow system[6] has been developed for kinetic solution scattering experiment using synchrotron radiation.

With the stopped-flow system, Kuwajima and coworkers[7] have investigated both the unfolding and refolding reactions of various globular proteins. They showed that the integrated SAXS intensity is an appropriate measure for the direct monitoring of fast intramolecular globularization during protein refolding. They observed two fast kinetic processes for bovine carbonic anhydrase and two fast (each within two seconds) as well as two slow (within 500 seconds) kinetic processes for yeast phosphoglycerate kinase. Typical examples of the kinetic curve obtained through SAXS are shown in Fig. 38.[7] The kinetic processes reflect both protein intramolecular globularization and its intermolecular association. Thus, globularization of a protein molecule is not too fast in some cases, and can be measured by synchrotron SAXS combined with the stopped-flow technique. Generally, the formation of the backbone secondary structure is too fast to monitor by the stopped-flow CD measurement. It is very likely that the direct measurement of globularization by SAXS in

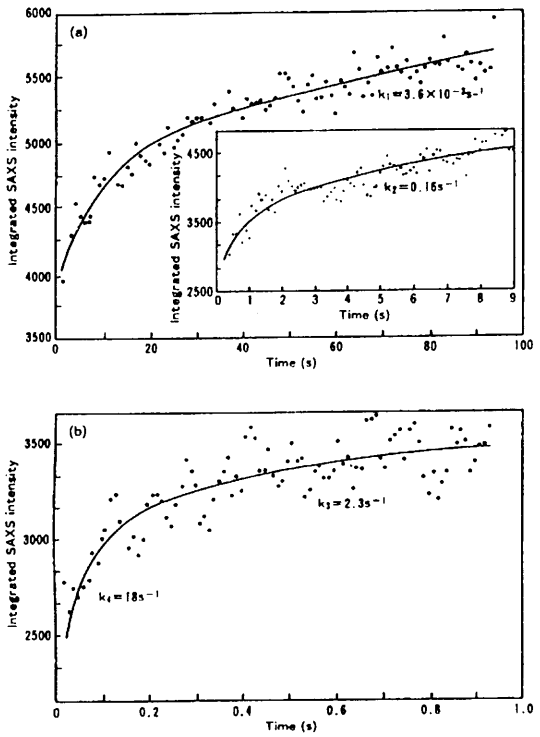

Fig. 38 Time-dependent refolding of yeast phosphoglycerate kinase induced by a concentration jump of urea from 4M to 0.9M. The time intervals are (a) 100 seconds, (inset), 10 seconds, (b) and 1 second.

combination with other physicochemical techniques can throw light on the interrelation between secondary structure formation and globularization during protein folding, which is still a major problem in the folding study.[7]

M. Kataoka, Osaka University

References

1) H. Yoshino, Y. Izumi, K. Sakai, H. Takezawa, I. Matsuura, H. Maekawa and M. Yazawa, Biochemistry 35 (1996) 3288.
2) M. Kataoka, A. Persechini, F. Tokunaga and R. H. Kretsinger, Proteins: Struct. Funct. Genet. 25 (1996) 335.
3) M. Kataoka and Y. Goto, Folding & Design 1 (1996) R107.
4) Y. O. Kamatari, T. Konno, M. Kataoka and K. Akasaka, J. Mol. Biol. 259 (1996) 512.
5) M. Kataoka, K. Kuwajima, F. Tokunaga and Y. Goto, Protein Sci. 6 (1997) 422.
6) H. Kihara, J. Synchrotron Rad. 1 (1994) 74.
7) G. V. Semisotnov, H. Kihara, N. V. Kotova, K. Kimura, Y. Amemiya, K. Wakabayashi, I. N. Serdyuk, A. A. Timchenko, K. Chiba, K. Nikaido, T. Ikura and K. Kuwajima, J. Mol. Biol. 262 (1996) 559.

G. STRUCTURE AND FUNCTIONS OF PROTEINS

The beam lines for protein crystallography in the Photon Factory have also been very active last year. As mentioned in the previous reports,[1,2] plenty of studies in the field of structural biology were done using a Weissenberg camera and multi-functional camera systems for macromolecular crystals, established by N. Sakabe and his group. In addition to two well-organized beamlines, BL6A and BL18B, a new beamline, BL6B, was open for use in experiments of protein crystallography from 1996. The BL6B beamline was constructed by the Sakabe TARA project of the University of Tsukuba, in which both industrial and academic crystallographers join as active members. In the beamlines for protein crystallography, the numbers of users and proposed projects have been greatly increased during these years. This fact has caused a serious problem in this field, in that the beamtime assigned for each user is always insufficient to perform the proposed experiments, even after the BL6B beamline became available.

In this review, the following three topics for new protein structures are described as examples of activity by using the above beamlines: 1) positive regulator OmpR from *Escherichia coli*,[3] 2) hydroxylamine oxidoreductase from *Nitrosomonas europaea*[4,5] and 3) DNA photolyase from *Anacystis nidulans*.[6] It should also be mentioned that there are many remarkable studies in addition to the above three, such as eukaryotic (pea seedling) amine oxidase,[7] catalase (by time-resolved crystallography),[8] the SMN toxin,[9] human lysosomal sulfatase[10] and so on.

1. POSITIVE REGULATOR OmpR FROM *Escherichia coli*

The crystal structure of the C-terminal DNA-binding domain of OmpR (OmpR-C), a positive regulator involved in osmoregulation expression of the ompF and ompC genes in *Escherichia coli*, has been determined at 2.2 Å resolution.[3] In this structure, the 'turn' region in a helix-turn-helix variant motif,

consisting of 11 residues, forms an RNA polymerase contact site.

In *Escherichia coli*, expression of the major outer membrane porin proteins, OmpC and OmpF, is regulated at the transcriptional level in response to medium osmolarity. Two regulatory factors, OmpR and EnvZ, are involved in this osmoregulation. OmpR is the cytoplasmic activator protein, which binds to the recognition sequence in both the ompC and ompF promoters. As is the case for many other response regulators, the 239 amino acid OmpR consist of two distinct domains: the N-terminal half domain of OmpR contains a site that is phosphorylated and the C-terminal half exhibits an inherent DNA-binding ability specific to the cognate promoters.

The structure was solved by the multiwavelength anomalous diffraction (MAD) method. MAD data for selenomethionyl (Se-Met) protein were collected at three different wavelengths 0.9794 Å, 0.9796 Å and 0.9000 Å from a single crystal at 100K using multifunction camera for macromolecular crystallography on the BL-18B. The crystallographic R-factor is 0.226 for 97.6% of the expected data between 10.0-2.2 Å.

The OmpR-C structure is shown in Fig. 39. The structural features of the C-terminal a-helical domain of OmpR-C, consisting of a three-helix bundle with a β-hairpin, have been found in several DNA-binding proteins. The structure of OmpR-C has a helix-turn-helix (HTH) motif with a second helix as a recognition helix, as found in most of the a-helical DNA-binding proteins. The classical HTH motif was characterized by close contacts of non-polar residues in two helices and glycine at the turn region. Although helices of the OmpR-C are well superimposed on other HTH proteins, the contact between two helices at the turn region is different from the canonical ones. There is no small hydrophobic residue at the contact region between two helices, nor any glycine residue at the turn region. Hydrophobic residues Leu185 at α2 and Ile201 and Ile205 at α3 make a contact site between the two helices in OmpR-C. The HTH structure of OmpR-C is best characterized by the large loop between α2 and α3. A four-residue stretch of Ser-Ala-Met-Glu in the loop forms α 3_{10} helix with the Ala196 residue folding toward the interior of the molecule to avoid being exposed to the solvent. This location most likely creates a contact region with RNA polymerase. OmpR may have evolved so as to optimize the contact to RNA-polymerase while conserving the hydrophobic core structure as well as the DNA interaction site.

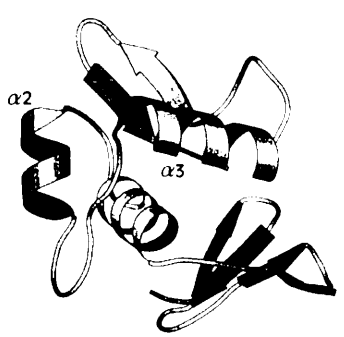

Fig. 39 Structure of the C-terminal domain of OmpR (OmpR-C) from *Escherichia coli* where two helices α2 and α3 form a helix-turn-helix (HTH) motif.

2. HYDROXYLAMINE OXIDOREDUCTASE FROM *Nitrosomonas europaea*

The crystal structure of hydroxylamine oxidoreductase from a nitrifying chemoautotropic bacterium, *Nitrosomonas europaea* has been determined at 2.8 Å resolution.[4]

Hydroxylamine oxidoreductase, one of several abundant periplasmic c-type cytochromes, performs the second step in the oxidation of ammonium to nitrite, a critical part of the nitrogen cycle in the respiratory system. Energy generated by hydroxylamine oxidoreductase in the form of an electrical potential can flow in both forward and reverse directions. The former, resulting in a gain of energy, passes electrons to the electron transport chain comprising cytochrome c-554, cytochrome c-552 and the terminal oxidase, while the latter occurs to restore the cycling energy of the system by supplying electrons either to ammonia monooxygenase for the production of hydroxylamine, or to ATP-dependent reverse electron transfer for the production of NAD(P)H. Hydroxylamine oxidoreductase has molecular mass of ca. 67,000 M_r per monomer, including seven c-type hemes and a novel heme, P460 and has been shown to exist in an oligomeric state in vivo.

The structure was determined by a multiple isomorphous replacement method including anomalous dispersion effects. The crystals have hemi-hedral twinning characteristics, but the diffraction data could be collected from a single crystal by the use of the Weissenberg camera for macromolecular crystallography with synchrotron radiation at BL-6A.[5]

The crystallographic R-factor is 0.230 for 99.1% of the expected data between 8.0-2.8 Å.

It was elucidated that hydroxylamine oxidoreductase is a trimer and is shaped like a head of garlic. The overall structure is shown in Fig. 40. The trimer has a size of about 100 Å in both maximum diameter and length, and has a large central cavity (30 Å wide and 15 Å deep) at its bottom. Twenty-four hemes lie in the center bottom of the trimeric molecule, localized in four clusters within each monomer. The heme clusters within the trimer are aligned to form a ring that has inlet and outlet sites. The inlet is occupied by a novel heme, P460, and there are two possible outlet sites per monomer formed by paired hemes lying within a cavity or cleft on the protein surface. The structure suggested pathways by which electron transfer may occur through the precisely arranged hemes and provides a framework for the interpretation of previous and future biochemical and genetic observation.

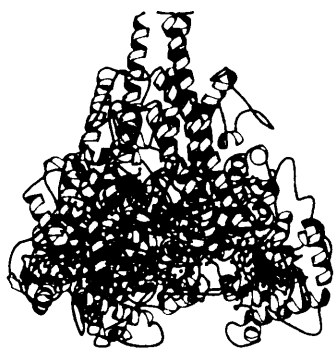

Fig. 40 Trimer structure of hydroxylamine oxidoreductase from *Nitrosomonas europaea*.

3. DNA PHOTOLYASE FROM *Anacystis nidulans*

The crystal structure of DNA photolyase from a cyanobacterium *Anacystis nidulans* has been determined at 1.8 Å resolution.[6] The structure, in comparison with that of *E. coli* photolyase indicated direct evidence for chromophore accommodation at different binding sites by common primary and tertiary structures

Photoreactivation is a light dependent repair mechanism mediated by photolyase which binds specifically to pyrimidine dimer lesions in UV-irradiated DNA. On subsequent illumination with visible or near-UV light the dimer is split. Photolyases contain two functionally different chromophoric cofactors: a light-harvesting cofactor which is either 8-hydroxy-5-deazaflavin (8-HDF) or 5,10-methenyltetrahydrofolic acid (MTHF) and the catalytic cofactor which is reduced FAD.

The structure of the 8-HDF type photolyase from *Anacystis nidulans* was determined by a multiple isomorphous replacement method, including anomalous dispersion effects. Figure 41 presents a ribbon model of the photolyase structure. The three-dimensional structure contains a helical and an α/β domains with a backbone structure which can be superimposed with that of MTHF type photolyase from *E. coli*. The FAD catalytic cofactor is bound in a very similar way in both photolyases, but the light-harvesting cofactor, located in the α/β domain, is bound at completely different positions: 8-HDF inside the molecule compared to MTHF at the molecular surface. The amino acid sequences of *A. nidulans* and *E. coli* photolyases are very homologous with 39% identical and 13% similar residues. This is a first example that homologous primary and tertiary structures in closely related proteins recognize two different types of cofactors at different binding-sites. The crystal structure revealed a distance of 17.5 Å between the chromophores, giving rise to an efficiency of 97% for energy transfer between 8-HDF and FAD.

K. Miki, Kyoto University

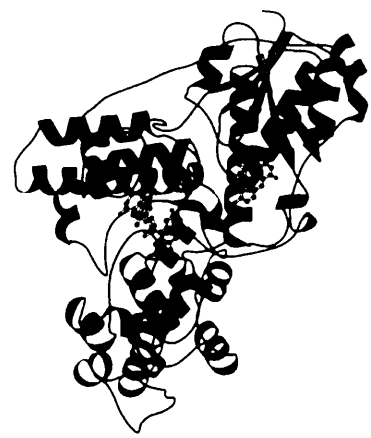

Fig. 41 Structure of 8-HDF type photolyase from *Anacystis nidulans*.

References

1) T. Tsukihara, Photon Factory Activity Report 12 (1994) S-29.
2) Y. Mitsui, Photon Factory Activity Report 13

(1995) S-24.
3) H. Kondo, A. Nakagawa, J. Nishihira, Y. Nishimura, T. Mizuno and I. Tanaka, Nature Struct. Biol. 4 (1997) 28.
4) N. Igarashi, H. Moriyama, T. Fujiwara, Y. Fukumori and N. Tanaka, Nature Struct. Biol. 4 (1997) 276.
5) N. Igarashi, H. Moriyama, T. Mikami and N. Tanaka, J. Appl. Cryst. (1997) in the press.
6) T. Tamada, K. Kitadokoro, Y. Higuchi, K. Inaka, A. Yasui, P. E. de Ruiter, A. P. M. Eker and K. Miki, submitted for publication (1997).
7) V. Kumar, D. M. Dooley, H. C. Freeman, J. M. Guss, I Harvey, M. A. McGuirl, M. C. J. Wilce and V. M. Zubak, Structure 4 (1996) 943.
8) P. Gouet, H.-M. Jouve, P. A. Williams, I. Andersson, P. Andreoletti, L. Nussaume and J. Hajdu, Nature Struct. Biol. 3 (1996) 951.
9) T. Kashiwagi, N. Kunishima, C. Suzuki, F. Tsuchiya, S. Nikkuni, Y. Arata and K. Morikawa, Structure 5 (1997) 81.
10) C. S. Bond, P. R. Clements, S. J. Ashby, C. A. Collyer, S. J. Harrop, J. J. Hopwood, and J. M. Guss, Structure 5 (1997) 277.

H. RADIOBIOLOGICAL PROCESSES

A monochromatized photon beam from synchrotron radiation allows us to analyze the relationship between the amount of energy locally deposited by radiation and the induced types of DNA damage, and further to investigate the induction mechanisms of DNA damage. A correct understanding of the mechanism may lead to an improved efficiency of radiotherapy of cancer, and to estimate the risk of exposure to low-dose radiation from the environment. Especially, experiments on the effects of low-dose radiation are practically impossible due to a difficulty to detect very rare phenomena. Extrapolation based on the reasonable mechanism of radiation action would be the only way for a correct assessment of the risk. The followings are topics in this field obtained recently.

1. INDUCTION OF SINGLE STRAND BREAK(SSB) AND DOUBLE STRAND BREAK(DSB) IN PLASMID DNA.

In aqueous systems, radiolytic products, such as H and OH radicals, of water play the most important role in the induction of radiation biological effects. The radiation chemical yields (μmol/J) of these species are among the most basic quantities in radiation biology. The yield of Fe^{3+} in a Fricke solution is a convenient measure of the combined yields of these products, that is (yield of OH) + 2(yield of H_2O_2) + 3(yield of H). The yields of Fe^{3+} induced by monochromatic photons from 1.8 to 10 keV were recently measured by Watanabe et al(1995); the measured yields decreased along with a decrease in the photon energy. This photon-energy dependence can be reproduced by simulation calculations. The decrease in the yields can be explained by an enhanced recombination of the primary radiolytic products that are produced more densely by photons with lower energies. It has not yet been studied how the enhanced recombinations of primary products by low-energy X-rays affect the induction of DNA strand breaks. Tomita et al measured the yields of single- and double-strand breaks (ssb and dsb) of plasmid DNA in dilute aqueous by monochromatic X-rays at 2.147, 2.153, 7.129 and 10 keV and compared with the yields of ferrous ion oxidation in a Fricke solution measured simultaneously.

Experiments for the Fricke solution were carried out as follows. Irradiation of monochromatic X-rays was performed at beamlines BL-27A and BL-27B of the Photon Factory, 2.147 and 2.153 keV (the K-absorption peak of phosphorus) at BL-27A, and 7.129 (just above the K-absorption edge of iron) and 10.00 keV at BL-27B. A one hundred ml sample solution was placed in an irradiation chamber with a 7.9-μm Kapton window of 8×10 mm^2. The irradiation was performed under aerobic conditions at room temperature, with constant stirring by a glass-coated iron stirrer. After X-ray irradiation, the optical densities of irradiated and unirradiated solutions were immediately measured using a spectrophotometer at 304 nm. Plasmid DNA solution was irradiated in the exactly same conditions as the Fricke solution. Plasmid pBR322 DNA was diluted to 0.02 g DNA/l in a TE buffer (10 mM Tris, 1 mM EDTA, pH 8.0). Immediately after X-ray irradiation of the plasmid DNA solutions, they electrophoresed in 1.7% agarose slab gel to separate closed circular (form I, intact), open-circular (form II, having ssb) and linear (form III, having dsb) forms of DNA. After staining with ethidium bromide, the fluorescence images of these bands were taken by a cooled CCD camera, and the

Table 3 Yields of DNA strand breaks and ferric ion irradiated with monochromatic X-rays.

Photon energy	Radiation chemical yield (μmol/J)[a]		
(keV)	Fe^{3+}	SSB	DSB
2.147	1.01 +- 0.01	(2.76 +- 0.07) x 10^{-5}	(6.35 +- 0.13) x 10^{-7}
2.153	1.02 +- 0.01	(2.84 +- 0.03) x 10^{-5}	(6.80 +- 0.19) x 10^{-7}
7.129	1.21 +- 0.01	(3.68 +- 0.05) x 10^{-5}	(5.07 +- 0.11) x 10^{-7}
10.00	1.23 +- 0.01	(4.05 +- 0.07) x 10^{-5}	(4.82 +- 0.15) x 10^{-7}

a) The errors of each values are the standard errors.

integrated fluorescence intensity was quantified by the NIH Image. The yields of the ssb and dsb were calculated from the relative fractions of these bands.

The radiation chemical yields (μmol/J) of the ferric ion in the Fricke solution are shown in Table 3. The yields decreased along with a decrease in the photon energy; the values were in good agreement with the values previously reported.

The number of ssb increased linearly with the absorbed dose, whereas the number of dsb seemed to increase linearly until 0.03 dsb/plasmid. At higher doses, however, it increased linear-quadratic with the absorbed dose. Thus, all of the data for ssb and those below 0.03 for dsb were fitted by straight lines using a least-squares method and the yields of ssb and dsb calculated from the slopes of these lines are listed in Table I. The yields of ssb showed the same photon-energy dependence as those of ferrous ion oxidation, but were slightly remarkable. On the contrary, the yields of dsb increased along with a decrease in the photon energy, resultantly, the ratios of dsb/ssb increased from 0.012 at 10 keV to 0.023 at 2.147 keV. These results indicate that ssb and dsb are induced, at least partly, through different primary events. The ssb seems to be induced mainly by the diffusive active species of water, which can be measured by the oxidation yields of the Fricke solution. On the contrary, the dsb induction did not correlate with these yields, but seemed to be related to the primary-event density, which increases at lower-photon energies, because those photons produce lower-energy secondary electrons having higher LETs. This might support our hypothesis that the high RBE (relative biological effectiveness) phenomena are due to the higher density of primary energy deposition event.

References

1) Watanabe, R., Usami, N. and Kobayashi, K. Int. J. Radiat. Biol., **68**, 113-120 (1995)

2) Tomita, M., Hieda, M., Watanabe, R., Takakura, K., Usami, N., Kobayashi, K., and Hieda, K., Radiat. Res., (1997) in press

2. NON-REPAIRABLE DAMAGE PRODUCED BY AUGER EFFECT

Auger effect has been attracting much attention of radiobiologists since it produces energy deposition events with high density, and hence, is expected to induce severe biological effects. It was reported that the Auger effects at phosphorus atom in DNA molecule induce enhanced biological effects, such as lethality and mutagenesity. It was also found, however, that the yield of DNA strand breaks on the basis of absorbed energy did not show an enhancement enough to explain the enhancement in biological effects. From these observation, it was hypothesized that the biological enhancement by Auger effects could be explained by the quality of the DNA damage, not by the quantity. Usami et al suggested from their results using yeast cells that the difference in quality may be observable from the viewpoint of reparability. Recently, Maezawa and Suzuki succeeded in demonstrating the reparability of damage by Auger effect by exploiting premature chromosome condensation(PCC) technique in mammalian cell lines. PCC is a technique to measure the number of chromatin damage of cells in interphase. In interphase cells chromosomes can not be seen microscopically, since they are dispersed as chromatins in cellular nuclei. When these cells are fused artificially with other cells in mitosis, maturation promoting factors in latter cells diffuse into the former cells and chromosome condensation is induced in the former cells, which visualizes the chromosome. When chromatin breaks occur in a cell, the number of chromosomes visualized by PCC become larger than the intact cells, due to the fragmentation; number of excess fragments per cell represent the number of the

chromatin breaks in the irradiated cells.

The used cell line was V79, and these cells cultured in monolayer in petri dishes were irradiated with monochromatic soft X-rays around the K-shell absorption edge of phosphorus at BL-27A in an atmospheric condition. Irradiated cells were assayed for lethality and PCC immediately. In other experiments irradiated cells were kept in the incubator to allow repair of the damage before the assay.

The killing-enhancement ratio, which was defined as the ratio of the lethality at a given energy to that at 2.146 keV(below the edge), was 1.3 at 2.153 keV (resonance absorption peak) and 1.0 at 2.160 keV(above the absorption edge) for cells plated immediately after irradiation for colony formation. The number of excess fragments per cell increased linearly with the dose, and the slope of these lines at different conditions were compared. The enhancement factors based on the slope at 2.146 keV was 2.1 at 2.153 keV, and 1.1 at 2.160 keV in the absence of repair incubation. When cells were allowed to repair, chromatin breaks decreased to 40% and 75% of the values in the absence of repair at 2.146 keV and 2.160 keV, respectively. However, no significant decrease in the number of chromatin breaks was observed at 2.153 keV irradiation. (Fig. 42) These results clearly indicate that the Auger cascades after K-shell absorption of phosphorus produces the unreparable chromatin breaks in mammalian cells.

K. Kobayashi, PF

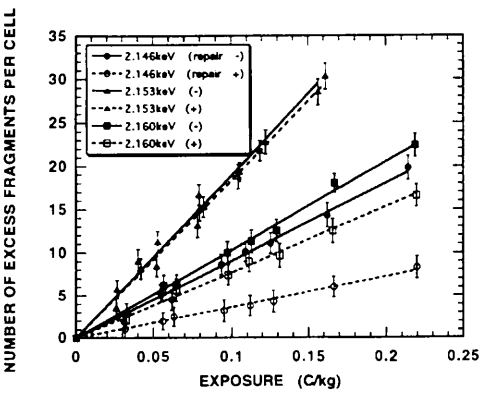

Fig. 42 Number of chromosome fragments induced by monochromatic soft X-rays. Chromosome damage induced by Auger effect of phosphorus (2.153 keV) was hardly repaired.

I. MEDICAL IMAGING

The following medical imaging systems are developing using synchrotron radiation at mainly AR, NE-5A (bending beamline), and also AR, NE-1A (multipole wiggler beamline) and PF, BL-14C (vertical wiggler beamline). Available photon flux density at 33 keV at NE-1 is about 20 - 40 times greater than that available at NE-5A and BL-14C.

(A) Two-dimensional intravenous coronary angiography system[1,2,3,4]
(B) High resolution monochromatic X-ray CT system[5,6]
(C) Fluorescent X-ray CT system[7]
(D) High resolution angiography system using a HARP-TV camera[8,9]
(E) Fluorescent X-ray imaging system using a metal target[10]

A summary of detector of medical imaging system is given in Table 4.

Table 4 Medical imaging system

system	detector	spatial resolution
A	Image intesifier - TV	150 μm
B	CCD line-sensor	1 - 10 μm
C	Ge SSD	3 mm
D	HARP-TV	30 - 50 μm
E	Image intesifier - TV	150 μm
	Cd Te line-sensor	500 μm

1. DEVELOPMENT OF A CLINICAL IMAGING SYSTEM FOR INTRAVENOUS CORONARY ANGIOGRAPHY

The first human examinations of intravenous coronary angiography using a two-dimensional imaging system, an image intensifier - TV system, was done at the Accumulation Ring (AR) on May 23rd and 29th in 1996 under the collaboration work between the University of Tsukuba and the National Laboratory for High Energy Physics.

We have been developing a two-dimensional imaging system for intravenous coronary angiography using synchrotron radiation. An advantage of our system is that two-dimensional dynamic imaging of the cardiovascular system can be achieved due to its two-dimensional radiation field which is generated by means of asymmetrical reflection of a crystal, and the field thus generated is then visualized by means of the

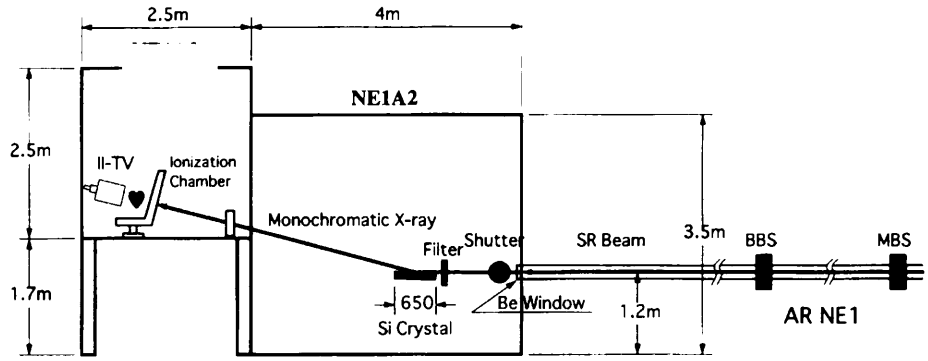

Fig. 43 Schematic diagram of the two-dimensional imaging system for clinical applications at NE-1. A large-size asymmetrically cut Si crystal with (311) diffracting planes was used to expand the SR beam and an image intensifier coupled with a TV camera was used as a two-dimensional detector.

two-dimensional imaging system, an II -TV system (TOSHIBA RTP9211G). Practical applicability of the system has already been confirmed in animal experiments at NE-5A[11] by using synchrotron radiation produced by a bending magnet at the Accumulation Ring.

We have achieved development of the clinically applicable system with the large-size radiation field using synchrotron radiation produced by a multipole wiggler (MPW) that can generate a monochromatic X-ray radiation of intense enough for clinical application at NE-1A[12]. Practical clinical application of this beamline ; NE1A, in settings necessitated further development and preparation of the following apparatuses and test run using phantoms in prior to clinical application:

(1) Monochromator system for creating large-size view area
(2) High-speed X-ray shutter for imaging with intervals of 2-4 msec
(3) High-speed-driven aluminum filter for modulating the intensity of monochromatic X-ray radiation to decrease the radiation dose onto a patient.
(4) Clinical hutch: special station coping with patients
(5) Special interlock system for clinical use

Figure 43 shows the schematic diagram of the clinical imaging system at NE-1. We prepared a special station; NE-1A3, for clinical examinations. A large Si(311) crystal with the size of 650 mm by 80 mm was set in NE-1A2 at about 40 m apart from the source point. The silicon plate was placed on a copper plate which was located on a goniometer and was equipped with a pipe for water cooling. The dimension of the X-ray radiation was 8 mm vertically by 80 mm horizontally at the point as a characteristic feature of the MPW beam line; NE-1. The vertical beam size of 8 mm was increased to approximately 130-150 mm by asymmetrical reflection from the crystal. The surface of the crystal was ground with No. 1200 mesh silicon carbide in an attempt to achieve as large integral intensity as possible. For the purpose of reducing X-ray exposure dose to patients as much as possible, e.g. at the time of setting a position of patients, a high-speed X-ray shutter and a high-speed-driven aluminum filter were placed before the crystal. The high-speed X-ray shutter chosen was of stainless-steel rotating drum type having aperture windows for transmission of the radiation beam for 4 ms[13]. The intensity of monochromatic X-ray radiation of 33 keV could be modulated within a range of 1/1-1/1000 by changing the thickness of aluminum filter within a range of 0 mm to 30 mm. This filter was driven by an electromagnetic motor. The distance between the front of the new hutch and the crystal was approximately 4 m, and the monochromatic X-ray radiation was transmitted to the hutch through a pipe in a direction 13 degrees upwards from the crystal. At an entrance of the hutch, a calibrated 20-ml ionization chamber of free air type was arranged for measuring the X-ray exposure dose to patients. Figure 44 shows a photograph of the clinical station, NE-1A3. An ionization chamber, an II-TV system , a chair for patient, an auto-injector for contrast material can be seen.

Four patients (from sixty years old to seventy five years old) were examined using the system. The AR was operated at 5.0 GeV to decrease the 3rd higher harmonics X-ray photons from a silicon crystal to less than 3% at the surface of a patient. Average stored current was 20 mA. Images were taken at above the K-

Fig. 44 Photograph of the clinical station, NE-1A3. An ionization chamber, an II-TV system , a chair for patient, an auto-injector for contrast material can be seen.

edge energy (33.34 keV or 37 keV) and those images were digitized to 1024 × 1024 × 10 bits by a DSA imaging system (TOSHIBA DFA200A). Two or three injections were done for each patient to detect left and right coronary arteries at LAO (left anterior position) and RAO (right anterior position). Images were recorded in 5 to 10 sec at the rate of 30 images a sec. Each image was taken in 4 msec using a fast X-ray shutter. Maximum surface dose to a patient was limited up to 100 rad for each patient by medical doctors. The photon flux density before a patient was about 10^{10} photons/mm^2/s. Contrast material, total amount of 40 ml, was injected into the carotid vein or arm's vein per one examination.

The advantage of the two-dimensional imaging system for coronary angiography was confirmed by the examinations. Right and left coronary arteries of each patient could be detected. It was easy to distinguish between coronary arteries and pulmonary arteries in dynamically moving images. The details of the patient's examinations will be reported.[14] The examination was approved by the Ministry of Education, Science Sports and Culture, the Ministry of Health and Welfare, and the Science and Technology Agency.

K. Hyodo, PF

References

1) S. Ohtsuka, et. al.: Circulation **88**(1993)205.
2) S. Ohtsuka, Y. Sugishita, K Hyodo : SR News 7(1994)21.
3) Y. Itai, et al.: PF Activity Report, #11(1994)427.
4) K. Hyodo, et al.: Synchrotron Radiation in the Biosciences (1994)653,Oxford University Press, Oxford.
5) T. Takeda, et al.: Journal of Computer Assisted Tomography **18**(1994)98.
6) T. Takeda, T. Maeda, K. Hyodo : PF Activity Report #11(1994)428.
7) T. Takeda, T. Ito, K. Kishi, et. al. : Medical Imaging Technology **12**(1994)537.
8) H. Mori, et. al.: Circulation **89**(1994)863.
9) H. Mori, et al.: Radiology **201**(1996)173.
10) C. Uyama, et al.: PF Activity Report #10(1993)413.
11) K. Hyodo, K. Nishimura and M. Ando: Handbook on Synchrotron Radiation **4**(1991)58 Elsvier Science Publishers B.V., Netherlands.
12) K. Hyodo, M. Ando, Y. Oku, et. al.: to be published.
13) Y. Oku, K. Hyodo, M. Ando, et. al.: to be published.
14) S. Otsuka, Y. Sughisita, T. Takeda, et al.: to be published.

J X-RAY MICROBEAMS AND MICROSCOPY

1. SOFT X-RAY SPECTROMICROSCOPY OF A CELL

In a cell, there are many functional structures which range in size between 10nm and 100nm. These structures have a high degree of organization among each other, and interact with each other. Soft X-ray microscopy is a candidate for a unique new method to observe ultrastructural details in cells and to permit advances in studies of the relationships between these cellular structural elements.

The advantages of soft X-ray microscopy in biology over other microscopic methods have been summarized as follows: (1) soft X-ray microscopy is expected to have the potential to observe physiologically unaltered biological specimens in a hydrated condition at a resolution higher than available with optical microscopy; (2) three-dimensional observations of thick biological specimens may be possible at high resolution; and (3) imaging and analysis of the local distribution of elements and chemicals in a whole cell may be possible. Our research is focused on the third advantage.

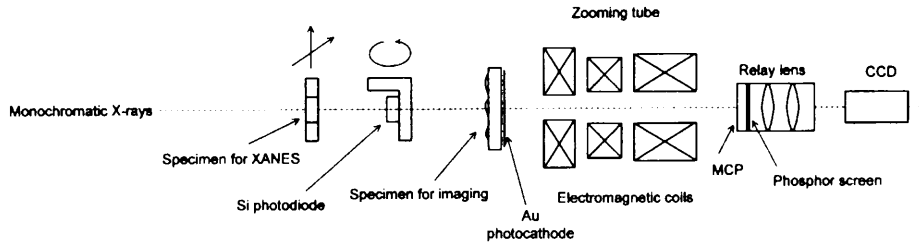

Fig. 45 Schematic layout of soft X-ray spectromicroscopy composed of spectroscopy and contact microscopy.

Biological molecules mainly comprise low atomic-number elements, such as carbon, nitrogen, oxygen, calcium and phosphorus. These elements have K or L absorption edges in a soft X-ray region. In addition, an X-ray absorption near-edge structure (XANES) is often significant in relation to the chemical nature of each molecule. Therefore, it is of interest to study the imaging method using an X-ray absorption spectrum of each biological molecule. The method is called spectromicroscopy. With soft X-ray spectromicroscopy, it may be possible to identify structures in physiologically unaltered cells by the contrast of their own components and chemical structures. This approach was first developed for imaging calcium in bone using an absorption peak in XANES at Ca-L edge, and was then applied to the distribution of DNA in a chromosome using an absorption peak in XANES of DNA at the C-K edge with scanning soft X-ray microscopy at National Synchrotron Light Source, Brookhaven National Laboratory.

For the purpose of soft X-ray spectromicroscopy of biological specimens over a wide range of wavelengths from 0.1nm to 10nm, we have developed an X-ray contact microscopy system using an electronic zooming tube which is a two-dimensional detector of soft X-rays with a resolution higher than 0.5 mm. The tube has the following features: (1) no optical elements are required for imaging specimens at the resolution of the detector; (2) images obtained with different wavelengths can be directly compared; and (3) the detector is applicable to a wide wavelength range of X-rays, even shorter than 1 nm down to 0.1 nm.

Figure 45 shows a schematic layout of the microscopy system. The system consists of two tandem parts: one is a spectroscopy chamber for thin films of biomolecules using a silicon photodiode as a detector; the following part is for imaging dried biological specimens using an electronic zooming tube in combination with an image processor. Monochromatic X-rays were supplied from BL-11A (Grasshopper Monochromator), and BL-11B for the wavelength range of 1.5-10 nm with a resolution of $\lambda/\Delta\lambda \sim 1000$, and the range of 1.7-3.5 keV with a resolution of $\Delta E \sim 1$-1.5 eV.

With this system, we have succeeded to perform the X-ray contact microscopy of dried HeLa cells (cultured human cells) with various wavelengths of X-rays from 1.5-10 nm which include K-absorption edges of carbon, nitrogen and oxygen, and L-absorption edges of iron, calcium and sulfur. Figure 46 shows the absorption spectra of HeLa cells at typical intracellular areas corresponding to the nucleus, nuclear-cytoplasm interphase, cytoplasm and surface area including cell membrane. With the results, the relative fraction of elements in local areas could be estimated. Also if the thickness is known, the absolute number of elements detected in the spectra may be determined. The results suggest that the system may be applicable to image chemical natures in biomolecules using a specific absorption peak in the XANES profiles.

XANES reflects the local chemical structures

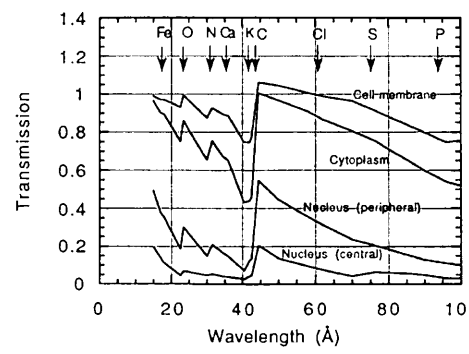

Fig. 46 Absorption spectra of a HeLa cell at typical intracellular areas. The absorption edges of major elements are shown by arrows.

around an element. For imaging the chemical nature, the first part of the system is used to obtain the peak position of XANES. XANES of biomolecules including DNA, proteins, and sulfur-containing amino acids and peptides were measured at the absorption edges of the constituent elements (carbon, nitrogen, oxygen, phosphorus and sulfur). DNA had different absorption profiles from those of nuclear protein histone at every absorption edge tested. The comparison of XANES from S-H with S-S in closely related compounds showed a slight, but significant, shift of the absorption peak at the S absorption edge. These results strongly suggested the useful applicability of the XANES peaks to molecular imaging in a cell.

Molecular imaging in a cell using the wavelength at the peak position of the XANES profile for DNA-P is now under way. The following result is an example of our trials. Figure 47 shows an XANES profile of DNA at the energy between 2.14 keV and 2.20 keV. Then, images of dried mitotic HeLa cells were obtained at an energy of 2.1528 keV (peak position) and at 2.1490 keV. The ratio of the two images will give an image of DNA-P in a mitotic HeLa cell. The result is shown in Fig. 48. In the cell, some fibrous structures were significant. The structures may correspond to chromosomes. Although image is not sufficient for biological study at present, the results clearly show that spectromicroscopy of the cell has a promising potential in biology, provided that the resolution of the image is improved.

Kunio Shinohara, Univ. of Tokyo

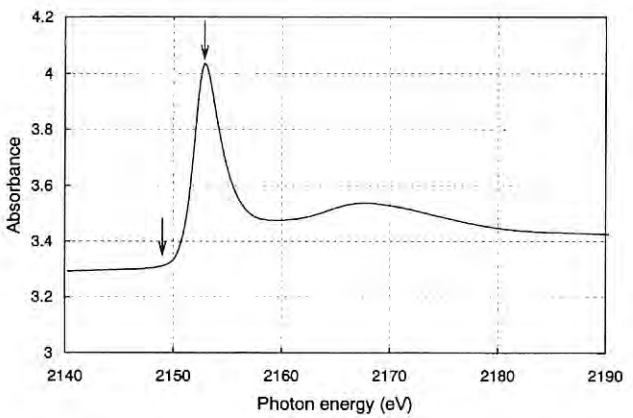

Fig. 47 XANES profile of DNA at the energy region of the P-K edge.

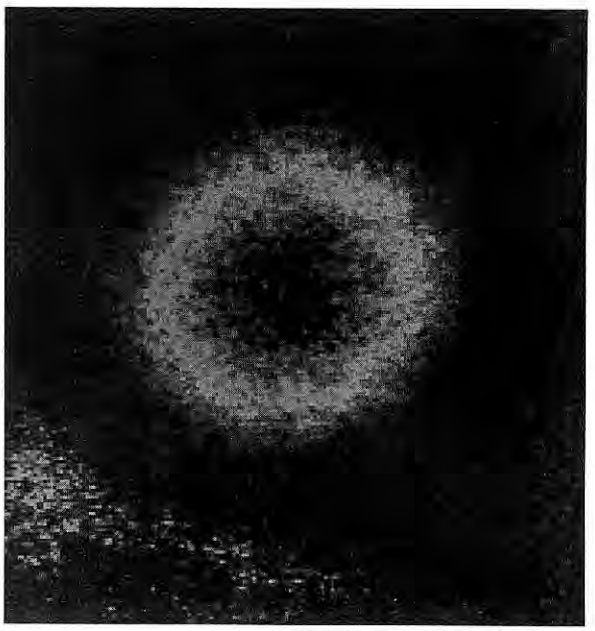

Fig. 48 X-ray spectromicroscopy of a dried mitotic HeLa cell obtained by DNA-P absorption. The image was obtained by the ratio of two images observed at the wavelengths shown by arrows in Fig.47.

2. MONITORING OF METAL EXPOSURE BY X-RAY IMAGING

Hair samples provide a historical record of trace element levels. They have been widely used for biological monitoring of health condition and for industrial or environmental exposure to heavy metals because of its easy collection from the population. We have applied the X-ray imaging for a monitoring of metal exposure for Pb-smelter.

XRF measurements were made at BL-4A, PF utilizing energy dispersive SR-XRF system with monochromatic X-ray microbeam obtained by multilayer monochromator and K-B type focusing optics. Energy of X-ray used was 14.38 keV. Two dimensional analysis was carried out by placing a sample on a XY stage. The X-ray intensity data of the Zn Kα and Pb Lα fluorescence lines of each point were processed with a personal computer and results were shown as a tone from black to white classified into 14 degrees from maximum to minimum, that are linearly proportional to the 14 levels of the element concentrations.

Differential imagings of Zn and Pb in the cross hair section of the smelter were obtained as shown in

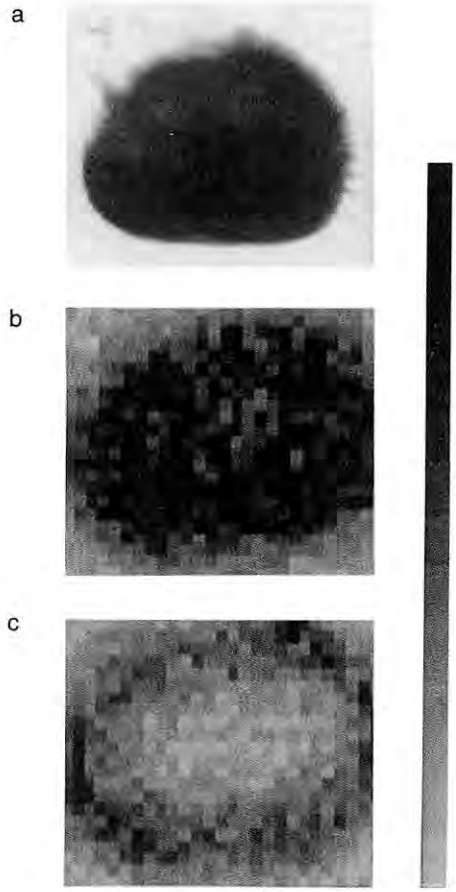

Fig. 49 Light microscopic photographs (a) and SR-XRF imagings of Zn (b) and Pb (c) on the hair cross section from the Pb-smelter. The thickness of the hair specimen, which was embedded in acrylic resin, was 25 μm. The scanning condition of XRF imaging was 23 × 31 steps with 5 μm/step and 10 s/step collection time.

Fig. 49. Pb localized in the surface of the hair cuticle, while Zn accumulated more in the cortex compared to the medulla and the cuticle. The Pb concentration in the hair was extremely high (220 μg/g) compared to the normal level (5-50 μg/g). Taken together, the smelter was considered to be exposed to Pb exogenously.

To confirm this hypothesis, we have extended the X-ray imaging to rat hair samples obtained from endogenous- and exogenous- exposure model of mercury. Samples of the exogenous exposure model were prepared by immersing hairs of untreated rat in a methylmercury chloride (MMC) solution (1 ppm) for 90 min. Hairs of the MMC-administered rats (orally, 10 mg Hg/ kg/day × 5 days) were used as samples of

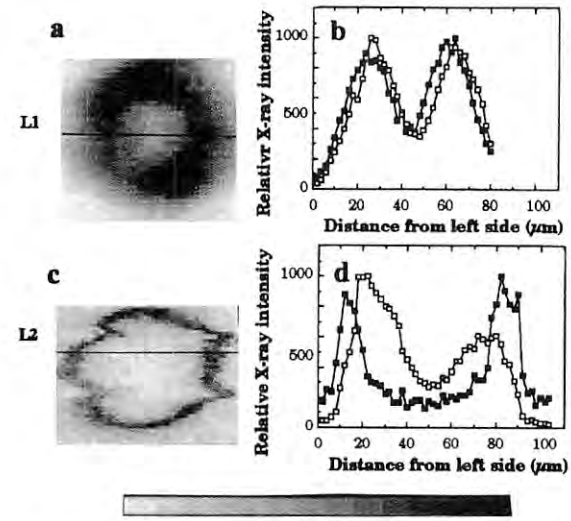

Fig. 50 Hg fluorescence intensity distribution (a and c) and profiles of Hg and S (b and d) on hair cross sections of endo- (a and b) and exogenous (c and d) exposure to MMC. Hg and S were excited with 14.38 keV X-rays and the X-ray intensity data of the Hg Lα and S Kα fluorescence lines were collected for 10 sec/point. The sample scanning conditions were 40 × 40 (a) and 52 × 37 (c) with 2 μm/step. (b) and (d) represent line plots of fluorescence intensity for Hg (■) and S (□) on the center lines (I1 and L2) of the hair cross sections. The sample thickness was 25 μm and Hg concentrations of these hair samples were 271 μg/g (a and b) and 204 μg/g (c and d), respectively.

endogenous exposure model.

A dominant site where Hg distributed following the exogenous exposure to Hg, was the surface of the hair cuticle, but not the cortex and medulla (Fig. 50c), whereas the endogenous exposure to the metal resulted in a preferential accumulation of Hg in the hair cortex than on the medulla or cuticle (Fig. 50a). To confirm the difference in Hg distribution by endogenous and exogenous exposure to the metal, relative X-ray intensities of Hg and S in these specimens were plotted (Fig. 50b and d) because S is a major element included in hair protein as cysteinyl residues. As expected, a distribution curve of Hg was almost the same of that of S in the endogenous exposure model. In case of the exogenous exposure to Hg, however, the heavy metal accumulated in the outer area than S, indicating that Hg is likely to be distributed by external adsorption. In other words, SR-XRF imaging technique enables us to distinguish between intake of Hg and the external adhesion.

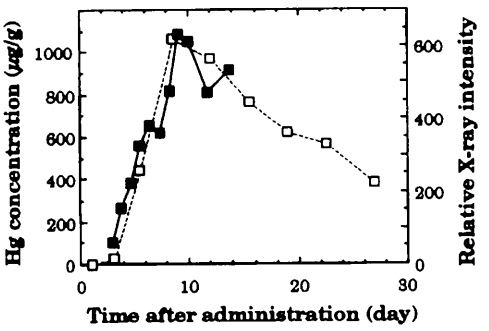

Fig. 51 Plots of fluorescence intensity of Hg by SR-XRF and Hg concentration by FAAS for the hair of the rats administered MMC. ■, the mean of the relative fluorescence intensity of Hg for each analytical point on the hair cross section; □, Hg concentrations determined by FAAS. The samples of SR-XRF imaging were obtained at every 1 mm position from the root end of the MMC-treated rat hair and their times equivalent to 2.9, 3.7, 4.5, 5.5, 6.5, 7.3, 8.3, 9.2, 10.1, 11.9 and 13.9 days. The times of the plots by FAAS were at 2, 4, 7, 10, 14, 17, 21, 24, and 30 days.

Furthermore, when the dynamics of Hg concentrations in hair of a rat administered MMC determined by flameless atomic absorption spectrometry (FAAS) were plotted with the relative X-ray intensities of the metal obtained from the hair cross section of the same rat, the regression lines gave a relative coefficient of 0.929 (Fig.51). Thus, we suggest that SR-XRF technique is suitable to determine a degree of Hg exposure using only a single hair.

S. Homma-Takeda, Y. Kumagai, and N. Shimojo,
University of Tsukuba

K. THEORY

1. THEORY FOR LUMINESCENCE AND RAMAN SCATTERING IN THE SOFT X-RAY REGION

In the field of the soft X-ray spectroscopy of solids, one of the most important things is to determine the density of states (DOS) of the valence band of each solid. The standard method to obtain information concerning this DOS is the photoemission spectroscopy (PES). So far, this method has greatly contributed to the development of solid state physics. However, this method has some weaknesses, since the probe in this method is the emitted electron itself. In some cases, the kinetic motion of this electron may be disturbed by a solid surface which is different from one by one, and, hence, the information obtained by DOS will be blurred.

On the other hand, the soft X-ray radiation spectroscopy (SXRS) is now being proposed as a new method to determine the DOS. This method is rather free from the aforementioned weaknesses, because its probe is soft X-rays, radiated from a solid. In Fig.52, we have schematically shown a set of optical processes relevant to this SXRS. This is a resonant second-order optical process, being different form the PES, which is a first-order process. At the first step of the SXRS, as shown in Fig. 52, an electron is resonantly excited from a core band to a conduction band by an incident soft X-ray. We can thus obtain a conduction electron and a vacancy (core hole) in the core band, which has no dispersion. At the second step, a valence electron, as well as the excited electron in the conduction band, can go down to the core band by radiating a secondary soft X-ray. By analyzing the energy distribution of the radiated X-ray, we can obtain information about the DOS.

There have been various experimental reports obtained by using this SXRS method in the resonance region. From these results, we can clearly see that there are two typical but rather different components in the observed spectra. One is a component whose peak in the spectra shifts as the incident energy changes. We

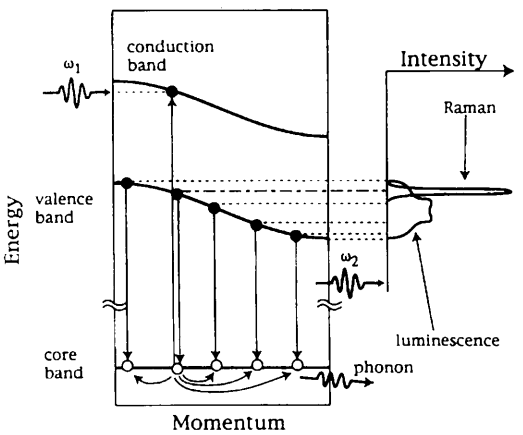

Fig. 52 Schematic three-band system for the resonant second-order optical process (left portion) and the spectrum of the X-ray radiation (right portion). The phonon energy is not indicated explicitly.

can call it the Raman component, according to the conventional terminology of optics in the visible region. Another is a component whose spectral shape does not change, even if an incident energy is changed. We can call it luminescence. The observed relative intensity between these two components varies from solid to solid.

In the present stage of theoretical studies for the SXRS, however, there is no systematic method to clarify why the whole spectrum separates into the Raman component and the luminescence one. It is also unknown how information of the DOS is included in its spectral shape. The purpose of the present study was to clarify these points theoretically. For this purpose, we have taken a typical three-band system in an insulator, which is composed of a dispersionless core band, a conduction band and a valence one, with wide energy gaps among them. Phonons with a finite dispersion were assumed to couple weakly with a core hole created by the incident X-ray. Using this model, we calculated the resonant second-order optical process, comprising the excitation of an electron from the core band to the conduction band by the incident soft X-ray, and a subsequent transition from the valence band to the core band by radiating another soft X-ray. When the energy of the incident X-ray is given, the momentum of the core hole is well defined by the resonance condition, as can be easily seen from Fig. 52. However, its the momentum is dissipated due to an interaction with phonons. The time required for this dissipation (dissipation time) is determined only by the dispersion of the phonon energy, because the core band has no energy dispersion. If the X-ray radiation occurs after this dissipation has been completed, we obtain luminescence, as schematically shown in Fig. 52. In this case, the spectral shape fully reflects the DOS, being independent of the incident energy. However, if the radiation occurs before the dissipation, we obtain the Raman component. In this case, the spectral shape has a sharp peak, being much different from the DOS, and depending on the incident energy. The relative intensity between these two components is determined by three factors: the dissipation time, strength of the core-hole--phonon coupling and a lifetime of the core hole, itself. By this theoretical framework, we have concluded that there are various cases, i.e., Raman-dominant cases, luminescence-dominant cases and intermediate ones, in good agreements with recent experiments.

Figure 53 shows a numerical result, which was calculated with a condition that the lifetime of the core hole is longer than the dissipation time. In this figure, the resonance spectra comprise of the small Raman components and the large luminescence ones, and the luminescence component fully reflects the DOS of the valence band. Therefore, we can say that the luminescence dominant case is realized by this condition. On the other hand, Fig. 54 shows a numerical result under the condition that the lifetime of the core hole is shorter than the dissipation time, contrary to the previous case. In this case, we can see that the resonance spectra comprise the large Raman

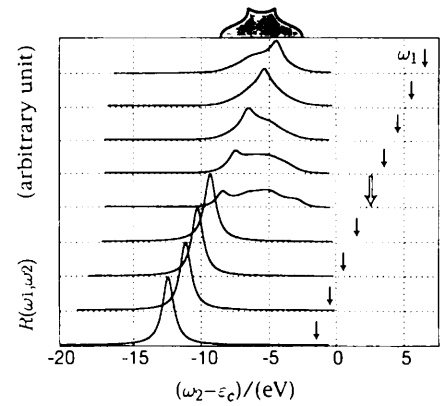

Fig. 53 Calculated SXRS spectra with a long lifetime of the core hole. ω_1 and ω_2 denote the incident energy and the energy of the radiated X-ray, respectively. ε_c denotes an energy of the core hole (constant value). The arrows indicate the incident energies. The outlined large arrow indicates the energy of resonance with the conduction band edge. The shaded curve on the upper horizontal axis is the DOS

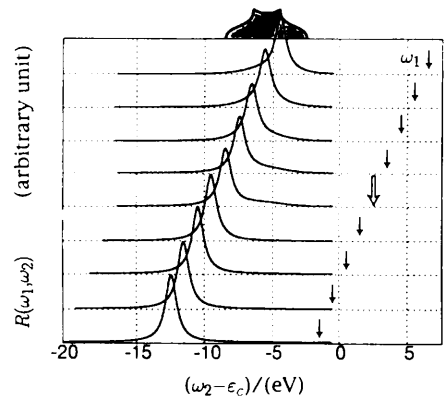

Fig. 54 Same as Fig. 53, but with a short lifetime of the core hole.

components and the very small luminescence ones. Therefore, the Raman dominant case is realized under this condition.

In summary, we have clarified how the DOS of the valence band appears in the SXRS spectra, and why these spectra separate into the Raman component and the luminescence one.

2. NEW PATH-INTEGRAL THEORY FOR THE LIGHT-ABSORPTION SPECTRA OF MANY-ELECTRON SYSTEMS IN INSULATING STATES DUE TO A STRONG LONG-RANGE COULOMB REPULSION

2.1 Introduction

A theoretical treatment for the optical response functions of strongly correlated systems is still the target of a great challenge for physicists. The insulating ground state caused by the strong Coulomb repulsion has large quantum fluctuations due to the low-energy collective excitations of spin. In addition to these spin fluctuations, light induces charge fluctuations, such as a charge-transfer(CT) exciton, which is a bound state of a photo-generated electron and a hole at neighboring sites due to the long-range part of the Coulomb interaction. This charge excitation is closely related to the optical response, but must be influenced by spin fluctuations. Therefore, to consider the electron-correlation effects on the optical-response functions, we should treat not only charge and spin excitations, but also the coupling between them, which seems to be strong and nonlinear.

In fact, there is experimental data which show strong coupling between the charge and spin excitations in the Ni-Br complex. This complex is a typical quasi-one-dimensional(quasi-1D) half-filled electron system in an insulating state caused due to the strong Coulomb repulsion between 3d electrons. The absorption spectrum of the Ni-Br complex shows an exotic shape.[1] It consists of a sharp peak and a very long tail extending toward the high-energy region from this peak. The sharp peak corresponds to CT exciton, while the long tail seems to come from the multiple-spin excitation induced by the creation of CT exciton.

In this report we formulate a new path-integral theory for the optical responses from the insulating states. In this theory, Coulomb repulsions including both short-and long-range parts are reduced into a time-dependent one-body Hamiltonian with only two kinds of Ising-spin variables per site to be summed up. The sum over the Ising-spin configurations will be performed according to quantum Monte-Carlo techniques.

2.2 Method

2.2.1 Reduction of the Coulomb repulsion into time-dependent one-body Hamiltonian

The Coulomb repulsion is generally represented by

$$H_I = \frac{1}{2}\sum_{l,l'} U(l-l')n_l n_{l'}, \tag{2.1}$$

where $n_l = n_{l\alpha} + n_{l\beta}$. By using the relation between $U(l)$ and its Fourier transform ($u(q)$) as

$$u(q) = \sum_l e^{-iql} U(l),$$

$$U(l) = \frac{1}{N}\sum_q e^{iql} u(q), \tag{2.2}$$

we can rewrite H_I in the following form[2]:

$$H_I = -\frac{u}{2}\sum_l \left(S_l^2 + C_l^2\right) + uN_e, \tag{2.3}$$

where $S_l = n_{l\alpha} - n_{l\beta}$, $N_e = \sum_l n_l$, and $C_l = \sum_q \frac{1}{N}\sum_q \sqrt{\frac{u_q}{u}} \cos q(l-l')n_{l'}$.

According to Trotter's formula, we can divide the partition function of this total Hamiltonian into one-body and two-body terms, as

$$Tr\left(e^{-\beta H}\right) = Tr\left[\left(e^{-\Delta H_1} e^{-\Delta H_2}\right)^L\right] + 0\left(\Delta^2\right), \tag{2.4}$$

where $\beta = 1/k_B T$ and $\Delta = \beta / L$. Then, the two-body terms are reduced by discrete Hubbard-Stratonovitch transformations into one-body terms with Ising-spin variables $\sigma(l)$ and $\omega(l)$, such as

$$e^{\frac{1}{2}\Delta u S_l^2} = \frac{1}{2}\sum_{\sigma(l)=\pm 1} e^{\sqrt{\Delta u}\sigma(l)S_l} + 0\left(\Delta^2\right),$$

$$e^{\frac{1}{2}\Delta u C_l^2} = \frac{1}{2}\sum_{\omega(l)=\pm 1} e^{\sqrt{\Delta u}\omega(l)C_l} + 0\left(\Delta^2\right), \tag{2.5}$$

We should note that these formulae introduce errors having the same order as that of Trotter's formula, and, thus, are always valid when Trotter's decomposition is valid. As a result, we obtain a path-integral form for $e^{-\beta H}$ as

$$e^{-\beta H} \to \int Dx T_\tau \exp\left\{-\int_0^\beta d\tau \left[H_0\{\tau\} - \sum_l x_s(l,\tau)S_l\{\tau\} - \sum_l x_c(l,\tau)C_l\{\tau\}\right]\right\}, \tag{2.6}$$

where H_0 is a one-body term. T_* is the time-ordering operator; the time arguments (τ) of operators $H_0\{\tau\}$, $S_1\{\tau\}$ and $C_1\{\tau\}$, represent only this time ordering. Therefore, these operators have no real time dependence, in contrast to the Heisenberg representation, defined in §2-B. Only $x_S(l,\tau) = \sqrt{u/2\Delta}\sigma(l,\tau)$ and $x_C(l,\tau) = \sqrt{u/2\Delta}\omega(l,\tau)$ are really time-dependent. $\int Dx$ symbolically denotes the sum over $x_S(l,\tau)$ and $x_C(l,\tau)$. Thus, the Coulomb repulsion including the arbitrary long-range part, is reduced into a time-dependent one-body Hamiltonian with two kinds of Ising-spin variables per site.

2.2.2 Optical responses and Green's functions

A single particle spectrum ($N(\omega)$), which corresponds to the photo-emission spectrum and an inverse one, is derived from an analytic continuation of a Fourier transform of a one-body Green's function, that is defined by

$$\bar{G}^\sigma(q,\tau) = \sum_l e^{iql}\bar{G}^\sigma(l,\tau),$$
$$\bar{G}^\sigma(l-l',\tau-\tau') = \sum_{\{x\}} G^\sigma(l,\tau,l',\tau',x) = \sum_{\{x\}}\left\langle T_* a_{l\sigma}(\tau)a^\dagger_{l'\sigma}(\tau')\right\rangle_x. \quad (2.7)$$

The absorption spectrum, on the other hand, is derived from an analytic continuation of the current correlation function, which is expressed by two-body Green's functions. The current operator for the 1D system is represented by

$$J = iD\sum_{l\sigma}\left(a^\dagger_{l\sigma}a_{l+1\sigma} - a^\dagger_{l+1\sigma}a_{l\sigma}\right), \quad D = \vec{p}\cdot\vec{e}T, \quad (2.8)$$

where $\vec{p}$, $\vec{e}$, and T are the polarization vector, the chain direction, and the dipole matrix element between two neighboring orbitals, respectively. Therefore, the current correlation function becomes

$$\bar{F}(\tau) = \langle J(\tau)J'(0)\rangle = D^2\sum_{l_1,l_2\sigma}\{\bar{K}^\sigma(l_1,l_1+1,l_2,l_2+1,\tau) + \bar{K}^\sigma(l_1+1,l_1,l_2+1,l_2\tau)$$
$$-\bar{K}^\sigma(l_1,l_1+1,l_2+1,l_2,\tau) - \bar{K}^\sigma(l_1+1,l_1,l_2,l_2+1,\tau)\}. \quad (2.9)$$

where we define the two-body Green's function as

$$\bar{K}^\sigma(l_1,l_1+1,l_2,l_2+1,\tau) = -\sum_{\{x\}}\left\langle T_* a^\dagger_{l_1\sigma}(\tau)a_{l_1+1\sigma}(\tau)a^\dagger_{l_2\sigma}(0)a_{l_2+1\sigma}(0)\right\rangle_x. \quad (2.10)$$

In our formulation, the Bloch-De Dominics theorem is available for decoupling the average of the many-body operator into the products of one-body Green's functions,[2] defined by eq(2.8) and (2.6). In eq.(2.10); we neglect the contractions between l_1 and l_1+1, and between l_2 and l_2+1, because they are irrelevant to the optical response. As a result, the two-body Green's function, which is relevant to the optical response, becomes

$$\bar{K}^\sigma(l_1,l_1+1,l_2,l_2+1,\tau) = -\sum_{\{x\}}\left\langle T_* a^\dagger_{l_1\sigma}(\tau)a_{l_1+1\sigma}(\tau)a^\dagger_{l_2\sigma}(0)a_{l_2+1\sigma}(0)\right\rangle_x. \quad (2.11)$$

We can now use quantum Monte-Carlo techniques to sum over the spin configurations $\{x\}$.

The one-body Green's function and the current correlation functions are related to the spectral functions by

$$\bar{G}(\tau) = \frac{1}{N}\sum_{q\sigma}\bar{G}^\sigma(q,\tau) = \int\frac{d\omega}{2\pi}\frac{e^{-\omega\tau}}{1+e^{-\beta\omega}}N(\omega),$$
$$\bar{F}(\tau) = -\int\frac{d\omega}{2\pi}\frac{e^{-\omega\tau}}{1-e^{-\beta\omega}}\Delta(\omega). \quad (2.12)$$

The optical conductivity spectrum ($\sigma_1(\omega)$) is proportional to $\Delta(\omega)/\omega$. We have obtained the spectral functions $N(\omega)$ and $\Delta(\omega)$ by a least-squares method with the conditions $N(\omega) \geq 0$ and $\Delta(\omega) \geq 0$, respectively.

2.3 Result and Discussion

We have applied our method to the 1D half-filled extended Hubbard model with a system size of $N = 24$, and imposed the periodic boundary condition. Its Hamiltonian is

$$H = -t\sum_{l\sigma}a^\dagger_{l\sigma}a_{l+1\sigma} + U\sum_l n_{l\alpha}n_{l\beta} + V\sum_l n_l n_{l+1}. \quad (3.1)$$

We considered only the region $U>2V$, in order to exclude the appearance of the charge density wave ordering. In the following, all the energies are normalized by the magnitude of the transfer energy (t).

2.3.1 New peaks due to an electron correlation effect

In this subsection we consider the absorption spectra of the Hubbard model (V=0). The new peaks corresponding to the multiple excitation of electron-hole pairs appears on the high-energy side of the main peak unless the Hubbard gap is very large, as shwon in Fig. 55. This is because a photo-generated electron and a hole excite other electron-hole pairs through an interaction arising from a fluctuation term that is the difference between the MF Hamiltonian and the exact one. When U increases, the probability for such multiple excitation of electron-hole pairs decreases, because the energy gap becomes larger and the band width becomes smaller.

In an extended Hubbard system with a sufficiently large V to create CT exciton, the CT exciton peak has

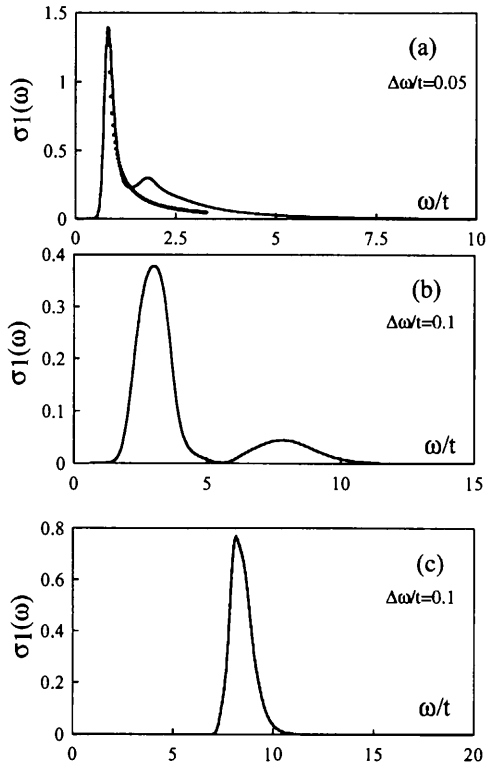

Fig. 55 Optical conductivities ($\sigma_1(\omega)$) for the Hubbard model with U=3 and β =15(a), U=5 and β =5(b), and U= 10 and β =5(c). The spectra are normalized so that the integrated value over the frequency is 1. The dotted line in Fig. 54a was obtained from the one-body picture based on the direct interband transition.

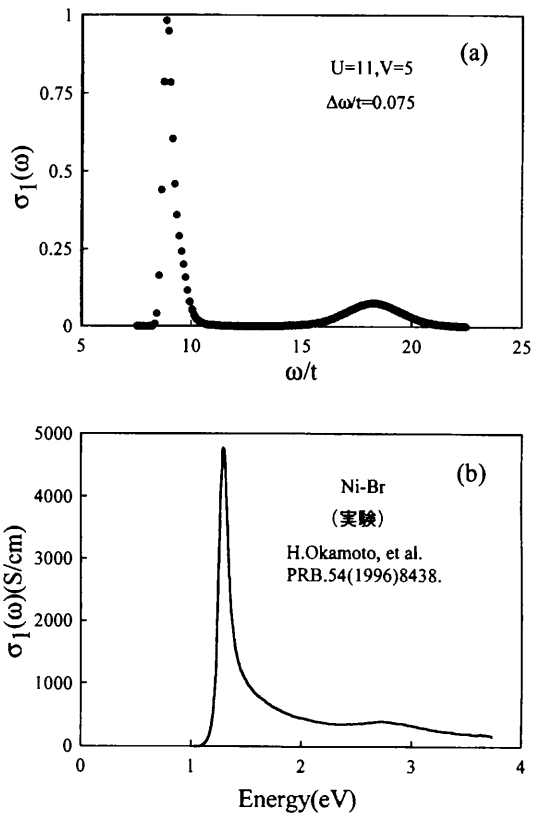

Fig. 56 Optical conductivities ($\sigma_1(\omega)$) for the extended Hubbard model with (U,V)=(11,5) and β =5(a), and the experimental result for the Ni-Br compound(b). The numerical result(a) is normalized.

an infrared divergence-like structure, which arises from the simultaneous excitation of the CT exciton and magnons conserving the spin quantum number as shwon in Fig. 56a. This result clearly shows the nonlinear coupling between the CT exciton and collective spin excitations within the single-band extended Hubbard model. In other words, the charge and spin of the electron are unseparable in this system. Figures 56a and b show that our result qualitatively coincides with the experimental result obtained for the Ni-Br complex, which is a typical quasi-1D insulator caused by a strong Coulomb repulsion.

K. Nasu, PF

References

1) H. Okamoto et al., Phys. Rev. B**54**, 8438 (1996).
2) K. Nasu, J. Phys. Soc. Jpn, **65**, 2285 (1996).

Experimental Facilities

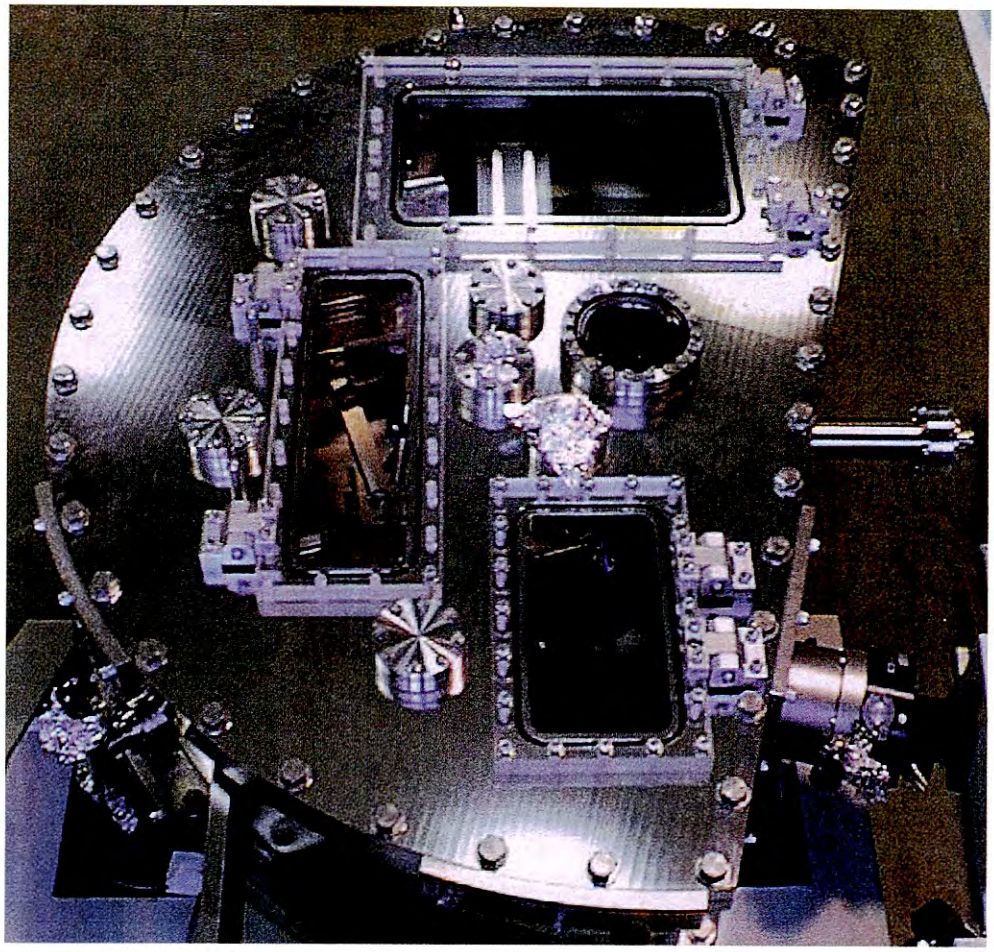

Secondary X-Ray spectrometer, "Escargot"

CONTENTS

A. BEAMLINES

1. NEW BEAMLINES IN OPERATION

1.1 BL-2C, Varied-Space Plane Grating Monochromator in a Configuration with Sagittal Focusing and a Convergent Beam

To meet the demands of sophisticated experiments in the field of soft X-ray spectroscopy, a new soft X-ray grazing-incidence monochromator with a varied-space plane grating has been commissioned on undulator beamline BL-2. In the design of the *Varied-space Plane Grating Monochromator*, the configuration of Sagittal *focusing and a Converging beam* was adopted.[1] Therefore, the monochromator is called SC-VPGM. The slope-error effect of the focusing mirrors and heat load due to radiation are reduced in the sagittal-focusing condition, compared to tangential focusing. The results of an analytical estimation and ray-tracing simulation show that a resolving power of 10000 - 20000 can be obtained over the full energy range of 250 to 1400 eV.

Figure 1 shows a schematic view of SC-VPGM. The aperture determines the acceptance angle of $0.1^{V} \times 0.3^{H}$ mrad^2 from the undulator radiation source into the monochromator. A bent cylindrical mirror (M_0) vertically focuses the beam on entrance slit S_1 in the sagittal-focusing configuration. The divergent beam from S_1 is converged by a cylindrical mirror (M_1), which is also in the sagittal-focusing configuration. The focal point of the M_1 mirror is located behind the grating, and is considered to be a virtual source image for the grating. Two gratings of 1000 and 2200 l/mm are interchangeable *in-situ*, and cover an energy range from 250 to 1400 eV. The diffracted light is focused on exit slit S_2 in the vertical direction with a deviation of 1.6 mm in the direction of the optical axis. The monochromatized soft X-rays from S_2 are focused on the sample position by a spherical mirror (M_2) for vertical focusing and a cylindrical mirror (M_3), which is in the sagittal-focusing configuration for horizontal focusing. The combination of mirrors M_2 and M_3 is optimized in order to make a tiny spot size.

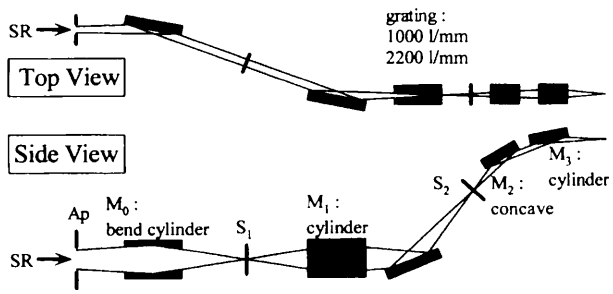

Fig. 1 Schematic view of the optical layout of BL-2C.

Test operations of SC-VPGM have been performed concerning three points: resolving power, photon flux, and spot size. First, the resolving power has been estimated from the absorption spectra of several gaseous samples. The K-shell photoabsorption spectrum of N_2 molecules is shown in Fig. 2, which was measured with a grating of 1000 l/mm and slit widths of S1 = 70 μm and S2 = 15 μm. The vibrational structure can be clearly seen. The resolving power was evaluated by fitting a Voigt function to the spectrum. As a result, the FWHM of the Gaussian profile representing the transmission function of the monochromator was determined to be 40.9 meV at a photon energy of 400 eV. The FWHM of 40.9 meV corresponds to a resolving power E/ΔE of 10000. This result is nearly equal to the calculated one.[1] In addition, the Ne 1s photoabsorption is shown in Fig. 3, which was measured with a grating of 2200 l/mm and slit widths of S1 = 100 μm and S2 = 15 μm. The fourth peak of excitation to the 6p orbital is clearly revealed. The FWHM of the transmission function by the fitting process has been evaluated to be 117 meV, which corresponds to 7500 at a photon energy of 890 eV. From these evaluations, it is recognized that the typical resolving power is from 5000 to 10000 over the entire energy range. This implies that SC-VPGM is one of the monochromators with the highest resolving power in the soft X-ray region.

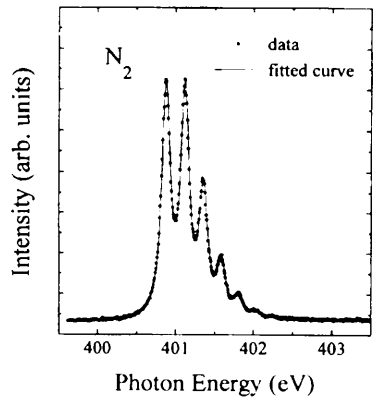

Fig. 2 $1s\sigma \rightarrow \pi^*$ absorption spectrum of N_2 molecules. The dots are absorption data, and the solid line is the fitted curve.

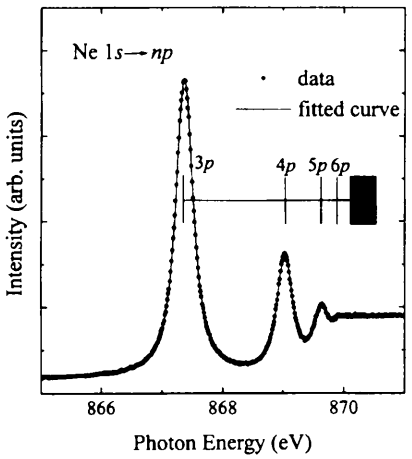

Fig. 3 $1s \rightarrow np$ absorption spectrum of Ne atoms. The dots are absorption data, and the solid line is the fitted curve.

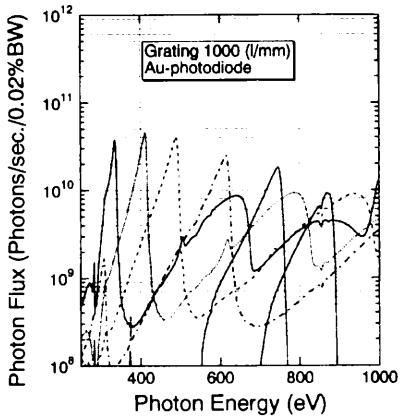

Fig. 4 Absolute photon flux measured by a Au photo-diode. To measure the undulator spectra, the 1000 l/mm grating was used.

Secondly, the photo-current at the sample position was monitored by using a Si photo-diode and a Au photo-diode. Taking the photo-current and the quantum efficiencies of the diode into account, the absolute photon flux was calculated. The result is shown in Fig. 4, which was measured with a grating of 1000 l/mm and using a Au photo-diode. The different lines in the figure represent the spectra of the undulator radiation for different undulator gaps. It can be understood that linking the maximum points of each spectra makes a smooth envelope curve corresponding to the effective photon flux. A measurement on the grating of 2200 l/mm has also been accomplished. The results indicate that a photon flux of more than 10^{10} photons/s/0.02% BW is obtainable over the entire energy range.

Lastly, the spot size at the sample position was measured by combining the photo-diode and knife-edges. The knife-edges in front of the photo-diode could be smoothly moved by micrometers. The photo-current curve as a function of the knife-edge positions has been expressed by a shape like a step function. As a result, the spot size described by the full broadening width of the step function is $0.1^{V} \times 0.9^{H}$ mm^2. This poor spot size will be improved by the adjusting the M_0, M_2 and M_3 mirrors.

References

1) Y. Yan and A. Yagishita, KEK Report 95-9 (1995).

1.2 BL-11A, A Soft X-Ray (80-1200eV) Station with a VLS Plane Grating Grazing-Incidence Monochromator

BL-11A, where the Grasshopper monochromator was formerly used, was reconstructed with a new grazing-incidence monochromator. This beamline is to be used mainly for spectroscopic measurements of solids or solid surfaces in the soft X-ray region (80 - 1200eV). Since the light source is not an undulator, but a normal bending magnet, the optical design was made[1] so as to achieve not extreme high resolution, but stability over a wide energy range for EXAFS measurements on a C, N, or O *K*-edge.

Figure 5 schematically shows the layout of the beamline. Horizontally, 5 mrad synchrotron radiation is deflected and partly focused by a cylindrical mirror (M0), and then focused verticaly by another cylindrical mirror (M0') to the entrance slit (S1). The monochromator consists of a spherical mirror (Mi , i = 1 or 2) and a plane grating with a varied line spacing (VLS-PG). To cover a wide energy range, two spherical mirrors (M1 and M2) for different included angles and

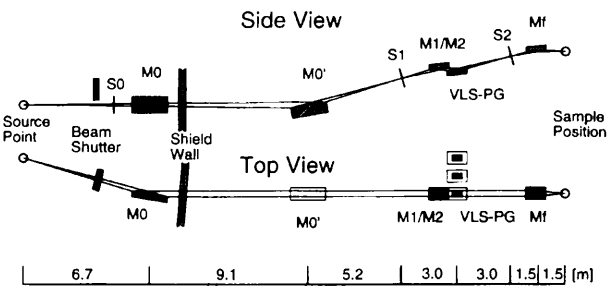

Fig. 5 Layout of BL-11A.

three gratings with different groove densities are interchangeable without breaking the vacuum.

By the end of FY1996, three gratings were tested. The first one has a groove density of 800 l/mm made by a mechanical ruling technique. Figure 6 shows the photo-ion spectrum of Ar gas in the 2*p* excitation region recorded with the first grating. The second one has nearly the same groove parameters, but was made by a holographic recording method with aspheric wavefronts.[2] The N_2 1s→π* spectrum shown in Fig. 7 clearly demonstrates that the quality of the grating is sufficiently good. Figure 8 shows the spectral distribution with the holographic grating and M2, which was measured by the photo-current from a gold-coated tungsten mesh. Due to the benefit of the smooth surface of the holographic grating, scattered light is effectively suppressed compared to that from a mechanically ruled grating. Although commissioning with the last grating (mechanically ruled 300 l/mm) has not yet been sufficient, it has been confirmed that photons with an energy down to 80 eV are obtainable.[3]

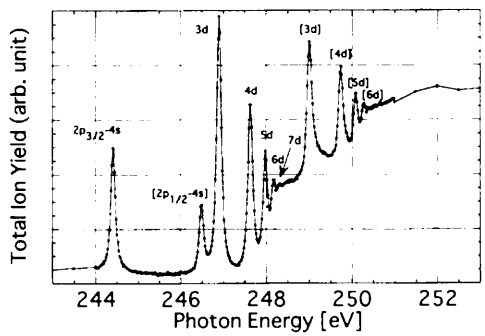

Fig. 6 Photo-ion spectrum of Ar gas at Ar $L_{2,3}$ edges recorded with a mechanically ruled VLS grating.

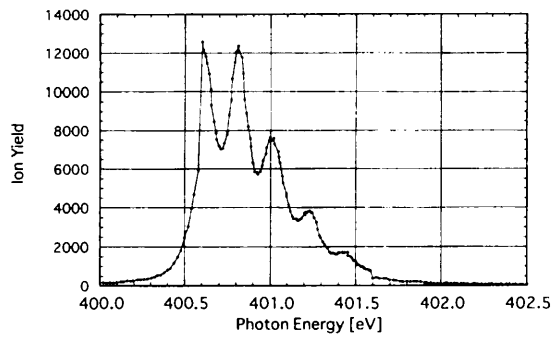

Fig. 7 Photoion spectrum of gas-phase N_2 at the N 1s → π* region recorded with a holographic VLS grating.

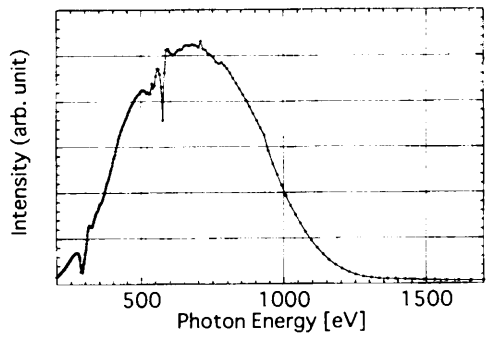

Fig. 8 Spectral distribution of the monochromator (800 l/mm holographic grating and M2).

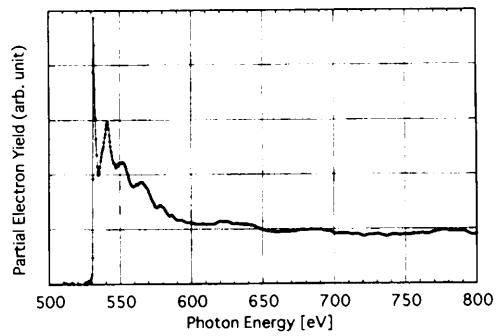

Fig. 9 Oxygen K-edge surface EXAFS spectrum of submonolayer-adsorbed methoxy species on Ni(111).

As a first example of EXAFS measurements of a surface adsorbate, Fig. 9 shows the oxygen *K*-edge spectrum for submonolayer-adsorbed methoxy (CH_3O-) species on Ni(111). The analytical results are described in the "Users' Reports" section of this volume.[4]

References

1) K. Amemiya, Y. Kitajima, T. Ohta, and K. Ito, J. Synchrotron Rad. 3 (1996) 282.
2) K. Amemiya, Y. Yonamoto, T. Ohta, Y. Kitajima, K. Ito, K. Sano, T. Nagano, M. Koeda, H. Sasai, and Y. Harada, to be published in SPIE Proceedings.
3) Y. Kitajima, K. Amemiya, Y. Yonamoto, T. Ohta, T. Kikuchi, T. Kosuge, A. Toyoshima, and K. Ito, to be published in J. Synchrotron Rad.
4) K. Amemiya, Y. Kitajima, Y. Yonamoto, S. Terada, T. Yokoyama, and T. Ohta, in this volume.

1.3 BL-12A, Beamline for Optical-Element Characterization

BL-12A has been refreshed to be dedicated for the characterization of VUV and soft-x-ray optical

elements. A 2-m Vodar-type monochromator was designed by Maezawa and Yamazaki, and was installed at this beamline in 1992.[1] The reflectometer for the characterization of optical elements designed by Mitani *et al.*[2] has been recently settled 8 m downstream from the monochromator. The mechanical stability of the monochromator is, therefore, required to supply a stable beam for the reflectometer. For this requirement, the translation mechanism to drive the grating was improved in 1996. To evaluate the beamline performance, the output spectrum of the monochromator and the beam stability were evaluated.

A 1200-l/mm grating was mounted to the monochromator. A gold mesh was positioned downstream from the 4-dimension slit to measure the output spectra of the beam emergent from the monochromator. Using both a fluorescent screen and a SUS-304 photoelectron emitter, the beam position and the cross-sectional profile were observed at a distance of 3 m from the monochromator, where other experiments will be carried out in accordance with the beamline schedule, and of 7 m, just before the reflectometer. With the fluorescent screen, we visually observed the position of the beam footprint, while by shifting the emitter the position and the profile of the beam were precisely measured.

Figure 10 shows an output spectrum measured with the photocurrent from the gold mesh for a slit width of 100 μm. A broad peak is dominant in the low-energy region. A strong dip in the vicinity of 300 eV is due to the absorption by hydrocarbon deposited on the optical elements. As can be seen, monochromatized photons are expected to be available, even at 1 keV. The number of output photons was roughly estimated to be about 10^9 photons/s around 150 eV for a ring current of 300 mA.

The beam size was 2 mm by 3 mm in the horizontal and vertical dimensions at 3-m distance, while it was 10 mm by 1 mm at 7 m. Unfortunately, the beam was observed to shift horizontally by 5 mm at 3 m over a wavelength scan from the 0th order to 100 eV. However, the move was quite regular. Besides, no vertical shift was observed. A similar shift was also observed at 7 m. This result means that the last improvement for the monochromator was successfully carried out. The horizontal shift seems to have originated from a small tilt of the monochromator.

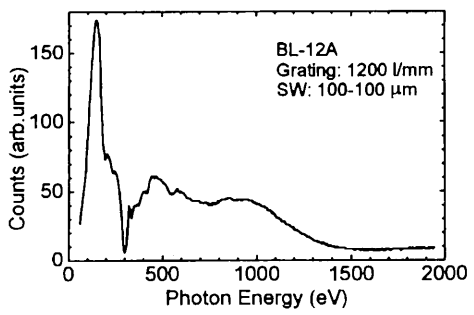

Fig.10 Output spectrum of the monochromator in BL-12A.

Owing to the mismatch in the radius of curvature for the sagittal focus of the postfocusing mirror, the focusing quality, and thus the photon number, would be insufficient for some experiments. However, it is sufficient for the characterization of optical elements for soft X-rays.

References

1) Photon Factory Activity Report **#10** (1993) I-2.
2) S. Mitani, T. Namioka, M. Yanagihara, K. Yamashita, J. Fujita, S. Morita, T. Harada, T. Sasaki, S. Sato, T. Miyahara, T. Koide, A. Mikuni, W. Okamoto, and H. Maezawa, Rev. Sci. Instrum. **60** (1989) 2216.

1.4 BL-6B, Beamline for the TARA Project

BL-6B has been constructed as a beamline for the Tsukuba Advanced Research Alliance (TARA) Sakabe Research Project for monochromatic macromolecular crystallography using a Weissenberg camera and an imaging plate.

The beamline consists of a bent plane mirror and an asymmetrically cut Si(111) triangle monochromator, which are located at 19.5 m and 23.0 m from the source point, respectively. The monochromator is located in the experimental hutch, and the distance to the detector surface is 1.4 m. The specifications of the mirror and the monochromator are as follows:

Mirror: Platinum-coated (1000 Å thick) silicon
Size: 1000 × 100 × 50 mm
Radius curvature: ca. 2.2 km
Glancing angle: 3 mrad
Cut off wavelength: ca. 0.4 Å

Monochromator: Bent triangle Si(111)
Wavelength: 0.9 Å-1.8 Å
Asymmetrically cut angle: 7.8°
Size: 150 mm × 40 mm

With the present optics, a photon flux of 1.7×10^{10}

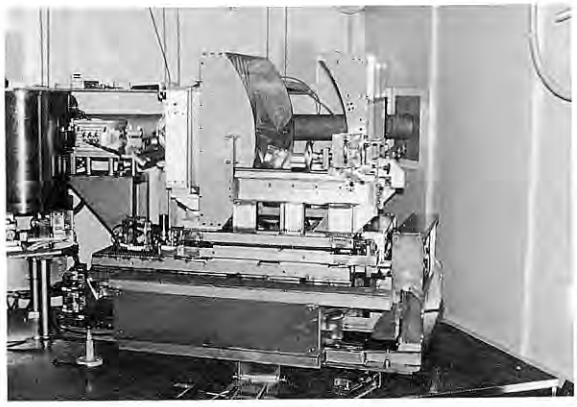

Fig.11 Weissenberg camera for BL-6B.

photons/s in a spot of 0.2 mm × 0.2 mm at the sample position is available at a wavelength of 1.0 Å.

A device (Fig. 11) to integrate diffraction data was designed for BL-6B. The design was based on the Weissenberg camera for macromolecular crystallography.[1-3] The device includes two large size imaging-plates (400 × 800 mm IP) as a detector and a cylindrical cassette. Considering both the spatial resolution of the diffraction spots on the IP and the resolution of a crystal-structure analysis, we chose a cassette with a camera radius of 573 mm. Two IPR4080s (the IP reader that Sakabe developed for the large format IP (400 × 800 mm)) were installed. An Oxford cryocooler was also installed for cryocrystallography. Some initial results at this station are described in this volume.

A new type of the monochromator has been designed to provide a focused beam over a wide wavelength range by the simultaneous tuning of the asymmetric factor and the radius of curvature. The asymmetric cut angle and the curvature radius are variable over the range of 0 - 15.5° and ∞ - 40 m, respectively. This station will be operational in November, 1997, with the new-type monochromator.

References

1) N. Sakabe, J. Appl. Crystallogr. **16** (1983) 542.
2) N. Sakabe, Nucl. Instrum. Methods A**303** (1991) 448.
3) N. Sakabe, S. Ikemizu, K. Sakabe, T. Higashi, A. Nakagawa, N. Watanabe, S. Adachi and K. Sakai, Rev. Sci. Instrum. **66** (1995) 1276.

2. BEAMLINES UNDER CONSTRUCTION AND PLANNING

2.1 BL-9A, Design of a New XAFS Beamline

BL-9A was constructed by NEC corporation in 1986.[1] Here, a basic study of lithography by using soft synchrotron radiation from a bending magnet was carried out. With the completion of the studies, the Photon Factory was kindly permitted to use the site, thanks to a generous offer by NEC corporation.

In order to meet the increasing demand for XAFS experimental stations, and also to enable carrying out more sophisticated XAFS experiments, it was decided to construct a new XAFS beamline at BL-9A in late 1995. The specifications of the beamline were discussed with many users through the XAFS users' mailing list (XSJ-ML).

Through discussions, the main specifications of BL-9A were decided as follows:

1. The focus size should not change with a variation in the X-ray energy.
2. The lower energy limit should be expanded from 4 keV to ca. 2.1 keV in order to enable experiments on P, S and Cl.
3. The maximum energy should be ca. 15 keV in order to realize a high flux.
4. A semi-micro focus size of less than 1 mm^2 should be realized in order to apply the XAFS technique to samples of limited quantity.
5. The intensity should be higher than that obtained at BL-12C [2] without loosing the energy resolution.

In order to realize Specification 1, we decided not to adopt sagittal focusing optics, which is used at BL-7C.[3] According to our experience, it was very difficult to readjust the radius of the sagittal focusing crystal because of a deformation of the crystal. In order to compensate for the deformation, the parallelism between the two crystals had to be adjusted at each point, which wasted time and caused crystal fatigue. We therefore decided to adopt one or two mirrors as focusing element(s).

The number and thickness of windows installed in the beamline were minimized in order to increase the transmission of lower energy X-rays. A 0.1 mm thick Be window is to separate the UHV condition of the front end of the beamline and the low vacuum of the branch beamline. Another 0.1 mm thick Be window is

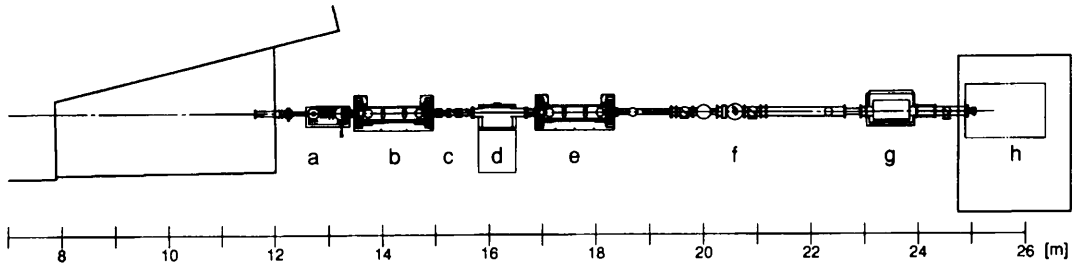

Fig.12 Plan view of BL-9A. The main components are a branch beam shutter and an entrance slit (a), a beam collimating mirror (b), a Be window (c), a double-crystal monochromator (d), a focusing mirror (e), a down stream shutter (f), a higher order rejecting mirror (g) and an experimental hutch (h).

to separate the vacuum of the beamline and the atmosphere. Although most of experiments will be carried out in the atmosphere, the latter window can be removed when the experiment is carried out *in vacuo*.

A mirror chamber for BL-9B and the hutches for BL-9A and 9C limited the focus position at 25.3 m and the space permitted to install beamline components, which didn't permit us to adopt 1:1 focusing by a toroidal mirror. The following optics were compared:

1. Focusing by a toroidal mirror.
2. Focusing by a rotating ellipsoid mirror.
3. Focusing by two rotating paraboloid mirrors which were arranged like a chair conformation.
4. Focusing by two rotating paraboloid mirrors which were arranged like a boat conformation.
5. Focusing by two toroidal mirrors instead of rotating paraboloid ones (chair and boat conformations).
6. Focusing by a paraboloid mirror and a toroidal one.

Among these, design 4, which gave the highest intensity without loosing the energy resolution, was adopted.

In this design, the monochromator can accept the whole vertically diverged beam without sacrificing the energy resolution as the beam is made parallel both vertically and horizontally by the first mirror. This optical system is expected to provide a five-times higher flux compared with design 1 when a 0.2 mm square receiving slit is used, which is one order higher than that realized at BL-12C. By using two mirrors, the horizontal acceptance of the beam line increased to 3 mrad at the cost of manufacturing expenses. Higher order reflections are minimized by using double-parallel aligned mirrors. The reflecting surface can be selected from Ni and Rh according to the required photon energy. A plan view of BL-9A is shown in Fig. 12.

The beamline components are being set up during the long shutdown period in 1997. It will be completed by the end of FY1997.

References

1) Photon Factory Activity Report **#4** (1987) 88, 163, ibid. **#5** (1988) 189, ibid. **#6** (1989) I-13, 217, 218.
2) M. Nomura and A. Koyama, KEK Report, 95-15 (1996).
3) M. Nomura, A. Koyama and M. Sakurai, KEK Report, 91-1 (1991).

2.2 Renewal of BL-10C Optics

BL-10C, one of the oldest beamlines in the Photon Factory, has provided focused monochromatic X-rays for experiments, such as small-angle scattering of enzyme and other macromolecule solutions, since commissioning of the PF. The beamline comprises a double-crystal monochromator and a bent cylindrical focusing mirror. The mechanism of bending the mirror, which was constructed in 1982, is rather old fashioned and is very difficult to adjust and to obtain the optimum focusing condition. During a 10-month shutdown in 1997 for improving the emittance of the storage ring, renewal of the optical components was planned. Since the optical system is appropriate for accepting synchrotron radiation from the low-emittance ring, the optical system, itself, will be conserved. The monochromator, which has two independent goniometers, was overhauled and the mirror bender was replaced by a new one having an updated bending mechanism (Fig.13). The reflecting angle of the mirror, which acts as a high-energy cut mirror, was lowered from 16 mrad to 14 mrad in order to increase

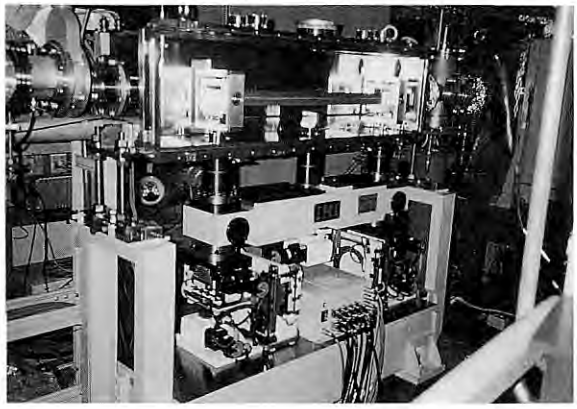

Fig.13 New focusing mirror chamber with the new mirror bending mechanism installed at BL-10C.

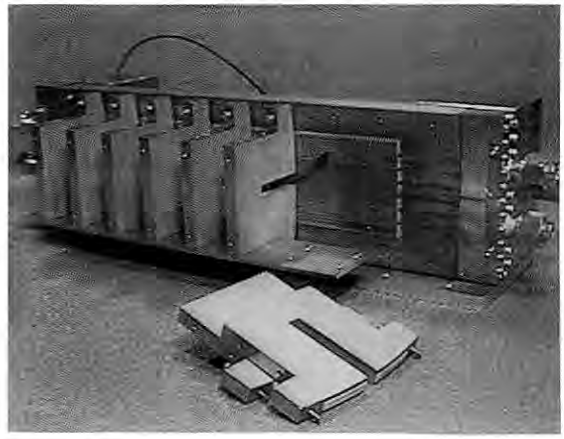

Fig.14 Outlook of the doubly curved monochromator for BL-13B2.

the intensity of X-rays at the high-energy side of the available energy region (4 -10 keV). The renewed beamline is expected to provide well-focused monochromatic X-rays to the experimental station from November, 1997. At the same time, the experimental station BL-10C will become a dedicated station for the small-angle scattering of solution samples, since a new station (BL-15B2) will be finished for X-ray surface/boundary diffraction experiments, which has been carried out at this station until now. The design and construction of BL-15B2 will be described in the next volume.

3. IMPROVEMENT OF BEAMLINE

3.1 A Doubly Curved Monochromator for BL-13B2

During the 1996 summer shutdown, a new monochromator was installed in BL-13B2, the end station of the multipole wiggler beamline. Proceeding to the type-S proposal (96S002), a focusing optics was exclusively designed for X-ray diffraction experiments under simultaneous high-temperature and high-pressure conditions, like those at the earth's interior. Due to the very small sample volume, a high photon-flux density is required for *in-situ* experiments at such extreme conditions, which are achieved by using diamond-anvil cells (DAC) and a CO_2 laser-heating device adopted to an angle-dispersive X-ray powder-diffraction system, using an Imaging Plate as a detector.

However, the optical design is strongly restricted by a space problem: i.e. no extra space for further optical components on the existing beamline. Inside the experimental hutch, a doubly curved crystal monochromator was installed as a single-focusing optics at 33 m from the source point. Figure 14 shows a photo of the monochromator. An asymmetrically cut Si(220) doubly curved crystal is applied to obtain focused monochromatic X-rays on the sample. The crystal is mounted on a water-cooled cylindrically polished copper holder with eight holding plates. Liquid In-Ga alloy is inserted between the crystal and the holder to obtain good thermal and mechanical contacts. According to the Johann geometry, the asymmetrical cut crystal is bent with a meridian radius (R1) of 161.1 m by using a bending mechanism adopted to the copper holder in order to converge synchrotron radiation in the horizontal direction. For sagittal focusing in the vertical direction, the crystal is bent along the cylindrical shape of the holder with a radius (R2) of 0.307 m. The size of the Si crystal is 2 mm × 70 mm × 300 mm (thickness, width and length). There are two kinds of channels in both surfaces: 0.3 mm wide × 1.7 mm deep channels in the longitudinal direction on the front and 0.5 mm wide × 0.3 mm deep channels in the transverse direction on the back in order to obtain a smooth curvature of the crystal. In the front surface the channels are filled by molybdenum wires (0.25 mm ϕ) to avoid stray scattering from the bottom surface. The remaining ribs with 0.6 mm width can only diffract monochromatic X-rays. The focus size is approximately 0.4 mm and 0.3 mm in the horizontal and vertical direction, respectively, at the focus point 1.5 m downstream from the monochromator with an energy of 30 keV.

Preliminary studies with Garnet as a sample were

carried out during the autumn beamtime in 1996. The new unknown phase is observed at 35 GPa. The new monochromator performs a one-order higher photon flux density than BL-18C, which has also been commissioned for diffraction experiments at high pressure and/or low-temperature conditions.

B. NEW INSTRUMENTATION

1. HIGH-RESOLUTION PHOTOELECTRON SPECTROMETER

A new high-resolution photoelectron spectrometer has been constructed and opened for users. Figure 15 shows a side view of this spectrometer. It consists of an analyzer chamber, a sample-preparation chamber, a SCIENTA SES-200 hemispherical electron analyzer and vacuum pumps. The analyzer chamber and the electron analyzer are doubly shielded with μ-metal sheet from the magnetic field. Photo-emitted electrons are retarded and transferred to the entrance slit of the analyzer through electronic lenses. The mean radius of the electron path in the analyzer is 200 mm, and the energy-resolved electrons are focused on a two-dimensional position-sensitive detector without an exit slit. The pass energy can be chosen from 2 to 500 eV in 9 steps. The electron detector consists of a micro-channel plate and a phosphor screen, which is imaged by a charge-coupled device (CCD) camera. Images on the screen represent the energy distribution along the radial direction of the electron orbit, while they represent spatial information from where electrons are emitted along the perpendicular direction. Users can take signals from a restricted area of samples by ignoring the light spots on uninteresting regions of the screen. The light spots are counted for every line of the CCD camera simultaneously by the electronics, and data are transferred to a computer and accummulated statistically. Due to simultaneous counting for multi-energy electrons, a higher throughput has been achieved.

A He-flow-type cryostat is mounted on the manipulator, and the sample temperature can be controlled from ~ 10 K to room temperature. The sample holder is electrically isolated from the cryostat with a sapphire sheet in order to utilize total electron-yield measurements. The analyzer chamber can be evacuated to ~ 8×10^{-11} Torr by a 1500 l/s turbo-molecular pump with a 150 l/s backing turbo-molecular pump and a 60 l/s ion pump. The preparation chamber is equipped with a diamond file and a Au evaporation source.

The energy resolution of this spectrometer was tested by measuring the photoelectron spectrum of Au near to the Fermi level at 20 K using the He I resonance line from a He-discharge lamp (Fig.16). The experimental spectrum was fitted by a model function, derived as follows: 1) The density of states (DOS) for Au was assumed to be a linear function of the binding energy near to the Fermi level. 2) A model function was produced as a convolution of the DOS multiplied by the Fermi-Dirac distribution function of the measurement temperature and a Gaussian, whose width was the resolution of the spectrometer. The width of the Gaussian was an adjustable parameter. According to

Fig.15 Outlook of the high-resolution photoelectron spectrometer.

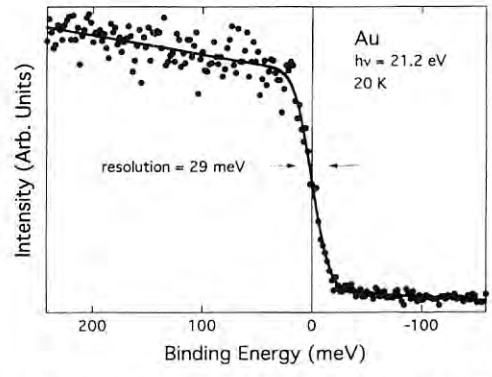

Fig.16 Photoelectron spectrum of Au near to the Fermi level.

the fitting result, the energy resolution of this spectrometer was evaluated to be 29 meV in the full-width at half-maximum. The experimental results using this spectrometer are described in the "Scientific Disciplines" and "Users' Reports" section of this volume.

2. SPECTROMETER FOR POLARIZED SOFT X-RAY RAMAN SCATTERING (BL-2C)

Soft X-ray Raman scattering has been studied in order to understand the electronic structures of condensed matter. If we can know the polarization dependence of the soft X-ray Raman scattering, it will give us more information about the symmetry of the relevant electronic states. Thus, a soft X-ray emission spectrometer system for polarized soft X-ray Raman scattering was newly designed and installed on the undulator beamline BL-2C in November, 1996.

The system comprises an analysis chamber, a soft X-ray emission spectrometer, a preparation chamber, and an air-lock chamber. Figure 17 shows a schematic of the system. With the two differentially pumped rotary feedthroughs, the spectrometer is rotatable by 90° together with the analysis chamber around the axis along which the synchrotron radiation enters. It is designed so that the sample position at the manipulator does not change when it rotates. The electric field of the radiation is polarized in the horizontal plane in undulator beamline BL-2C. Therefore, when S-G (in Fig. 17) is in the horizontal direction, depolarized Raman scattering spectra can be measured. On the other hand, when S-G is in the vertical direction, the polarized Raman scattering spectra can be measured.

The spectrometer was designed on the basis of Rowland circle geometry. It consists of an inci dence slit, gratings, and an area detector with a multichannel plate. The slit is located 10 mm apart from the sample. The distance between the slit and the grating is constant. The position of the detector is numerically positioned at the Rowland circle by three-axes controls. Two gratings are installed in the spectrometer, and are interchangeable *in-situ* in the vacuum. Three laminar-type spherical gratings cover the energy range from 18 to 1200 eV. The parameters of the spectrometer are listed in Table I. The area detector is used to accomplish high energy resolution, because the image at the MCP position has astigmatic coma abberations. The available slit widths are 10, 20, 50, 100, and 300 μm. In the case of the 10 μm slit, we will be able to obtain an energy resolution of 0.1 eV for a photon energy of 500 eV with the 5 m radius grating. The analysis chamber can be isolated by a vacuum valve from the preparation and air-lock chambers. Then, the sample preparations do not interfere with the soft X-ray emission measurements. A sample mounted on the holder of the manipulator can be cooled down to 15 K by a He-refrigerator. The photoelectron spectrometer is also equipped in order to calibrate the energy of the excitation light.

Table 1. Grating design parameters of the polarized soft X-ray Raman spectrometer.

Grating No.	Groove Density (l/mm)	Energy Range (eV)	Radius (m)	Incident Angle (deg)
1	300	18 - 200	3	86.2
2	1200	180 - 1000	5	87.7
3	2400	700 - 1200	7	88.4

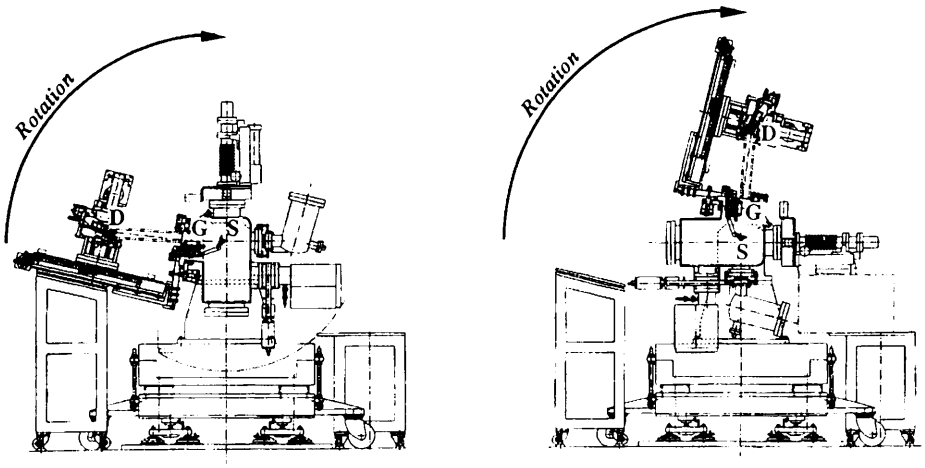

Fig.17 Outline of the polarized soft X-ray Raman spectrometer (front side view). (S) sample (rotation center) (G) gratings (D) detector.

The soft X-ray emisson spectra of several transition-metal compounds and rare-earth compounds have been measured. A preliminary experiment for the polarization dependence of the emission spectra was carried out on CaO.

3. SECONDARY X-RAY SPECTROMETER, "ESCARGOT"

X-ray emission spectroscopy gives us a lot of scientific information. By using the resonant Raman scattering, we can get the electronic (and also magnetic) structure of the materials. By using the non-resonant inelastic scattering, we can do the Compton scattering experiment, X-ray Raman experitment, and S(q, ω) experiment. A secondary X-ray spectrometer was made for X-ray emission spectroscopy. The designer named this apparatus "Escargot" after its outside shape, as shown in the photograph on the opening page of the "Experimental Facilities" section.

The specimen is set at the center of the chamber and the focus point of the incoming monochromatized X-rays obtained from the beamline. The scattered radiation is analyzed in the vertical plane by a cylindrically bent crystal, the Bragg angle of which can be changed from 80° to 60°. The analyzed X-rays are detected by the position-sensitive proportional counter (PSPC). The sample and the detector are arranged on the center axis of the analyzing crystal cylinder, so that we can obtain sagittaly focused and meridionaly energy-dispersive X-rays. Figure 18 shows the inside mechanism to change the incident angle of the crystal together with the detector. This assembly can be rotated in "Escargot" to vary the scattered angle over the range of 0° ~ 90° from the incident X-rays. The length from the center axis and the analyzing crystal is 50 cm.

The position-analysis method of the PSPC is the charge-division type. The resistive anode of the PSPC is a carbon fiber 7 mm in diameter, and its resistance is 4.2 kW per cm. The entrance window is made of a 1-mm thick beryllium plate, and the sensitive area of the window is 10 × 100 mm^2. The distance between the anode and the entrance window is 10 mm. The pressure of the flow gas (Ar + 10% CH_4) was controlled to be 8 atm at the test experiments.

When the flux of the incident beam was estimated to be ~ 10^{11} photons/s and the Ge(333) crystal was used as an analyzer, the typical counting rate at the Gd $L\alpha_1$ fluorescence peak from a Gd-Co amorphous thin layer with 33 at.% Gd and 67 at.% Co was 200 cps, and that of the full energy range around the Gd $L\alpha$ fluorescence lines was on the order of 4000 cps. The total energy resolutions were measured as 1.4 eV around the Gd $L\alpha$ fluorescence lines (6.06 keV), which were limited by the incident photon energy resolutions in the present stage.

Fig.18 Photograph of the inside mechanism of the secondary X-ray spectrometer, "Escargot".

4. APPLICATION OF POLARIZATION-TUNABLE X-RAY OPTICS TO MCXD SPECTRA MEASUREMENTS

New polarization-tunable X-ray optics using an X-ray phase plate were developed[1] and successfully applied to magnetic circular X-ray dichloism (MCXD) spectra measurements at BL-15C.

The experimental setup is schematically shown in Fig. 19. The incident white radiation from the bending magnet is monochromated by a pair of Si(111) crystal. Subsequently, a transmission X-ray phase plate transforms the horizontal polarization to circular. For the phase plate, a (001)-oriented diamond crystal slab is

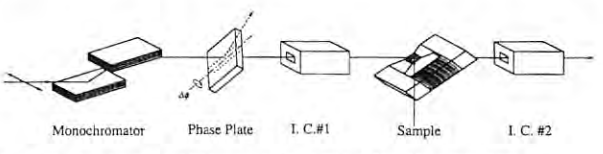

Fig.19 Experimental setup for the MCXD spectra measurements.

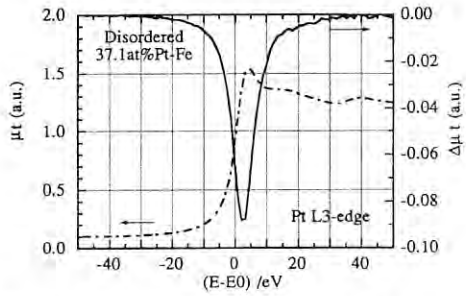

Fig. 20 Measured MCXD and XANES spectra on a disordered 37.1 at% Pt - Fe alloy sample at the Pt L_3-edge (E_0 = 11.565 keV).

usually used. The incident beam intensity to the sample is monitored by an ionization chamber and the transmitted intensity by another ionization chamber. The magnetic field is applied parallel to the sample plane and the field direction is tilted by 45° with respect to the incident beam direction.

For example, Fig. 20 shows the measured MCXD and XANES spectra. The spectra were measured on a disordered 37.1 at% Pt - Fe alloy sample at the Pt L_3-edge (E_0 = 11.565 keV). The obtained MCXD spectra are in good agreement with the MCXD spectra measured with the elliptical multipole wiggler on BL-28B.[2]

References

1) K. Hirano, T. Ishikawa, and S. Kikuta, Rev. Sci. Instrum. **66** (1995) 1604.
2) H. Maruyama, A. Koizumi, K. Kobayashi, and H. Yamazaki, Jpn. J. Appl. Phys. **32** (1993) 290.

5. A NEW SYSTEM OF THE YOUNG'S INTERFEROMETER

A new system of the Young's interferometer was constructed to measure the spatial coherence of the synchrotron radiation in the soft X-ray region[1] (Fig.21).

A grazing-incidence grating monochromator of vertical dispersion and the Young's interferometer with a horizontally separated double slit were united into one apparatus (Fig. 22). The entrance slit was fabricated of about 10 μm thick nickel sheets by the photo-forming method. Two apertures of $d \times l_1 = 5\ \mu m^H \times 100\ \mu m^V$ were placed parallel with a separation D = 30, 50, 100, 150 and 200 μm. All of the dimensions (l_1, d and

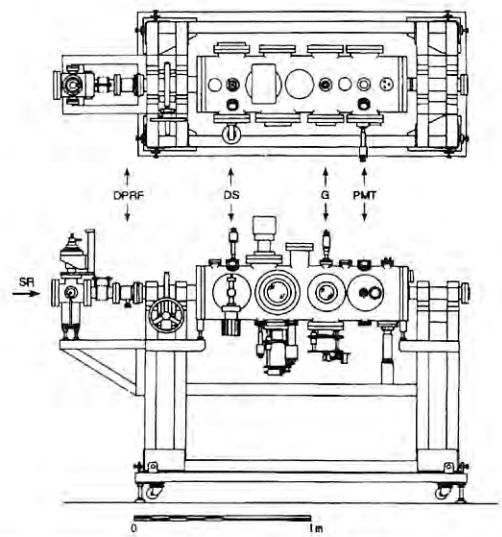

Fig. 21 Outlook of the Young's interferometer.

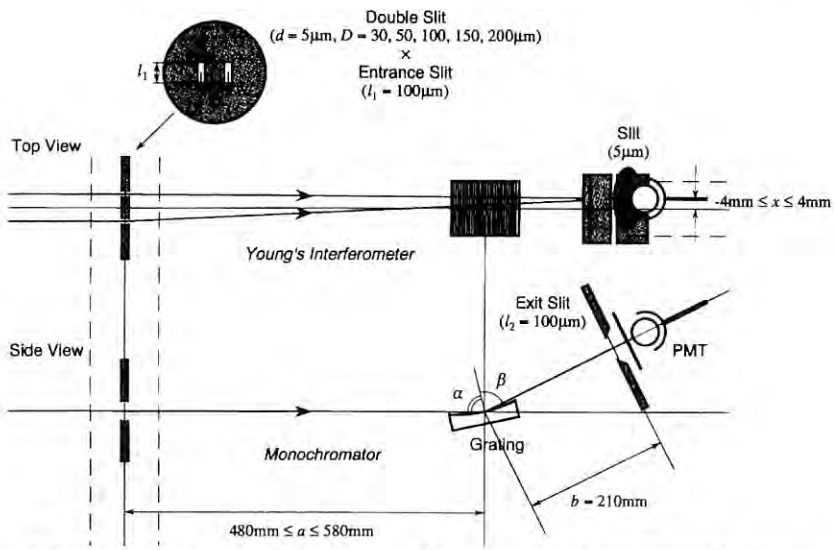

Fig. 22 Design of the Young's interferometer with top and side views.

D) have a tolerance of one micron. The monochromatizing resolution depends on the slit length (l_1), while the interference pattern depends on the width (d) and the separation (D). Although four spherical gratings are present, three of them can be installed into the chamber. Their groove densities and radii of curvature are (600 *l*/m, 2 m), (1200 *l*/mm, 2 m), (600 *l*/mm, 4 m), and (1200 *l*/mm, 4m). One can choose the best suited one among the three according to the wavelength while keeping the vacuum. The exit-slit width is changeable up to 500 μm. A photomultiplier tube covered with a 5 μm vertical slit is scanned horizontally to detect the pattern. It is driven by a two-phase stepping motor and a reduction-gear assembly. The scanning range is 8 mm. The whole system mentioned above can be rotated around the optical axis using a differentially-pumped rotary feed-through, which enables a measurement of the transverse coherence along an arbitrary orientation. Some experiments by this system have been performed at BL-12A and BL-28A.[2]

References
1) T. Hatano et al., Rev. Sci. Instrum., to be submitted.
2) Y. Takayama, T. Hatano, W. Okamoto, T. Miyahara, and Y. Kagoshima, in this volume.

6. (X, eX) COINCIDENT SPECTROMETER BY MEASURING BOTH OF ENERGIES ON THE COMPTON SCATTERED PHOTON AND THE RECOILED ELECTRON

It is well known that the 3-dimensional electron momentum density (3D-EMD) can be evaluated by a coincidence measurement between the Compton X-ray photon and the recoiled electron (X, eX). A new (X, eX) coincident spectrometer by measuring both the energies on the photons and the electron is reported.

The usual (X, eX) spectrometer has been used to measure the following three physical values: the directions of both Compton-scattered photons and electrons, and the energy of the photons by a Ge solid-state detector. Since the energy resolution has been limited by the detector, it is hard to obtain a better momentum space resolution than 0.5 a.u. The present system is designed to measure the energy of electrons by means of a time-of-flight method, which is realized by single-bunch operation at the AR. We have successfully achieved a momentum space resolution of 0.3 a.u., and have also demonstrated the possibility to measure the state-selective 3D-EMD by using a binding-energy effect.

Figure 23 shows a schematic view of the system. Compton-scattered X-rays are detected by a Ge solid-state detector (energy / momentum resolution of ~ 0.48 keV / 0.7 a.u.) placed at a scattering angle (θ) of ~ 150°; recoiled electrons are detected by a micro-channel-plate electron detector mounted at ϕ ~ 12.5°. The energy of the incident X-rays is 65.0 keV. The average energies of Compton-scattered X-rays and recoiled electrons are 52.5 and 12.5 keV, respectively. The electron energy is measured by a time-of-flight method. The photodiode used to obtain a timing trigger is placed at the upper side of the incident X-rays. The path length of the electron flight is 2.00 m, and the time resolution of the system is ~ 230 ps, which comes from the bunch length and the time resolution of the electronics. The over-all electron energy resolution is 0.19 keV, which is much better than that by a photon detector, and a 0.3 a.u. momentum space resolution can be achieved.

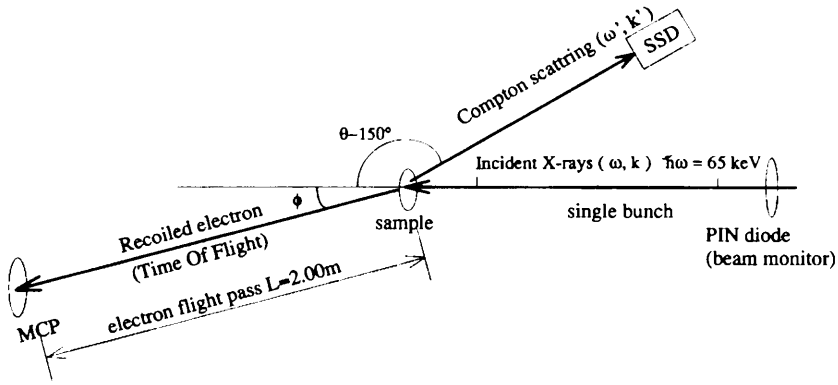

Fig. 23 Schematic view of the (X, eX) coincidence spectrometer system.

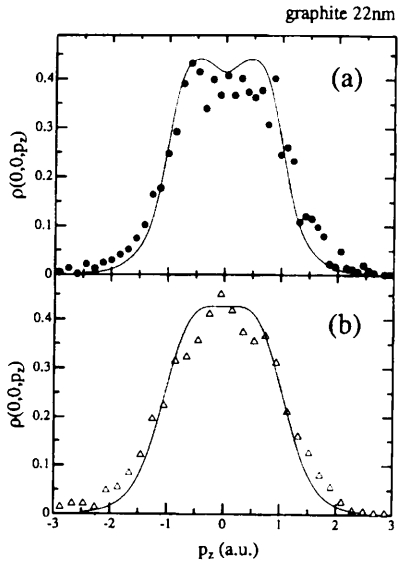

Fig.24 3D-EMD; ρ(0, 0, pz) of graphite obtained by the energy-measurements of (a) recoiled electron and (b) Compton scattered X-ray photon. The solid line is from convoluted EMD calculations of Gao *et al.*[1] obtained within a mixed-basis pseudo-potential approach.

Figures 24(a) and (b) show an example of a comparison between the 3D-EMDs ρ(0, 0, pz) of graphite obtained by measurements of the energies on the recoiled electrons and Compton scattered X-rays, respectively. The solid lines are the EMD calculations by Gao *et al.*,[1] obtained within a mixed-basis pseudo-potential approach. These lines are already convoluted with the experimental resolutions: 0.3 a.u. and 0.7 a.u., respectively. There is a remarkable difference between both experimental data at the region near to $p_z \sim 0$ in Figs. 24(a) and (b). The data in Fig. 24(a) clearly show a flat-top profile; on the other hand, those in Fig. 24(b) show a Gaussian-like peak profile. This fact can be understood based on the difference in the momentum space resolution; these data are in good agreement with the theoretical calculations within the statistical accuracy. Furthermore, in the present system, a measurement of the energies for Compton-scattered photon and the recoiled election tells us which electron state the coincident event comes from by using an energy conservation law and the binding energy. A preliminary experiment has been carried out, and the possibility of state-selective 3D-EMD has been demonstrated. The details concerning these are presented in the "Users' Reports" section of this volume.[2]

References

1) C. Gao, A. L. Ritter, J. R. Dennison, and N. A. Holzwarth, Phys. Rev. B 37 (1988) 3914.
2) M. Itou, S. Kishimoto, H. Kawata, K. Eu, H. Nagamori, H. Sakurai, and F. Itoh, in this volume.

7. A MULTI-ELEMENT SSD FOR FLUORESCENT XAFS (BL-12C)

Fluorescent XAFS is a powerful tool for studying the structure of dilute samples, such as a dopant in materials, biological samples etc. Ionization chambers designed for fluorescent XAFS are usually used[1] combined with a filter/slit system. However, the fluorescent signal is buried in the scattering background etc. when the concentration of the species of interest decreases.

If the fluorescent signal can be separated from other background, the quality of the XAFS spectrum is improved. A 19-element pure germanium solid state detector (SSD) was introduced in BL-12C in 1995 for this purpose. The idea is similar to the pioneering multi-SSD developed by Cramer *et al.*[2] However, it has been improved in some points, as described below:

i) The counting rate of the system is much higher in order to meet the high flux obtained at BL-12C.[3]
ii) The energy resolution is better.
iii) The system is compact so as to fit in the narrow experimental area.
iv) The live time of the system is correctly evaluated in order to correct for the counting loss of the system.

A photograph of the detector is shown in Fig. 25. Nineteen pure Ge detectors having a diameter of 11 mm each (Canberra GL0110P) are arranged. Pentafet preamplifiers (®Link) are used in order to increase the throughput without sacrificing the energy resolution. All of the preamplifiers are reset simultaneously when a reset signal is generated, which is controlled by a preamplifier reset control (PRC) module. This is important to evaluate the live time of the preamplifiers correctly. The output of the preamplifiers are treated as usual, and finally counted by CAMAC scalers. The scalers and a timer idle during the reset period of the preamplifiers, which is also controlled by PRC.

The average energy resolution was 147 and 246 eV for Mn Kα X-ray from ^{55}Fe when the shaping time of spectroscopy amplifiers were set to 6 and 0.25 μs, respectively. Here, the ICRs (incoming count rate)

Fig. 25 Photograph of the 19-element SSD. 19 Pentafet preamplifiers and a high-voltage buffer are arranged below the cryostat.

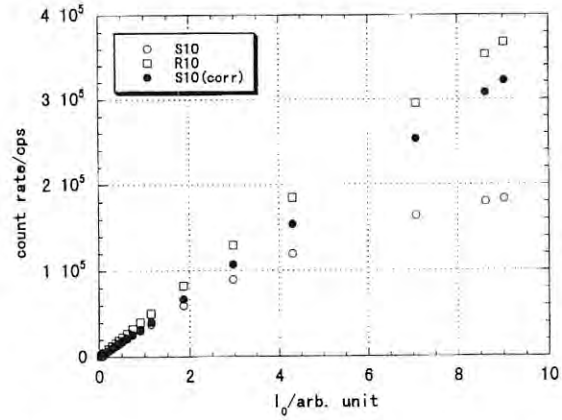

Fig. 26 Relationship between raw windowed fluorescent count rate (S10), incoming count rate (R10) and I0 measured by an ionization chamber (I_0). The windowed fluorescent count corrected for deadtime (S10(corr)) is also included.

were set to 6 and 50 kcps, respectively.

The throughput of the system was measured by counting the Cu Kα fluorescent X-rays from a copper foil irradiated by monochromatic X-rays. The incoming X-ray intensity was controlled by adjusting the opening of a slit placed after the focusing mirror and monitored by an ionization chamber. The counting loss is usually corrected by relying on the linearity of ICR. However, it is found that ICR is not exactly linear, and whose deadtime cannot be neglected when a short shaping time, such as 0.25 μs, is used. Therefore, the deadtime of ICR was also evaluated as well as that due to the spectroscopy amplifier etc. An example of the throughput and that corrected for both deadtimes are shown in Fig. 26. As shown in the figure, this system can be used up to 350 kcps/ch, which corresponds to 6.6 Mcps in total. Applications of this detector can be found in the "Users' Reports" section.

References

1) F. W. Lytle, R. B. Greegor, D. R. Sandstrom, E. C. Marques, J. Wong, C. L. Spiro, G. P. Huffman and F. E. Huggins, Nucl. Instrum. Methods, **226** (1984) 542.
2) S. P. Cramer, O. Tench, M. Yocum and G. N. George, Nucl. Instrum. Methods, A**266** (1988) 586.
3) M. Nomura and A. Koyama, KEK Report 95-1 (1995).

8. A FAST DETECTOR USING STACKED AVALANCHE PHOTO DIODES FOR X-RAY DIFFRACTION EXPERIMENTS

A fast detector was developed using stacked avalanche photodiodes (APDs) for X-ray diffraction experiments, particularly for an electron-density study. In the experimental approach, several kinds of effects limit the accuracy of the observed structure factors. They are extinction, multiple scattering, absorption, counting statistics, thermal diffuse scattering, etc. Regarding the counting statistics, if we use a detector that has a wide linearity, we can obtain a better accuracy without using attenuators and a careful correction for the dead time of the counting system. The detectors using APDs are just suitable for this purpose since they have a fast output of nanoseconds and a low-noise property.[1)]

The counting system with the APD detector was installed at beamline BL-14A in April, 1996. Figure 27 schematically shows the system.[2)] The detector has four avalanche photodiodes stacked parallel to the direction of the incident beam. Each device has a detection area of 2.8 mm in diameter and a depletion region of 120 μm thickness. On the opposite side of the n+ -p junction, the wafer was etched from the surface, and only a thin dead layer of the p+ layer remains there. Thus, the X-ray beam can go through the device. By stacking four APD plates, we can obtain an efficiency of 54% in total at 16.53 keV. This is

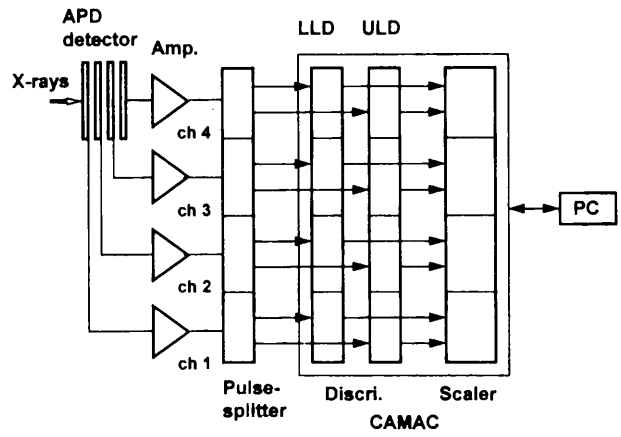

Fig. 27 Counting system with an APD detector.

three-times as large as that for a single device.

Four fast amplifiers were used for amplifying the signal from each APD. The APD devices were contained in a small stainless-steel chamber with a beryllium window 130 μm thick. The chamber and amplifiers were mounted together on a 2θ arm of the four-circle diffractometer at BL-14A. The signal from each amplifier was processed by a pulse-splitter to obtain two signals that have just the same waveform. They were sent to individual channels of a discriminator. By setting both the low- and high-levels for discrimination, we could record the counts between a width in pulse height for each channel with a counter. Setting the threshold levels of the discriminators and reading data in each channel of the counter were controlled by a personal computer with CAMAC.

The behavior of the system was measured with 16.53-keV (0.75 Å) X-rays in the multi-bunch mode of the PF ring. The width of the amplifier output was only 3.2 ns at the bottom width. The width of the discriminator output was set to a minimum, 1.7 ns at the half width, and the pulse-pair resolution was 3.3 ns. The maximum counting rate of the counter was 300 MHz. As a result, the upper limit of the linearity was more than 10^8 counts/s. The sum of the outputs for each channel had a saturation of 4.5×10^8 counts/s at input rates higher than 1.0×10^9 photons/s since the saturation of each channel was 1.14×10^8 counts/s. Thus, a dynamic rage of more than 10^{10} was obtained because the noise level of the APD detector was less than 10^{-2} counts/s.

We next obtained the R factors by the APD detector and by a NaI(Tl) scintillation detector with attenuators. A silicon single crystal of 70 μm in diameter was used as a sample for the evaluation. The integrated intensity of the diffraction peaks was measured at 16.53 keV. The number of observed reflections reached 1300. Thus, the R factor by the APD detector was given by 0.0056 and that by NaI with attenuators was 0.0153 for 60 independent reflections. This result shows us that the APD detector enables a simple and accurate measurement of the reflection intensities without attenuators and a dead-time correction.

References

1) S. Kishimoto, Rev. Sci. Instrum. 66 (1995), 2314.
2) S. Kishimoto, N. Ishizawa and T. P. Vaalsta, KEK Proceedings 97-8 (1997), 254

C. SUMMARY OF EXPERIMENTAL STATION AND BEAMLINE OPTICS

Figures 28 and 29 are the latest plan views of the SR laboratory area of the PF and AR, respectively, schematically showing the arrangement of the experimental stations now in operation.

Tables 2 and 3 summarize the experimental stations in operation at the PF 2.5-GeV ring and AR (6.5 GeV) with the names of the spokespersons. The basic characteristics of X-ray beamlines are listed in Table 4 and the types of monochromators for VUV and soft X-ray beamlines are summarized in Table 5.

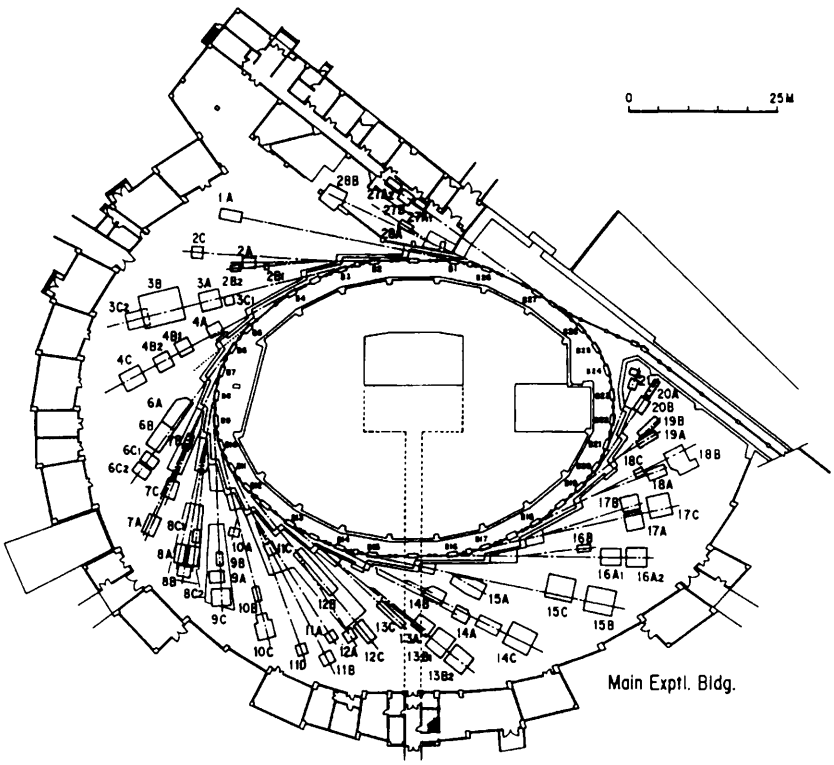

Fig. 28 Plan view of the experimental hall of PF 2.5-GeV storage ring.

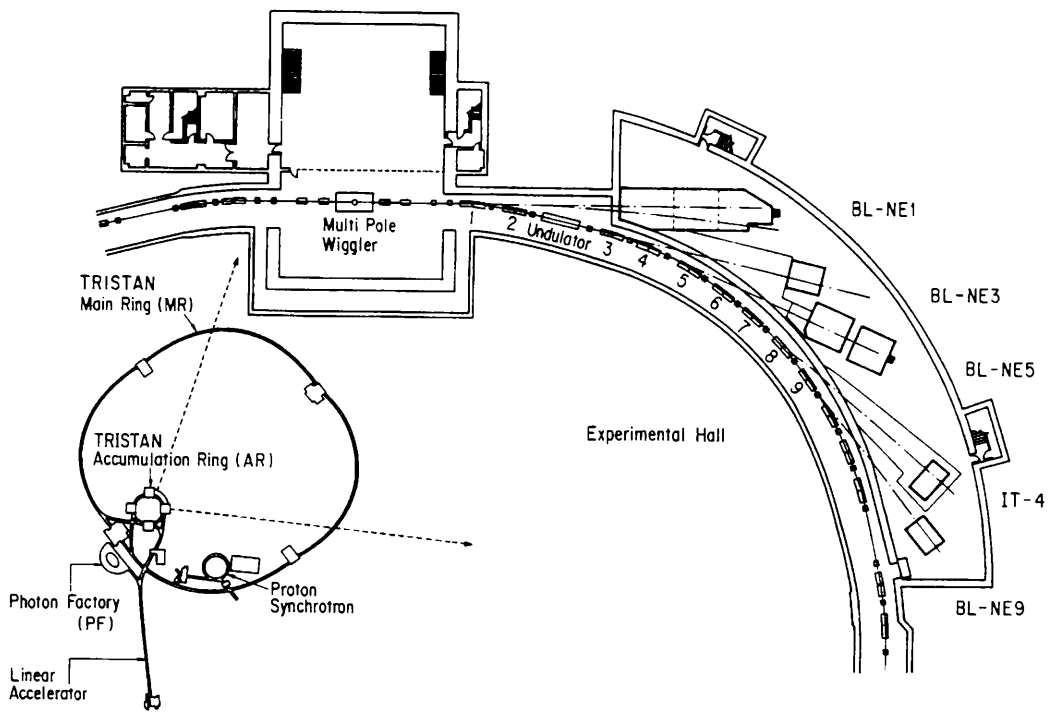

Fig. 29 Plan view of the synchrotron radiation laboratory area of the TRISTAN Accumulation Ring (AR).

Table 2 List of Experimental Stations at PF Storage Ring

Experimental Station		Spokesperson
BL-1		
A	[NTT] Solid surface analysis	S. Maeyama [NTT] A. Yagishita (until Mar. '97) H. Kato (since Apr. '97)
BL-2	(Undulator)	
A	Soft X-ray spectroscopy	Y. Kitajima
B1	Soft X-ray microscopy (until Mar. '97)	Y. Azuma (until Mar. '97)
B2	Soft X-ray spectroscopy (until Mar. '97)	Y. Azuma (until Mar. '97)
C	Soft X-ray spectroscopy	M. Watanabe
BL-3		
A	X-ray diffraction and scattering	M. Tanaka
B	VUV and soft X-ray spectroscopy	E. Shigemasa (until Mar. '97) Y. Azuma (since Apr. '97)
C1	X-ray diffraction	H. Kawata
C2	X-ray topography in milli-Kelvin region (for solid helium) (until Mar. '97)	H. Kawata
C2	X-ray magnetic Bragg scattering by means of white X-rays (since Apr. '97)	H. Kawata
BL-4		
A	Trace element analysis, X-ray microprobe	A. Iida
B1	Micro-crystal and -area structure analysis	K. Ohsumi
B2	Powder diffraction	K. Ohsumi
C	X-ray diffraction	Y. Murakami
BL-6		
A	Macromolecular crystallography by Weissenberg camera	N. Watanabe (until Mar. '97) N. Igarashi (since Apr. '97)
B	[TARA] Macromolecular crystallography by Weissenberg camera	N. Sakabe [TARA], M. Suzuki
C1	X-ray diffraction at low temperatures	O. Shimomura (until Mar. '97) Y. Murakami (since Apr. '97)
C2	Accurate lattice spacing measurement	M. Ando
BL-7		
A	[RCS] Soft X-ray photoelectron spectroscopy	H. W. Yeom [RCS], K. Ito
B	[RCS] Surface photochemical reaction and angle resolved photoelectron spectroscopy	H. W. Yeom [RCS], K. Ito
C	X-ray spectroscopy and diffraction	M. Nomura
BL-8		
A	[Hitachi] Soft X-ray spectroscopy	Y. Hirai [Hitachi], A. Yagishita
B	[Hitachi] EXAFS	Y. Hirai [Hitachi], A. Yagishita
C1	[Hitachi] X-ray lithography	Y. Hirai [Hitachi], A. Yagishita
C2	[Hitachi] X-ray tomography and X-ray microscopy	Y. Hirai [Hitachi], A. Yagishita
BL-9		
A	XAFS	M. Nomura
B	[NEC] Photochemical reaction	I. Nishiyama [NEC], M. Nomura
C	[NEC] EXAFS and X-ray topography/diffraction	H. Kimura [NEC], M. Nomura
BL-10		
A	X-ray diffraction/scattering, crystal structure analysis	M. Tanaka
B	XAFS	N. Usami
C	Small-angle X-ray scattering of enzymes, surface diffraction	K. Kobayashi
BL-11		
A	Soft X-ray spectroscopy	Y. Kitajima
B	Surface EXAFS, soft X-ray spectroscopy	Y. Kitajima
C	VUV spectroscopy (solid state)	H. Kato
D	Angle-resolved photoelectron spectroscopy	K. Ito

Experimental Station		Spokesperson
BL-12		
A	Characterization of VUV-SX optical elements, soft X-ray spectroscopy	T. Miyahara (until Sep. '96) K. Ito (since Oct. '96)
B	VUV high-resolution spectroscopy	K. Ito
C	XAFS	M. Nomura
BL-13	(Multipole wiggler/Undulator)	
A	Accurate lattice parameter measurement	O. Shimomura (until Mar. '97) T. Kikegawa (since Apr. '97)
B1	Surface-sensitive XAFS, X-ray diffraction	O. Shimomura (until Mar. '97) T. Kikegawa (since Apr. '97)
B2	High pressure & high temperature X-ray diffraction	O. Shimomura (until Mar. '97) T. Kikegawa (since Apr. '97)
C	[NIMC] Soft X-ray photoemission spectroscopy and XAFS	A. Nishijima [NIMC] A. Yagishita (until Mar. '97) E. Shigemasa (since Apr. '97)
BL-14	(Vertical wiggler)	
A	Crystal structure analysis, EXAFS	S. Kishimoto
B	High-precision X-ray optics	K. Hirano
C	General purpose (X-rays)	O. Shimomura (until Mar. '97) K. Hyodo (since Apr. '97)
BL-15		
A	Small-angle X-ray scattering of muscle and alloys	K. Hirano
B	White X-ray topography and X-ray magnetic Bragg scattering	H. Kawata
C	High-resolution X-ray diffraction	K. Hirano
BL-16	(Multipole wiggler/Undulator)	
A	General purpose (X-rays)	K. Takeshita (until Sep. '96) H. Kawata (since Oct. '96)
B	Soft X-ray spectroscopy	E. Shigemasa
BL-17		
A	[Fujitsu] XAFS	S. Komiya [Fujitsu], A. Iida
B	[Fujitsu] Photochemical vapor deposition	S. Komiya [Fujitsu], A. Iida
C	[Fujitsu] Grazing incident X-ray diffraction, X-ray fluorescence analysis	S. Komiya [Fujitsu], A. Iida
BL-18		
A	[ISSP] Angle-resolved photoelectron spectroscopy of surfaces and interfaces	A. Kakizaki [ISSP] T. Miyahara (until Sep. '96) A. Yagishita (since Oct. '96)
B	Macromolecular crystallography (Weissenberg and Laue)	N. Watanabe
C	X-ray powder diffraction at non-ambient conditions	O. Shimomura (until Mar. '97) T. Kikegawa (since Apr. '97)
BL-19	(Revolver undulator)	
A	[ISSP] Spin-resolved photoelectron spectroscopy (Mott detector)	A. Kakizaki [ISSP] T. Miyahara (until Sep. '96) A. Yagishita (since Oct. '96)
B	[ISSP] Spin-resolved photoelectron spectroscopy (SPLEED) [ISSP] Soft X-ray emission spectroscopy	A. Kakizaki [ISSP] S. Shin [ISSP] T. Miyahara (until Sep. '96) A. Yagishita (since Oct. '96)
BL-20		
A	VUV spectroscopy	K. Ito
B	[ANBF] White and monochromatic beam general purpose X-ray station	G. Foran [ANBF], K. Ohsumi

Experimental Station		Spokesperson
BL-21	[Light Source Division] Beam position monitoring	T. Katsura [Light Source Div.]
BL-27	(Beamline for experiments using radioisotopes)	
A	Radiation biology, soft X-ray photoelectron spectroscopy	K. Kobayashi
B	Radiation biology, X-ray diffuse scattering	K. Kobayashi
BL-28	(Elliptical multipole wiggler/Undulator)	
A	VUV and soft X-ray spectroscopy with circularly polarized undulator radiation	T. Miyahara (until Sep. '96) T. Koide (since Feb. '97)
B	Spectroscopy and scattering with polarized X-rays	T. Iwazumi

NTT Nippon Telegraph and Telephone Corporation
TARA Tsukuba Advanced Research Alliance
RCS Research Center for Spectrochemistry, The University of Tokyo
NIMC National Institute of Materials and Chemical Research, Agency of Industrial Science and Technology
ISSP Institute for Solid State Physics, The University of Tokyo
ANBF Australian National Beamline Facility

Table 3 List of Experimental Stations at AR

Experimental Station		Spokesperson
BL-NE1	(Elliptical multipole wiggler/Undulator)	
A1	High resolution Compton and magnetic Compton scattering	H. Kawata
A2	Spectroscopy and scattering with circularly polarized X-rays	T. Iwazumi
B	Spectroscopy and microscopy with circularly polarized soft X-rays	Y. Kagoshima (until Sep. '96) T. Koide (since Feb. '97)
BL-NE3	(Undulator)	
A1	Nuclear resonant scattering	X. Zhang
A2	Surface and interface diffraction (until Mar. '97)	H. Sugiyama (until Mar. '97)
BL-NE5		
A	Angiography and X-ray computed tomography	K. Hyodo
C	High pressure and high temperature X-ray diffraction	T. Kikegawa
BL-NE9		
B	[Accelerator Department] Vacuum science and technology	K. Kanazawa [Acc. Dept.]

Table 4 X-Ray Beamline Optics

Branch Beam Line	Acceptance Horiz. (mrad)	Beam Size (H × V) (mm)	Photon Flux at Sample Position	Type of Monochromator	Energy Resolution ($\Delta E/E$) $\times 10^{-4}$	Photon Energy (keV)	Mirror	Reference
BL-3A	4	100×5 4×0.1		Double Crystal Si(111) Sagittal Focusing	~ 2	4 ~ 25	Collimating and Focusing Mirrors (Fused Quartz)	1 - 3
BL-3C1/C2	2	20×4		None		4 ~ 30	None	4, 5
BL-4A	6	50×4 4×1		Double Crystal Sagittal Focusing	~ 2	4 ~ 20	None	6
BL-4B1	4.5	50×5		Double Crystal Si(111)	~ 2	4 ~ 35	None	7
BL-4B2	4.5	50×5		Double Crystal Si(111)	~ 2	4 ~ 35	Bent Cylinder	
BL-4C	3	1.0×0.6		Flat Double Crystal Si (111)	~5	6~23	Bent Cylinder	8, 9
BL-6A	4	2.5×1		Bent Si(111) (α = 0, 6.0°, 7.8°, 9.5°, 11.4°, 13.7°, 16.5°)		5 ~ 25	Bent Plane Fused Quartz	10
BL-6B	4	8×1	1×10^{10}/6mm^2 (8 keV, 300 mA) (1×10^{11} when focused)	Double Crystal Si(220), Si(111), Si(311) Sagittal Focusing with Si(111)	~ 2	4 ~ 25 (4 ~ 13)	None	11 - 13
		1.7×0.2		Bent Si(111) α = 7.8°			Bent Plane Si Pt-coated	(Since Apr. '96) 14
BL-6C1	4	37×5		None		8 ~ 30		4, 5, 15
BL-6C2	0.5	5×5		Channel-Cut Si (111)	7.5	8 ~ 33	None	
BL-7C	4	8×1	1×10^{10}/6mm^2 (8 keV, 300 mA) (1×10^{11} when focused)	Double Crystal Si (111) Sagittal Focusing	~ 2	4 ~ 20 (4 ~ 13)	Double Mirror Fused Quartz Focusing	11 - 13
BL-8C1/C2	5	50×5	6×10^{8}/mm^2 (10 keV, 300 mA)	Channel-Cut Si(220), Si(111), Si(400)	~ 2	5 ~ 40	None	
BL-9C	5	150×5		Double Crystal Si(111) Sagittal Focusing	~ 2	5 ~ 25	None	

Branch Beam Line	Acceptance Horiz. (mrad)	Beam Size (H × V) (mm)	Photon Flux at Sample Position	Type of Monochromator	Energy Resolution ($\Delta E/E$) $\times 10^{-4}$	Photon Energy (keV)	Mirror	Reference
BL-10A	1	10×3		Si(111), Si(311) Quartz(100), PG(002) Curved Si(111) (α ~ 4°, 8°)	50 ~ 5	5 ~ 25	None	16
BL-10B	2	8×1	$1\times10^{9}/7mm^{2}$ (10 keV, 300 mA)	Channel-Cut Si(311)	1	6 ~ 30	None	
BL-10C	4	6×1.5	$\sim10^{10}/9mm^{2}$ (8 keV, 100 mA)	Double Crystal Si(111)	2	4 ~ 10	Bent Cylinder	
BL-12C	2	1.3×0.6	$5\times10^{10}/1mm^{2}$ (8.0 keV, 300mA) w.Si(111)	Double Crystal Si(111) Si(311)	~ 2	6~23	Bent Cylinder	17
BL-13A	1			Double Crystal Si(220)	~ 0.1	4 ~ 30	None	18
BL-13B1/B2	4	4×1		Double Crystal Si(111), Si(220) Sagittal Focusing	~ 2	4 ~ 30	Bent Plane Fused Quartz	18
BL-14A	1.28 (Vertical)	2×1 at focus 5×38		Double Crystal Si (111) Si (311) Si (553)	2	5.1 ~ 19.1 9.9 ~ 35.6 22.7 ~ 84.5	Bent Cylinder Pt-coated Fused Quartz	19
BL-14B	2.2 (Vertical)	5×30		Double Crystal Si(111), Si(220), Si(311)	2	5.2 ~ 57	None	
BL-14C	1.3 (Vertical)	10×40		Double Crystal Si(111), Si(220)	2	5.5 ~ 69	None	
BL-15A	2	0.7×0.8 at focus	$9\times10^{10}/6mm^{2}$ (8.0 keV, 150 mA)	Bent Crystal Ge(111) (α = 8.0°)	~ 10	5.6 ~ 12.4	Bent Plane, Fused Quartz	20
BL-15B	0.14	5×5		None		3.5 ~ 34	None	
BL-15C	2	60×6		Double Crystal Si(111)		4 ~ 30	None	
BL-16A	1	2.4×0.2	$\sim1\times10^{13}$ (8.3 keV, 300 mA)	Double Crystal Si(111) Sagittal Focusing	~ 1	4 ~ 25	Bent Plane (Pt on SiC) for Vertical Collimating Bent Plane (Pt on SiO_2) for Vertical Focusing	21

Branch Beam Line	Acceptance Horiz. (mrad)	Beam Size (H × V) (mm)	Photon Flux at Sample Position	Type of Monochromator	Energy Resolution ($\Delta E/E$) $\times 10^{-4}$	Photon Energy (keV)	Mirror	Reference
BL-17A	4	100×10		Double Crystal Si(111)	~ 2	5 ~ 13	None	22
BL-17C	1	20×5		Double Crystal Si (111)	~ 2	5 ~ 13	None	23
BL-18B	2	1.2×0.4	1.1×10^{10} (12.4 keV, 300 mA) Si(111)	Double Crystal Si(111) Si(220) Ge(111) Ge(220)	~ 2	6 ~ 30	Bent Cylinder Fused Quartz, Pt-coated	24
BL-18C	1	0.07×0.04		Double Crystal Si(111)	~2	6~25	Cylinder Fused Quartz, Pt-coated (H,V)	
BL-20B	2	26×3		① Channel Cut Si(111) ② Double Ctystal Sagittal focusing Si(111)	~ 2	4 ~ 25	None	25
BL-27B	4	100×10		Double Crystal Si(111)	~ 2	4 ~ 20	None	26
BL-28B	H: 4 V: 0.2	2.4×0.3	3×10^{10} (9 keV, 300 mA) Si (220) Pc ~ 0.5	Double Crystal Si(111) Si(220) InSb(111)	3 (at 6.3 keV)	2 ~ 10	Pre-mirror Bent Cylinder Si Pt- & Ni-coated Post-mirror Bent Plane Fused Quartz Pt- & Ni-coated	27
BL-NE1A1	2	2×0.5	5×10^{12} (60 keV, 35mA)	Double Bent Crystal Si(111)	8 (at 60 keV)	40 ~ 180		28, 29
BL-NE1A2	2	80×4 3×4 3×0.5		Double Crystal Si(111) Sagittal Focusing Si(111) Sagittal Focusing + Bent Mirror	2	6 ~ 28		28, 30
BL-NE3A1 3A2	H:0.3 V:0.03	15×2	1×10^{3} (14.4 keV)	Double Crystal Si(111) High-resolution Monochromator Nuclear Monochromator of Single Crystal $^{57}Fe_2O_3$(777)	1 5×10^{-3} 1×10^{-7}	5 ~ 25 8 ~ 26 14.4		31

Branch Beam Line	Acceptance Horiz. (mrad)	Beam Size (H × V) (mm)	Photon Flux at Sample Position	Type of Monochromator	Energy Resolution ($\Delta E/E$) $\times 10^{-4}$	Photon Energy (keV)	Mirror	Reference
BL-NE5A	10	150×8	5×10^{8} (33.2 keV)	Asym.Cut Single Crystal Si(311) ($\alpha = 4° \sim 6°$)	60	20 ~ 40		32, 33
				Double Crystal Si (311)	1	25 ~ 70		
BL-NE5C	3	60×5		Double Crystal Si (111)	1	30~ 100		34

References

1) S. Sasaki et al., Rev. Sci. Instrum. **63** (1992) 1047.
2) K. Kawasaki et al., Rev. Sci. Instrum. **63** (1992) 1023.
3) T. Mori and S. Sasaki, Rev. Sci. Instrum. **66** (1995) 2171.
4) T. Nakajima et al., Nucl. Instrum. Meth. A**261** (1987) 308.
5) T. Nakajima et al., Rev. Sci. Instrum. **66** (1995) 1440.
6) A. Iida et al., Rev. Sci. Instrum. **66** (1995) 1373.
7) K. Ohsumi et al., Rev. Sci. Instrum. **66** (1995) 1448.
8) H. Iwasaki et al., Rev. Sci. Instum. **60** (1989) 2406.
9) Photon Factory Activity Report 1995 #13 (1996) E-1.
10) N. Sakabe et al., Rev. Sci. Instrum. **66** (1995) 1276.
11) M. Nomura and A.Koyama, KEK Internal 93-1 (1993).
12) M. Nomura et al., KEK Report 91-1 (1991).
13) M. Nomura and A. Koyama, in " X-ray Absorption Fine Structure" , ed. by S. S. Hasnain, Ellis Horwood, Chichester, 1991, p.667.
14) Photon Factory Activity Report 1995 #13 (1996) C-1.
15) Photon Factory Activity Report 1982/83 (1984) V-25.
16) S. Sasaki, Rev. Sci. Instrum. **60** (1989) 2417.
17) M. Nomura and A. Koyama, KEK Report 95-15 (1996).
18) Photon Factory Activity Report 1994 #12 (1995) C-6.
19) Y. Satow and Y. Iitaka, Rev. Sci. Instrum. **60** (1989) 2390.
20) Y. Amemiya et al., Nucl. Instrum. Meth. **208** (1983) 471.
21) Photon Factory Activity Report 1994 #12 (1995) E-3.
22) Photon Factory Activity Report 1988 #6 (1988) I-15.
23) Y. Horii et al., Rev. Sci. Instrum. **66** (1995) 1370.
24) N. Watanabe et al., Rev. Sci. Instrum. **66** (1995) 1824.
25) R. F. Garret et al., Rev. Sci. Instrum. **66** (1995) 1351.
26) H. Konoshi et al., Nucl. Insrtum. Meth. A**372** (1996) 322.
27) T. Iwazumi et al., Rev. Sci. Instrum. **66** (1995) 1691.
28) H. Kawata et al., Rev. Sci. Instrum. **60** (1989) 1885.
29) Photon Factory Activity Report 1994 #12 (1995) E-4.
30) T. Iwazumi et al., Rev. Sci. Instrum. **63** (1992) 419.
31) X. Zhang et al., Rev. Sci. Instrum. **63** (1992) 404.
32) K. Hyodo et al., Handbook on SR **IV**, (1991) 55.
33) Y. Itai et al., Rev. Sci. Instrum. **66** (1995) 1385.
34) T. Kikegawa et al., Rev. Sci. Instrum. **66** (1995) 1335.

Table 5 VUV and Soft X-ray Beamline Optics

Branch Beamline	Acceptance Horiz./Vert. (mrad)	Type of Monochromator	Grating Groove Density (l/mm)	Photon Energy (eV)	Beam Size (mm)	Typical Resolving Power (E/ΔE) and Photon Flux (/s)	Reference
BL-7B (RCS)	6 4	1m Seya-Namioka	1200 2400	5 ~ 50	1 × 1	1000	1
BL-11C	4.8 3	1m Seya-Namioka	1200	4 ~ 35	~1 ϕ	1000	2
BL-12B	5 3.6	6.65 m Off-Plane Eagle	1200 4800	5 ~ 30	——	2.5×10^5 10^4	3 - 5
BL-20A	28 5	3m Normal Incidence	1200 2400	5 ~ 40	2 × 1	3000 ~ 30000 10^{12} ~ 10^8	6
BL-1A (NTT)	4 0.5	Grating/Crystal	1200 2400	50 ~ 900	4 × 1	500	7
BL-2B2 Undulator	K = 0.55 ~ 2.2 λ_u = 6 cm	Grazing Incidence R = 10 m α = 89°	1200 2400	250 ~ 1600	< 0.2 ϕ	500 ~ 5000	8 - 10
BL-2C Undulator	K = 0.55 ~ 2.2 λ_u = 6 cm	Varied-Space Plane Grating	1000 2200	250 ~ 1400	0.9 × 0.1	5000 ~ 10000 10^{11} ~ 10^{10}	
BL-3B	10 2	Grazing Incidence R = 24 m α+β = 165°	200 600 1800	10 ~ 280	< 2 ϕ	200 ~ 3000 10^{12} ~ 10^9	11, 12
BL-7A (RCS)	6 1	Plane Grating	1200 2400	10 ~ 1000	2 × 1	500	13
BL-8A (Hitachi) (~ Jun. '96)	0.5 1	Varied-Space Plane Grating	800 2400	40 ~ 1800	5 × 1	1000	14
BL-8A (Hitachi) (Oct. '96 ~)	0.5 1	SX700 Plane Grating	1221	38 ~ 2300	5 × 1	2000 10^{10}	
BL-11A (~ Dec. '95)	1 0.5	Grazing Incidence R = 2 m α = 88° Grasshopper Mark VII	600 1200 2400	40 ~ 1000	< 1 ϕ	200 ~ 2000	15
BL-11A (Apr. '96 ~)	5 1	Varied-Line-Space Plane Grating	300 800	80 ~ 1200	2 × 1	500 ~ 5000 10^{12} ~ 10^9	16
BL-11D (~ Dec. '95)	1.5 2	Grazing Incidence R = 2 m α+β = 154°	600 1200 2400	20 ~ 150	1.5 ϕ	100 ~ 1500	17
BL-11D (Apr. '96 ~)	4 2	Grazing Incidence On-blaze Mount R_1 = 52.5 m R_3 = 22.5 m	2400	G_3 20~280 G_1 200~1200			
BL-12A	2.2 0.34	Grazing Incidence R = 2 m α = 88°	1200	30 ~ 1000	2 × 3	1000 10^9	18
BL-13C Undulator	K = 0.3 ~ 4.2 λ_u = 18 cm	Grazing Incidence R = 50 m α+β = 173.2°	750	140 ~ 1000	5 × 1	1000 ~ 6000 10^{12} ~ 10^{10}	19, 20
BL-16B Undulator	K = 0.5 ~ 5.75 λ_u = 12 cm	Grazing Incidence R = 24 m α+β = 168.6°	400 900 2000	40 ~ 550	< 1 ϕ	1000 ~ 10000 10^{12} ~ 10^{10}	21, 22

Branch Beamline	Acceptance Horiz./Vert. (mrad)	Type of Monochromator	Grating Groove Density (l/mm)	Photon Energy (eV)	Beam Size (mm)	Typical Resolving Power (E/ΔE) and Photon Flux (/s)	Reference
BL-18A (ISSP)	2 2	Grazing Incidence R = 3 m α+β = 160° R = 6.65 m α+β = 167.5°	300 600 1200 500	7 ~ 150	< 1 φ	1000~2000 10^{11} ~	23
BL-19A Revolver Undulator (ISSP)	K = 1.0 ~ 9.0 λ_u = 16.4 cm K = 0.5 ~ 1.25 λ_u = 5 cm	Grazing Incidence R = 2 m α+β = 160° R= 4 m α+β = 170°	600 1200 600 1200	12 ~ 250	< 0.7 φ	1000 10^{12}	24, 25
BL-19B Revolver Undulator (ISSP)	K = 0.5 ~ 2.5 λ_u = 7.2 cm K = 1.0 ~ 5.0 λ_u = 10 cm	Varied-space Plane Grating	800 2400	10 ~ 1200	< 0.5 φ	400~4000 10^{12} ~10^{11}	24
BL-28A Helical Undulator	K_x = 0.23 ~ 3 K_y = 0.23 ~6 λ_u = 16 cm	Grazing Incidence R = 2 m α+β = 160° R = 4 m α+β = 170°	600 1200 600 1200	15 ~ 250	< 0.5 φ	1000 10^{10}	26
BL-NE1B Helical Undulator	K_x = 0.2 ~ 3 K_y = 0.2 ~6 λ_u = 16 cm	Grazing Incidence R = 10m β = 89°	1200 2400	250 ~ 1800	~ 0.8 × 0.2	1000~5000 10^{11} ~10^{9}	27, 28
BL-1A (NTT)	4 0.5	Grating/Crystal InSb (111) Si (111)	____	1800 ~ 4000	4 × 1	2000	7, 29
BL-2A Undulator	K = 0.5 ~ 2.2 λ_u = 6 cm	Double Crystal InSb (111) Si (111)	____	1760 ~ 5000	< 1 φ	8000 10^{10}	8, 30, 31
BL-8B (Hitachi)	3 0.5	Double Crystal InSb (111) Si (311)	____	1700 ~ 14000	1.9 × 0.5	5000	32
BL-11B	4 0.6	Double Crystal InSb (111), Ge (111)	____	1760 ~ 3910	5 × 2	2000 10^{10}	31, 33, 34
BL-27A	5 0.5	Double Crystal InSb (111)	____	1800 ~ 6000		2000	35
BL-2B1 Undulator	K = 0.55 ~ 2.2 λ_u = 6 cm	Zone Plate	____	400 ~ 830	~ 0.01 φ	50	36 - 38
BL-9A* (NEC)	5 0.3	Oscillating Mirror	____	____	____	____	39
BL-9B (NEC)	10	Plane + Toroidal Mirrors	____	____	15 × 20	____	39
BL-17B (Fujitsu)	8 1	Toroidal Mirror	____	____	10 × 1	____	____

* shut down at the end of 1995

References

1) H. Namba et al., Rev. Sci. Instrum. **60** (1989) 1917.
2) Photon Factory Activity Report 1982/1983,(1984) V-15.
3) K. Ito et al., Appl. Opt. **25** (1986) 837.
4) K. Ito et al., Appl. Opt. **28** (1989) 1813.
5) K. Ito and T. Namioka, Rev. Sci. Instrum. **60** (1989) 1573.
6) K. Ito et al., Rev. Sci. Instrum. **66** (1995) 2119.
7) T. Kawamura et al., Rev. Sci. Instrum. **60** (1989) 1928.
8) H. Maezawa et al., Nucl. Instrum. Meth. A**246** (1986) 310.
9) H. Maezawa et al., Rev. Sci. Instrum. **60** (1989) 1889.
10) A. Yagishita et al., Rev. Sci. Instrum. **63** (1992) 1351.
11) A. Yagishita et al., Nucl. Instrum. Meth. A**306** (1991) 578.
12) S. Masui et al., Rev. Sci. Instrum. **63** (1992) 1330.
13) H. Namba et al., Rev. Sci. Instrum. **60** (1989) 1909.
14) M. Itou et al., Appl. Opt. **28** (1989) 146.
15) M. Yanagihara et al., KEK Report 84-17 (1984).
16) K. Amemiya et al., J. Synchrotron Rad. **3** (1996) 282.
17) T. Miyahara et al., Jpn. J. Appl. Phys. **24** (1985) 293.
18) Photon Factory Activity Report 1992 #10 (1993) I-2.
19) M. Matsubayashi et al., Rev. Sci. Instrum. **63** (1992) 1363.
20) H. Shimada et al., Rev. Sci. Instrum. **66** (1995) 1780.
21) E. Shigemasa et al., KEK Report 95-2 (1995).
22) Photon Factory Activity Report 1995 #13 (1996) E-2.
23) S. Suzuki et al., Activity Report of SRL-ISSP **60** (1989).
24) A. Kakizaki et al., Rev. Sci. Instrum. **60** (1989) 1893.
25) A. Kakizaki et al., Rev. Sci. Instrum. **63** (1992) 367.
26) Y. Kagoshima et al., Rev. Sci. Instrum. **63** (1992) 1289.
27) Y. Kagoshima et al., Rev. Sci. Insturm. **66** (1995) 1696.
28) Y. Kagoshima et al., Rev. Sci. Instrum. **66** (1995) 1534.
29) S. Maeyama et al., Photon Factory Activity Report 1995 #13 (1996) 6.
30) Y. Kitajima et al., Rev. Sci. Instrum. **63** (1992) 886.
31) Y. Kitajima, J. Elec. Spec. Relat. Phenom. **80** (1996) 405.
32) K. Ogata et al., Photon Factory Activity Report 1994 #12 (1995) 164.
33) T. Ohta et al., Nucl. Instrum. Meth. A**246** (1986) 373.
34) M. Funabashi et al., Rev. Sci. Instrum. **60** (1989) 1983.
35) H. Konishi et al., Nucl. Instrum. Meth. A**372** (1996) 322.
36) Y. Kagoshima et al., Jpn. J. Appl. Phys. **29** (1989) L 172.
37) Y. Kagoshima et al., Rev. Sci. Instrum. **60** (1989) 2448.
38) Y. Kagoshima et al., Rev. Sci. Instrum. **63** (1992) 605.
39) Photon Factory Activity Report 1988 #6 (1989) I-13.

Accelerator Operations, Researches and Developments

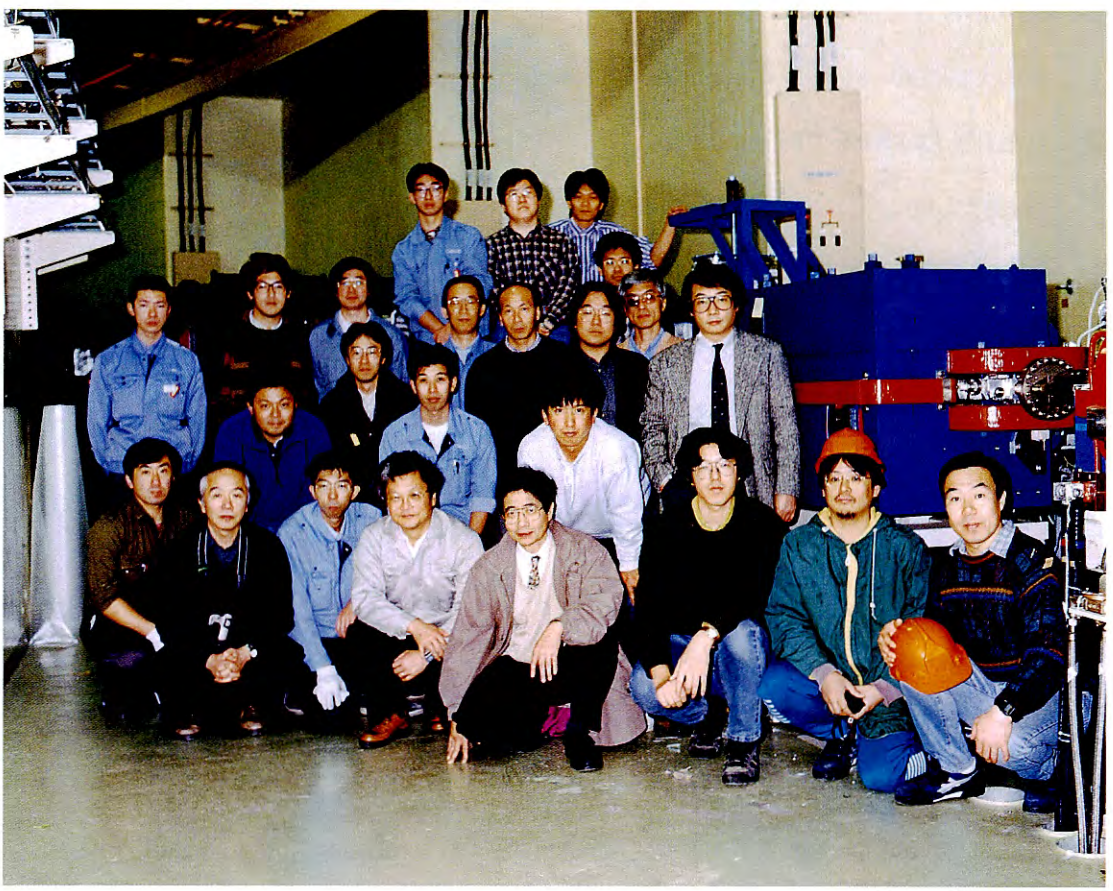

Ready to start! Before starting a large reconstruction of the PF ring to the low emittance configuration, staffs of the PF light source division took a commemorative photograph in the ring tunnel in January, 1997.

You can jump to the article by clicking its title.

CONTENTS

A. INJECTOR LINAC

During this period, the linac was stably operated. The operation statistics for this period are listed in Table 1.

The cumulative usage hours of klystrons and the averaged fault rate with averaged applied anode voltage are shown in Tables 2 and 3, respectively.

Table 1 Operation and failure times during this period.

Date	Operation time (hrs)	Failure time (hrs)	Operation rate (%)
1995			
Sep. 11 - Dec. 27	2568	23.8	99.0
1996			
Mar. 25 - Jun. 22	2792	12.1	99.6
1996			
Oct. 14 - Dec. 16	1490	13.8	99.0

Cumulative status of klystrons up to the end of this term are summarized in Table 4. Twenty klystrons operated for more than 15,000 hours were replaced by upgraded ones.

Table 3 Averaged fault rate and averaged applied voltage to klystrons.

Period	Fault rate (/day tube)	Applied voltage (kV)	Total operation (tube days)
1985/8-1986/7	1.0	238	5,600
1986/8-1987/7	1.0	239	7,740
1987/8-1988/7	1.0	240	9,990
1988/8-1989/7	0.6	241	10,510
1989/8-1990/7	0.3	244	10,690
1990/8-1991/7	0.2	246	10,750
1991/8-1992/7	0.1	248	10,140
1992/8-1993/7	0.1	247	10,010
1993/8-1994/7	0.1	245	10,580
1994/8-1995/7	0.1	246	9,210
1995/8-1997/3	0.3	243	11,160

Table 2 Cumulative usage hours of klystrons during the past years.

Period	Total	Unused	Failed		Living		MTBF
	No.of tubes	No.of tubes	No.of tubes	Mean age (hours)	No.of tubes	Av.op.time (hours)	(hours)
up to 1987/7	106	4	52	4,400	50	9,600	13,600
up to 1988/7	120	2	67	4,500	51	11,400	13,500
up to 1989/7	140	5	82	6,400	53	12,400	14,400
up to 1990/7	158	6	98	8,500	54	11,200	14,700
up to 1991/7	176	14	107	10,100	55	11,100	15,800
up to 1992/7	191	24	113	10,800	54	13,400	17,100
up to 1993/7	203	19	123	10,800	56	15,300	17,700
up to 1994/7	217	30	130	10,900	57	17,800	18,700
up to 1995/7	230	34	138	11,200	58	19,000	19,200
up to 1997/3	268	47	159	13,900	58	11,500	18,400

Table 4 Cumulative status of BI-cathode klystrons up to March 1997 corresponding to the year of production. Unused tubes are those which have never been used in the klystron gallery. STB (stand-by) tubes are those which have been used in the gallery and can be used there again.

Fiscal year of product	Total No. of tubes	Unused No. of tubes	Living No. of tubes	(STB Working)		Av.op.time (hours)	Failed No. of tubes	Causes (arcing	window	others)	Mean age (hours)	Cumulative operation (tube-hours)	MTBF (hours)
				e-	e+								
1987	7	0	3	0	3	0	45,256	4	0	1	3	26,664	242,422	60,606
1988	20	1	3	3	0	0	10,467	16	1	4	11	27,948	478,574	29,911
1989	18	1	3	0	3	0	37,689	14	1	7	6	20,465	399,582	28,542
1990	18	3	4	1	3	0	13,348	11	0	5	6	16,724	237,362	21,578
1991	15	1	8	6	2	0	9,862	6	1	4	1	4,241	104,340	17,390
1992	12	2	8	6	2	0	15,694	2	0	2	0	6,295	138,143	69,072
1993	14	2	12	1	11	0	6,812	0	0	0	0	——	81,739	——
1994	13	2	11	0	11	0	4,025	0	0	0	0	——	44,276	——
1995	23	18	5	0	5	0	1,322	0	0	0	0	——	6,612	——
1996	15	15	0	0	0	0	——	0	0	0	0	——	——	——
total	155	45	57	17	40	0	19,984	53	3	23	27	20,044	1,733,050	32,699

B. PF STORAGE RING

1. SUMMARY OF THE STORAGE-RING OPERATIONS

1.1 Summary of Operations

The 2.5-GeV PF storage ring was operated smoothly during the operation period from September, 1995, to December, 1996. The operation statistics during fiscal year 1996 are summarized in Fig.1-4 and Table 5. The statistics are very similar to those of the last fiscal year (1995). Synchrotron radiation was supplied for research experiments during a net user time of 3390 hours, which included single-bunch operations for 157 hours. During the usual multibunch operation, beams were injected once a day, at 9 o'clock in the morning. The average beam currents during the user runs were 300 mA (multibunch mode) and 41 mA (single-bunch mode), respectively. The failure time was about 1% of the total operation time.

After the end of user runs in 1996, a large upgrade (High Brilliance Project) of the PF ring to a low-emittance lattice started. This project is now well under way, the current status of which is reported in the next section. During machine times for accelerator research and tuning, many studies were performed. These include a measurement of the longitudinal wake potential by means of a photon counting system, the application of an interference method for measuring very small beam sizes, and the development of a longitudinal phase-space monitor. The results of the studies are briefly reported in Section 3.

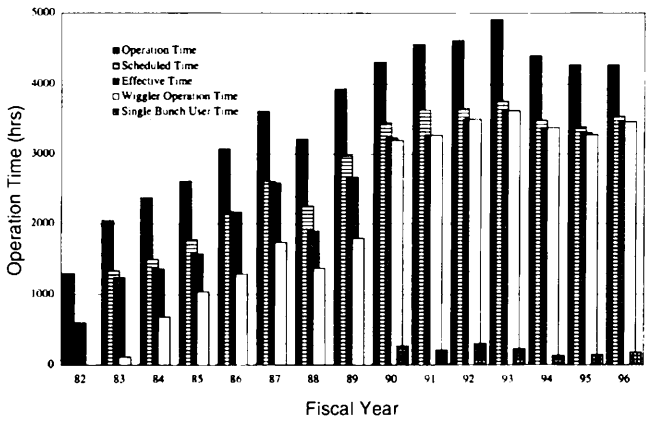

Fig. 1 Operation times of the PF storage ring.

Table 5 Statistics of the storage-ring operation during fiscal year 1996 (from Apr.1996 to Mar.1997).

	Multi-bunch	Single-bunch	Total
Ring Operation Time (hours)	—	—	4246.0
Scheduled user time (hours)	3360.0	176.0	3536.0
Net user time T (hours)	3233.0	157.0	3390.0
Time used for injection (hours)	75.0	14.0	89.0
Integrated current in T (A hours)	969.0	6.0	975.0
Average current in T (mA)	299.7	40.6	—
Number of injections	160	24	184
Interval between injections (hours)	20.0	7.0	—

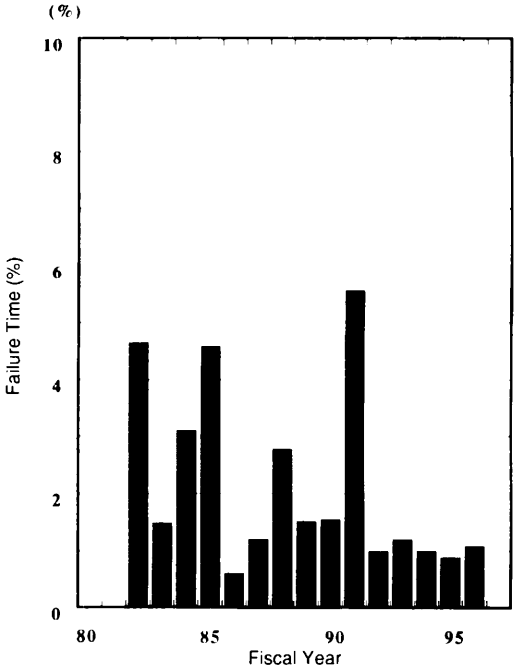

Fig. 2 Rate of failure time of the storage-ring operation.

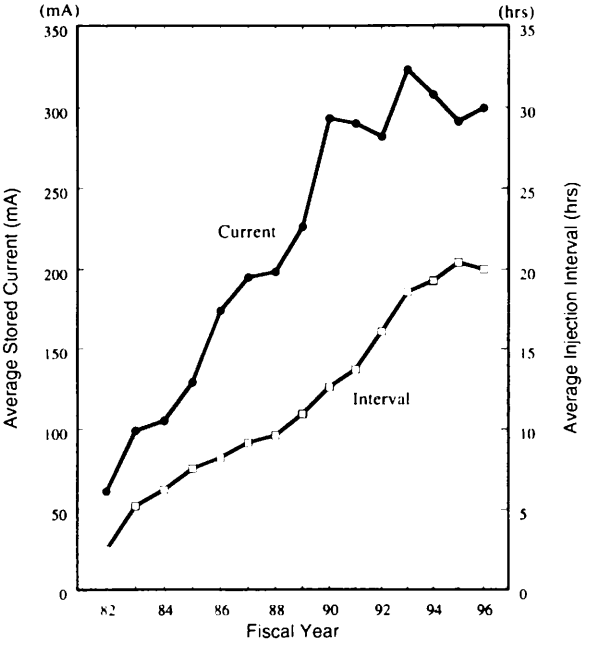

Fig. 3 Average stored currents and injection intervals.

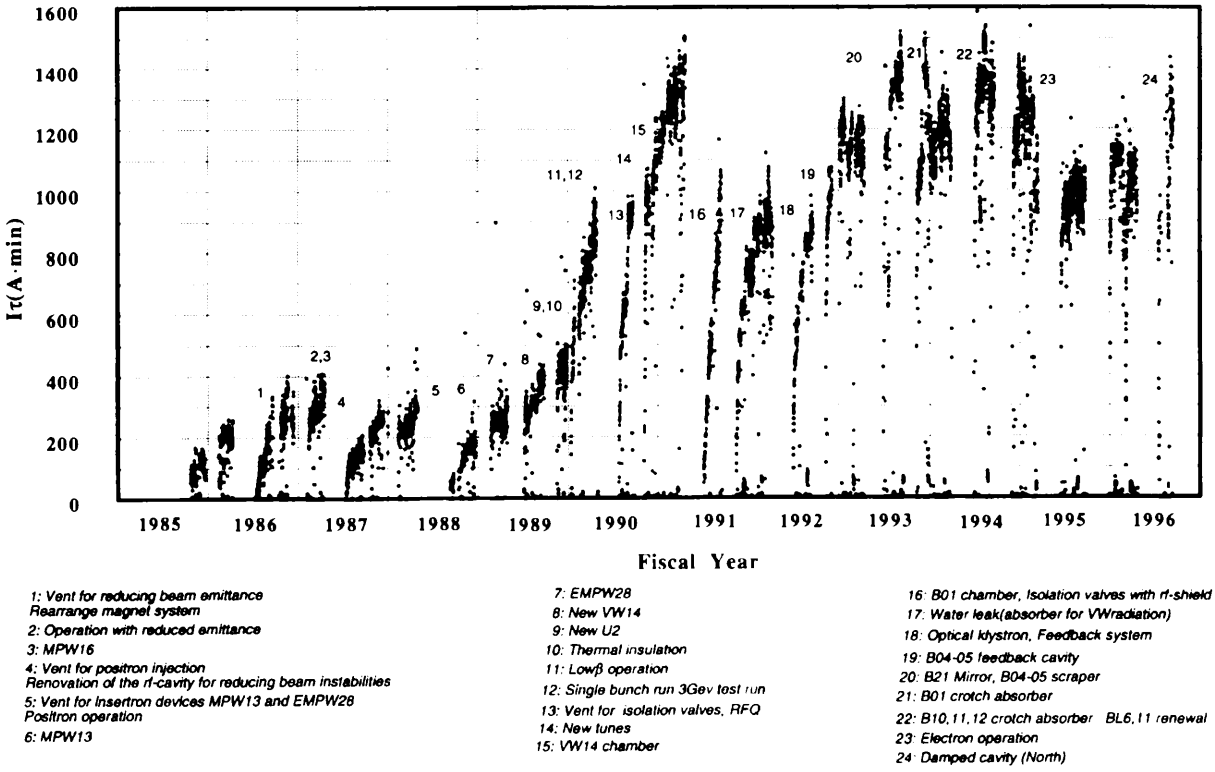

Fig. 4 Historical change in $I \cdot \tau$, the product of the beam current and beam lifetime.

1.2 Trial Operation of High-Current Accumulation

We usually stored an initial beam current of about 400 mA for user runs, and also had experiences of 500-mA storage in past machine studies and tunings. On December 16, 1996, at the end of the autumn user run, we tried to store a higher beam current in the PF ring. We started out a trial operation with a beam current of 500 mA, and then gradually accumulated the beam in steps of 30 mA. During the operation, we monitored the beam profile, closed orbit distortion (COD) and RF conditions. We also monitored the temperatures of the beam-duct wall at typically five locations as well as the outlet water temperatures of crotch absorbers at two locations. The vacuum pressures in the ring, measured with 48 BA-type ionization gauges, were recorded every second. This was because an abnormal pressure rise might have shown us a sign of a possible accident to vacuum ducts or photon absorbers due to a high heat load, although a pressure rise due to photodesorption is not a serious obstacle for accumulating a higher current. One hour after the operation started, a beam current of 600 mA was successfully stored. The average ring pressure was about 6.5×10^{-10} Torr at that time, and the beam lifetime was about 750 minutes at beam currents of from 640 mA to 620 mA. We finally accumulated a maximum beam current of 773 mA, the record stored current in the PF ring. The vacuum pressure went up to 1.2×10^{-9} Torr at this time. Due to limited machine time, as well as the currently approved beam current (less than 800 mA) by a law, we stopped the study at this level. We thus capped the phase-I stage (before the upgrade to low-emittance lattice) of the PF ring with this achievement.

Although we observed some longitudinal beam instabilities during operation, they were not so serious regarding the storage of high currents. This suggested that the new damped cavities, which were substituted for two cavities among four during the last summer shutdown, were very useful for avoiding beam instabilities. We also experienced rf trips four times. Since the input couplers were not fully conditioned under such a high input power at this time, this problem will not be serious during future operations. An rf-related issue during this operation is also reported in subsection 2.5.

Fig. 5 Display of the stored current, showing the maximum record in the PF storage ring.

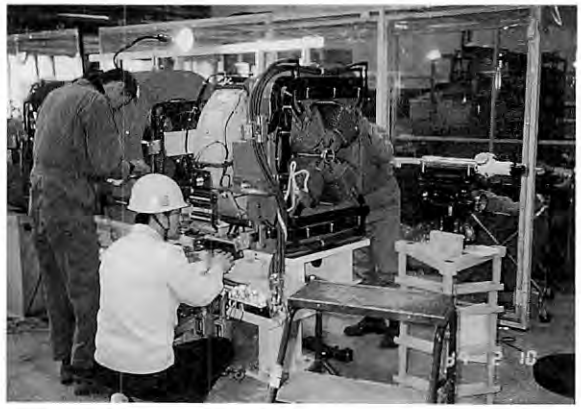

Fig. 6 Alignment of the new magnets on a common girder.

2. HIGH-BRILLIANCE PROJECT

Reconstruction of the PF ring is now in progress. After this reconstruction, the PF ring will be able to provide much brilliant synchrotron radiation to users, as a consequence of the reduced emittance by a factor of five. Sixteen normal cell sections, which occupies about one third of the ring, are under reconstruction. At the same time, many storage-ring components, such as injection kickers, beam monitors and accelerating cavities, are being upgraded. The reconstruction work began in December, 1996, and is well under way. It will be completed at the end of September, 1997. The current status of this project is reported hereafter.

2.1 Magnet Lattice

In advance of the scheduled shutdown for the reconstruction, all of the new quadrupole and sextupole magnets were measured in their magnetic fields. These magnets were then mounted on common girders. A group of two quadrupoles and two sextupoles were installed on a common girder, and were aligned with each other to a precision of better than ±100 μm (see Fig. 6). Thus, the assembled girders will be delivered to the storage ring.

Reconstruction of the storage ring began from December, 1996, just after the end of the operation. All of the vacuum chambers in the normal cell sections were removed in January, 1997. After that, all of the magnets in these sections, except for the bending magnets, were removed. Base plates for the new girders were then installed on the floor. The transportation and

Fig. 7 New power supplies for the quadrupole magnets as installed.

installation of the new magnets will start in April, 1997. It is planned that the magnet installation, including the alignment and connection of the cooling water pipes together with power-supply cables, will be completed before the end of June, 1997. Test operations of the entire magnet system will take place after that.

New power supplies for the quadrupoles and sextupoles were installed in the PF power-supply building next to the light source building (see Fig.7). New power supplies for the steering magnets were also completed. Since the old steering power supplies had unipolar outputs together with a relay to turn over the polarity, there existed slight current jumps at zero crossing. This was improved by replacing all of the power supplies by new bipolar ones. The power

supplies for the quadrupoles and the steering magnets in the beam transport line were also replaced. All of the magnet power supplies will be controlled by a new control system comprising a workstation and a VME system.

2.2 Vacuum System

About half of the beam ducts of the PF ring will be replaced by new or improved ones. This modification is mainly related to the following improvements: 1) replacement of the focusing magnets and their arrangement; 2) renewal of the kicker magnets and a change in their location; and 3) installation of a new fast feedback system. All new beam ducts were manufactured before the scheduled shutdown. Just after the ring was shut down, the reconstruction work began. The beam ducts to be replaced or improved were first removed (see Fig. 8).

The main part of the replacement takes place in normal-cell sections where the number of focusing magnets will be doubled. Sixteen normal-cell ducts are necessary for these sections. The design of the normal-cell duct was fixed after the fabrication of a prototype one. A typical view of the normal-cell section is shown in Fig. 9. A bending part of the old duct was reused for the new duct. The straight part was newly designed so as to be fit for the new magnets. Due to the limited space, no bellows can be mounted between a crotch part and its downstream beam position monitor, both of which are fixed points. In order to precisely set these fixed points, the normal-cell duct was assembled within an accuracy of 1 mm. The effective pumping speed in the new duct was maintained so that a ring pressure of below 3×10^{-10} Torr could be kept. In order to reduce the broadband impedance, the inner walls of different

Fig. 8 Removing the present normal-cell duct for remodeling.

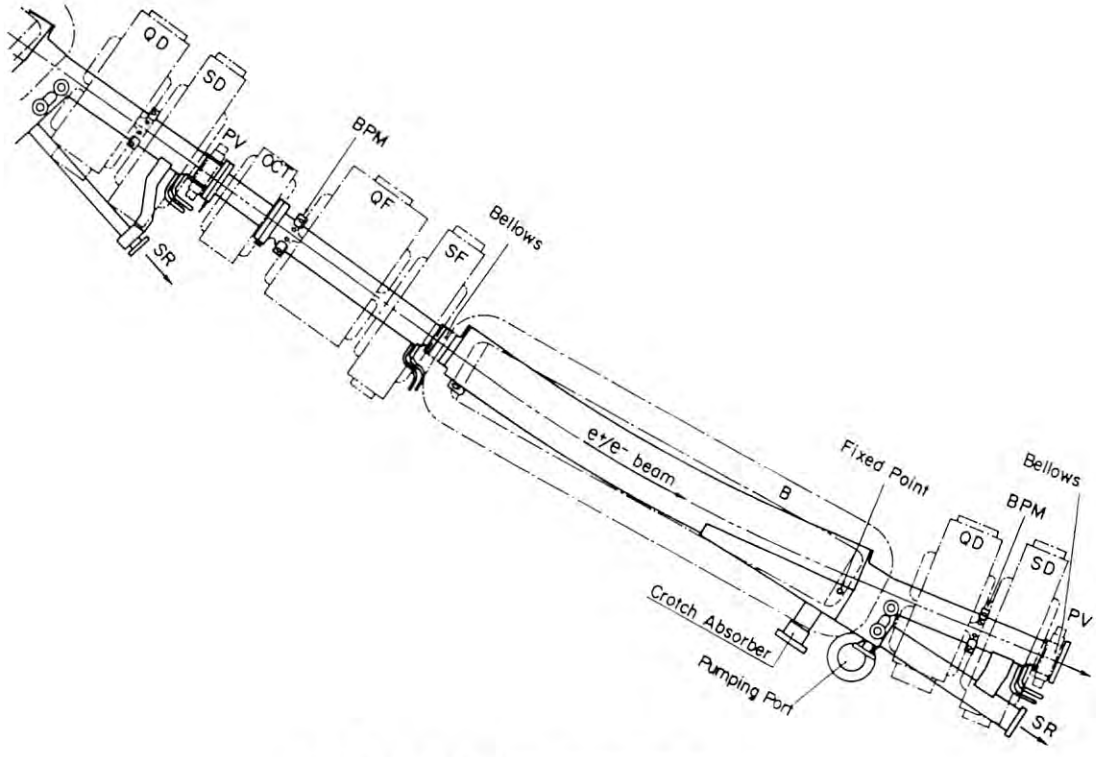

Fig. 9 View of the new normal-cell section.

cross-sectional parts are connected as smoothly as possible. In addition, every new bellows and flange connection have rf shields. All straight parts were fabricated in FY 1995. By assembling these parts and some spare ducts, three normal-cell ducts were completed before the shutdown. Another thirteen ducts are being fabricated by remodeling the present normal-cell ducts. Figure 10 shows a picture of where the normal-cell duct are being remodeled. Eight of these ducts were completed in FY 1996 and the remainder five will be fabricated in FY 1997.

Fig. 10 Normal-cell duct being remodeled.

Because of the narrower bore radius of the new focusing magnets, the physical aperture of the new straight ducts has been reduced. However, due to a reduction in the betatron functions under the new optics, a slightly improved beam lifetime due to the vacuum pressure can be expected if the pressure is the same. The Touschek lifetime, on the other hand, limits the beam lifetime only under the very low-pressure conditions in multibunch operations. Figure 11 shows the consequent beam lifetime as a function of the vacuum pressure.

Kicker ducts for the new kicker magnets were also fabricated. The kicker duct is shown in Fig.12. The ceramic parts of all four kicker ducts have the same shape. They were manufactured by sintering and planing. In order to keep a wide vertical aperture, the top and bottom walls were made to be thin. On the other hand, special ducts equipped with electrodes were installed for fast feedback. These ducts are used to pick-up beam signals as well as to give correction kicks to the beam.

Every beam duct is pre-baked and filled with dry nitrogen gas until installation. We intend to start-up the

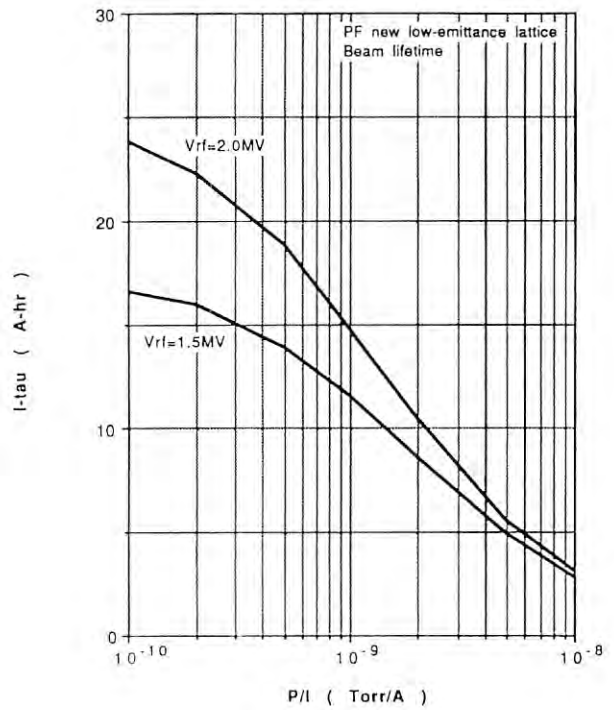

Fig.11 Calculated beam lifetime that is expected under the low-emittance configuration.

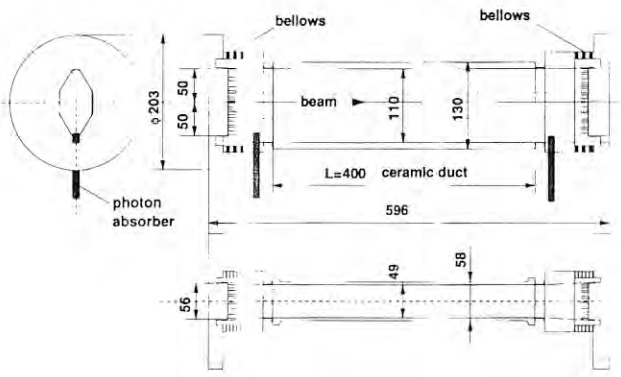

Fig.12 New ceramic duct for kicker magnets.

ring vacuum without in-situ baking, expecting that sufficient wall cleaning by synchrotron radiation will take place during a reasonable conditioning period.

2.3 Beam Monitor System

2.3.1 Calibration of the New BPM

Before installing new-type beam-position-monitors (BPMs), every BPM assembly was calibrated on a test stand in order to determine the electrical center of the BPM relative to its mechanical center. A precise

determination of the offset of each individual BPM is important for commissioning and operating the storage ring.

Shown in Figure 13 is the test stand used for the calibration. The BPM assembly was mounted vertically on the stand. A steel wire of 300μm in diameter was strung coaxially, and simulated the beam. Both ends of the wire were connected to N-type connectors. The wire was precisely aligned using a spring tensioning device located at the lower end. The calibration was performed at a frequency of 500 MHz, the signal-detection frequency of the BPM electronics. RF signals emerging from the button electrodes were multiplexed in a SP4T switch and transmitted to a network analyzer for measuring their intensities. The electrical offsets were then obtained using the BPM sensitivity, which was derived from a simulation based on the boundary element method.

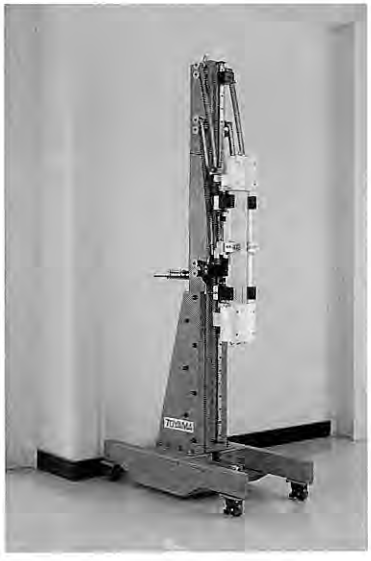

Fig.13 Test stand for calibrating the electrical center offsets of the new-type BPMs.

Figure 14 shows the distribution of measured electrical-center offsets for the new-type BPMs. The horizontal and vertical offsets of each BPM are shown as closed circles. All of the measured offsets are less than 500μm, and typically 200μm, in both directions. This is in good agreement with a simulation result of ~200μm, which was obtained from the boundary element method by assuming a fabrication error. In Fig. 14, the offsets of electrical center for old-type BPMs are also shown for a comparison. The offsets for the

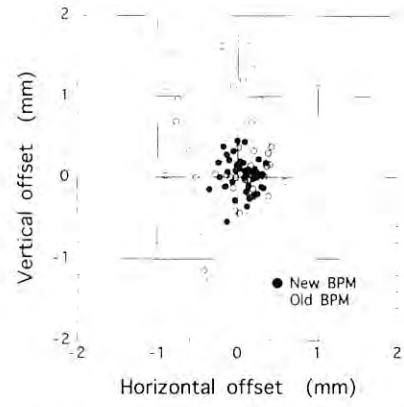

Fig.14 Distribution of the measured offsets of the electrical center relative to the mechanical center.

new-type BPMs were about 1/2 - 1/3 of those of the old-type. Both the horizontal and vertical offsets of the new-type BPMs are nearly zero on the average, which indicates that no systematic errors were introduced during the course of fabricating the Q-ducts and BPM assemblies. These measured offsets for all BPMs will be stored on a computer and used to calculate the beam position.

In order to accurately determine the BPM offsets relative to the magnet axis, a beam-based calibration method will be very useful. This method has the advantage that it can eliminate various error sources, including mechanical alignment errors of the BPM assemblies or residual offsets of the signal-processing electronics.

2.3.2 Measurement of the Injection Orbit by a Single-pass BPM System

A single-pass BPM system, used to measure the injection orbit, has been prepared. The purpose of this system is to correct injection orbit error in advance of the beam storage at commissioning of the low-emittance lattice.

The signal-processing method was reported in the last activity report. The bipolar bunch signals of button electrodes were recorded in real time using a high-speed waveform digitizer. The beam positions were derived from the ratio of the four-button signals. The signals from several BPMs were combined by the aid of RF combiners, and then detected with a single waveform digitizer. The combined signals were discrete pulse trains, and each pulse was well resolved on the

time axis. Sixteen BPMs were connected to the signal-processing system, and the injection orbit during the 1st to 4th turns could be measured with one injection pulse. The resolution of the position measurement was estimated to be about 0.2 mm for a typical electron charge of 0.2 nC with a pulse duration of 2 ns.

A measurement result of the injection orbit under the usual condition is shown in Fig.15. The horizontal (X) and the vertical (Y) beam positions are indicated by the solid circles. The solid line of the upper graph is the orbit calculated based on the design parameters of the PF ring, not including the injection bump. The measurement points well lie on the calculated line. An orbit correction based on the single-pass measurement was also attempted. This system was proved to be useful for a COD correction without any stored beam.

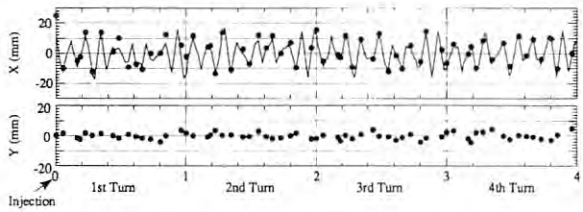

Fig.15 Measurement of the injection orbit using the singles-pass BPM system.

Reference

1) T. Honda, M. Katoh, A. Ueda, M. Tadano, Y. Kobayashi and T. Mitsuhashi, "Measurement of injection orbit using a single pass BPM system at the PF ring", to be appeared in the Proceedings of 1997 Particle Accelerator Conference, 12-16 May 1997, Vancouver, B.C., Canada.

2.4 Injection System

A full-scale model of a 6.25Ω traveling-wave kicker magnet and a line-pulser type power supply were designed and constructed for the high-brilliance project. The parameters of the magnet are listed in Table 6. A ceramics plate was used as the capacitor dielectric because of its large dielectric constant and high insulation performance for high-voltage pulses (up to 30 kV in peak). A general view of the magnet without a top safety cover is shown in Fig.16. The magnet is driven by a newly constructed line-pulser type power supply having a characteristic impedance of 6.25Ω. The parameters of the power supply are listed in Table 7. The pulse-forming line is 35 m long,which produces high-voltage pulses having a pulse length of 350 nsec. The shape of the output pulse from the power supply is shown in Fig.17.

Table 6 Magnet design parameters.

Magnetic length	345 mm
Gap height	60 mm
Gap width	170 mm
Peak field	942 Gauss (at 4500 A)
Characteristic impedance	6.25 Ω
Field propagation time	187 nsec
Number of cells	30
Inductance per cell	31.9 nH
Capacitance per cell	815 pF
Dielectric material	alumina ceramics
Molding material	epoxy regin

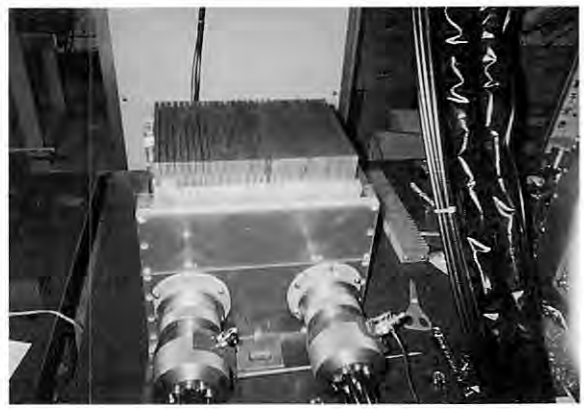

Fig.16 General view of the 6.25Ω traveling-wave kicker magnet.

Table 7 Parameters of the kicker power supply.

Maximum output voltage	30 kV
Maximum output current	4500 A
Output pulse length	350 nsec
Characteristic impedance	6.25 Ω
PFL length	35 m

The total performance of the kicker magnet system including a ceramic vacuum chamber was tested. The shapes of current pulse at the entrance and exit leads of the magnet were measured by a current transformer (Pearson 110A). The result is shown in Fig. 18. Due to a small miss matching in the magnet (i.e., extra capacitance between the electrode and an outer shielding box), the shape of the current pulse at the exit lead was deformed. The pulse shape of the total magnetic field was measured by a long search coil

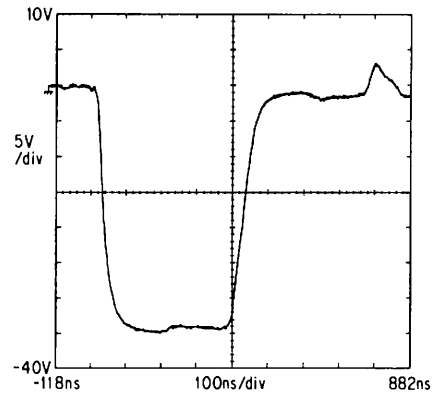

Fig.17 Output pulse shape of the line-pulser type power supply.

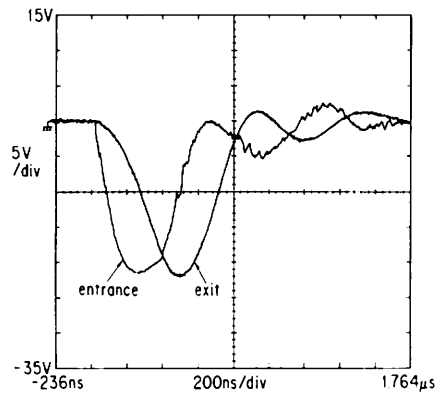

Fig.18 Shapes of the current pulse at the entrance and exit leads of the magnet.

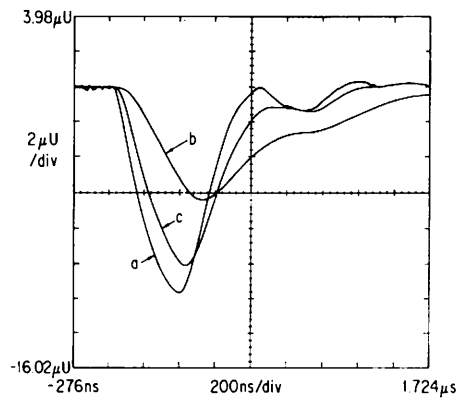

Fig.19 Pulse shapes of the total magnetic field measured by a long search coil.
a) Without ceramic duct, b) with ceramic duct having a homogeneous titanium coating, c) with ceramic duct having a slit coating.

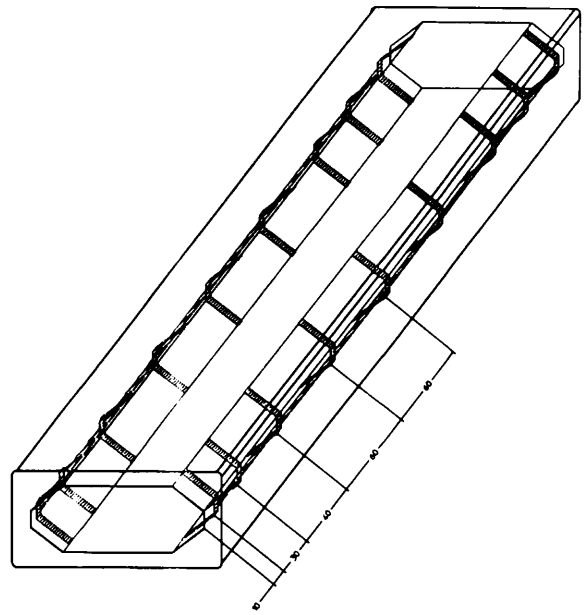

Fig. 20 Slit pattern of the Ti coating on the ceramic duct.

(3mm × 600mm, 1 turn). The result is shown in Fig.19. In this measurement, the magnetic field was partly shielded by the eddy current excited in the metal coating of the ceramic duct. At first, we applied a titanium coating of 1μm thickness. With this coating, the magnetic field was reduced by 50%, as shown in Fig.19. To prevent this field drop by the eddy current, we applied a pattern of slits to the metal coating, as shown in Fig. 20. With this coating, the field drop was reduced to 7%, as shown in Fig.19.

2.5 Beam Test of New Damped Cavities

As reported in the previous activity report,[1] some of the rf cavities of the PF ring have been replaced by new damped cavities,[2-9] which were developed by a collaboration between KEK and the Institute of Solid State Physics (ISSP) of the University of Tokyo. During the summer shutdown in 1996, two of the four present cavities were first replaced by new ones. These new damped cavities, together with two old ones, were successfully operated during the last scheduled user run from October to December, 1996. High-current storage was also attempted on Dec. 12, 1996, as reported in Section 1.

Figure 21 shows a schematic view of the damped cavity. The cavity has beam ducts with a somewhat large diameter. Higher order modes (HOM's), whose frequencies are above the cutoff frequency of the duct,

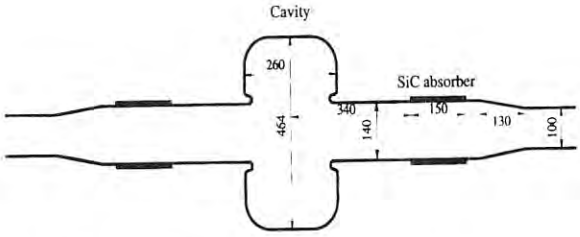

Fig. 21 Schematic view of the damped cavity.

propagate out to the beam duct and are absorbed by silicon carbide (SiC). Although HOM's below the cutoff frequency still remain in the cavity, these can be detuned so as not to introduce any coupled-bunch instability. This frequency-shift method,[10,11] using two fixed tuners to detune the HOM's, was first developed at the Photon Factory.

The unloaded Q of the accelerating mode was 39500 with two fixed tuners, a movable tuner and an input coupler attached. The shunt impedance of the accelerating mode is estimated to be 6.9 MΩ. The SiC is a kind of sintered SiC. It has an inner diameter of 140 mm, an outer diameter of 160 mm and a length of 150 mm. The resistivity of the SiC was about 50 Ωcm in the frequency range of 1-5 GHz. The SiC is fixed inside of the copper duct by a shrink-fit process. The copper duct has a water-cooling channel on the outer surface. Since the SiC has good thermal conductivity, the temperature rise of the SiC duct is negligible under the usual operation of the PF ring.

Conditioning of the cavity was carried out in both the CW and pulse modes. An rf power of up to 90 kW (CW) and 120 kW (pulse) was input to the cavity during the conditioning. Figure 22 shows two damped cavities installed in the ring. An input coupler was attached to the upper port of the cavity. A movable tuner was set in the side port. Two fixed tuners were placed at the other side port and the bottom port. In the figure, a part of the wave guide has been removed. An evacuation chamber was placed between the cavities, which has two 400 l/s ion sputter pumps, two Titanium sublimation pumps, a vacuum gauge and a quadrupole residual gas analyzer. The base pressure was in the range of 10^{-10} Torr after baking.

Figure 23 shows the vacuum pressure and the output power of the klystron during the first beam storage after the installation of new cavities. Since each cavity was driven by one klystron, the klystron power in the figure shows the input power to each cavity. The

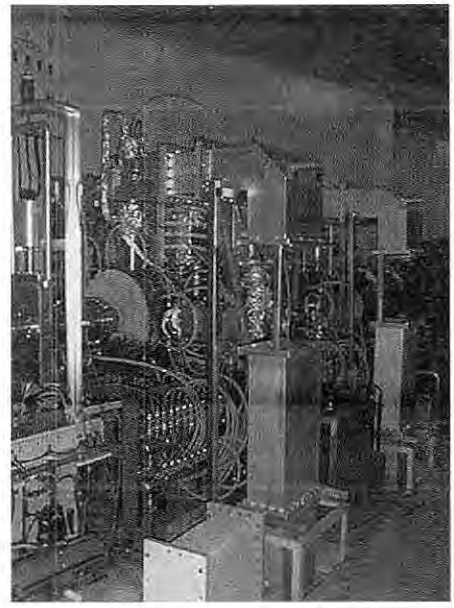

Fig. 22 New damped cavities installed in the ring.

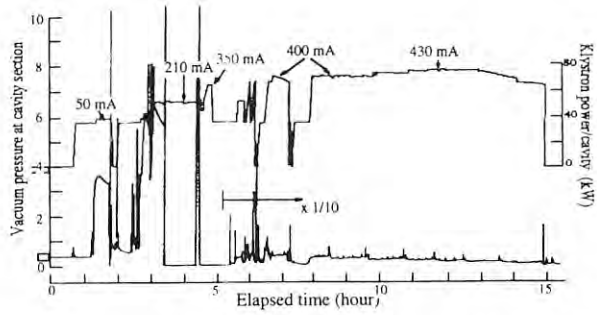

Fig. 23 Change of the vacuum pressure during the first storage.

stored current is given in the figure. The vacuum pressure ranged around 10^{-8} Torr before an elapsed time of about 5 hours, and 10^{-7} Torr after that time. As can be seen in the figure, the vacuum pressure became higher with increasing the stored current, and then gradually decreased. Apart from such a slow change of the vacuum pressure, there existed burst outgassing. The worst one among such bursts took place at an elapsed time of about 3.5 hours; however, the peak pressure did not exceeded the range of 10^{-7} Torr. About 10 hours after the first beam injection, a stored current of more than 400 mA was attained without any serious rf or vacuum problem.

The conditioning using a beam continued for 4 days with a maximum stored current of 500 mA. After the conditioning, the base pressure decreased to the

range of 10^{-9} -10^{-10} Torr at a stored current of 350 mA. No burst outgassing was observed during the usual operation after conditioning.

The detuning of the HOM's was quite successful. We could not detect any transverse coupled-bunch instability. The longitudinal coupled-bunch instability was still observed. However, it is considered to have been due to the old-type cavities, since the frequency of the beam spectrum was different from the resonance frequency of the HOM's in the new cavities.

At the end of the scheduled user run in 1996, we tried to store the electron beam as much as possible. The record of the stored current in the PF ring has so far been around 500 mA. Figure 24 shows the new record that was achieved. As mentioned above, CW conditioning of the cavities was performed below an input power of 90 kW. During the operation, the vacuum pressure began to rise when the input power exceeded 90 kW, which included wall dissipation and beam loading. Because the cavity gap voltage during this operation was lower than that under conditioning, it was suggested that the outgassing came from the input coupler. A maximum stored current of 773 mA, a new record at the PF ring, was achieved, although the beam was down at 743 mA in the figure. No transverse coupled-bunch instability was observed up to the maximum current. A longitudinal instability was clearly seen on the spectrum analyzer, though it was not very harmful. The injection rate did not decrease drastically, and the quality of the beam seen in the SR light monitor was not so different from that at a low stored current. We could not find any difficulties to operate the ring at such a high current, except for the lifetime of the beam, which could be overcome by conditioning under high current operations.

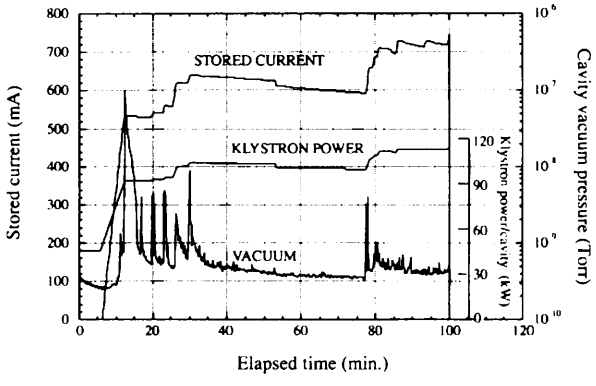

Fig. 24 Change of the vacuum pressure at a high stored current.

References

1) PHOTON FACTORY ACTIVITY REPORT 1995, #13, p. A-14.
2) T. Koseki, M. Izawa and Y. Kamiya, Proceedings of the 1993 Particle Accelerator Conference, Washington, D.C., Vol. 2 (1993) p. 930.
3) T. Koseki, Y. Kamiya and M. Izawa, Proceedings of the 9th Symposium on Accelerator Science and Technology, 1993, Tsukuba, Japan, p. 246.
4) T. Koseki, Y. Kamiya and M. Izawa, Proceedings of the 4th European Particle Accelerator Conference, Vol. 3 (1994) p. 2152.
5) T. Koseki, Y. Kamiya and M. Izawa, Rev. Sci. Instrum, **66** (1995) 1926.
6) T. Koseki, M. Izawa and Y. Kamiya, 1995 Particle Accelerator Conference and International Conference on High-Energy Accelerators, Dallas, TX, May 1-5, 1995, p. 1794.
7) T. Koseki et al., Proceedings of the 5th European Particle Accelerator, SITGES (Barcelona), 10-14 June, 1996, p. 1988.
8) M. Izawa, T. Koseki, Y. Kamiya and T. Toyomasu, Rev. Sci. Instrum. **66** (1995) 1910.
9) M. Izawa et al., Proceedings of the 5th European Particle Accelerator, SITGES (Barcelona), 10-14 June, 1996, p. 2006.
10) M. Izawa, H. Kobayakawa, S. Sakanaka and S. Tokumoto, KEK Internal 88-7, 1988.
11) H. Kobayakawa, M. Izawa, S. Sakanaka and S. Tokumoto, Rev. Sci. Instrum. **60** (1989) 1732.

2.6 Control System

2.6.1 Renewal of the Control System

A renewal of the PF ring control system is under way. The present minicomputers (FACOM S-3000 series) are to be replaced to workstations and VME systems. The VME systems are used to perform real-time processing of the equipment, and the Unix workstations take charge of upper-level controls. Software, such as equipment drivers and man-machine interfaces, is under development. The new control system for the magnet power supplies will be commissioned in October, 1997, as the first stage of the upgrade.

The main power supplies for bending and quadrupole magnets have so far been controlled via CAMAC interfaces which are directly connected to

CAMAC drivers of minicomputers. These CAMAC interfaces are kept in the new system, and are driven by a VME system. A CAMAC server process is prepared in the VME to manage any access requests from the workstations. On the other hand, present NIM controllers for small power supplies, such as steering magnets, are replaced by a VME system. These magnets can be handled in a similar manner as that of CAMAC.

In order to asynchronously exchange data between different control processes which are distributed in the system, a "Data Channel" system was developed (see Fig. 25). Data storage called "Data Channel (DCh)" is prepared in the shared memory of the server computer. The DCh is divided into "channels", each of which has "members" to keep data. The address of data is uniquely identified by a combination of "channel" and "member". A DCh server process handles DCh read/write requests from various control processes. By using simple DCh service routines, client processes are able to exchange data through the DCh. The creation of DCh members is conducted by the client processes. The DCh server dose not care about the contents of data, and only takes part in read/write operations.

The DCh keeps only the latest updated data, such as the machine parameters or operation conditions. In order to keep a log data for later use, a collector process periodically gathers the data in DCh and saves them into a database. On-demand data storage is also possible by sensing request flags.

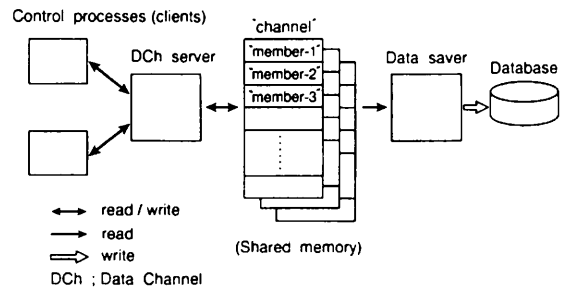

Fig. 25 Schematic view of "Data Channel".

2.6.2 Renewal of Insertion-Device Control

There are five permanent-magnet insertion devices, three undulators and two multipole wigglers, working at the PF ring. Each insertion device had been controlled by an individual personal computer (PC) so far. Since these PC's have no connection to a computer network, it had been impossible for users to change insertion-device gaps via the network. When the users wanted to change the gap, they needed to phone an operator to do it. The operator then went to the PC's in the next room, and typed a command. After the operation was finished, it was announced to the users. In order to simplify this troublesome way, a renewal of the insertion-devices control system is underway. As the first trial case, a new control system for multipole wiggler #13 (MPW #13) was constructed.

A VME system and a workstation are used for the new control system. The VME system, which comprises a CPU board and a GPIB interface, substitutes for the old PC. It is linked to an exclusive network which is dedicated to the light-source control. The workstation (hp715) is also connected to the network and communicates with users. With this system, each user in the experimental hall sends a gap-change request using his own PC. The request is received by the workstation, and is then, checked if permitted under the current operation together with if it is within the allowable range for independent tuning (that is, the gap range within which the gap change does not influence other users). If these conditions are fulfilled, the request is accepted. The workstation then sends a request to the VME system, and the gap change is performed.

It was ascertained that the basic function of the new system worked well. After further tests and the addition of some functions, this system will be open to users in 1997. The control system for the remaining four devices will be renewed during fiscal year 1997.

2.6.3 New Online-database Logging System for the Synchrotron Radiation Beam-Line Control System

There are twenty-two beam-line front-ends at the 2.5-GeV storage ring that feed synchrotron radiation through the branch beam lines to the Experimental Hall. The beam-line front-ends have a number of components and sensors to be controlled, including vacuum valves and beam shutters, more than one hundred in total, as well as interlock devices, vacuum pressure gauges and valve-driving units. These beam lines are automatically controlled by the Beam Line Control System that comprises twenty-two computers and a host computer VAX Station 4000/90 (~30MIPS,

80 MB of memory) running under VAX/VMS. The host collects all operational data and control data of the beam lines.

There have been further necessities to allow the operators to retrieve any combinations of control data for the beam lines. This functionality is particularly important for the Beam Line Group to improve the performance of the beam lines, and to analyze any sign that would suggest the presence of some malfunctioning behavior of a beam-line component beforehand. This is also true for predictive maintenance; the Beam Line Group monitors the closing/opening times of the vacuum valves to an accuracy of 0.1 seconds. The opening/closing times should be within the ordinal ranges to ensure the safety of synchrotron-radiation experiments.

For these reasons, a new on-line Logging System has thus been designed and implemented using the Oracle database[1] where all control data, including the operational status and set-up values for the beam lines, are automatically logged. Figure 26 shows a simplified block diagram of the operation Logging System. The Logging System has a real-time capability to fetch any event signals as well as static data. When an operational condition changes or when the status of a device changes, the Beam Line Control System automatically notifies event data representing the device status of the Event Manager on the VAXStation 4000/90. The VAX has two 2GB disks for the system, database management, user applications, and a 4.5GB-disk for data storage.

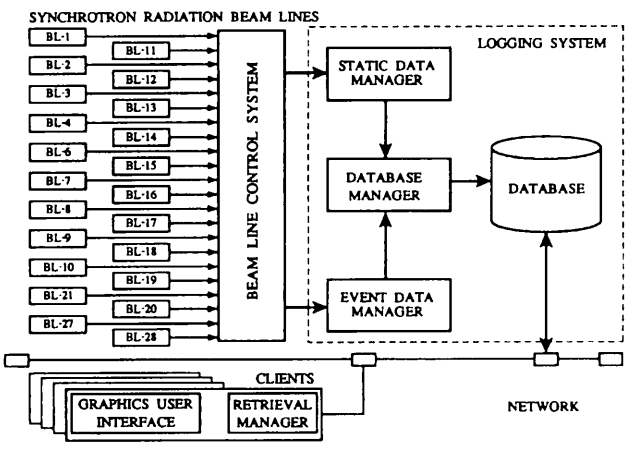

Fig. 26 Block diagram of the Operation Logging System for synchrotron-radiation beam lines at the Photon Factory.

There are two categories of operational data available from the Beam Line Control System: event data and static data. Each dada has a time stamp with an accuracy of 20 ms. The first category includes asynchronous event data acquired from digital ON/OFF pick-ups attached to the vacuum valves, shutters and interlocks. There are approximately 2000 pick-ups in total. The maximum rate of event signals reaches ~300 events/sec when all beam lines have to simultaneously close/open due to radiation-safety reasons. The second category includes static analog data that are periodically measured at a specified interval, ranging from 3 seconds to one minute. The static data includes the beam current of the storage ring, pressures signals measured at the middle point of the beam line and the storage ring at an interval of three seconds. The total amount of data to be logged into the Logging System reaches approximately 35 million items, consuming 1.5 GB of disk space per year.

Upon receiving event data, the Event Manager attaches a time stamp to the event data, and forwards the event data to the Database Manager after making compliance checks in terms of the validity of the event data. The Static Data Manager fetches static data at specified time intervals associated with the devices to be measured. The Static Data Manager attaches a time stamp and device code to the measured value, and then sends it to the Database Manager. Then, the Database Manager stores the data to a specified table in the database. All operational data stored in the database are archived for at least three years.

A Graphics Interface for operators is a client on the network, which is implemented using Motif widgets. An operator can choose any items associated with devices to be searched. The Retrieval Manager encapsulates these items into a packet, and queries the Logging System across the network. Then, the Retrieval Manager receives a reply from the database through the Request Manager, transferring the reply to the Graphics User Interface to display the results.

The Logging System using a database for the synchrotron radiation beam lines at KEK came into actual operation in the beginning of 1995 to replace the existing logging file system. The Logging System has been reliably operating for several years, providing better performance than the ancestor logging file system, even to the degree of acquiring real-time event operational data from the beam lines. The Logging System provides a means to improve the performance

of the beam lines, and is useful for determining the cause of a problem in a beam line.

Reference

1) N. Kanaya et al., "Operation Logging System Using the Database for the Synchrotron Radiation Beam Lines at the Photon Factory," to be appeared in the Proceedings of the 1997 Particle Accelerator Conference, 12-16 May 1997, Vancouver, B.C., Canada.

3. MACHINE STUDIES

3.1 Measurement of the Longitudinal Wake Potential

In order to measure the medium-range longitudinal wake field, the decay time of which is longer than the minimum bunch spacing (2ns in the PF ring), but shorter than the revolution period (624ns), a test bunch method was developed. In this method, a main bunch and several test bunches are simultaneously stored in the ring. A longitudinal wake potential generated by the main bunch having a large charge is probed with the test bunches. The beam currents of the test bunches are made so small that the interaction among them via vacuum vessels is negligible. The lengths or static phase shifts from the synchronous phases of the test bunches are measured as a function of the beam current of the main bunch. Since these parameters of the test bunches have to be precisely measured under the existence of a large background signal from the main bunch, a wide dynamic range is required for the measurement system. An excellent time resolution is also necessary for measuring small phase shifts. For this purpose we employed a photon-counting system having a dynamic range larger than 10^5 and a time resolution better than 10ps. The measuring system was installed in beamline BL-21.

With the photon-counting system, time-averaged particle distributions within the bunches are measured. Since coherent oscillations of test bunches excited by the main bunch affect the bunch-length measurement, the effect of the oscillation was estimated. The rms amplitudes of the oscillations observed with a digital oscilloscope were smaller than 10ps. Their contribution to the bunch-length measurement was less than 1ps.

In order to check the reliability of the system, the lengths of the test bunches were first measured without

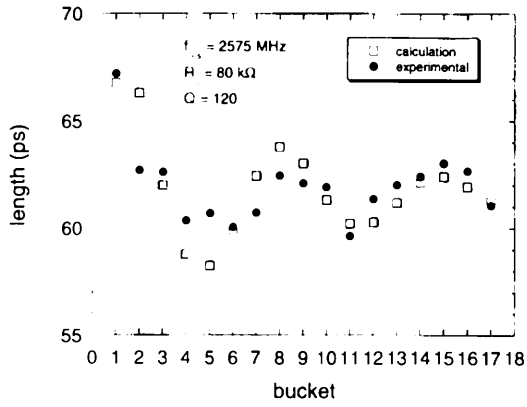

Fig. 27 Bunch lengths of the test bunches. The main bunch was stored in the 0th bucket, and its beam current was 30 mA. The squares and circles show the calculated and measured bunch length, respectively.

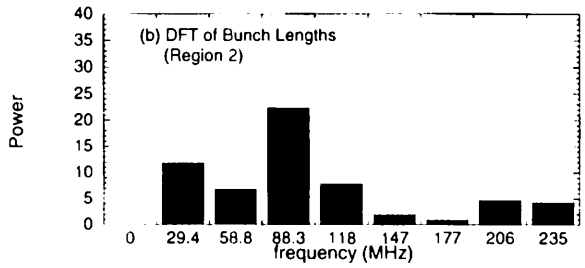

Fig. 28 DFT of the lengths of the test bunches.

accumulating the main bunch. The result was close to the natural bunch length within the reproducibility of the measurement. After this confirmation, we measured the lengths of the test bunches, which were stored in the 1-17th buckets, as a function of the beam current of the main bunch stored in the 0th bucket. Figure 27 shows an example of the measurement in which the beam current of the main bunch was 30mA.

In order to specify the impedance source, the data of the bunch lengths were analyzed using the Discrete Fourier Transform (DFT). The result is shown in Fig. 28. The main frequency component is 88MHz, as shown in the figure. Considering the sampling theorem, the related frequency component is $n \cdot f_{rf} \pm 88\ MHz$. A resonator model with a resonant frequency of 2575MHz, a quality factor of 120 and a shunt impedance of 80kΩ explains the measured data quite well, although we were not able to determine the impedance source so far. Squares in Fig. 27 show the bunch lengths calculated with this model.

Reference

1) K. Tamura, Ph.D. thesis, Hiroshima University, March 1997.

3.2 Development of a Longitudinal Phase Space Monitor

In addition to the transverse phase-space monitor which was previously reported,[1,2] a longitudinal phase-space monitor was developed at the PF ring. The use of both transverse and longitudinal monitors allows us to observe beam oscillations in six-dimensional (x, x', y, y', ϕ, δ) phase space.

With the longitudinal phase-space monitor, both the phase oscillation and momentum deviation of a single bunch can be simultaneously observed. A block diagram of the phase detection circuit is shown in Fig. 29. The phase deviation (ϕ) of the synchrotron motion was detected by measuring the phase difference between the beam signal from the button electrode and an rf signal. The rf frequency component (500.1 MHz) of the beam signal and the rf signal from a master oscillator were first converted to an IF frequency (60 MHz). The beam signal was fed to a limiting amplifier in order to avoid any current dependence. The phase difference between these signals was then detected. After a low-pass filter of 10 MHz, the output signal was digitized with a 20-MHz, 8 bit flash ADC, and the data was immediately sent to the stored memory. An external clock signal, synchronized to the beam revolution, was used for the start of ADC and the memory control. The data accumulated in the memory were transferred to the on-line computer through a GP-IB interface. On the other hand, the momentum deviation (δ) was detected from the transverse beam position at a location of finite dispersion, using the transverse phase-space monitor system. The momentum deviation was deduced by $\delta = \Delta x/\eta$, where η is the dispersion function and Δx is the horizontal position. To reject the betatron motion from the horizontal displacement, a filter process was performed off line.

Table 8 Orbit- and RF-related parameters of the PF ring

Beam Energy	E (GeV)	2.5
Betatron tune	ν_x / ν_y	8.45/3.30
RF frequency	f_{RF} (MHz)	500.1
RF voltage	V_{RF} (MV)	1.7
Harmonic number	h	312
Revolution frequency	f_{rev} (MHz)	1.6029
Energy Spread	σ_ε	0.00073

The experiment was performed under single-bunch operation with a beam current of 10 mA. The machine parameters during the experiment are given in Table 8. To check the performance of the phase-detection circuit, the beam response to an rf phase modulation was first measured. Sinusoidal phase modulation was applied to the accelerating field using a phase shifter. The frequency and amplitude of the phase modulation were set to be 30.13 kHz and 1.6 degrees, respectively. Figure 30 shows the digitized data taken over 16000 turns. An FFT spectrum of the data is displayed in Fig. 31, where the frequency range was set to be from 10 to 50 kHz. Two peaks were

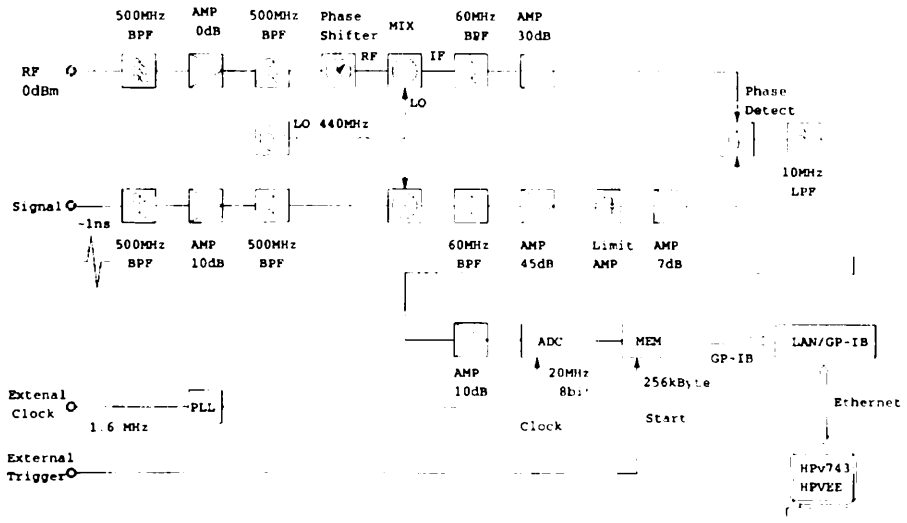

Fig. 29 Block diagram of the phase-detection circuit.

observed in this range; the first peak at 30.13 kHz was induced by the RF phase modulation and the second peak at 36.49 kHz was due to a coherent synchrotron oscillation caused by a longitudinal single-bunch instability. The amplitude of the first peak is expected to be proportional to the modulation amplitude. To calibrate the output digital data to the phase-oscillation amplitude, the measurement was performed for different modulation amplitudes. The result is given in Figure 32, which shows the amplitudes of the first peak versus the phase-modulation amplitude. The good linear relation between the output signal and the modulation amplitude suggested that the linearity of the phase detection circuit is quite good over 8 degrees. After some data processing, a phase resolution of about 0.136 degrees was deduced.

As shown in Fig.31, the measured data include contributions from the RF phase modulation and the longitudinal single-bunch instability. Since the instability was so strong, we could not remove it in the experiment. Instead, these oscillations were distinguished using a filter process on an off-line computer. The momentum deviation was also deduced by similar processing. Figure 33 shows the results of a longitudinal phase-space plot for both oscillations

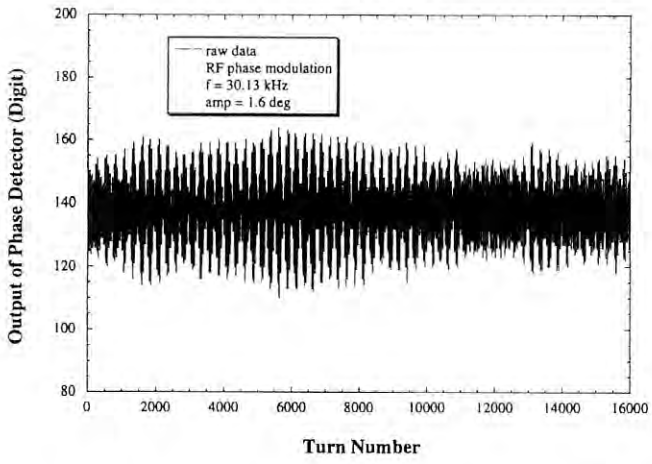

Fig.30 Digitized output data of the phase-detection circuit.

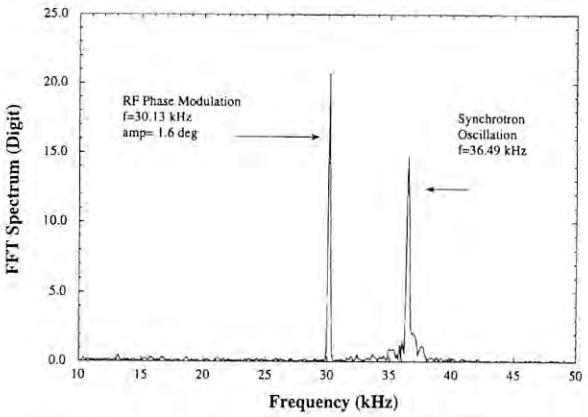

Fig. 31 FFT spectrum of the digitized output data.

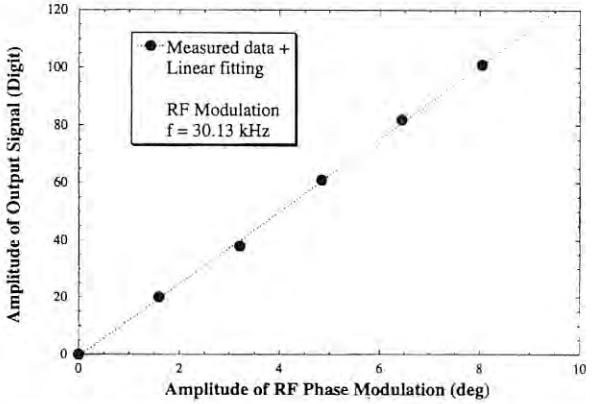

Fig.32 Calibration for converting the digitized output data to the phase value.

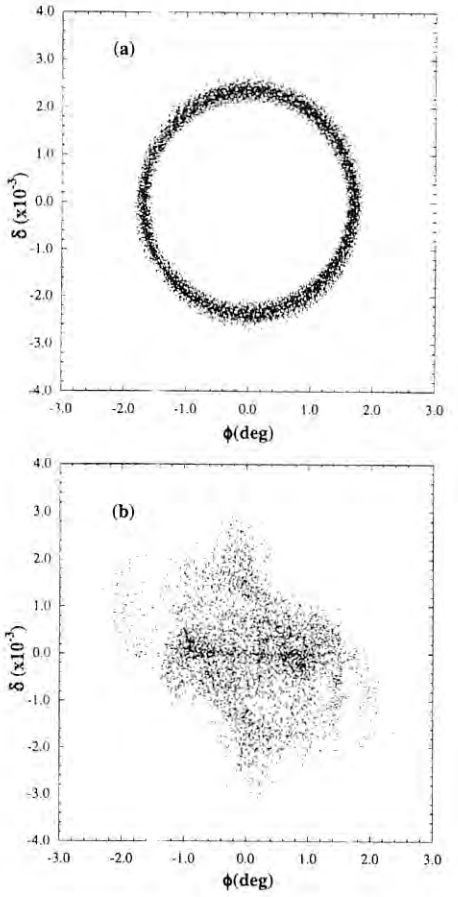

Fig.33 Longitudinal phase-space plots caused by: (a) the RF phase modulation, and (b) the single bunch instability. Data taken over 16000 turns are plotted in the figures.

induced by the RF phase modulation (a) and by the single-bunch instability (b).

It was shown that the longitudinal phase-space monitor has a good performance. A fruitful study on the beam dynamics is foreseen using this monitor.

References

1) PHOTON FACTORY ACTIVITY REPORT 1995, #13, p. A-18.
2) Y. Kobayashi, T. Mitsuhashi, A. Ueda and T. Kasuga, Proceedings of the Fifth European Particle Accelerator Conference (EPAC96), SITGES, June 1996, p. 1666.

3.3 Beam-Profile Monitoring of Synchrotron Radiation by Adaptive Optics

The beam-profile monitor, based on imaging of the synchrotron radiation (SR), is generally used for diagnosis of the high-energy accelerator. At the PF ring, a precise beam-profile monitor using visible synchrotron radiation was constructed.[1,2] A water-cooled mirror made of beryllium (Be) was used as an extraction mirror for the SR beam. The mirror is usually deformed by thermal expansion caused by absorption of the SR beam. The deformation of the mirror introduces a wavefront error (often amounts to more than a few λ where λ=633 nm), which makes a blurred beam image. In a previous experiment, this effect was partially eliminated by a deconvolution process under an off-line analysis.

We applied a technique of adaptive optics[3] to eliminate the wavefront error caused by the deformation of the Be-mirror. This offers us a more reliable means to observe the beam image. In order to measure a wavefront error caused by the Be-mirror, a Shack-Hartmann wavefront sensor[3] was designed and constructed. The wavefront error was then corrected by using an adaptive optical system.

In the Shack-Hartmann wavefront sensor, the wavefront is sampled by a multi-lens array conjugated with the mirror. Each lenslet cuts out a part of the wavefront. The local mean slope is measured by sensing the position of the diffraction-limited spot in the multi-lens array's focal plane. Figure 34 shows the result of a measurement of the wavefront error caused by the Be-mirror, which was observed using this sensor. It can be seen that the wavefront was deformed horizontally in a cylindrical way by about 2 μm (peak to valley). This deformation was caused by the baking process.

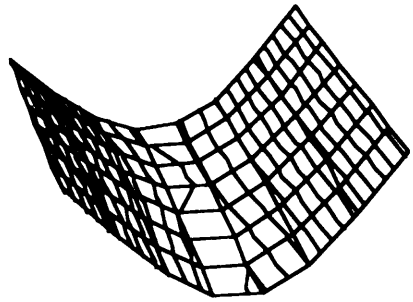

Fig. 34 Wavefront error caused by the Be-mirror.

Table 9 First 8 terms of the Zernike aberration coefficients.

Zernike aberration coefficients	
Piston or constant term	0.0
Tilt of wavefront	0.0
Focus shift	0.944
Astigmatism with axis at 0°	-2.110
Astigmatism with axis at 45°	0.000
Third-order coma along x-axis	-0.053
Third-order coma along y-axis	-0.098
Third-order spherical aberration	-0.224

The obtained wavefront error was analyzed using standard aberration theory. The circle polynomials of Zernike[4] are generally used to represent wavefront aberrations over a circular pupil. Each coefficient of the polynomials corresponds to a classified aberration. We applied an analysis of the Zernike's aberration coefficients, by a least-square fitting[5] of the complete circle polynomials of Zernike. The result of the first 8 terms of Zernike's aberration coefficients are listed in Table 9. Because the mirror was deformed in a cylindrical way, the aberration coefficient of the fourth term (astigmatism) is large. The thus-obtained coefficients were used to compensate the wavefront error.

We designed an adaptive optical system to compensate the wavefront error caused by the deformation of the Be-mirror. The layout of adaptive optics system is shown in Fig. 35. The deformable mirror is set in the conjugated plane of the Be-mirror. The surface of the deformable mirror is deformed as the conjugated surface of the Be-mirror using the data from the Shack-Hartmann wavefront sensor. The wavefront error on the Be-mirror is transferred on the deformable

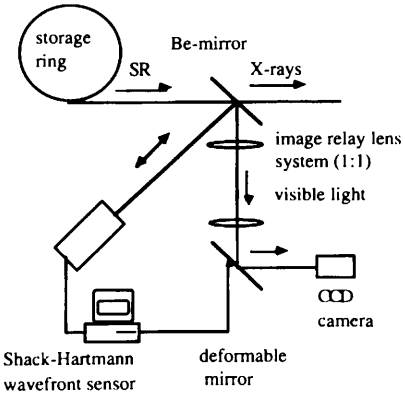

Fig.35 Layout of the adaptive optics system.

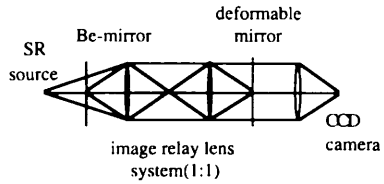

Fig.36 Optical principle.

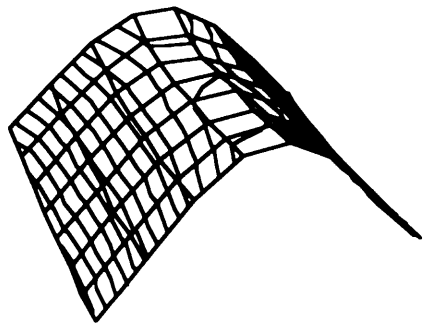

Fig.37 Shape of the deformable mirror used to cancel the wavefront error, as shown in Fig. 34.

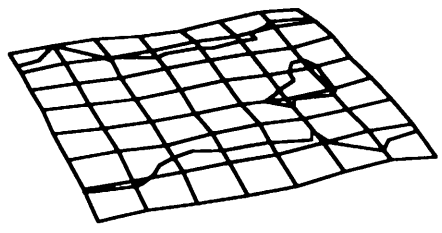

Fig.38 Subtraction of the two wavefronts, as shown in Figures 34 and 37.

mirror using the relay lens system (1:1) and compensated by the deformable mirror, as shown in Fig. 36. We used a deformable mirror (CILAS BIM 31), which is a "bimorph" type mirror. It is equipped with 31 electrodes that can be separately driven by ±400 V voltages. The shape of the deformable mirror used to cancel the wavefront error, shown in Fig. 34, is given in Fig. 37. The shape of the deformable mirror is just the opposite shape of the wavefront. The subtraction between the two wavefronts is shown in Fig. 38. The remaining wavefront error is less than $\lambda/8$.

References

1) T. Mitsuhashi, Proceedings of the Fifth European Particle Accelerator Conference, SITGES (Barcelona), June 1996, p. 1669.
2) PHOTON FACTORY ACTIVITY REPORT 1995, #13, p. A-20.
3) Robert K. Tyson, "Principles of Adaptive Optics", Academic Press.
4) M. Born and E. Wolf, "Principles of Optics", Pergamon Press, sixth edition (1980).
5) X. Tian, M. Itoh, T. Yatagai, Appl. Opt. **34** (1995) 7213.

3.4 Spatial Coherency of the Synchrotron Radiation at the Visible-Light Region and its Application for the Electron-Beam Profile Measurements

The principle of object-profile measurement by means of the spatial coherency of light is known as van Cittert-Zernike's theorem.[1] It is well known that A. A. Michelson measured the angular diameter of stars by this theorem.[2] We recently applied this method to measure the beam profile. At first, a basic investigation of the spatial coherence of synchrotron radiation (SR) in the visible light region was performed. In the second, a measurement of the vertical beam profile was demonstrated by applying this method.

3.4.1 Spatial Coherency of the SR for σ- and π-Polarized Components

In the vertical plane, the elliptical polarity of the synchrotron radiation is opposite against the median plane of the electron-beam orbit. Therefore, one can expect a phase difference of π in the interferograms corresponding to σ- and π-polarized components. If one divides the wave front of the light beam into two beams against the median plane, and then, couple them again to make an interferogram, the intensity of the interference fringe is given by

$$I_\sigma = (a_1^2 + a_2^2)\left\{1 + \frac{2a_1a_2}{a_1^2 + a_2^2}\cos(\delta)\right\}. \quad (1)$$

$$I_\pi = (a_1^2 + a_2^2)\left\{1 + \frac{2a_1a_2}{a_1^2 + a_2^2}\cos(\delta + \pi)\right\}. \quad (2)$$

where δ denotes the optical-path difference in phase: a_1 and a_2 denote the amplitudes of the light beams corresponding to two optical paths in the interferometer. It is expected that there will be a phase difference of π in the the interferograms between the σ and π-polarized components.

A two-beam interferometer of the wave-front division type was designed and constructed by using polarized quasi-monochromatic rays. A schematic drawing of the interferometer is shown in Fig. 39. A double-slit assembly was applied for dividing the wave front. The distance between the two slits can be continuously changed from 5 mm to 80 mm. The resultant interferogram is measured by a CCD (Plinix, TM765) and an image processor (Spiricon, LBA-100A).

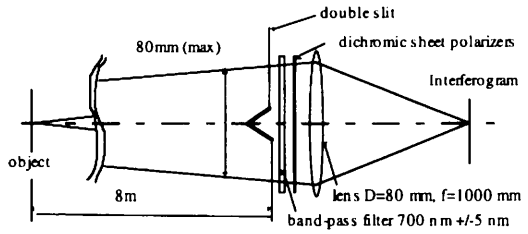

Fig.39 Design of the interferometer.

In order to confirm the above-mentioned characteristics of the SR, interferograms were measured for both the σ- and π-polarized components of the synchrotron light at optical laboratory 2 of BL-27. Observed intereferograms corresponding to the σ- and π-polarized components are shown in Fig. 40, which include the interference effect together with a diffraction effect. Comparing these two interferograms, it can be seen that there is a phase difference of π between them, as expected. For measuring the beam profile, one (σ) of the polarized components was selected.

For later use, the absolute value (visibility) and phase of the complex degree of spatial coherence were measured by changing the distance of the double slits from 5 mm to 15 mm. The results are shown in Figures 41 and 42. As shown in Fig. 41, the visibility was almost zero at a slit distance of 15 mm. This means that the beam profile had no more higher spatial frequency parts of the Fourier component.

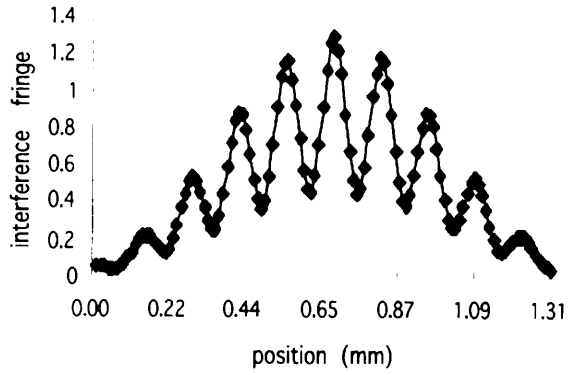

a) interferogram by σ -polarized components.

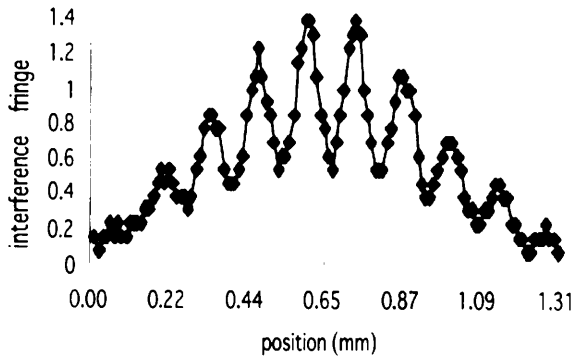

b) interferogram by π-polarized components.

Fig.40 Results of interferograms for the σ- and π-polarized components. The distance between the double slits is 5 mm.

3.4.2 Application of the Spatial Coherency for a Vertical Beam-Profile Measurement

Light emitted by an object of finite size generally does not have a perfect spatial coherence, but has a certain degree of coherence. It is possible to reconstruct the profile of the object from the data of interferograms which are taken for various distances of double slits. Since the interferograms are very sensitive to the object size, this method will be particularly useful for measuring small beam sizes, such as a vertical beam-size measurement for very low-emittance beams.

According to van Cittert-Zernike's theorem, the object profile is obtained by a Fourier transform of the complex degree of spatial coherence. Let $f(\Theta)$ denote the profile of an object (in our case, the beam) as a function of the angular diameter Θ, and let $\gamma(D)$ denote the complex degree of spatial coherence, these values are related by the following Fourier transform relation:

$$\gamma(D) = \int f(\Theta)\exp(-ikD\Theta)d\Theta \qquad (3)$$

$$= C(D) + iS(D),$$

where $C(D)$ and $S(D)$ denote the cosine and sine Fourier transforms of $f(\Theta)$, respectively. The interferogram is then given by

$$I(\theta) = 1 + |\gamma(D)|\cos\{kD(\theta+\varphi)\}, \qquad (4)$$

and

$$\varphi = \tan^{-1}\frac{S(D)}{C(D)}. \qquad (5)$$

Therefore, from the data of the absolute value and phase of the complex degree of spatial coherence, we can reconstruct the beam profile by the Fourier transform. The result of the vertical beam profile, obtained from the data of Figs. 41 and 42, is shown in Fig. 43. A least-square beam size σ by a second-order moment was 214 μm.

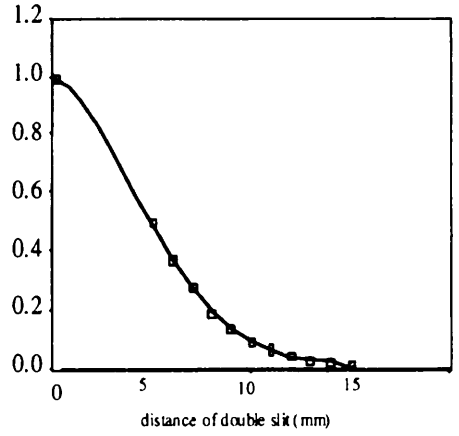

Fig. 41 Absolute value of the complex degree of spatial coherence, which was obtained from the measurement.

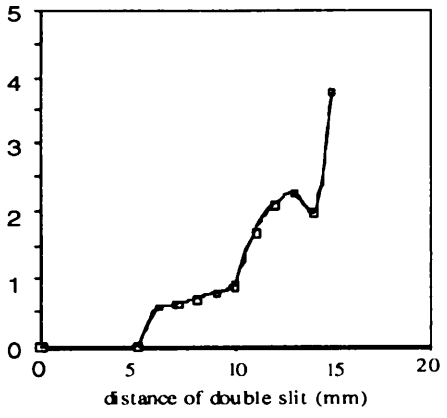

Fig. 42 Phase of the complex degree of spatial coherence obtained. The vertical axis denotes the phase in radians.

Due to the phase term of the complex degree of spatial coherency, the beam profile had an asymmetric distribution. This asymmetry in the distribution curve was mainly caused by a deformation of the extraction mirror for the synchrotron light. A large astigmatism term had been observed by the in situ measurement of the surface flatness of the mirror.[3] In a similar technique as the noise-elimination processing for electronic signals it is possible to eliminate an asymmetric part of the Fourier components of the complex degree of spatial coherency. As the easiest way, we tried to neglect the Fourier sine terms. The result is shown in Fig. 44. Comparing Fig.44 with Fig. 43, the asymmetric part caused by the mirror

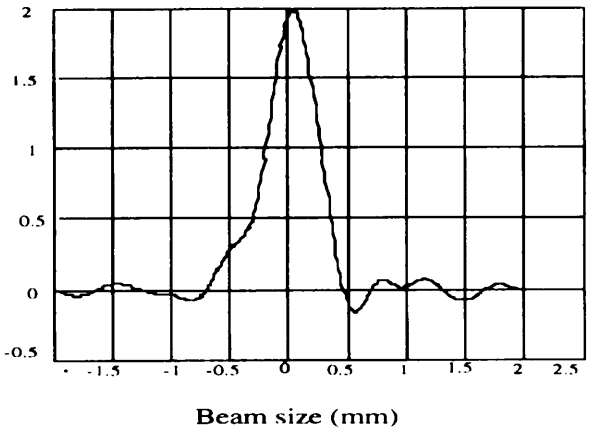

Fig. 43 Beam profile obtained by a Fourier transform of the complex degree of coherence.

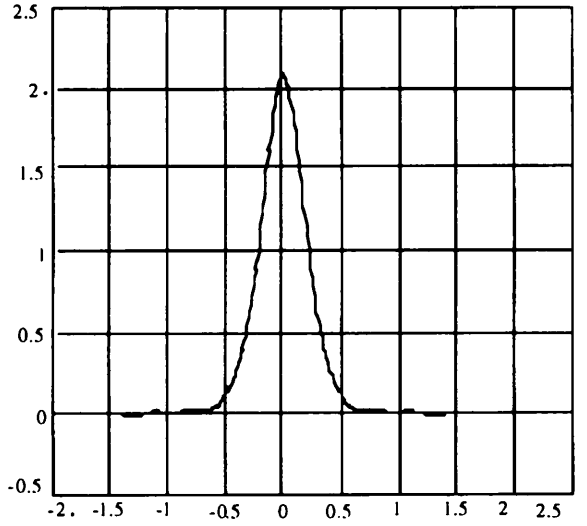

Fig. 44 Beam profile obtained by a Fourier cosine transform. The abscissa is the beam size (mm).

deformation was eliminated. The least-square beam size in Fig. 44 is 202 μm. This technique is very useful for eliminating unknown effects (asymmetric terms of the wavefront aberration) of the optical components between the object and the image plane. It should be noted that we cannot apply this technique for the following cases: 1) an optical system having a symmetric wave-front error, such as a spherical aberration and 2) a beam having an asymmetric distribution in original.

References

1) M. Born and E. Wolf, "Principles of Optics", Pergamon Press, sixth edition (1980) p. 508.
2) A. A. Michelson, Astrophys. J. **51** (1920) 257.
3) T. Mitsuhashi and M. Katoh, Proceedings of the Fifth European Particle Accelerator Conference, SITGES (Barcelona), June 1996, p. 1669.

3.5 Numerical Study for a Two-beam Instability due to Ion Trapping

The two-beam instability, caused by the interaction between ions and the electron beam, has been studied numerically. Ion-trapping phenomena have been observed at the PF ring for a long time. Under the recent vacuum conditions, a coupled-bunch instability due to ion trapping can be observed above a threshold current of about 40mA if the ring is uniformly filled and the octupole magnets are turned off. In order to obtain a better understanding of the instability due to ion trapping, a numerical analysis was performed. The study is briefly introduced here and the details are described in ref.1).

Positive ions, which are produced due to ionization of residual gas by the beam, are trapped by an attractive force. The ions oscillate at a frequency determined by the potential of the electron beam. The oscillation frequency is expressed by

$$\omega_i = \sqrt{\frac{2n_e r_e c^2}{M_i/m_e}\frac{1}{\sigma_x(\sigma_x+\sigma_y)}}, \qquad (1)$$

where n_e , $\sigma_{x,y}$ are the line density and the size of electron beam, respectively, and M_i , m_e are the masses of the ion and electron, respectively. The oscillation frequency (ω_i) of ions is $2\pi \times 1.19$ MHz at a beam current of I=40mA, betatron functions of $\beta_{x,y}$=10m and x-y coupling of 1%. This frequency is very close to the coherent frequency ($(1-\Delta\nu_y)\omega_0$) of the beam. The coupled-bunch instability is induced by coupling between the coherent motions of the beam and ions.

The coupled motion of the beam and ions trapped in the beam potential was studied by using a simulation method based on a rigid Gaussian-beam model. The equations of motion for a bunch and ions are expressed as follows:

$$\frac{d^2 x_e}{dt^2} + K(s)x_e = \frac{r_e}{2}\sum_{j=1}^{N} F_G(x_e - x_{i,j};\sigma(s))\delta(s-s_i). \qquad (2)$$

$$\frac{d^2 x_{i,j}}{dt^2} = \frac{N_e r_e c^2}{2M_i/m_e} F_G(x_{i,j} - x_e;\sigma(s))\delta(t-t(s_i)). \qquad (3)$$

where x_e and x_{ij}, are the positions of the electron bunch and the j-th ion, respectively, F_G is given by the Bassetti-Erskine formula and N_e is the number of electrons in a bunch. N_i is the number of ions, which are represented by macro particles in the simulation.

The residual gas components in the vacuum chamber are mostly CO and H_2 in the PF ring. A typical spectrum consisted of 48% for CO and 41% for H_2. The ionization cross section of CO is about 6-times higher than that of H_2. We then assume that CO plays a dominant role in the two-beam instability, and neglect other species of ions.

Figure 45 shows the vertical coordinate of all bunches which pass through a certain location in the ring when the two-beam instability occurs. It can be seen that the bunch pattern shows coherent motion at the frequency of $(1-\Delta\nu_y)\omega_0$. Figure 46 shows the growths of the coupled-bunch mode for some cases of vacuum pressure. The growth time was 1200 turns (1200 times the revolutions period) for a partial pressure of 10^{-9} Torr for CO gas. Since the actual pressure is about half or less than this, the growth time would be ~2000 turns or more. The instability can be controlled by introducing Landau damping by means of octupole magnets. The growth time obtained from the

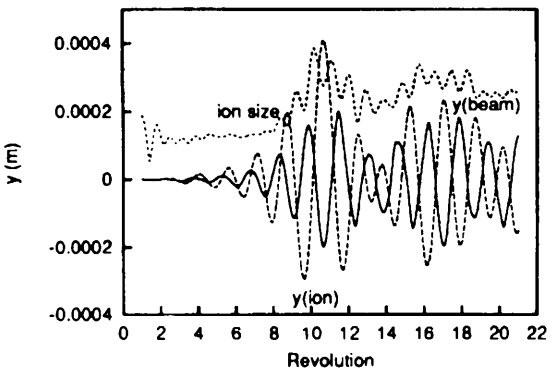

Fig. 45 Coupled-bunch pattern due to ion trapping.

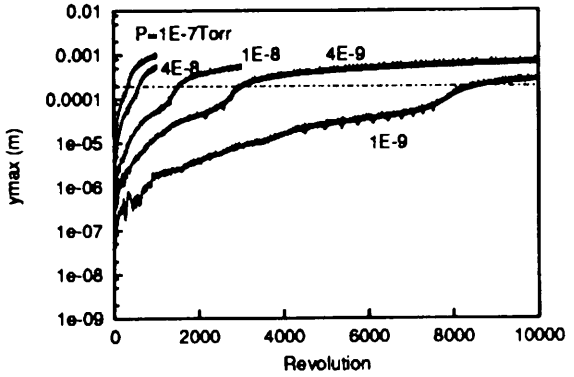

Fig.46 Growth of the bunch amplitude at various vacuum pressure.

simulation was consistent with the Landau damping time which is required to cure the instability.

Reference

1) K. Ohmi, KEK Preprint 96-160, to be appeared in Phys. Rev. **E55**.

4. STORAGE RING SPECIFICATIONS

This section contains principal specifications of the 2.5-GeV PF ring to provide quick and handy information for users and machine physicists. These parameters are under the present lattice configuration, that is, before reconstruction to the low-emittance lattice. Detail specifications and parameters are available through the World Wide Web (URL: http://pinecone.kek.jp/pfring.status.html).

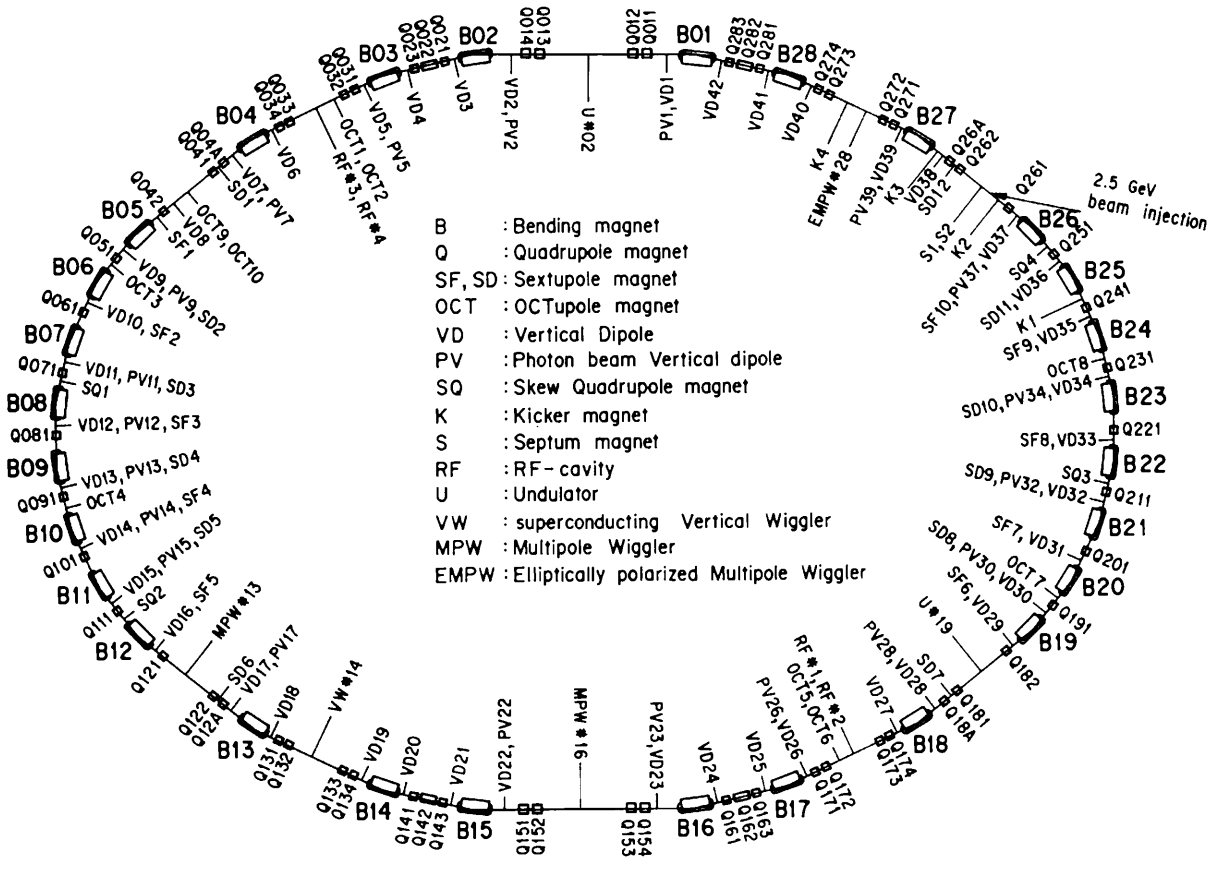

Fig.47 Ring lattice components.

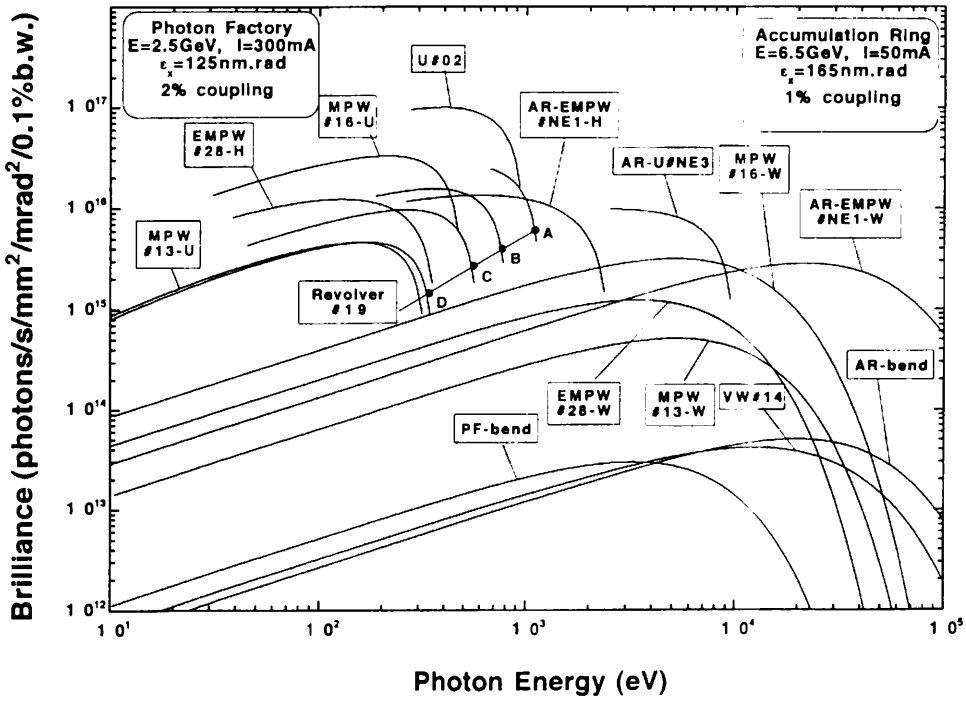

Fig.48 Synchrotron radiation spectra.
Brilliance of radiation vs. photon energy for the insertion devices (U#02,MPW#13,VW#14,MPW#16,Revolver#19 and EMPW#28) and the bending magnet (Bend) of the PF, and for the insertion device (EMPW#NE1) of the AR. The name of each source is assigned in Table 10. Several insertion devices have both undulator and wiggler modes, which are denoted by U or W, respectively. The spectral curve of each undulator (or undulator mode of multipole wigger) is a locus of the peak of the first harmonics within the allowable range of K-parameter. Spectra of Revolver#19 are shown for four kinds of period lengths.

Table 10 Insertion devices

Calculated spectral performances of the bend source and 6 insertion devices at the Photon Factory. E/I: beam energy and current, λ_u: period length, N: number of periods, L: length of undulator or wiggler, G_y (G_x): minimum vertical (horizontal) gap height, B_y (B_x): maximum vertical (horizontal) magnetic field, P: pure configuration, H: hybrid configuration, S.C.: superconducting magnet, σ_x, σ_y: horizontal or vertical beam size, $\sigma_{x'}$, $\sigma_{y'}$: horizontal or vertical beam divergence, K_y (K_x): horizontal (vertical) deflection parameter, ε_1 / ε_c: photon energy of the first harmonic (critical energy in the case of bend source or wiggler), $\Delta\varepsilon/\varepsilon$: relative bandwidth, Pc: degree of circular polarization, $\mathcal{D}$: photon flux in unit solid angle (photons /s •mrad² •0.1%b.w.), $\mathcal{B}$: brilliance (photons /s •mm² •mrad² •0.1%b.w.), P_T: total radiated power, $dP/d\Omega$: power in unit solid angle. Different operating modes of undulator and wiggler are denoted by -U and -W, respectively.

Name	E/I	λ_u	N	L	G_y (G_x)	B_y (B_x)	Type of	σ_x	σ_y	$\sigma_{x'}$	$\sigma_{y'}$	K_y (K_x)	$\varepsilon_1/\varepsilon_c$	$\Delta\varepsilon/\varepsilon$	$\mathcal{D}$	$\mathcal{B}$	P_T	$dP/d\Omega$
	GeV/mA	cm		m	cm	T	magnet	mm	mm	mrad	mrad		keV				kW	kW / mrad²
Bend								0.74	0.26	0.38	0.037		4.0		3.5E13	2.9E13		0.060
U#02		6.0	60	3.6	2.8	0.4	H (NdFeB)	0.78	0.11	0.16	0.022	2.25	0.28	0.029	5.2E16	9.7E16	0.68	2.7
MPW#13-W		18.0	13	2.5	2.7	1.5	H (NdFeB)	1.66	0.17	0.15	0.019	25 0	6.2		9.7E14	4.9E14	6.7	2.6
-U												2.0	0.108	0.086	5.7E15	3.2E15	.042	0.19
VW#14					5.0	5.0	S.C.	1.05	.096	0.16	0.025		20.8		2.2E13	3.4E13		0.18
MPW#16-W	2.5 / 300	12.0	26	3.1	1.9	1.5	H (NdFeB)	0.78	0.11	0.16	0.022	16 8	6.2		1.8E15	3.1E15	8.3	4.9
-U												2.0	0.162	0.050	1.6E16	2.8E16	0.12	0.52
Revolver		5.0	46	2.3	3.0	0.28	H (NdFeB)	1.66	0.17	0.15	0.019	1.3	0.637	0.021	4.1E16	2.3E16	0.21	1.27
#19		7.2	32			0.41	H (NdFeB)					2.7	0.176	0.039	2.1E16	1.2E16	0.44	1.54
		10.0	23			0.53	H (NdFeB)					5.0	0.0436	0.047	6.9E15	3.8E15	0.78	1.53
		16.4	14			0.62	P (NdFeB)					9.5	0.0078	0.066	1.2E15	6.3E14	1.05	1.09
EMPW#28		16.0	12	1.9	3 (11)	1 (0.2)	P (NdFeB)	1.05	.096	0.16	0.025							
-W												15 (1)	4.2 (Pc=89%)		2.5E14	3.4E14	2.3	0.38
-U												1 (1)	.18 (Pc=99%)	0.11	6.3E15	9.8E15	0.02	0.058

Table 11 General parameters of the PF storage ring.

Energy		2.5 GeV	(0.75 GeV to 3 GeV)
Initial stored current	(multi-bunch)	400 mA	(max 773 mA)
	(single bunch)	65 mA	(max 104 mA)
Emittance		130 nm·rad(horizontal) ~2 nm·rad(vertical)	
Circumference		187 m	(bending radius=8.66 m)
RF frequency		500.1 MHz	(harmonic number=312)
Injection		2.5-GeV Linac	(positron/electron)
Beam lifetime		60 h (at 300 mA)	I·τ ≥18 A·h (at ~250 mA ~ 350 mA)
Vacuum pressure		≥ 3×10^{-9} Torr (at 300 mA) P/I ~ 8×10^{-10} Torr/A (at ~250 mA ~ 350 mA) ~ 3×10^{-11} Torr (at 0 mA)	
Insertion devices		Superconducting vertical wiggler 5T 60 period undulator K=1.78~0.1 26 period multipole wiggler/undulator 1.5T~0.04T Four way revolver type undulator 14 period multipole wiggler Elliptically polarized multipole wiggler	
SR channels		SR experiment 22 Beam diagnosis 3	

Table 12 Beam parameters.

	Horizontal tune ν_x	8.45
	Vertical tune ν_y	3.30
	Momentum compaction factor α	0.015
	Natural chromaticity ξ_x	-15.8
	ξ_y	-8.6
	Bunch length σ_z	1.5 cm
	Transverse damping time	7.8 msec
	Longitudinal damping time	3.9 msec
	Energy spread	7.3×10^{-4}
	Radiation loss	400 keV

Table 13 Summary of Beamline Front Ends in FY 1996.

Beamline	Affiliation	Source	Spectral range	Status
BL-1	KEK-PF and NTT	Bending magnet (B1)	VUV and soft X-ray	in operation
BL-2	KEK-PF	60-period undulator	Soft X-ray	in operation
BL-3	KEK-PF	Bending magnet (B2 & B3)	VUV and soft X-ray	in operation
BL-4	KEK-PF	Bending magnet (B4)	X-ray	in operation
BL-5	KEK-PF	Multipole wiggler/undulator	-	under installation
BL-6	KEK-PF	Bending magnet (B6)	X-ray	in operation
BL-7	KEK-PF and University of Tokyo	Bending magnet (B7)	VUV and X-ray	in operation
BL-8	Hitachi Ltd.	Bending magnet (B8)	VUV and X-ray	in operation
BL-9	Nippon Electrical Co. (NEC)	Bending magnet (B9)	VUV and X-ray	in operation
BL-10	KEK-PF	Bending magnet (B10)	X-ray	in operation
BL-11	KEK-PF	Bending magnet (B11)	VUV and soft X-ray	in operation
BL-12	KEK-PF	Bending magnet (B12)	VUV	in operation
BL-13	KEK-PF	27-pole wiggler/undulator	Soft and hard X-ray	in operation
BL-14	KEK-PF	Superconducting vertical wiggler	Hard X-ray	in operation
BL-15	KEK-PF	Bending magnet (B15)	X-ray	in operation
BL-16	KEK-PF	53-pole wiggler/undulator	Soft and hard X-ray	in operation
BL-17	Fujitsu Ltd.	Bending magnet (B16 & B17)	VUV and X-ray	in operation
BL-18	ISSP and KEK-PF	Bending magnet (B18)	VUV and X-ray	in operation
BL-19	ISSP and KEK-PF	Multi-undulator	VUV	in operation
BL-20	KEK-PF	Bending magnet (B20)	VUV and X-ray	in operation
BL-21	KEK-PF	Bending magnet (B21)	Beam diagnosis	in operation
BL-27	KEK-PF	Bending magnet (B27)	Soft X-ray and X-ray	in operation
BL-28	KEK-PF	25-pole wiggler/undulator	Circularly polarized VUV and soft X-ray	in operation

C. TRISTAN AR

In the period from September, 1995, to December, 1996, the TRISTAN Accumulation Ring (AR) was used for such purposes as: 1) synchrotron radiation (SR) research, 2) a machine study for the KEK B factory (KEKB) and 3) injection to the TRISTAN Main Ring (MR), which was operated as a light source.[1] The operation summary and operation statistics of the AR are given in Table 14 and 15, respectively.

Operation for SR research was carried out without any serious problems. The machine and beam parameters of the AR are given in Table 16. A beam current of 40 mA was stored in a single bunch, as usual. The beam energy was set at 6.5 GeV, except for the period during April to June, 1996, when it was lowered to 6 GeV because the maximum RF voltage was decreased due to the replacement of several APS cavities to a prototype of the super conducting cavity for the KEKB. The major hardware problems which affected the SR research were two vacuum leaks at the bellows and a ground fault at the bus bar which is connected to a power supply.

The machine study for the KEKB was carried out at an energy of 2.5 GeV. In the filling of 16 bunches a beam current more than 500 mA was successfully stored using prototypes of super-conducting and room-temperature RF cavities for the KEKB. A prototype of bunch-by-bunch feedback system worked well to suppress the coupled-bunch instability. A data-logging system was developed based on EPICS, which is the control system of the KEKB. The logging system collects such data as the beam current, vacuum pressure, cavity status and temperature of the bellows, ceramic

chambers and gate valves. The system, especially the temperature monitor, will be useful for future operation of the AR.

Reference

1) This activity report.

Table 14 Operation summary of TRISTAN AR (From Sep. 1995 to Dec. 1996).

Operation period	
1995. 9.14 - 12.27	SR research and injection for the TRISTAN MR
1996. 3.28 - 6.17	SR research and machine study for the KEKB
7. 1 - 7.22	Dedicated machine study for the KEKB
10.17 - 12. 2	Dedicated machine study for the KEKB

Table 15 Operation statistics of TRISTAN AR (From Sep. 1995 to Dec. 1996).

	Time(hr)
SR research and MR injection	2934
Machine study and beam tuning for the AR	1699
Suspended operation due to MR study	459
Failure	186
Others	171
Total	5449

Table 16 Machine parameters of TRISTAN AR.

Energy	6.5 GeV
Natural emittance	293 nm rad
Circumference	377 m
RF frequency	508.6 MHz
Bending radius	23.2 m
Energy loss per turn	6.66 MeV
Damping time	
horizontal	2.5 ms
vertical	2.5 ms
longitudinal	1.2 ms
Natural bunch length	18.6 mm
Momentum compaction factor	0.0129
Natural chromaticity	
horizontal	-14.3
vertical	-13.1
Stored current	40 mA
The number of bunches	1
Beam lifetime	240 min.

Collaborations

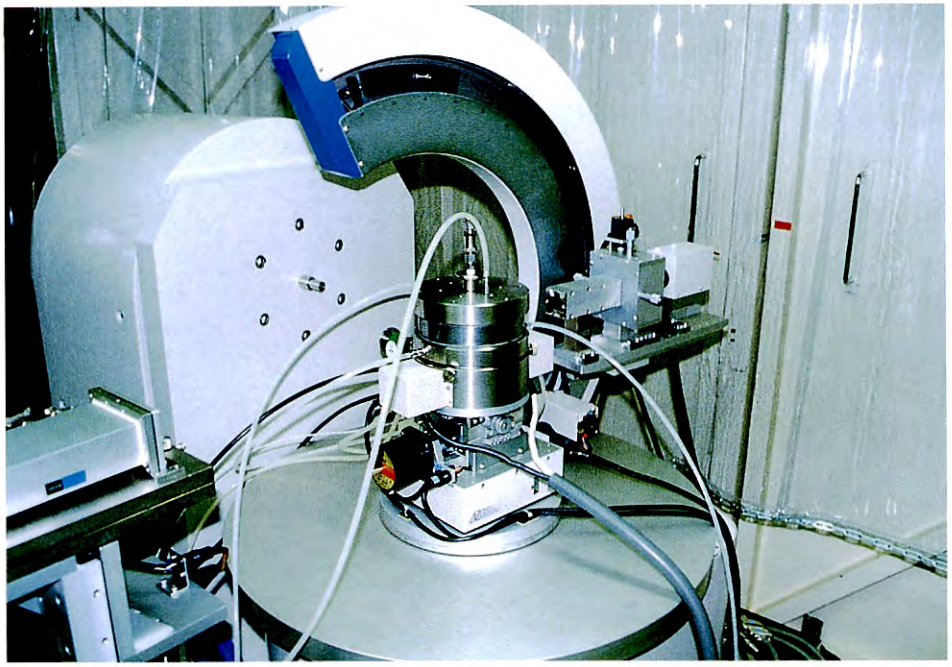

Grazing incidence X-ray diffractometer of Fujitsu beamline (BL-17C)

You can jump to the article by clicking its title.

CONTENTS

A RESEARCH CENTER FOR SPECTROCHEMISTRY, UNIVERSITY OF TOKYO

1. PRESENT STATUS OF BL-7A AND 7B

For BL-7A, equipped with a plane-grating monochromator, a Pt-coated toroidal mirror made of Glidcop (alumina dispersed Cu) was installed in 1994. The performance of the mirror was studied during the first machine time. It was found that a single peak was split to a double peak due to incomplete shape if the whole area of the mirror was irradiated. This obliged us to reduce the aperture, which caused an intensity reduction if we need sufficient resolution. Nevertheless, some interesting results were obtained for monolayer coveraged surfaces. NEXAFS studies of organic polymers were also carried out.[1,2]

No improvement has been made on BL-7B (Seya-Namioka monochromator) after replacing the first mirror by a Si mirror. A number of studies have been carried out at this beamline, and especially, Prof. Suga's group has actively worked on photoemission studies, photoelectron diffraction and holography studies.

2. RESEARCH ACTIVITIES USING BL-7A AND 7B

2.1 Photon stimulated desorption of the NO/Si(111) surface[3]

Figure 1 shows the UPS spectra of a Si(111) 7 × 7 clean surface and a NO-adsorbed surface at 90 K, measured at a photon energy of 35 eV. There are three prominent peaks and one shoulder in the spectrum of the NO adsorbed Si(111) surface. These structures are

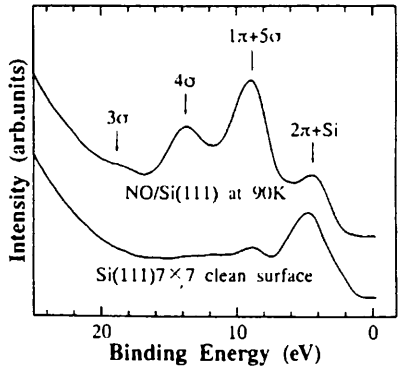

Fig. 1 UPS spectra of a Si(111) 7×7 clean surface and NO/Si(111) surface at 90 K.

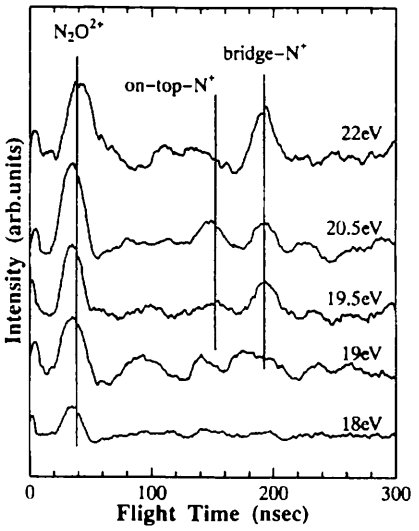

Fig. 2 TOF spectra excited at different photon energies.

assigned to the 2π (4.4 eV), 1π + 5σ (9.0 eV), 4σ (13.8 eV) and 3σ (19.0 eV) molecular orbitals. Figure 2 shows the TOF spectra at different photon energies around 20 eV, which roughly corresponds to the 3σ orbital (mainly O 2s) excitation. The dominant desorbed ion species excited in this photon energy range have been identified as H^+, two kinds of N^+, and N_2O^{2+}. From the photon energy dependence, the threshold energy of the bridge-N^+ was estimated to be 19 eV, which was nearly the same as that of the on-top N^+, although the latter was less prominent. This suggests that the desorption process takes place through an Auger excitation mechanism, such as the Knotek-Feibelmann model, since N^+ is desorbed after excitation of the 2s core of the O atom. Since the excitation of the 3σ orbital causes the desorption of N^+ from both the bridge and on-top site NO, it seems reasonable to suppose that the molecularly adsorbed NO on the Si(111) surface sits with N up and O down on the surface, and that the N^+ ion desorbs from this molecularly adsorbed NO.

2.2 Photoelectron holography of the Si(001) surface[4]

The two-dimensional photoelectron angular distribution of the Si(001) surface has been measured at BL-7A at several photon energies by using a two-dimensional display-type analyzer developed by Daimon et al. A Si(001) clean surface was prepared by

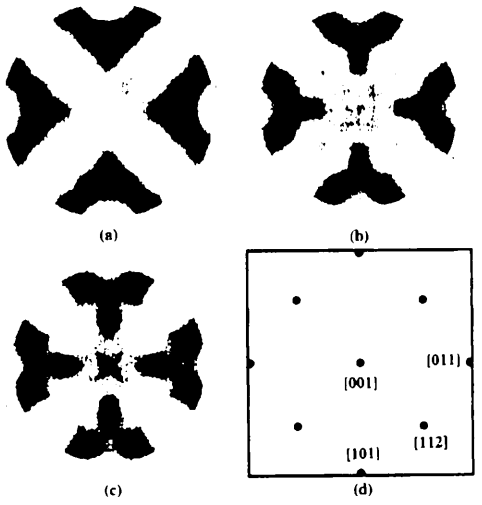

Fig. 3 Si 2p photoelectron diffraction patterns from a Si(001) surface. The photoelectron kinetic energies are (a) 350,(b)450, and (c)650 eV. The figure (d) shows the position of crystallographic axes such as [112] and [011] in these patterns.

repeated heating for 5 s up to 1523 K under a pressure of 10^{-8} Pa. The surface quality was confirmed by the observation of a clear 2 × 1 LEED pattern. Figure 3 shows the Si 2p photoelectron diffraction patterns at kinetic energies of 350 eV, 450eV and 650 eV. The [112] and [011] directions are marked in Fig. 3 (d). The brighter regions correspond to a stronger photoemission intensity. The center of the picture is the surface normal direction [001]. The edge of the picture corresponds to a polar angle (θ) of 47°. The patterns were normalized by the transmittance efficiency pattern, and averaged utilizing the fourfold and horizontal and vertical mirror symmetry.

In order to interpret the patterns, three-dimensional images were calculated with several algorithms: (1) a basic method with a Fourier transformation at one kinetic energy over k space, considering the phase factor due to the path-length. (2) an energy summation of the above results, (3) a Fourier transformation within small k-space windows, and (4) their combinations. Atomic images produced by these methods were compared with the crystal symmetry. The results show that the energy-summed small-window method, called SWEEP, gives the best images.

Photoelectron diffraction experiments were also carried out for kish graphite[5] and TaS_2[6] to reveal the band structure around the Fermi edge.

2.3 Adsorption of acetylene and ethylene on the Si(001) 2×1 surface studied by NEXAFS and UPS[7]

The structures of unsaturated hydrocarbons, such as acetylene and ethylene on Si(001) have been studied with HREELS, and theoretical calculations by many groups and a number of models have been proposed. Polarization-dependent NEXAFS is known to provide useful information about adsorbed structures. In the present study, the adsorbed structures of acetylene and ethylene on a Si(001) 2×1 surface were investigated by C K-NEXAFS and UPS at BL-7A and 7B.

Figure 4 shows the C K-NEXAFS spectra of acetylene and ethylene on Si(001) at normal and grazing-incident angles, compared with those of the corresponding gaseous molecules. As for acetylene, the π* resonance shows a clear polarization dependence: the π* orbital parallel to the surface remains, while that normal to the surface diminishes. The π* peak disappears in the spectrum of ethylene on Si(001). These results indicate that the π* orbital normal to the surface has formed a chemical bond with the Si dangling bonds. On the other hand, the σ*(C-C) peaks of acetylene and ethylene on Si(001) move

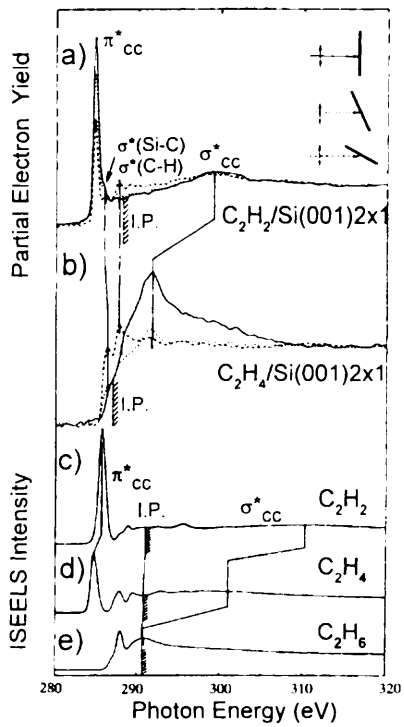

Fig. 4 C K-NEXAFS spectra of acetylene and ethylene adsorbed on a Si(001) surface. Gaseous EELS spectra of acetylene, ethylene and ethane by A.P.Hitchcock are also shown for the comparison.

significantly to the lower energy side and coincide with those of gaseous ethylene and ethane, respectively. The relative energy of the σ* resonance from the ionization threshold is related to the C-C bond length. In the present case, the bond distances, R(C-C), in acetylene and ethylene on Si(001) are estimated to be 1.35 Å and 1.52 Å, respectively.

In the UPS spectra, the peak associated with the dangling bond, almost disappears upon molecular adsorption. These results give firm evidence of the Si-dimer maintained di-σ structure model for both cases.

References

1) H. Ishii et al., J. Electron Spectrosc. **76** (1995) 553.
2) S. Narioka et al., Phys. Rev. B**52** (1995) 2362.
3) K. Sakamoto et al., J. Electron Spectrosc. 80 (1996) 125.
4) T. Nakatani et al., J. Synchrotron Rad. **3** (1996) 239.
5) H. Nishimoto et al., J. Electron Spectrosc. **78** (1996) 465.
6) H. Nishimoto et al., Solid State Comm. **98** (1996) 671.
7) F. Matsui et al., Surf. Sci. submitted.

B. SYNCHROTRON RADIATION LABORATORY, INSTITUTE FOR SOLID STATE PHYSICS, UNIVERSITY OF TOKYO

1. INTRODUCTION

The Synchrotron Radiation Laboratory of the Institute for Solid State Physics, University of Tokyo, has constructed the Revolver undulator and three beamlines (BL-18A, BL-19A and BL-19B) in the Photon Factory, and has opened them to general users in collaboration with the staff members of the Photon Factory. These beamlines have been constructed aiming to be dedicated to advanced solid state spectroscopies, such as angle-resolved photoelectron spectroscopy (ARPES) of surfaces and interfaces (BL-18A), spin-resolved photoelectron spectroscopy of magnetic materials (BL-19A) and soft X-ray fluorescence spectroscopy (BL-19B). In the fiscal year of 1996, 28 publications appeared in refereed journals. In the following we describe a few recent scientific activities and new developments in these beamlines.

2. SCIENTIFIC ACTIVITIES

BL-18A was opened to users in 1991, and since then many active users have investigated the electronic structures of various materials in this beamline. Recent studies performed in this beamline are ARPES experiments of metal and semiconductor surfaces, magnetic semiconductor surfaces and metal over layers on Si-single crystal surfaces.[1-6] Figure 5 shows the Si 2p core level photoelectron spectra of In adsorbed Si(001) surface measured with 132 eV.[1] Precise information on the chemical bonding between In and Si dimers and its dependence on the Si(001) surface structure has been obtained by curve-fitting analyses.

Beamlines BL-19A and BL-19B were constructed to be dedicated to solid state spectroscopies which need high intensity of light from the undulator. In BL-19A, spin-resolved photoemission experiments on magnetic materials have been carried out.[7-9] Figure 6 shows spin-resolved valence-band satellites of ferromagnetic Ni(110).[9] From the spin polarization of the satellites and their photon energy dependence, it was shown that the valence band satellite could be interpreted by the multiplet configuration of $3d^8$ and $3d^7$ final states

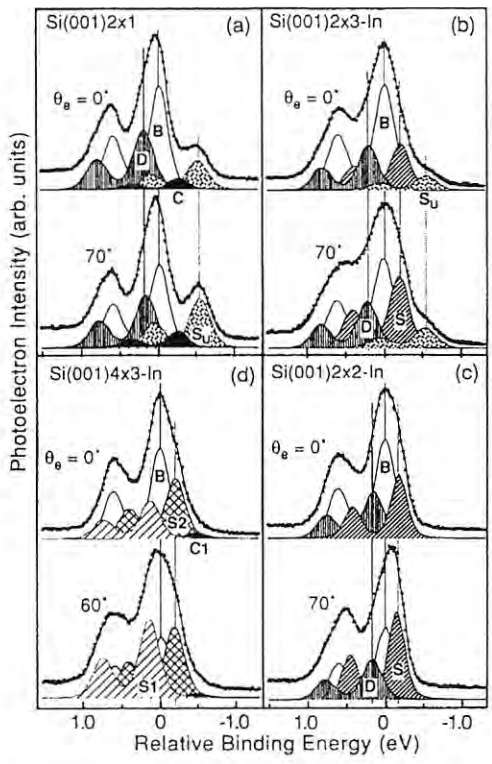

Fig. 5 Si 2p core level photoelectron spectra of In adsorbed Si(001) surfaces measured with 132 eV.

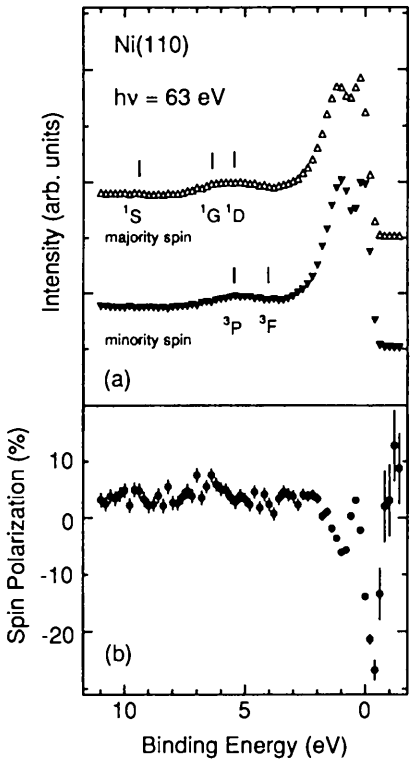

Fig. 6 Spin-resolved valence band satellites of ferromagnetic Ni(110).

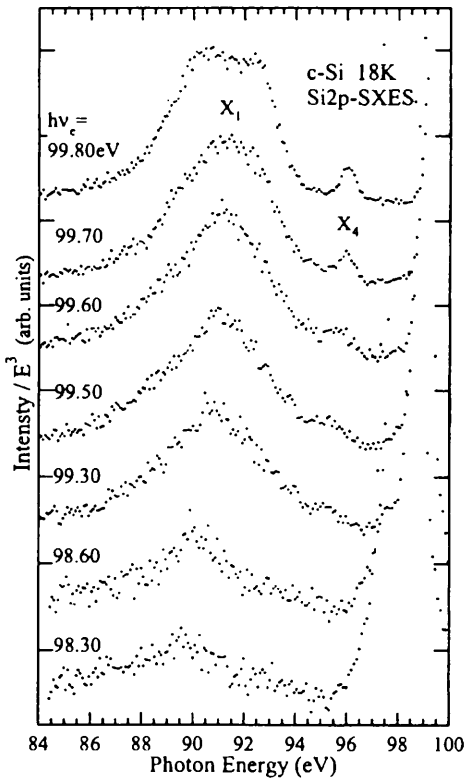

Fig. 7 $L_{2,3}$ soft X-ray emission (SXE) spectra of Si measured at various photon energies which correspond to the excitation to the virtual states below the $L_{2,3}$ core exciton.

reflecting the strong electron correlation in the Ni valence states.

At BL-19B experimental apparatuses for soft x-ray fluorescence spectroscopy measurements were opened to users, and many experiments have been performed.[10-12] Figure 7 shows the $L_{2,3}$ soft x-ray emission (SXE) spectra of Si measured at various photon energies, which correspond to the excitation to the virtual states below the $L_{2,3}$ core exciton.[12] The abscissa is the SXE photon energy and the ordinate is the SXE intensity divided by the cube of the photon energy. By energy analyses of the Raman shifts, it was confirmed that the Raman scattering resonates at the $L_{2,3}$ core exciton, which is made around the X_1 conduction minimum and that the elementary excitation of the Raman scattering is the valence exciton, which is a transition from X_1 or X_4 points to X_1 conduction minimum.

3. NEW DEVELOPMENTS

Soon after BL-19A was opened to users in 1992, a design study and the construction of a compact-size Mott detector started, since the 100 keV Mott detector at BL-19A could not easily be dismounted from the beamline and transferred to the other beamline to utilize the circularly polarized light. After three years of research and development, a compact 40-keV Mott detector was completed and achieved a figure of merit of 1.9×10^{-4}, which is one of the highest levels of small Mott detectors ever constructed.[13] The new Mott detector (shown in Fig.8) is now combined with an angle-resolved photoelectron spectrometer, and dedicated to spin- and angle-resolved photoemission spectroscopy using a He discharge lamp. The new apparatus will be moved to BL-19A and opened to users in the very near future.

References

1) H. W. Yoem et al., Phys. Rev. B 53, 1948 (1996).
2) H. W. Yoem et al., Phys. Rev. B 54, 4456 (1996).
3) H. W. Yoem et al., Surf. Sci. 365, 328 (1996).
4) S. H. Oh et al., J. Electron Spectrosc. Relat. Phenom. 83, 77 (1997).
5) C. Y. Park et al., J. Korean Phys. Soc. 30, 225 (1997).

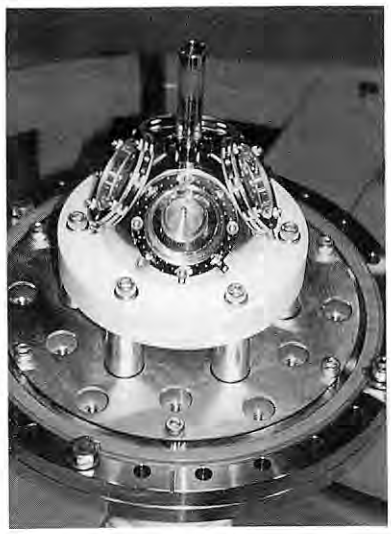

Fig. 8 Compact 40-keV Mott detector with a figure of merit of 1.9×10^{-4}, which is one of the highest levels of small Mott detectors ever constructed.

6) C. C. Hwang et al., J. Korean Phys. Soc. 30, 341 (1997).
7) K. H. Park et al., Phys. Rev. B 53, 5633 (1996).
8) K. Ono et al., Solid State Commun. 101, 739 (1997).
9) A. Kakizaki et al., Phys. Rev. B 55, 6678 (1997).
10) M. Fujisawa et al., Rev. Sci. Instrum. 66, 1584 (1995).
11) S. Shin et al., Phys. Rev. B 52, 15082 (1995).
12) S. Shin et al., Phys. Rev. B 53, 15660 (1996).
13) S. Qiao, PhD Thesis (University of Tokyo, 1997).

C. THE TSUKUBA ADVANCED RESEARCH ALLIANCE (TARA) SAKABE RESEARCH PROJECT

1. INTRODUCTION

The Tsukuba Advanced Research Alliance (TARA) Sakabe Research Project is a cooperative effort involving industry, government and universities to pursue an understanding of the maintenance of life and the perpetuation of species from a functional viewpoint. Advanced technologies are being developed to study the three-dimensional structures of biologically important molecules and to better understand the processes in which they are involved. The budget consists of donations from companies and subsidies from government organizations, such as Monbusho.

The members of this project include 88 scientists from 20 companies (13 of these companies have donated funding). Outside of industry, 44 scientists have come from universities and 8 from various research institutes.

2. TARA STATION AND FACILITIES

The experimental station of TARA was constructed at BL-6B. A Weissenberg-type camera using two 800 × 400mm large-format imaging plates (IP) as an X-ray detector was installed, and experiments were started in May, 1996. The radius of the IP cassette can be selected between 575.7mm and 967.9mm.

We have built a house for this project very close to the PF experiment hall. In this house there is a computer room (7.2m × 7.3m) and twelve small rooms (1.8m × 2.7m), of which three are used for resting while others are laboratories or offices. There are also four medium-size rooms used as a general office, larger laboratory, meeting room and library. Workstations, including an alpha station 5/266, two indigo2 high Impacts (R4400 and R10000), an S-4/5 and an alpha server 4000 are installed at the computer room. There are also many personal computers, such as Macs, Dells and NEC PCs, installed around the house. These computers are connected to the protein data- collection systems at BL-6A, BL-6B and BL-18B by 100 base Ethernet through optical fibers. Many software packages, such as WEIS, DENZO, QUANTA/CHARMm, Xsight, CCP4, PROTEIN, XTALVIEW, PHASES, XPLOR, O, MOLSCRIPT and ORTEP3, are provided.

These facilities are available to all protein co-users of the PF as well as members of TARA Sakabe research project.

3. PUBLICATIONS

A bulletin of the TARA Sakabe Project, called "Structure Biology", has been published. Although this project started only last year, already eleven papers have been published. Ryota Kuroki of Kirin Brewery Co., Ltd. and his coworkers showed that the substitution Thr 26 to His in the active site of T4 lysozyme causes the product to change from the α- to the β-anomer.[1] Noriyuki Habuka and Tsuyoshi Adachi of Japan Tabacco Inc. and their coworkers have determined the

structure of NS3 proteinase from the HCV BK strain by X-ray crystal analysis at 2.4 Å resolution.[2] Hirofumi Shoun and his coworker have isolated two isoforms of P450nor, termed P450norA and P450norB, and studied their nature.[3] Noriyoshi Sakabe of University of Tsukuba and his coworkers have studied the crystal structure of γ-Glutamil-transpeptidase from E.coli K-12.[4] Akio Takenaka of Tokyo Institute of Technology and his coworkers have reported on the crystallization and X-ray analysis of 3-isopropylmalate dehydrogenase.[5] H. Michel and S. Iwata of Max-Plank-Institute fur Biophysik and their coworkers have reported two papers.[6,7] Yukio Mitsui and Takamasa Nonaka of Nagaoka University of Technology and their coworkers have reported three papers.[8,9,10] Yuriko Yamagata of Osaka University and her coworkers have solved a DNA repair enzyme.[11]

References

1) R. Kuroki, L. H. Weaver and B. W. Matthews, Nature Structure Biology **2** (1995) 1007.
2) R. A. Love, H. E. Parge, J. A. Wickersham, Z. Hostomsky, N. Habuka, E. Woomaw, T. Adachi, and Z. Hostomska, Cell **87** (1996) 331.
3) K. Nakahara and H. Shoun, J. Biochem. **120** (1996) 1082.
4) H. Sakai, N. Sakabe, K. Sasaki, W. Hashimoto, H. Suzuki, H. Tachi, H. Kumagai, and K. Sakabe, J. Biochem. **120** (1996) 26
5) D. Tsuchiya, O. Matsumoto, T. Gorai, T. Sekiguchi, Y. Nosoh, and A. Takenaka, Acta Cryst. D**52** (1996) 1030.
6) S. Iwata, C. Ostermeier, B. Ludwig, and H. Michel, Nature **376** (1995) 660.
7) S. Iwata, M. Saynovits, T. A. Link, and H. Michel, Structures **4** (1996) 567.
8) N. Tanaka, T. Nonaka, M. Nakanishi, Y. Deyashiki, A. Hara, and Y. Mitsui, Structure **4** (1996) 33.
9) T. Senda, K. Sugiyama, H. Narita, T. Yamamoto, K. Kimbara, M. Fukuda, M. Sato, K. Yano, and Y. Mitsui, J. Mol. Biol. **255** (1996) 735.
10) N. Tanaka, T. Nonaka, T. Tanabe, T. Yoshimoto, D. Tsuru, and Y. Mitsui, Biochemistry **35** (1996) 7715.
11) Y. Yamagata, M. Kato, K. Yasumura, K. Tomita, K. Ihara, Y. Fujii, Y. Nakabeppu, M. Sekiguchi, and S. Fujii, Cell **86** (1996) 311.

D. NATIONAL INSTITUTE OF MATERIALS AND CHEMICAL RESEARCH (NIMC), AGENCY OF INDUSTRIAL SCIENCE AND TECHNOLOGY, MINISTRY OF INTERNATIONAL TRADE AND INDUSTRY

1. INTRODUCTION

In 1986, NIMC started the design and development of an undulator-based soft X-ray beam line in collaboration with PF and some other institutions, aimed at the application of high flux/high resolution soft X-rays to materials science, particularly to surface chemistry. After the installation of a 27-pole undulator at the PF ring, the soft-x-ray beamline (BL-13C) was designed,[1] following the Spherical Grating Monochromator (SGM) concept. The construction of the beamline was completed in 1991 and the first report on the performance was published in 1995.[2] Since then, BL-13C has been opened for and used by several user groups. During this period, NIMC, by collaboration with PF, has been in charge of the maintenance and improvement of BL-13C.

2. IMPROVEMENT OF THE BEAM LINE

At the end of FY1995, a replacement of the monochromator grating was performed, since the old mechanically ruled grating with a groove density of 750 gr/mm had problems with respect to the purity of monochromated X-rays. New gratings ruled by Shimadzu Co. Ltd. were made of SiC coated by gold with groove densities of 750 gr/mm and 350 gr/mm. Both of the gratings were holographically ruled with laminar shapes so that the higher harmonic diffraction light was minimized. The replacement resulted in the following advantages:

a) The energy range covered by the beam line has been expanded. The new grating with a groove density of 350 gr/mm covers the lower energy region down to 70 eV. As a result, for example, the Al L-edge absorption spectra can be measured at the beam line.
b) Because of the reflection feature of laminar gratings, photon fluxes at a higher energy region (> 500 eV) have been enhanced. For example, the flux at the Cu L-edge has become almost one magnitude more intense than before.

c) The interference light from gratings has been significantly suppressed. In addition, the new gratings have smaller amounts of adventitious carbon. Thus, the accuracy of I_0 correction in the absorption spectra has been greatly improved.

In the following fiscal year, the vertical focusing mirror (M2) as well as the controlling system were replaced. In the old system, a flat mirror made of SiO_2 was mechanically bent so that the cylindrical radius could be 125 m. The new system has employed a cylindrically shaped SiC (R=125 m) mirror with water cooling. This replacement has greatly improved the stability of the x-rays from the beam line, and has facilitated high energy-resolution spectra. At the same time, the goniometric system of the entrance slit was replaced so that the focusing on S1 by mirror M2 could be facilitated.

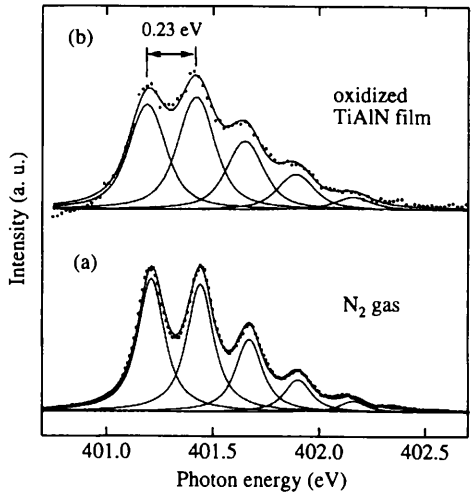

Fig. 9 N K-edge high-resolution absorption spectra of (a) molecular nitrogen and (b) oxidized TiAlN film.

3. SCIENTIFIC ACTIVITIES

Several studies using a high-flux/high-resolution undulator X-rays were performed in order to elucidate the surface and electronic structures of advanced materials during the latter half of FY95 and FY96.

NIMC investigated solid surface properties, particularly due to the interest in the catalytic properties. External surfaces of several kinds of zeolite particles were analyzed using photoelectron spectroscopy. The focus of the analysis was on depth-profiling by changing the analysis depth using energy-tunable SR X-rays. The study[3] elucidated the *real* surface composition of zeolite particles, which could never be analyzed by conventional X-ray sources. A part of the study was performed in cooperation with Petroleum Energy Center (PEC), which is a research organization funded by major Japanese petroleum refining companies. (PF-PAC, 94G184, 95G231)

Another project conducted by NIMC was analysis of the surface electronic properties of $La_{1-x}Sr_xCoO_3$ perovskites, which were known to have peculiar catalytic activities as oxidation catalysts. Through detailed analyses of the O K-edge and Co L-edge absorption spectra, together with the O1s and Co2p photoelectron spectra, the electronic structures of the surface oxygen species, which play important roles in catalysis, were successfully elucidated (PF-PAC, 95G232).

The Science University of Tokyo in collaboration with NIMC applied SR soft X-rays to the elucidation of the surface oxidation mechanisms of high-hardness coating metal nitride thin films. N K-edge absorption analyses were performed on virgin and high-temperature oxidized TiN, CrN and TiAlN films.[4] The analyses showed differences in the oxidation mechanisms of these films, which are evidently linked to the oxidation resistance of the films. An example of the high-resolution N K-edge spectra of partially oxidized nitride films is shown in Fig. 9. A comparison of the spectrum of an oxidized film (Fig. 9 (b)) with that of gaseous nitrogen molecules (Fig. 9 (a)) clearly showed the presence of molecular nitrogen in the interstices of the oxide matrices, which were formed during the course of the oxidation. This observation concluded a discussion on the intermediate species during the oxidation of the nitride films as to whether oxynitride, atomic nitrogen or molecular nitrogen was formed. In addition, a detailed analysis of the two spectra clarified the differences in the lifetime width and vibrational separation. These differences were discussed in relation to the electronic interaction between the interstitial molecules and the matrices[5] (PF-PAC, 94G185, 96G144).

The University of Tokyo conducted an X-ray photoelectron diffraction study on the CaO thin film formed on a CaF_2 single-crystal substrate. Taking advantage of high-flux and high-resolution X-rays, the signals from surface CaO were extracted by curve-fitting analyses of the Ca 2p photoelectron spectra. The results were successfully analyzed associated with theoretically calculated results (PF-PAC, 94G368).

Chiba University performed a photon-stimulated desorption (PSD) study on polystyrene films by inner-shell excitation, which enabled site-specific chemical bond cleavages. The analyses were performed on selectively deuterated polystyrene using a time-of-flight mass spectrometer under single-bunch operation modes of PF. By a comparison of the partial ion yield spectra of H^+ and D^+, the chemical sites responsible for the desorption of each deuterium could be determined[6] (PF-PAC, 95G386).

References

1) N. Matsubayashi, H. Shimada, K. Tanaka, T. Sato, Y. Yoshimura, and A. Nishijima, *Rev. Sci. Instrum.* **63** (1992) 1363.
2) H. Shimada, N. Matsubayashi, M. Imamura, T. Sato, Y. Yoshimura, T. Hayakawa, K. Hayakawa, A. Toyoshima, K. Tanaka, and A. Nishijima, *Rev. Sci. Instrum.*, **66** (1995) 1780.
3) H. Shimada, N. Matsubayshi, M. Imamura, T. Sato and A. Nishijima, *Catalysis Letters*, ***39*** (1996) 125.
4) F. Esaka, H. Shimada, N. Matsubayshi, M. Imamura, T. Sato, A. Nishijima, A. Kawana, H. Ichimura, T. Kikuchi and K. Furuya, *Thin Solid Films*, **281/282** (1996) 314.
5) F. Esaka, H. Shimada, N. Matsubayshi, M. Imamura, T. Sato, A. Nishijima, submitted to J. Electron Spectrosc. Relat. Phenom.
6) K. Okudaira, S. Yamamoto, N. Ueno, Y. Harada, M. Aoki, K. Fujii, T.Sekitani, K. Tanaka, M. Imamura, N. Matsubayashi, H. Shimada, M. rei Vilar, submitted to J. de physique IV.

E. THE AUSTRALIAN NATIONAL BEAMLINE FACILITY

1. INTRODUCTION

The Australian National Beamline Facility (ANBF) is a multi-purpose hard X-ray beamline installed at bending magnet port BL-20B. It has been operational since 1993 as an Australian national user facility. The funding and operation of the ANBF is now a part of the newly formed Australian Synchrotron Research Program (ASRP). The ANBF currently supports about 35 experiments per year. In addition, the ANBF collaboration with the Photon Factory has led to an increased usage of other beamlines at the facility by Australian research groups. Currently about 15 experimental teams per year make use of Photon Factory beamlines other than the ANBF (Fig.10).

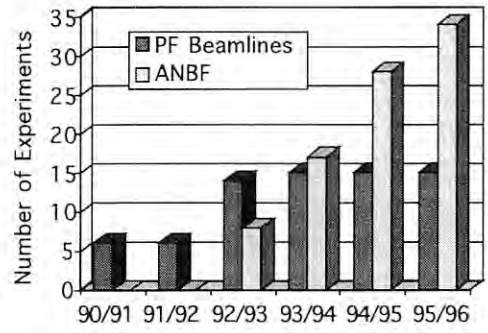

Fig.10 Number of Australian experiments conducted at the Photon Factory by financial year.

2. BEAMLINE DESCRIPTION

The ANBF is located at beamline 20B at the Photon Factory. The beamline is equipped with two monochromators which can be interchanged as required. The majority of experiments use a water cooled channel cut Si (111) monochromator. The second crystal has a "weak link" hinge actuated by a solenoid, allowing the monochromator to be detuned to reject higher order harmonics. A second monochromator, featuring a fixed exit beam height and sagittal focusing, was installed in October 1994. The second crystal is sagittally bent by a simple four point bender to focus the monochromatic X-ray beam in the horizontal plane with about 3:1 demagnification, and a gain of about 20. This monochromator is primarily used for grazing incidence surface diffraction measurements.

3. END-STATION INSTRUMENTATION

Two experimental stations are available at the ANBF. The main station is a multi-configuration vacuum Imaging Plate (IP) camera/diffractometer, which was primarily designed for high-resolution powder diffraction. It is usually operated as a Debye-Scherrer camera using IPs as detectors, so that a complete powder pattern (160° of 2-theta) is acquired simultaneously. In addition, the diffractometer can be operated in a time resolved mode whereby a set of large

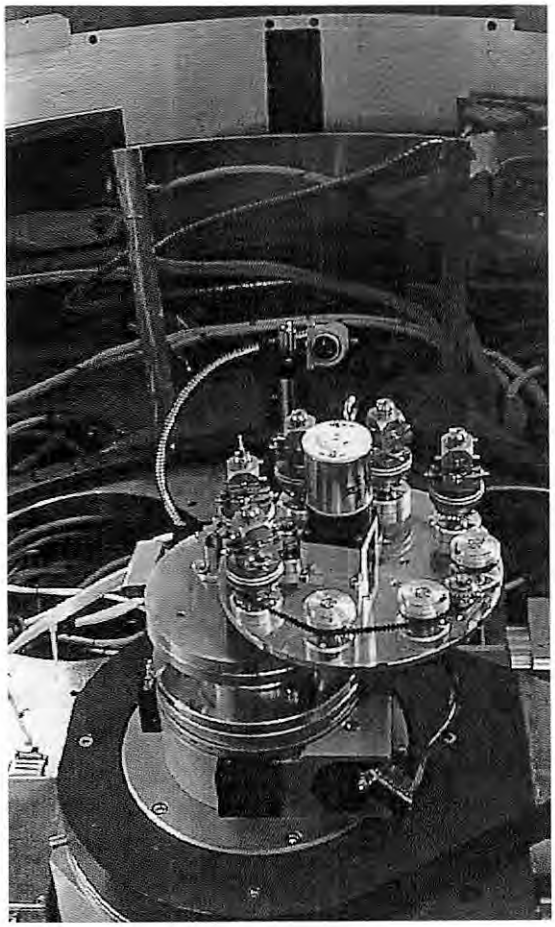

Fig.11 Capillary sample changer in use at the ANBF. Goniometer heads mounted on the changer plate are sequentially brought into the exposure position by rotating the plate.

screens are mounted inside the diffractometer, allowing a series of patterns to be recorded sequentially on a single set of IPs. This feature of the instrument is further exploited with the recent introduction of a capillary sample changer (Fig. 11). In this way, the full diffraction patterns of up to 8 samples can be collected on a single set of IPs and without breaking the vacuum in the diffractometer. The unique combination of IP detection and vacuum operation of the diffractometer makes it suitable for a number of other techniques. It can be configured for grazing incidence diffraction (solid samples only), reflectivity, triple-axis diffraction and small angle scattering (Bonse-Hart camera). Grazing incidence diffraction has proven particularly successful at the ANBF, and proposals for this technique have been steadily increasing in recent years.

The second station is an optical table primarily used for EXAFS and XANES, but also used for tomography, phase imaging and optics development. A complete range of EXAFS detection equipment is available, including a recently acquired 10 element germanium solid state advanced array detector. Currently XAFS and powder diffraction make up about two thirds of the experiments performed at the ANBF (Fig. 12).

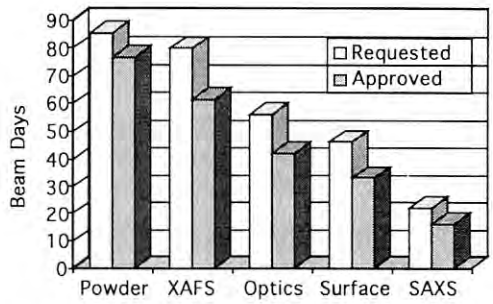

Fig.12 Beamtime allocation by experimental technique in 1995 and 1996.

4. AUSTRALIAN SOFT X-RAY SYNCHROTRON RADIATION RESEARCH

Australia also has a number of active soft X-ray research groups who make regular use of synchrotron radiation. This is a diverse group, ranging from angle resolved photoemission band mapping studies, to very applied uses of XPS and NEXAFS, and making use of many synchrotron facilities. The ASRP intends to sponsor increased use of the Photon Factory by these groups.

F. INDUSTRY BEAMLINES

F-1 NTT

1. Introduction

BL-1A is an NTT (Nippon Telegraph & Telephone Co.) beamline for semiconductor surface and interface analysis, which was constructed as a wide range energy beamline in 1983. The basic optics of this beamline, which consists of a grating/crystal monochromator (GCM) and a set of off-axis paraboloidal mirrors, has been hardly changed since beamline construction. Two

measurement systems are installed tandem at the beamline end: the former one is a surface structure analysis system equipped with an ultrahigh vacuum (UHV) goniometer and a molecular beam epitaxy (MBE) growth chamber for X-ray absorption fine structure (XAFS) and X-ray standing-wave (XSW) experiments using soft X-rays; the latter one is a surface analysis system equipped with a new electron analyzer (Scienta SES200) and an MBE growth chamber for photoemission experiments using VUV.

2. Surface structure analysis system at BL-1A

This measurement system consists of four chambers: fast entry, transfer, MBE growth, and analysis chambers. For in-situ XSW and XAFS measurements, samples prepared in the MBE chamber can be transferred through the transfer chamber to the analysis chamber without being exposed to air. The analysis chamber has a UHV compatible goniometer, which adjusts the sample to various Bragg-diffraction conditions. A conventional horizontal two-axis (theta and two theta) goniometer and two UHV compatible stepping motors are employed for operating as a normal four-circle diffractometer. The omega axis for scanning the incident angle uses the theta axle of the conventional goniometer inserted into the chamber through a differentially pumped rotary feedthrough. The chi and phi axes, driven by UHV compatible motors, are mounted on the omega axle in the chamber. During the summer shutdown of 1996, the UHV goniometer in the analysis chamber was remodeled as follows: a heater unit was added to the goniometer for the in-situ analysis of chemical reactions and two motors for driving the chi and phi axes were covered with metal jackets to block out the magnetic filed due to the motors, which disturbs photoelectron detection in the analysis chamber.

3. Experiments at BL-1A

At BL-1A, photoemission, XSW, XAFS and other measurements on mainly III-V compound semiconductor surfaces were carried out using VUV and soft X-rays monochromatized by the GCM. The chemical-bonding evolution of Se atoms upon InAs epitaxial growth on a Se-passivated GaAs surface, and the surface chemical-bonding structures of InAs(001) with and without Se-passivation and epitaxially grown InAs(001)-(2×4) and (4×2) surfaces were investigated by photoemission spectroscopy. Furthermore, the surface Fermi level (Ef) positions on the above-mentioned InAs(001) surfaces were determined in order to clarify the correlation of the Ef position with the surface-bonding structure. The annealing process of a GaAs(001) clean surface exposed to sulfur vapor was monitored by the XSW technique as a feasibility study of the remodeled UHV goniometer. N K-edge EXAFS of thin WSiN diffusion barrier layers were measured by means of secondary electron yield detection to study the correlation between the barrier capability and the local atomic ordering. The experiments using time-of-flight (TOF) mass spectroscopy and an X-ray crystal truncation rod (CTR) scattering were done for the first time at BL-1A. Photon-stimulated desorption H^+ ions from HF-treated Si(001) and thermally-grown SiO_2 were detected by TOF mass spectroscopy using soft X-rays of the single-bunch operation mode in the region of the Si K-edge. The CTR scattering spectra around the (002) Bragg reflection for S-terminated GaAs(001) surfaces were measured to analyze the detailed surface structure. Further, as the results of CTR scattering measurements in the S K-edge region, diffraction anomalous fine-structure (DAFS) signals for S atoms adsorbed on the GaAs(001) surface were observed in the CTR scattering spectra. These experimental results are reported as users' reports in this volume.

F-2 HITACHI

1. INTRODUCTION

On this beamline one can utilize synchrotron radiation (SR) from bending magnet B8 in the 40 eV to 35 keV energy range.[1] It has three branch beamlines: BL-8A (VUV to soft X-rays), BL-8B (soft X-rays to X-rays), and BL-8C (X-rays and white beam).

Several experiments can be performed at each station: BL-8A allows soft X-ray absorption spectroscopy, magnetic circular dichroism (MCD) measurements, X-ray photoelectron spectroscopy (XPS), micro-XPS, and soft X-ray reflection spectroscopy. BL-8B allows XAFS and fluorescent X-ray analysis. BL-8C1 allows lithography. BL-8C2 allows scanning X-ray microscopy, phase-contrast X-ray imaging (CT), X-ray reflectometry, and fluorescent X-ray interference measurements. In the following, we

describe recent progress of some experiments during FY 1995-1996.

2. RECENT PROGRESS

2.1 Installation of a Soft X-ray Monochromator

At BL-8A, after the summer run of 1996, we have replaced the varied-space plane grating monochromator with a new plane grating monochromator (SX-700) and tested its performance during the autumn run. We calibrated the value of the monochromatized photon energy (E) and its width (ΔE) by measuring the Ar-ion photoionization spectrum at a photon energy of Ar 2*p* threshold (~245 eV). The value of the energy resolution (E/ΔE) was estimated to ~2000, twice as good as that of the previous monochromator.

2.2 Full-Polarization Analysis at 146 eV

At BL-8A we have constructed an apparatus to measure both the full-polarization and magnetic circular dichroism (MCD).[2] A soft X-ray polarimeter at 146 eV consists of two V/C multilayer mirrors, one for a phase shifter and the other for an analyzer. ζ is the azimuth of the phase shifter and η is the azimuth of the analyzer (see user's reports in this issue). Elliptically-polarized X-rays emitted from the bending magnet with azimuth ψ were introduced into the polarimeter. The azimuth (η) was scanned from 0 to 360° at various values of ζ. We obtained sets of (ζ, η_0) for Ψ=0.0 and 0.267 mrad (corresponding to the left-handed ellipse), where η_0 gives the minimum detector output at ζ. The best-fit parameters of polarization were determined by fitting the following equation to the data (ζ, η_0):

$$\tan 2\eta_0 = -2V\alpha \frac{\cos\Delta\cdot\cos 2\Phi\cdot\sin 2(\zeta-\Theta)+\sin\Delta\cdot\sin 2\Phi}{\left(\alpha^2-1\right)+\left(V\left(\alpha^2+1\right)\cos 2\Phi\cdot\cos 2(\zeta-\Theta)\right)}$$

where Φ is the ellipticity angle, Θ the azimuth of the major axis of the ellipse, Δ the retardation angle, α the ratio of the amplitude reflectances of the phase shifter for the *s* and *p* component, and *V* the degree of polarization. We assumed the value of *V* to be 1.0, because SR is almost perfectly polarized. Figure 13 shows the observed sets of (ζ, η_0). The parameters Φ, Θ, Δ, and α were determined by fitting the above equation to the data. At Ψ= 0.267 mrad, the best fit-parameters were obtained as Φ=-21.5°, Θ=1.9°, Δ=158.5°, and α=29.3. The fitted value of Φ=-21.5°

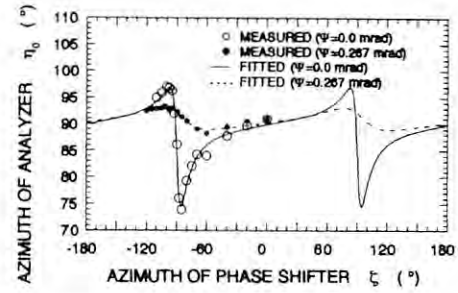

Fig. 13 Experimental results for the azimuth (η_0). The solid and dotted curves are the best-fit curves.

can be compared to the calculated value of Φ=-24.7°.

2.3 Soft X-ray Microbeam Application

At BL-8A, soft X-ray microbeam formation using a Wolter-type focusing mirror has been studied.[3] In our Wolter optics, the pinhole, as a source of the mirror, is located at the focal point of the refocusing mirror of the monochromator. The distance between the pinhole and the focal point of the Wolter mirror is about 1447 mm, and its demagnification is 1/29.8. The size of the finest focused beam achieved was 0.5 μm in the sagittal direction at 150 eV when the source size was 10 μmϕ.

Using this microbeam, we have developed a scanning photoelectron microscope (SPEM).[4] A high-precision x-y sample stage and a high efficiency electron energy analyzer have been developed for the SPEM. Figure 14 is a schematic drawing of the SPEM components, which are the focusing mirror, the sample-scanning stage, and the energy analyzer. The sample stage consists of a fine-movement x-y stage driven by piezoelectric devices mounted on a coarse-movement x-y stage driven by stepping motors. The step sizes and strokes of these stages are denoted in Fig.14. The

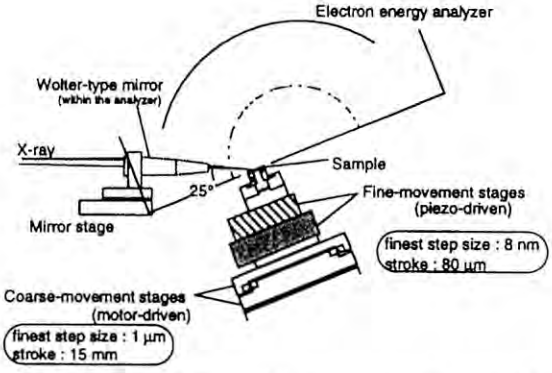

Fig. 14 Schematic drawing of the components around a sample of SPEM.

energy analyzer based on the concept of the display-type[5] energy analyzer was designed to collect photoelectrons effectively. The designed analyzer can collect photoelectrons emitted in a solid angle of 0.7 πsr.

The achieved lateral resolutions were 0.3 μm in the total photoelectron imaging mode,[4] and 0.8 μm in the core level phototelectron imaging mode (see user's reports of BL-8 in this issue).

2.4 X-ray Reflectometry using an Absorption Edge

Giant magneto-resistive (GMR) spin valve heads have been investigated for high recording density rigid disk drives. The layered structure of the heads consists of two ferromagnetic layers separated by a noble metal spacer of a few nm thickness. Precise structural characterization is important for the multilayers, since the magneto-resistance varies with the thickness of the ferromagnetic and noble metal spacer.

Most of the previous X-ray reflectometry has been based on the Cu-Kα line. In NiFe/Cu/NiFe multilayers, however, the difference in the refractive index between NiFe and Cu is small, and the characterization accuracy is not sufficient for precise thickness control.

We investigated the X-ray reflectometry using the Cu-Kβ and Cu absorption edge based on an anomalous dispersion effect as shown in Fig. 15. The final accuracy was found to improve in the order Cu-Kα < Cu-Kβ < Cu-K absorption edge, as shown in Fig. 16.

2.5 Phase-Contrast X-ray Computed Tomography

At BL-8C2 and BL-14B we have developed a phase-contrast X-ray CT[6] that is sensitive to lighter elements. This feature will lead us to observe soft tissues of ours bodies sensitively. At present, we have obtained images of cancerous portions of human tissues in collaboration with the University of Tsukuba.

3. FUTURE DEVELOPMENTS

In the autumn run of 1997 we will complete the optimization of the beamline optics for the SX-700 at BL-8A, i.e., adjustments of post-mirror system and higher-harmonics suppressor. We expect further to increase the monochromatized X-ray intensity and spectral resolution due to a reduced emittance of the PF ring.

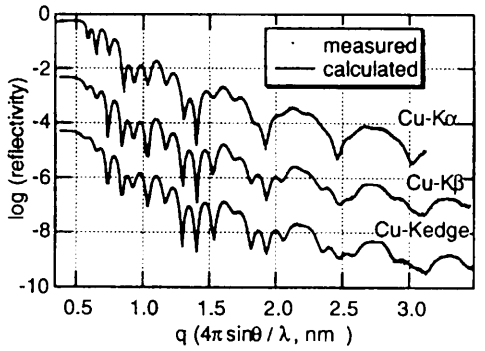

Fig.15 Measured and calculated reflectivities of NiFe(10nm)/Cu(10)/NiFe(10)/Ta(10)/glass multilayers obtained with Cu-Kα, Cu-Kβ, and Cu-K edge X-rays.

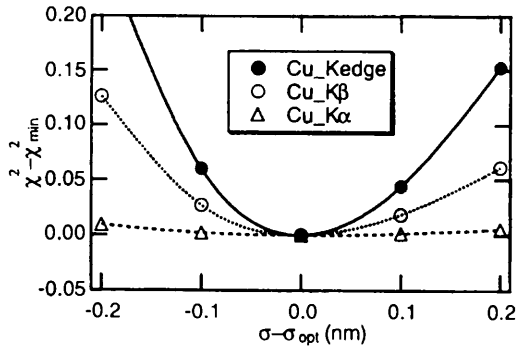

Fig.16 χ^2 distribution versus the interface width (σ) between the upper NiFe and Cu obtained by a least-squares method for the reflectivities, as shown in Fig.15.

$$\chi^2 = \sum \left(\log(I'_{exp}) - \log(I'_{cal}) \right)^2$$

References

1) Y. Hirai et al., Nucl. Instr. and Meth. A327 (1993) 256.
2) Y. Hirai et al., J. Electron Spectrosc. Relat. Phenom. 80 (1996) 385.
3) M. Hasegawa et al., Rev. Sci. Instr. 66 (1995) 1361.
4) M. Hasegawa, et al., J. Electron Spectrosc. Relat. Phenom. 80 (1996) 361.
5) H. Daimon, Rev. Sci. Instr. 59 (1988) 545.
6) A. Momose et al., Nature Medicine 2 (1996) 473.

F-3 NEC

1. INTRODUCTION

The NEC beamline consists of two branch beamlines, BL-9B and 9C. At BL-9B, photochemical-reaction studies are performed. And at BL-9C, structural analyses are carried out. The details of the

activities are described below. BL-9A, which was one of the NEC beamlines, was returned to the PF, as a public beamline.

2. PHOTOCHEMICAL REACTION STUDY

At BL-9B, the photon energy dependence of SR irradiation effect on Al-thermal-CVD was examined. Clear difference was observed between the valence- and core-electron excitations. The core electron excitation was found to be effective to suppress the CVD reaction, while the valence-electron excitation was effective in initiating the reaction. The mechanism of this drastic energy dependence was cleared by an AES chemical shift analysis of the surface layer, which was formed by a SR photochemical reaction.

3. STRUCTURAL ANALYSIS

At BL-9C, which is an X-ray diffraction- and XAFS-beamline, several kinds of experiments were carried out, as follows. Si surface imperfection was investigated using extremely asymmetric reflection, in which the glancing angle of the incident X-rays was near to the critical angle of total reflection.

The experiment of an energy-dispersive grazing incidence in-plane diffraction with white X-rays was carried out to study very thin poly-Si films.

Thin films of tantalum oxide, which is one of the promising high-ε materials for device applications, were studied by XAFS measurements in order to clarify the relation between the electronic properties and the structure. It was found that the electronic properties are strongly dependent on the oxygen deficiency, but not on the crystal structure (long range order), which is believed to be important.

Also, DAFS measurements were carried out on $SrTiO_3$ (STO) thin films in order to explain the complicated local structures from XAFS analysis. As a result, the STO crystal phase in the film was found to be an almost ideal structure, and the other phases were nearly amorphous, different from the STO structure.

4. RENEWAL OF BL-9C

In order to carry out advanced experiments for structural analysis, NEC decided to rebuild BL-9C. A new beamline is to be constructed at BL-9C during the shutdown in 1997. The optics of this beamline consists of a double-crystal monochromator and a bent cylindrical-mirror system. The main purpose of the optics is to realize a small beam size and a fixed beam position during measurements of the XAFS and DAFS spectra. The small beam size (less than 1mm square) is useful for XAFS and DAFS measurements for new materials and devices. The beamline is to be opened for use at the end of 1997.

F-4 FUJITSU

1. Introduction

The FUJITSU beamline BL-17 consists of two X-ray beamlines (BL-17A and BL-17C), both equipped with a Si(111) double-crystal monochromator for the characterization of electronic materials and a VUV beamline BL-17B to study photo-induced chemical reaction. At X-ray beamlines the diffraction, fluorescence and reflection techniques based mainly on the X-ray total external reflection condition have been applied to evaluate wafer surfaces and thin films.

2. New techniques and equipment

2.1 Grazing incidence X-ray diffraction

Grazing incidence is an appropriate geometry to evaluate thin films with high sensitivity, including the orientational or epitaxial relation to substrates. Since a large part of electronic samples are thin films, a grazing-incidence X-ray diffractometer[1] has been constructed at BL-17C. The titanium silicides ($TiSi_2$), widely used as gate electrodes or interconnections, are hard to evaluate by the conventional X-ray diffractometer, due to its thickness of around 30nm. The silicidation process has been investigated using this equipment. For electric use, its low-temperature phase C49 with high resistivity needs to be transformed into high-temperature phase C54 with low resistivity by thermal annealing. We found the existence of epitaxially grown components of C49 grains on a Si(001) substrate after low-temperature annealing of Ti, which is thermally stable and hard to transform into the C54 phase after high-temperature annealing[2] in addition to the effects of BF_2 ion implantation on the phase transition.[3] Recently, the attachment of a thermal-annealing furnace has been introduced in this diffractometer for the in-situ observation of the Al/Ti

alloying reaction, which has intimate relation to the electromigration of Al interconnects. The system, based on an electric heater in combination with conventional θ/2θ scanning, provided time dependent diffraction pattern of Al interconnects for every one minute.[4] A new annealing furnace based on a lamp heater and a PSPC system is in preparation to observe the structural change of materials during the rapid thermal-annealing (RTA) process frequently used in semiconductor fabrication.

2.2 X-ray reflectometry

X-ray reflectivity techniques were initially developed based on a grazing-incidence X-ray diffractometer to evaluate very thin SiO_2 films on Si including native oxide. During a course of this study, we found that the physical density of native oxide changes due to the chemical solutions used for wafer cleaning, whose structure influences the following growth of thermal oxides.[5] On thermally grown oxides, we found the existence of a high-density (~2.4g/cm^3), thin (~1nm) layer at the SiO_2/Si interface.[6] Its density exceeds that of Si, indicating the ordered or crystalline nature of the layer, in coincidence with the epitaxial crystalline component observed by a CTR study, and sheds new light on the oxidation of Si, the detailed mechanism of which is still not completely understood. With the success of the method, a new reflectivity equipment capable of observing X-ray fluorescence simultaneously has been introduced at BL-17A, where the background from air scattering has been reduced by the vacuum environment. This equipment has served to evaluate many materials, including CVD-SiO_2 film[7] or a thin metallic multilayer for a MR (magneto resistive) head.[8] A combination of reflectivity and angle dependent fluorescence will provide new information about thin films.

References

1) Y. Horii et al., Rev. Sci. Instrum. **66** (1995) 1370.
2) S. Komiya et al., Jpn. J. Appl. Phys. **35** (1996) 242.
3) H. Tomita et al., Jpn. J. Appl. Phys. **34** (1995) L876.
4) Y .Horii et al., in this Activity Report.
5) N. Awaji et al., Jpn. J. Appl. Phys. **34** (1995) L1013.
6) N. Awaji et al., Jpn. J. Appl. Phys. **35** (1996) L67.
7) N. Awaji et al., in this Activity Report.
8) Y. Kitade et al., Abstract of spring meeting of the Japan Society of Applied Physics (1997) 530.

Projects

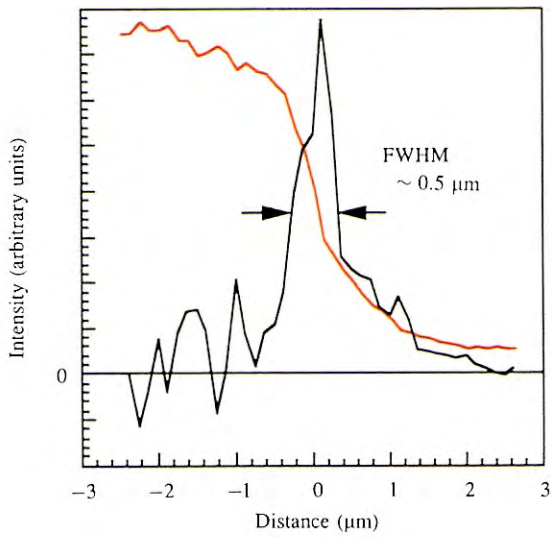

Fig. 1

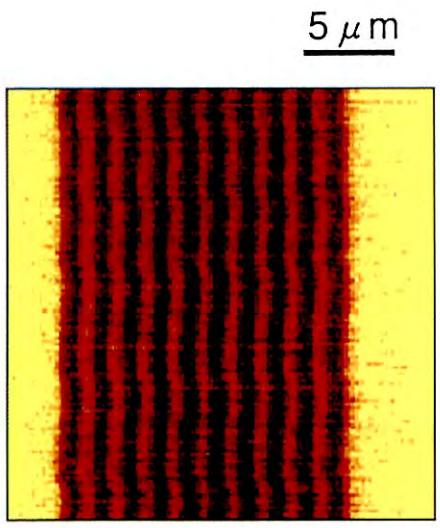

Fig. 2(a)

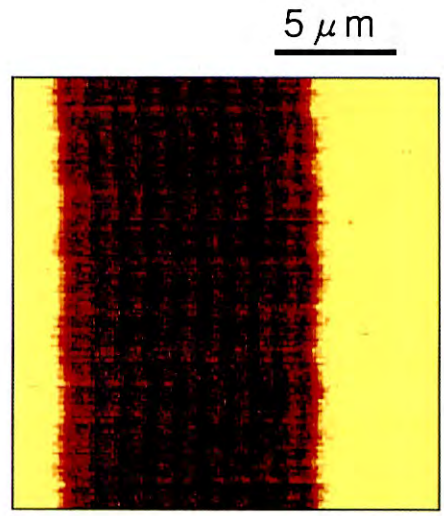

Fig. 2(b)

Results of X-ray microbeam experiments at the Tristan MR beamline.
Fig.1 Focused beam profile measured by knife-edge scanning: raw data (a red line) and its numerical derivative (black). A sputtered-sliced Fresnel zone plate is used as a focusing device of undulator radaition of 8.54 keV. The focused beam size is about 0.5 micron in FWHM.
Fig. 2. scanning microscopy images obtained with the focused X-ray beam of test patterns as a resolution specimen: (a) 0.9 micron line/0.9micron space pattern, and (b) 0.6 micron line/0.6 micron space pattern.

You can jump to the article by clicking its title.

CONTENTS

A. THE TRISTAN SUPER LIGHT FACILITY

1. GENERAL SUMMARY OF THE PROJECT

In the period of 1995.10.01-1995.12.28 almost all experiments planned using super brilliant synchrotron radiation from the Tristan Main Ring have been successfully carried out. The term from the middle of September 1995, when the KEK open house was held, till almost the end of October was spent for commissioning the modified lattice of the MR. This modification was done using three and a half months in the summer. The machine has achieved its successful operation condition at 8GeV for super brilliant synchrotron radiation.

The machine has been in operation beautifully during the experimental term until the last moment of the user run at the end of the year 1995 including the increasing acceleration energy up to 10GeV and running at that energy. Commissioning of the insertion device as a super brilliant light source and its associated beamline together with a giant monochromator were also successfully done.

The experiments of the following subjects have been proceeded according to a machine time allocation programme as shown in Table 1. Its schedule was rigorously retained.

MR95A: Production of Highly Brilliant Hard X-Ray Microbeam and Its Application.
MR95B: X-Ray Excited Process of Semiconductors.
MR95C: Production of Submicron Beam Made by a Grazing Incidence Mirror.
MR95D: High Speed Time-Resolved X-Ray Diffraction of Muscle Under Contraction Using a Single Fiber.
MR95E: X-Ray Parametric Scattering Induced by Intense Laser Light.
MR95F: Precision Measurement of Emittance.
MR95G: Intensity Correlation of X-Ray Photons Using Nuclear Resonance Scattering.
MR95H: Growth Control of Atomic Scale Crystal by X-Ray Wave Field.
MR95K: Development of Position Monitor Using a Diamond Plate.
MR95L: Development of Profile Monitor Using a Carbon Wire.

Their associated publications are as follows:

(1) Proceedings of the 10th ICFA Beam Dynamics Panel Workshop on the Fourth Generation Light Sources; the MR insertion device by S.Yamamoto, the MR beamline monochromator H.Sugiyama, and the MR project by M.Ando (Grenoble, January 22-25, 1996).
(2) Small-Angle X-ray Diffraction of Muscle Using Undulator Radiation from the Tristan Main Ring at KEK by N.Yagi, K.Wakabayashi, H.Iwamoto, K.Horiuchi, I.Kojima, T.C.Irving, Y.Takezawa, Y.Sugimoto, S.Iwamoto, T.Majima, Y.Amemiya and M.Ando, Journal of Synchrotron Radiation 3-6 (1996) 305-312.
(3) Fabrication of a Hard X-Ray Sputtered-Sliced Fresnel Phase Zone Plate by N.Kamijo, S.Tamura, Y.Suzuki, K.Handa, A.Takeuchi, S.Yamamoto, M.Ando, K.Ohsumi and H.Kihara, Review of Scientific Instruments 68-1 (1997) 14-16.
(4) Operation of an X-ray Undulator in the Tristan Main Ring as a Prototype of Future Super Light Sources by S.Yamamoto, H.Sugiyama, K.Tsuchiya and T.Shioya, Journal of Synchrotron Radiation 4-2 (1996) 54-59.
(5) Hard X-Ray Microbeam Experiment at the Tristan Main Ring Test Beamline of the KEK by Y.Suzuki, N.Kamijo, S.Tamura, K.Handa, A.Takeuchi, S.Yamamoto, H.Sugiyama, K.Ohsumi and M.Ando, Journal of Synchrotron Radiation 4-1 (1997) 60-63.
(6) Proceedings of the Meeting on "THE MR LIGHT SOURCE EXPERIMENTS" edited by K.Ohsumi, H.Fukuma and S.Kamada on March 6-7, 1996. KEK Proceedings 96-8.
(7) Proceedings of the Meeting on "THE MONOCHROMATOR FOR SYNCHROTRON RADIATION EXPERIMENTS AT MR" edited by H.Sugiyama and Y.Higashi on June 12, 1996. KEK Proceedings 96-7.

Many more papers are in process of publication. See in the text all the details achieved by each experiment. A part of the work was done by the Grant-in-Aid for Scientific Research from the Ministry of Education, Science, Sports and Culture to which we would greatly like to appreciate. Although the machine time was too short to use the super brilliant source, since we believe that we could have put in something new in prior to the commissioning of the SPring-8, we

Table 1 Time allocation for the above each experimental programme from September to December in 1995. The MR and B3 tunnel are located in the third basement, and B4 up-stream, B4 middle and B4 down-stream are in the fourth basement. The programmes MR95K and L could have been performed almost simultaneously while other experimental programmes were running.

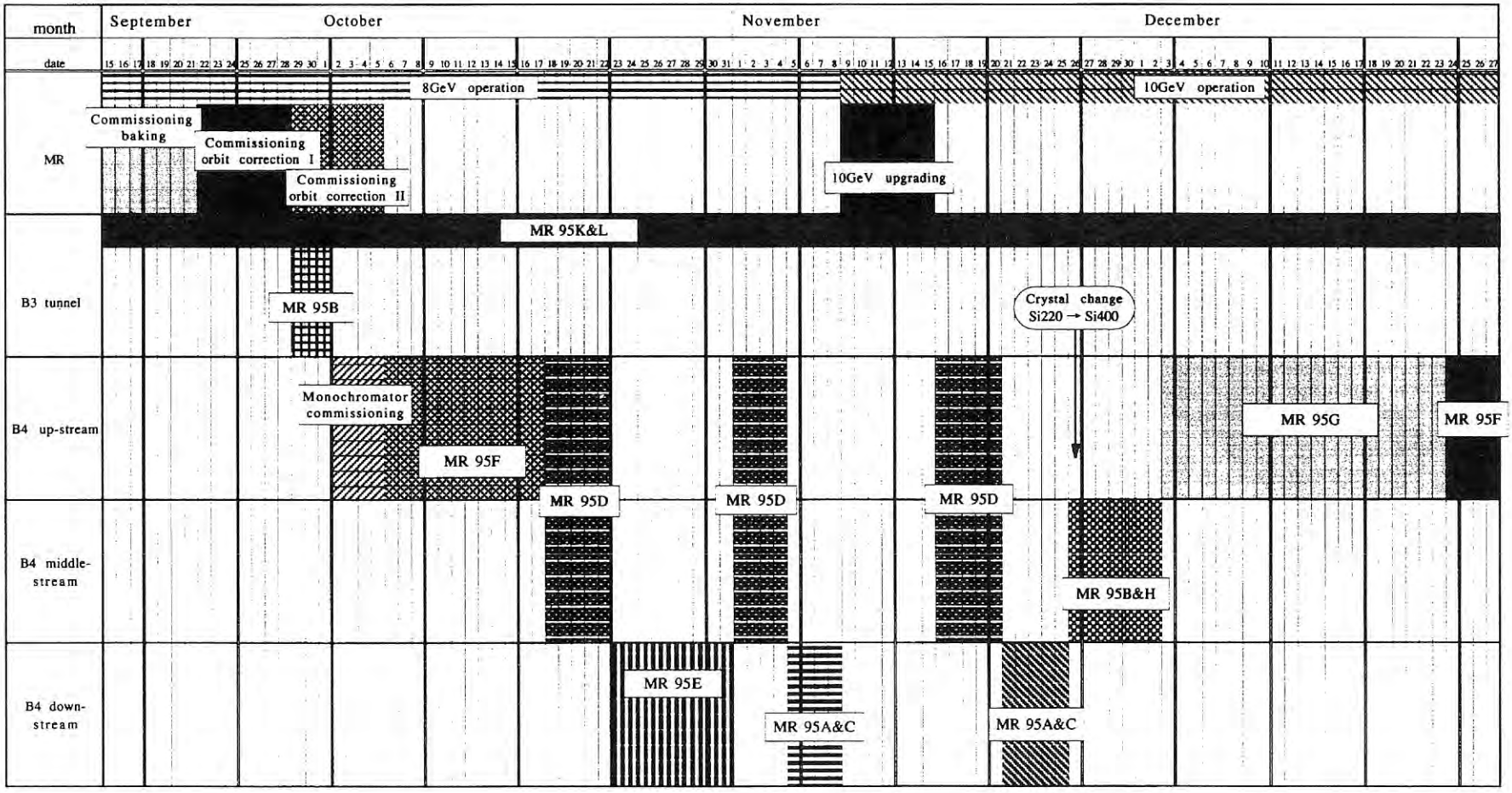

aim at obtaining a scope to view new scientific opportunities beyond the 3rd generation light sources and we need fostering international collaboration, as one of the tools, to facilitate the generation and application of coherent X rays.

M.Ando, PF

2. ACCELERATOR

The TRISTAN MR was operated as a light source from September to December, 1995, to pursue the possibility of using the MR as a future light source and to carry out research programs suitable at future light sources. The beam current was stored to a design value of 10mA in 8-bunch operation. The measurement of the acceptance showed that the chromaticity correction by the non-interleaved sextupole arrangement worked well. A feedback system suppressed any change in the orbit to the required level. A preliminary result of the emittance measurement shows that the horizontal emittance was about 7 nm.

The brief chronology of the MR light-source operation given in Tables 2 and 3 shows the design and achieved beam parameters there. In the following, the results of the commissioning and machine studies in this period are reported.[6),7)]

Table 2 Brief chronology of the MR-light source operation

Month/Day	Events
9/18	Beam tuning at 8 Gev started. The beam was successfully stored.
27	The injection efficiency was improved after the change of the betatron tunes.
29	The light beam reached to the first monochromator.
10/1-11	Emittance was optimized by a survey of betatron and synchrotron tunes.
14-18	Vertical emittance was reduced by the orbit scan at sextupoles.
18	Experiments by SR users started.
11/9	Feedback system for the stabilization of the closed orbit successfully worked.
11-15	Beam tuning at 10 GeV was done.
12	Field strength of the damping wiggler was adjusted to minimize emittance.
17	Stored beam current reached 16 mA.
12/1	Experiments at 10 GeV by SR users started.
24	Experiments by SR users finished.
24-27	Spectrum of undulator-light was measured.
27	Operation ended.

Table 3 Design and achieved parameters

		Design	Achieved
Beam energy	(GeV)	10	10
Number of bunches		8	1, 8, ,16, 32
Beam current	(mA)	10	10 :8 bunches 16:32bunches
Cell phase advance (horizontal)		90°	
(vertical)		90°	
Momentum compaction		0.00073	
Betatron tune (horizontal)		48.20	47.64
(vertical)		41.15	40.76
Natural chromaticity (horizontal)		-65	
(vertical)		-57	
RF voltage	(MV)	90	80-110
Synchrotron tune		0.073	
Damping wiggler field	(T)	1.2	1.17
Radiation damping time (trans./long.)	(ms)	30/15	
Natural bunch length	(mm)	5.3	
Natural emittance	(nm)	5.0	about 7
Orbit stability with feedback			
position (hor./ver.)	(μm)	±1500/±50	±30/±40
angle (hor./ver.)	(μrad)	±15/± 5	±5/± 5
Beam life time	(min)	120	210 at 10mA

2.1 Introduction

A plan to modify the MR for a light-source study has already been described1). The main features of the plan were: 1) installation of an X-ray undulator (5.4m long) and a photon beam line (100m long), 2) increase the betatron phase advance in a normal cell and, use the existing wigglers as emittance-damping wigglers to achieve low emittance, 3) a chromaticity correction based on the so-called non-interleaved sextupole arrangement to keep the dynamic aperture large, 4) removal of all superconducting cavities and 60% of the normal-conducting cavities and introduction of head-tail damping by high chromaticity to overcome the coupled-bunch instability, 5) introducing a feedback system to stabilize the slow orbit movement and 6) alkaline cleaning of the vacuum chamber surface to improve the expected worse vacuum pressure due to a new installation of the vacuum chambers in the place of the removed cavities.

2.2 Beam Tuning

For a chromaticity correction, sextupoles were excited based on a non-interleaved sextupole arrangement. In this arrangement sextupoles make a pair having the same strength. To confirm the validity of this arrangement, the energy and transverse acceptance were measured and compared with a simulation by the computer code SAD. Fig. 1 demonstrates that the measured energy and horizontal acceptances are consistent with the simulation. The measured vertical acceptance, which was one tenth of the simulation, can be explained by the physical aperture of the vacuum chamber for the undulator.

According to the result of a SAD simulation, the betatron tune was changed both horizontally and vertically for the sake of a larger acceptance. This change of tune improved the injection efficiency of the beam by 20~40%.

A low emittance was to be achieved by increasing the betatron phase advance in a normal cell from 60° to 90° in both the horizontal and vertical planes, and by using emittance-damping wigglers. Fig. 2 shows the emittance observed by a visible light monitor as a function of the wiggler field. The emittance has a minima around the design value of 1.17T.

Betatron and synchrotron tunes were surveyed in order to reduce the emittance. Fig. 3 shows the

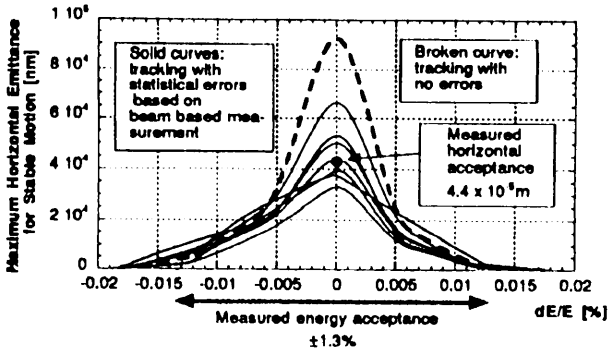

Fig. 1 Comparison of the acceptance between the measurement and simulation.

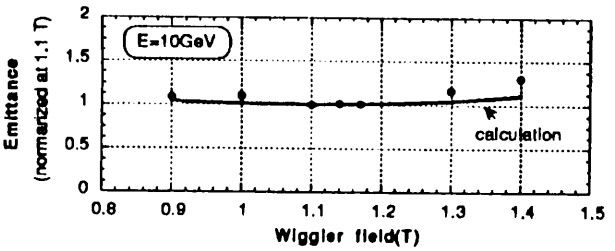

Fig. 2 Emittance vs. field of the damping wigglers.

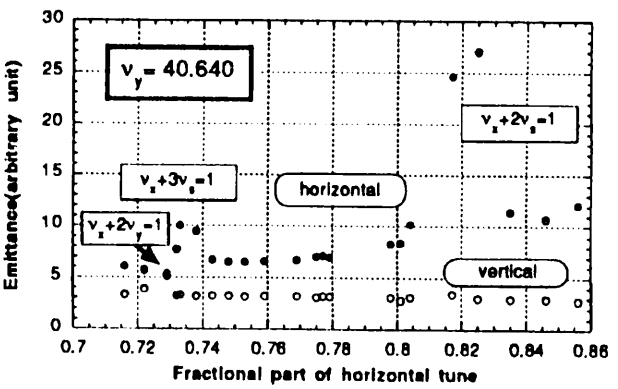

Fig. 3 Horizontal tune vs. emittance.

horizontal and vertical emittances as a function of the horizontal tune. The emittance was measured by a visible-light monitor. Growth of the horizontal emittance by coupling resonances is clearly observed. The operating point was set far from the resonances in order to avoid emittance growth.

The vertical orbit at a sextupole was swept while observing the vertical beam size in order to decrease the vertical emittance. This procedure was repeated for almost all of the sextupoles, and finally reduced the vertical emittance by 10%.

2.3 Orbit Stability and Feedback

The requirements were accumulated from the expected SR users on the orbit stability at the source point. They are summarized in Table 3.

In the preparation stage for the light-source operation, orbit movement was measured at the TRISTAN MR, and revealed that a fast movement of 3-100Hz was small enough, but that the slow movement needed to be stabilized by a feedback system to fulfill the requirements.

In the feedback system,[2] the position and angle of the beam at the center of the undulator were measured turn by turn by a pair of beam-position monitors. Four steering magnets were prepared for each of horizontal and vertical directions to control the position and angle of the beam at the center of the undulator. These steering magnets were fabricated by laminated steels to obtain a fast response of the magnetic field and to reduce the hysterisis effect.

The performance of the feedback is summarized in Table 3. The vertical angle is shown for about 5 hours with and without feedback in Fig. 4, as a typical example of the feedback performance. Data were taken every 2 seconds by averaging over 100 turns.

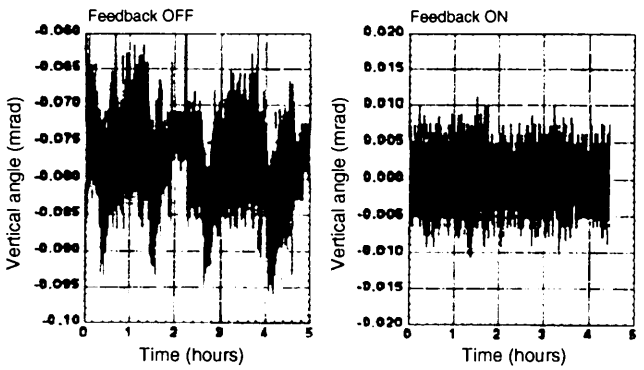

Fig. 4 Change in the vertical angle at the source point with and without orbit feedback.

2.4 Emittance Measurement

The emittance was measured by observing the visible light emitted from a bending magnet. Light was extracted from a vacuum chamber by a Be mirror, defined by a slit, and focused on a CCD camera by a lens having a focal length of 1000mm. The filter selected for light having a wavelength l was 500±5nm. The intensity of light accepted by the CCD camera was adjusted by a circular linear-wedge-type ND filter. All of the devices were located in the TRISTAN tunnel.

The image was projected onto the horizontal and vertical axes and fitted to a Gaussian distribution with linear background. The standard deviation of the distribution gives a beam size of $\sigma_{x,y}$(obs.).

$$\sigma^2_{x,y}(obs.) = \sigma^2_{x,y} + \sigma^2_d + \sigma^2_f + \sigma^2_a + \sigma^2_\beta + \sigma^2_{CCD}, \qquad (1)$$

where $\sigma_{x,y}$ is the horizontal and vertical beam size, expressed as $\sqrt{\varepsilon_{x,y}\beta_{x,y}}$, because the dispersion is negligibly small at the source point. sd is the broadening of the beam size by diffraction, and is determined vertically by the radiation angle of the synchrotron radiation (σ'_r) and horizontally by the Fraunhofer diffraction by the slit. sf arises because the camera accepts light emitted from a finite region (σ_l) along the orbit, and which is unfocused on the camera. The error due to astigmatism by a deformation of the Be mirror (σ_a) was estimated from the positions of the horizontal and vertical focal points, which shifted each other by 127mm(=Δf) when converted back to the source point. σ_β is caused by a change in the beta function ($\Delta\beta$x) of y in region σ_l. σ_{CCD} is the digitizing error by the CCD camera.

$\sigma_{x,y}$ (obs.) was measured as a function of the slit width (D) and compared with the theoretical $\sigma_{x,y}$ (obs.) calculated by (1) assuming various values of $\varepsilon_{x,y}$. The result shown in Fig. 5 indicates that horizontal and vertical emittance are about 7nm and 0.4-0.8nm, respectively.

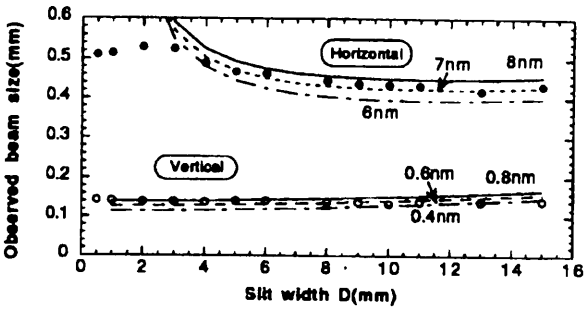

Fig. 5 Observed beam size vs. slit width.

2.5 Others

The achieved beam current was 10 mA and 16 mA during 8-bunch and 32-bunch operation, respectively. The head-tail damping rate was 3.3 ms horizontally and 1.3 ms vertically at on injection energy of 8 GeV when the bunch current was 1.4 mA.[3] This strong damping, which is ten-times higher than the radiation-damping rate, must have been helpful to suppress the coupled-bunch instability.

Table 4 Measured and calculated loss factors

		Measured	Calculated
Longitudinal	(10^{14}V/C)	6.3 - 8.0	4.1
Horizontal	(10^{15}V/C/m)	2.41 - 3.14	2.1
Vertical	(10^{15}V/C/m)	5.6 - 5.9	2.9

The longitudinal loss factor (k_L) and the transverse loss factor (k_T) in the ring were measured and compared with a calculation.[4] k_L was obtained by detecting the synchronous phase angle as a function of the current and k_T from the current dependence of betatron tunes. The calculations of the loss factors were made using the ABCI code which taking into account 40 RF cavities, 160 RF bellows, 32 gate valve bellows and 560 shielded bellows. The results of the measurement and the calculation are given in Table 4. The cause of the discrepancy between the measurement and the calculation is not yet understood.

The beam lifetime reached 210min at a beam current of 10 mA. This is longer than the expected lifetime of 2 hours after three months' operation. This better performance could be explained as being due to alkaline cleaning of the vacuum chamber to decrease the out-gas rate.

The vertical closed orbit depended on the gap height of the undulator. The amount of orbit change increased exponentially upon closing the undulator gap. The kick of 20 mrad at the undulator explains the change in the closed orbit observed by the 8-GeV beam at an undulator field of 2500 Gauss, and implies that the horizontal magnetic field amounting is 5.3Gm in the undulator. A simulation study was made to explore the effect of the horizontal magnetic field upon the characteristics of the undulator radiation.[5]

H.Fukuma, Acc. Dept. and S.Kamada, PF
for the TRISTAN light source commissioning group

References

1) S.Kamada et al., Rev. Sci. Instrum. 66(2), 1913(1995).
2) T. Mimashi et al., Int. Conf. on Acc. and Large Exp. Phys. Cont. Systems, Chicago, U.S.A. 1995.
3) N. Akasaka et al., Proc. of the EPAC96, Sitges,1996,p.1141.
4) C. Zhang et al, Proc. of the EPAC96, Sitges,1996,p.1075.
5) S.Kamada KEK Proceedings 96-8, 51(1996) in Japanese.
6) TRISTAN light source commissioning group, Proc. of the EPAC96, Sitges,1996,p.647.
7) Articles in the J.J.S.S.R.R. Vol.10,No.2,(1997) mostly in Japanese.

3. UNDULATOR FOR THE TRISTAN SUPER LIGHT FACILITY

3.1 Operation of the Undulator

Operation of the Tristan MR at 8 and 10 GeV for the superbrilliant-synchrotron-radiation experiment was started on Sept. 18, 1995, and the electron beam was stored as early as Sept. 20. As a source of synchrotron radiation (SR) in the hard x-ray region, a 5.4-m long 239-pole undulator, named XU#MR0, was constructed and installed in the MR, as reported previously.[1] The parameters of the XU#MR0 are given in Table 5. The spectrum corresponding to the designed performance of the MR (beam energy, E = 10GeV; beam current, I=10mA; natural emittance, ε_0=5nm·rad; and emittance coupling, κ=0.02) is shown in Fig. 6.

Table 5 Parameters of the XU#MR0.

Magnetic structure	Pure configuration
Magnetic material	NdFeB (B_r=12.8kG, iH_c =17kOe)
Period length	λ_u=4.5cm
Number of periods	120 [=3×40/unit undulator]
Magnet length	5.4m [=3×1.8m/unit undulator]
Maximum peak field	B=2.64kG
Maximum K	K=1.11
Range of magnet gap	3~50cm
Aperture	2.4cm

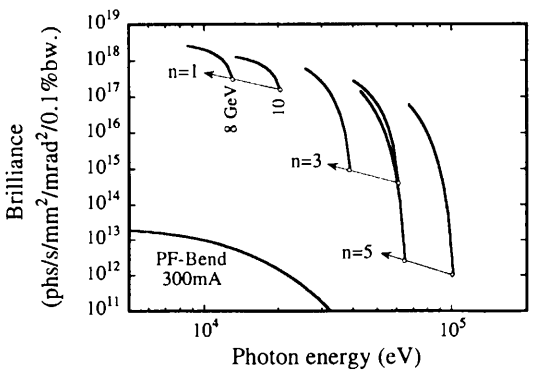

Fig. 6 Brilliance of radiation from the XU#MR0 in the cases of 8- and 10-GeV operation of the MR with a beam current of 10mA. Each curve shows the locus of the peak position of the n-th harmonic when K decreases from its maximum. The brilliance of the radiation from the PF-bending magnets at 300-mA operation is also shown for a comparison.

X rays from the XU#MR0 were successfully introduced to the beamline by using light axis monitors made of graphite wires[2]; the horizontal and vertical positions of the light axis were detected by these monitors, which were placed at 17 m, 49 m, and 84 m points from the center of the XU#MR0. The XU#MR0 provided X rays very stably for commissioning the double-crystal monochromator and for various types of utilization until the end of the test experiments on Dec. 27, 1995.[3]

Beam tuning the MR was performed at 8 GeV at first, since the injection energy of the MR was 8 GeV, and was followed by SR experiments at 8 GeV. The beam tuning was done again at 10 GeV before experiments at 10 GeV. This process was in a dilemma between the best-tuned operation of the MR for SR experiments and the longest time allocation for experiments under the condition of a strictly limited time allowed for the MR for SR operation (some 3.5 months). In order to carry out this process very quickly and efficiently, the vertical divergence (Σ_y) of the x-rays from the XU#MR0 was used as a measure of the status of the electron-beam quality in the MR after conversion to electron-beam divergence (σ_y) by a proper deconvolution, which took into account the effects from the divergence of the X-rays, themselves, and those from the optical elements used. The measurement of Σ_y was made by taking rocking curves of the Si400 analyzer placed after the Si400 double-crystal monochromator, the first crystal piece of which was cryogenically cooled by liquid nitrogen. Details concerning this measurement will be given elsewhere.[4]

3.2 Estimation of the electron-beam properties

During the beam-tuning process at 8 GeV, we found that σ_y amounted to some 20 μrad, which was four-times larger than the design value (4.5 μrad when ε_0=5 nm·rad and κ = 0.02 is achieved). After an intensive search of the operation parameters of the MR, including a reduction of the beam-current dependence of σ_y, made by the Tristan accelerator group, the beam quality was optimized and σ_y= 8.5 mrad was achieved. Further, in this process we found that σ_y was optimized by the long coil for the horizontal field correction.[4] A minimum value of σ_y (=7μrad) was obtained at a coil current of -8 to -10 A. This phenomenon suggests that changes in the ambient magnetic field occurred around the XU#MR0 in the MR under operation, and that these long coils are very useful to correct for this kind of change in the ambient field. A similar optimization of σ_y was also observed under 10-GeV operation of the MR; σ_y=7.6 μrad without a correction was optimized to σ_y= 6.6μrad at a correction current=-8A. This correction was kept constant during the SR experiments at 10 GeV.

A spectrum measurement as a characterization of the light source was finally performed at 10 GeV during the last three days of the MR operation for the SR experiments. Instead of the brilliance, we measured the on-axis photon flux density using the present optical system (Fig. 7). Radiation from the XU#MR0 was introduced to a PIN photodiode detector through an absorber made of aluminum and an x-y slit (with an aperture of 0.2×0.2mm^2), which were placed after the Si400 double-crystal monochromator. We used a PIN photodiode which was precisely calibrated[4] in a photon energy region from 7 to 40 keV. The use of an absorber of Al is for separating the first and second harmonics of the radiation from higher harmonics. The effects of absorption, which were caused from the graphite- and beryllium-windows, and air in the beam path, and those of reflection efficiencies and bandwidths of the monochromator were also taken into account for a correct estimation of the photon numbers.[4]

The measured spectrum is shown in Fig. 8 as solid circles. The parameters of the light source were: E=10GeV, I=10mA (normalized) and K=1.09 (the first harmonic energy of 13.1keV). Figure 8 also shows the result of a calculation (a solid curve) made with ε_0=14 nm·rad and κ=0.015 instead of the design values (ε_0=5 nm·rad and κ=0.02). An energy spread of 1.13×10^{-3} was also taken into account for this calculation.

The above selection of ε_0 and κ was made on the basis of the measured spectrum (Fig. 8). The

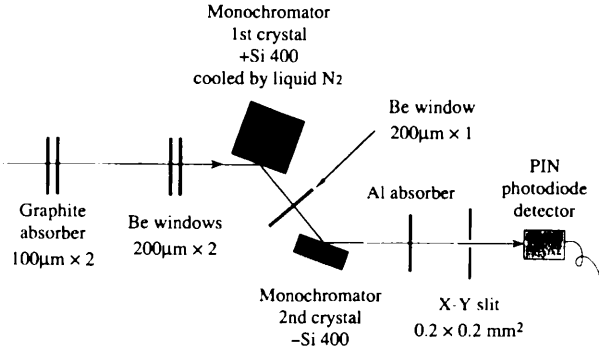

Fig. 7 Schematic diagram of the optics used for the spectrum measurement.

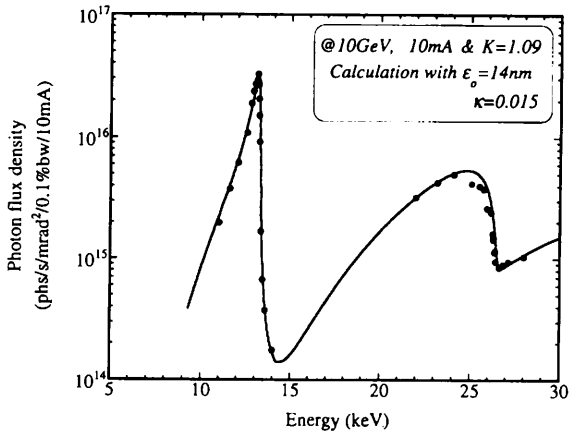

Fig. 8 Photon flux density of the radiation from the XU#MR0 with K =1.09 (the first harmonic energy is 13.1 keV) when the MR is operated at 10 GeV and 10mA. The solid circles indicate the observed results and the solid curve indicates the result of a calculation made with a natural emittance (ε_0) of 14 nm·rad, a emittance coupling (κ) of 0.015, and an energy spread of 1.13×10^{-3}.

combination of ε_0 and κ greatly affects (a) the flux density of each harmonic, (b) the bandwidth of each harmonic, and (c) the ratio of the flux density of an even harmonic to an odd one. Therefore, ε_0 and κ may be well constrained inversely by the observation concerning on the above three items. Figure 9 shows contour maps of (a) the flux density of the first harmonic (D_1) of the radiation from the XU#MR0, (b) the bandwidth of the first harmonic ($\Delta\omega/\omega_1$), (c) and the ratio of the second-harmonic flux density to the first (D_2/D_1), which were calculated as functions of ε_0 and κ using the same parameters as those used for the solid curve in Fig.8. The observed results of $D_1=3.3\times10^{16}$ photons/s/mrad²/0.1%bandwidth and $\Delta\omega/\omega_1=0.042$ (Fig.8) are explained only by the combination of ε_0=14 nm·rad and κ=0.015, as shown in Figs.9 (a) and (b). Since the number of unknowns to be obtained is two, the constraint conditions obtained from Figs.9 (a) and (b) are enough to determine the values of ε_0 and κ. The condition obtained from Fig.9 (c) can be used for a redundancy check. Although the observed values which form the second harmonic are somewhat scattered, the ratio D_2/D_1=0.165, obtained from smoothing these data, is consistent with the result shown in Figs.9 (c). In this contour, a combination of ε_0=14 nm·rad and κ=0.015 gives D_2/D_1 = 0.170. The agreement between the observation and the calculation strongly suggests that the electron-beam quality under

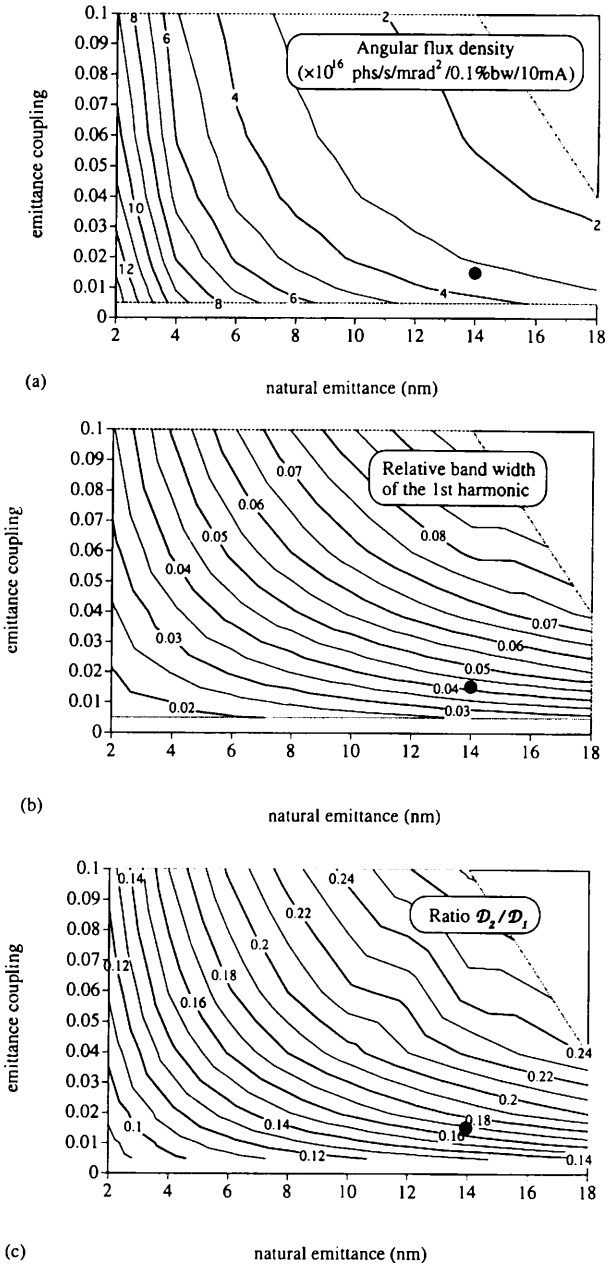

Fig. 9 Contour maps of (a) the flux density of the first harmonic (D_1) of the radiation from the XU#MR0, (b) the bandwidth of the first harmonic ($\Delta\omega/\omega_1$), (c) and the ratio of the second-harmonic flux density to the first (D_2/D_1), which were shown as functions of the natural emittance (ε_0) and the emittance coupling (κ). The solid circle indicates the point of the natural emittance, ε_0 = 14nm·rad, and the emittance coupling, κ = 0.015.

the present operation of the MR should be expressed by ε_0 = 14nm·rad and κ = 0.015 as an effective emittance in the XU#MR0, including the effects from the above-mentioned ambient horizontal field. Further, the value

of the vertical emittance (ε_y = 0.21 nm·rad), which was obtained on the basis of the observed value of $\sigma_{y'}$= 6.6 mrad using β_y = 4.8m (design value), is very consistent with the above inference of the emittance.

The above result, however, does not coincide with the designed values of the electron beam emittance (ε_0 = 5nm, and κ = 0.02), nor those (ε_x=7 nm and ε_y= 0.6 nm)[5] obtained independently by using SR from the bending magnet in the MR. This discrepancy gives rise to a possibility for the existence of some irregularities in the magnetic field of the XU#MR0, which brings in degradation of the spectral properties the XU#MR0 from its ideal value (3.6×10^{18} photons/s/mm^2/mrad^2/0.1%bandwidth when K= 0.97 with 10-GeV and 10-mA operation, in terms of brilliance) to the present one (6.9×10^{17} photons/s/mm^2 /mrad^2/0.1%bandwidth). In order to clarify an origin of this discrepancy, we reexamined the magnetic field of the XU#MR0 very critically. A spectrum obtained by a direct Fourier transformation of the magnetic field data shows that the degradation is negligibly small for, at least, the lower harmonics and our present estimation of the emittance well represents the beam properties in the MR when the experiments were performed.

S.Yamamoto, PF

References

1) S.Yamamoto, et al., J. Synchrotron Rad., **4**, 54 (1997).
2) Photon Factory Activity Report #13, P-8 (1996).
3) Photon Factory Activity Report #14 (this volume), Chapter "*Project*", Sections A-4 and A-5.
4) H.Sugiyama, et al., in preparation (1997).
5) Photon Factory Activity Report #14 (this volume), Chapter "*Project*", Section A-2

4. OPERATION AND PERFORMANCE OF THE BEAMLINE MR-BW-TL

The beamline MR-BW-TL operated well with good performance, except for two problems concerning the monochromator since the commissioning. The pressure of the beamline was maintained at less than the order of 10^{-9} torr at the upstream part, and less than the order of 10^{-4} torr at the downstream part from the beryllium windows through the operation. Upon commissioning the monochromator, the SR beam was obstructed by a vacuum duct comprising a welded bellows between the first and second piece of the monochromator. The vacuum duct deviated from the SR beam path as a result of a bend in the duct beyond our expectation. We reformed the duct by fitting a counterbalance. The liquid-nitrogen cooling system of the monochromator was also operated well. The consumption of liquid nitrogen for the monochromator was 2.2 liters/hour as the shutter opened and 1.9 liters/hour as the shutter closed. There was a very low degradation of silicon crystal of the monochromator. The rocking curve was measured by rotating the first crystal on Si 660 at a parallel setting with the first and second crystal of the monochromator at 26 keV. The full width at half maximum (FWHM) of this curve was 6.8 μrad. We concluded from this FWHM that the radius of curvature of the first crystal was more than 500 m. Intensity of the SR beam after the monochromator fluctuated during the last stage of the SR experiments. We suspect that the monochromator crystal vibrated due to the leakage of liquid nitrogen from the seal part. In fact, the sealant, which was Omniseal, deteriorated because of radiation damage, and the pressure of the vacuum chamber for the first crystal increased from the order of 10^{-5} torr to the order of 10^{-4} torr.

We often measured the vertical divergence angle about the first harmonics of undulator radiation. We employed (-, +, +) Si 220 or 400 setting using the first and second crystal of the monochromator and analyzer crystal in the experimental room for this purpose. We derived the vertical-angle dispersion ($\sigma_{y'}$) of the electron beam from the vertical divergence of the undulator radiation. Figure 10 shows a relation of the

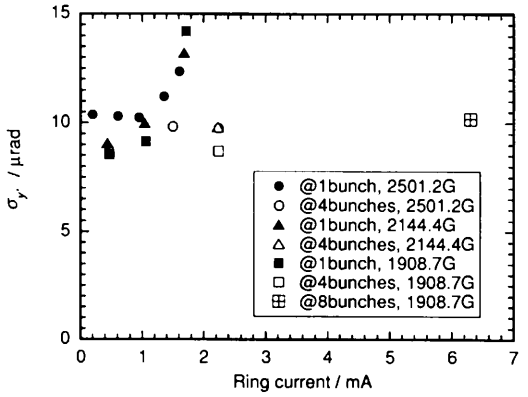

Fig. 10 Relation between vertical-angle dispersion ($\sigma_{y'}$) of the electron beam and the ring current of the MR. The closed symbols show $\sigma_{y'}$ at a single bunch, and the open symbols show $\sigma_{y'}$ at multi-bunches (4 or 8 bunches). Other numerical values show the magnetic-flux density of the undulator (undulator gap) on the measurement.

vertical-angle dispersion ($\sigma_{y'}$) and the ring current of the MR. The $\sigma_{y'}$ dramatically increased at over 1 mA of the ring current during single-bunch operation. During multi-bunch operation at below 1 mA of the ring current per bunch, however, the increase of $\sigma_{y'}$ was small at even several mA of total ring current. We experimented under the condition that the ring current per bunch was below 1 mA. We also measured the relation of the vertical angle dispersion ($\sigma_{y'}$) and the magnetic flux density of the undulator (gap of the undulator), as shown in Fig. 11. The $\sigma_{y'}$ increased with the magnetic-flux density of the undulator. This effect indicated that there was an extra horizontal magnetic field on the undulator for some reason or another. In fact, $\sigma_{y'}$ decreased, when a corrective horizontal magnetic field was applied in order to eliminate any extra magnetic field. We were not able to find the cause which differentiated among each set of measured $\sigma_{y'}$.

The spectrum of the undulator radiation was measured at the end of operation of the MR. The condition during the measurement was as follows: the *K* value of the undulator was 1.09, the MR was operated with 2 to 5 mA at 10 GeV, the measured range was 11 to 14 keV and its higher harmonics. The corrective horizontal magnetic field was applied during the measurement of the spectrum. A monochromator with (+, -) Si 400 setting was employed to measure the spectrum. The monochromator was calibrated by the energy of the nuclear-resonant scattering of ^{57}Fe (14.4 keV). An aluminum absorber and an x-y slit with an aperture of 0.2 × 0.2 mm^2 were set after the monochromator in that order. The intensity after the x-y slit was measured by means of a PIN photo-diode detector with a series of the thickness of the aluminum absorbers in range of 0 to 12 mm. The component of the first and second harmonics were separated by using the difference in the absorption coefficient for aluminum at each harmonic. The corresponding output current of the PIN detector at each harmonic was converted into the number of photons at each energy. Figure 12 shows the measured flux density corresponding to 10 mA operation of the MR as the closed circle and the theoretical one as the solid line. The measured flux density was derived from the aforesaid number of photons, which were corrected for the reflectivity and reflective width of the monochromator, absorption of matter on the SR beam and size of the x-y slit. The measured flux density is in good agreement with theoretical one, as shown in Fig.12. This result is evidence that the beamline operated with good performance, including the monochromator.

H. Sugiyama, PF

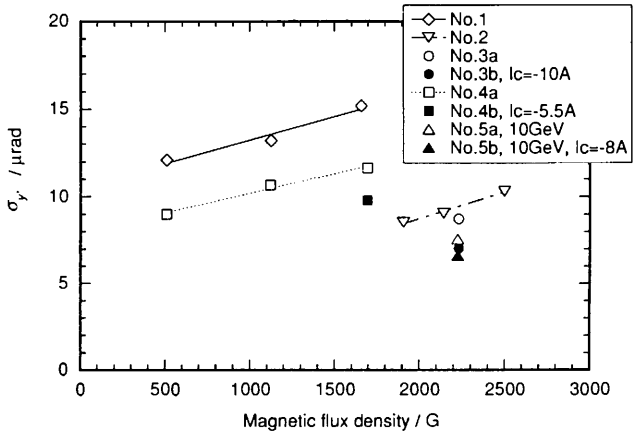

Fig.11 Relation between the vertical-angle dispersion ($\sigma_{y'}$) of the electron beam of the MR and magnetic flux density of the undulator (gap of the undulator). The closed symbols show $\sigma_{y'}$ with the corrective horizontal magnetic field, and the open symbols shows $\sigma_{y'}$ with the corrective horizontal magnetic field. "Ic" is the current of the coil for the corrective horizontal magnetic field.

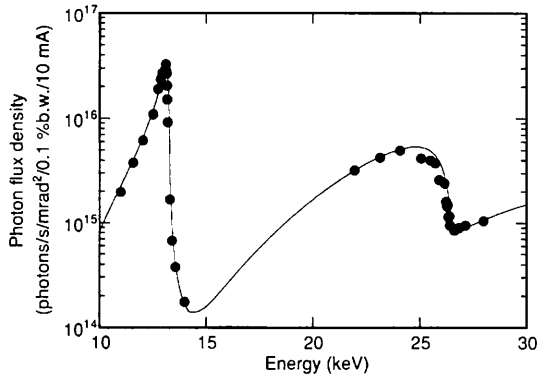

Fig.12 Spectrum of the undulator radiation at 10-GeV operation of the MR. The closed circles show the measured spectrum and the solid line shows the theoretical calculation.

5. RESULTS OF THE SUPER-BRILLIANT SR EXPERIMENTS

5.1 SUBMICRON X-RAY MICROBEAM PRODUCTION WITH A WOLTER-TYPE GRAZING-INCIDENCE MIRROR

X-ray microprobes have been developed for various spectroscopic and structural studies of matter

with spatial resolution. Detectable signals are fluorescent X-rays, photoelectrons, micro-X-ray diffraction, EXAFS and so on. There are several approaches to produce an X-ray microprobe. Among the various optical elements, grazing-incidence mirrors are very convenient focusing elements, because they can be used for a wide spectral range. Due to the large optical aberrations inherent to the single grazing-incidence mirror, it was difficult to produce a small X-ray spot of less than one micron. In order to produce a much smaller microbeam, these aberrations must be reduced. A Wolter type-I mirror is one of the best grazing-incidence mirrors which reduce aberrations considerably.[1] For a highly collimated beam a telescopic mirror system can be applied. The Wolter mirror consists of a paraboloidal and a hyperboloidal mirror which compensate aberrations in each other.

Figure 13 shows the parameters of a Wolter type-I mirror which is being developed for X-rays from an undulator. The average grazing angle (θ) is about 7 mrad and the mirror surface is coated with platinum, so that X-rays of less than 12 keV can be reflected. The total reflectivity of the mirror is calculated to be about 68% at 8.54 keV. The detailed fabrication process of the mirror was reported in a previous paper.[2] The surface roughness is smaller than 1 nm, which reduces the X-ray scattering remarkably.

A schematic diagram of the microbeam optics at MR is shown in Fig. 14. The distance between the undulator and the mirror is about 100m. The undulator has 120 periods and its period is 4.5cm long. X-rays were monochromatized at 1.45 Å (8.54 KeV) by two Si (220) crystals. The incident beam into the mirror was collimated by two slits(#1,#2). The divergent angle of the incident beam is approximately 3μrad (vertical) × 5μrad (horizontal), and that gave rise to a relatively large coherent area (vertical ~ 50μm, horizontal ~30μm) at the entrance plane of the mirror. We fixed the aperture of the slit #2 to be 110μm(vertical) × 120μm(horizontal). Just before the detector, a spatial filter was set up to cut the extra reflected beam and the scattered beam.

The storage ring was operated at 8 GeV and the beam current was several mA during our experiment. The shape of the X-ray microbeam was imaged with Fuji nuclear plates. As shown in Fig. 15, the X-ray microbeam in the focal plane was horizontally separated. This separation was caused by the surface undulation of the mirror. One of these microbeams could be chosen by adjusting the position of the spatial filter.

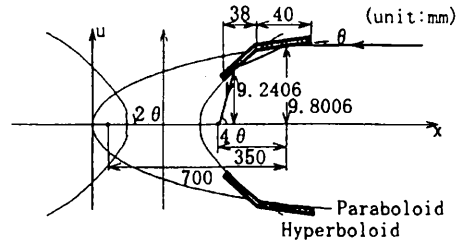

Fig.13 Parameter of a Wolter mirror.

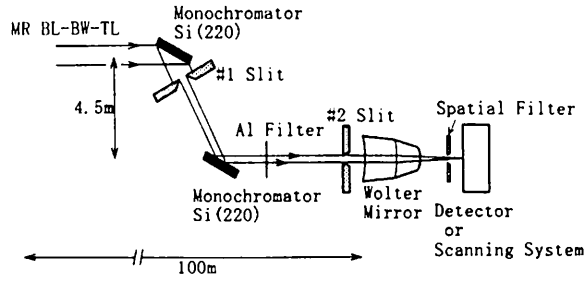

Fig.14 X-ray microbeam optics.

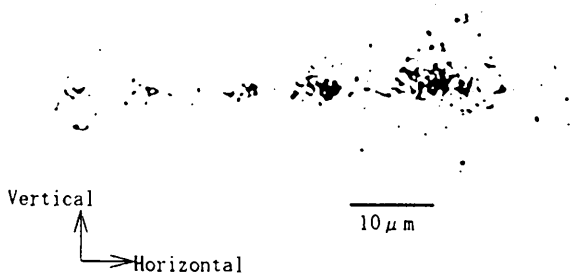

Fig.15 X-ray microbeam image.

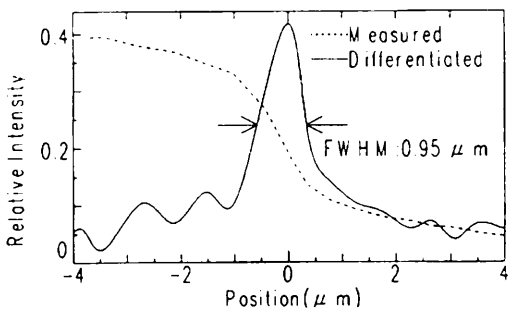

Fig.16 Beam profile measured by knife-edge scanning.

To evaluate the vertical diameter of one microbeam, a knife-edge test was made. The broken line in Fig. 16 shows the transmitted intensity profile of the microbeam. The beam diameter, which was

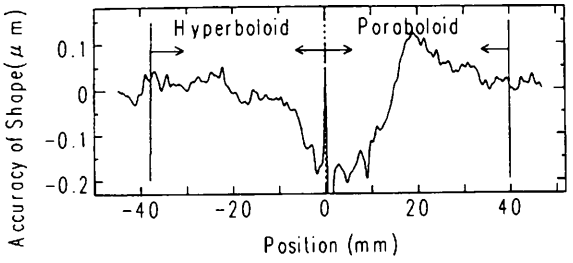

Fig. 17 Longitudinal surface profile of the Wolter mirror.

estimated by the vertical divergent angle of 3μrad, was less than 1μm. The smallest diameter of the microbeam was limited by the vertical divergent angle of 3μrad.

Figure 17 shows the longitudinal surface profile of the Wolter mirror. The mirror surface has some periodic undulation of about 1mm. The separation of the focal points shown in Fig. 15 might be explained by these undulations. Each focal spot was separated at intervals of about 10 μm. If we assume that these separations come from the grating-like surface structure, we can estimate the period of the surface undulation to be about 1.4mm. These values approximately coincide with the period of the undulation. The results show that the surface undulation of the mirror must be reduced to be as small as possible.

S.Aoki University of Tsukuba

References

1) H.Wolter, Ann.Phys. 10(1952) 94-114
2) T.Onuki, K. Sugisaki and S.Aoki, Proc.SPIE. 1720(1992) 258-263.

5.2 GENERATION OF HARD X-RAY MICROPROBE WITH SPUTTERED-SLICED FRESNEL ZONE PLATE

An X-ray microprobe with a sub-micrometer spot size is expected to be important technology for material science and biology. The nominal spatial resolution of about 1 μm has already been achieved using total-reflection mirror optics, multilayer-mirror optics and Fresnel zone-plate optics.[1-4] However, a sufficient probe intensity can not be obtained using second-generation SR light sources. The third-generation SR source is indispensable as a practical hard X-ray microprobe with a sub-micrometer probe size. In the TRISTAN-MR experiment, we have tried to generate a hard X-ray microbeam with a sub-μm beam size and with a sufficient beam flux for scanning microscopy.

5.2.1 Experimental setup (X-ray focusing optics)

A schematic diagram of the experimental set up is shown in Fig. 18. Undulator radiation passing through double graphite heat-absorbers and double beryllium windows is monochromatized with a Si 220 double-crystal monochromator. The X-ray energy is fixed at 8.54 keV during the experiment. The K-value of the undulator is tuned by changing the magnet gap as the output flux from the monochromator reaches maximum. The third beryllium window located between the first crystal and second crystal of the monochromator separates the vacuum from atmospheric pressure. Finally, the monochromatic X-ray beam impinges on an X-ray focusing device in air. The distance between the light source and the experimental station is about 100 m. A cross slit is placed between the first crystal and second crystal of the monochromator. The cross slit is used as a pseudo-point source for the microbeam experiment, and a demagnified image of the cross slit is generated at the focal point to generate a micro-focus X-ray beam. The distance between the cross slit and the X-ray focusing device is about 16 m.

In this experiment a sputtered-sliced Fresnel zone plate is used as the X-ray focusing device. The sputtered-sliced FZP has been fabricated by Kamijo and Tamura at Osaka National Institute.[5,6] The alternate Ag/C concentric multilayer (50 layers) are deposited onto Au wire substrate (47 μm in diameter) by magnetron sputtering. The film thickness (zone width) of the first inner layer is 0.4 μm, and 0.25 μm for the outermost layer. The diameter of the FZP is 80 μm. After deposition, the wire sample is sliced into a plate normal to the wire axis. Finally, the FZP is polished mechanically until it has an appropriate thickness. When the thickness of the FZP is more than 10 mm, the FZP operates as an amplitude-modulating zone plate, and the efficiency of the first-order diffraction is not

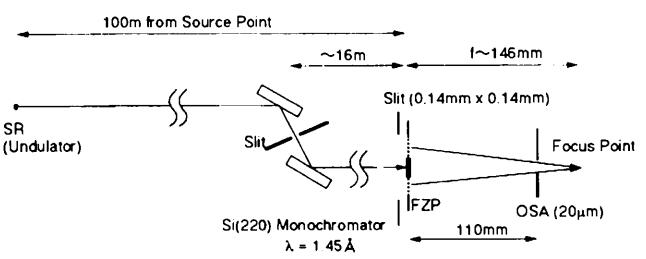

Fig. 18 Schematic diagram of the optical system. OSA: Order Selecting Aperture. FZP: Fresnel Zone Plate.

higher than $1/\pi^2$ (~10%). When the FZP is thinned to less than 10 μm, the zone plate becomes a phase-modulating zone plate, and the theoretical limitation of the first-order diffraction efficiency increases to 40%. The thickness of the FZP used in this experiment is estimated to be about 8-9 μm.

A preliminary test of X-ray focusing properties has been performed at BL-8C2 of the Photon Factory 2.5-GeV storage ring, and a focused beam size of 0.9 μm was been achieved at an X-ray energy of 8 keV. The diffraction efficiency for the first-order focus is about 10%. The FZP is apodized by the center beam stop (47 μm diameter gold). Taking the annular aperture of the FZP into account, the intrinsic diffraction efficiency achieved by the zone area is estimated to be about 16%. This value is larger than the theoretical limitation of the first-order diffraction efficiency for the amplitude-contrast FZP. Therefore, this FZP is considered to be phase-shifted.

The measured focal length is about 146 mm at an X-ray energy of 8.54 keV. In this experiment a demagnified image of the X-ray source is formed by the FZP to generate a micro-focus X-ray beam. When the cross slit placed between the first crystal and second crystal of the monochromator is used as a point-like X-ray source, the magnification (M) is defined by the equation M = f/L, where f (=146mm) is the focal length of the FZP and L (=16 m) is the distance between source and FZP. The slit width used in this experiment is estimated to be about 50 μm. When the slit width is 50 μm, a focused spot size of 0.5 μm can be derived by geometrical optics. When the source point of the undulator radiation is demagnified with the FZP, the focal-spot size depends on the source size. The designed source size is 300 μm (horizontal) × 50 μm (vertical), and source to FZP distance (L) is 100 m. Therefore, the focal spot size calculated by geometrical optics is 0.45 μm × 0.08 μm.

The FZP, bonded onto a graphite plate (1 mm thick), is mounted onto a manipulator. A cross slit (0.14 mm × 0.14 mm) is placed just in front of the FZP to reduce background noise. An order sorting aperture (OSA), a 20 μm-diameter pin-hole made of 0.2 mm-thick Ta plate, is used for selecting the first-order diffraction. Higher order diffraction and 0-th order light is perfectly eliminated with the OSA. The intensity of the focused X-ray beam is measured with an ionization chamber, or a NaI scintillation counter. Focused beam profiles are measured by knife-edge scans. The knife-edge, which is actually a gold wire of diameter 50 μm, is scanned with a translation stage driven by a stepping motor. The minimum step of the scanner is 0.025 μm. The line-spread-function of the optical system is derived from the numerical differential of the measured knife-edge scan profiles.

5.2.2 Results

The cross slit between the first and second crystal of the monochromator is used as a pseudo-point source for the X-ray focusing experiment. The focused beam profile measured by knife-edge scanning is shown in Fig. 19 a. A spot size (spatial resolution) of about 0.5 μm in full-width at half-maximum (FWHM) was achieved. This spot size is close to the diffraction-limited resolution of the FZP (0.3 mm). Therefore, the FZP used in this experiment is considered to be very near to that of the ideal zone plate.

The FZP was not a practical device at the bending magnet beamline of the Photon Factory 2.5 GeV storage ring, because of low efficiency and the small numerical aperture. However, by using the high-brilliance undulator radiation from the TRISTAN main-ring, a practical hard X-ray microprobe has been achieved. When the demagnified image of the undulator

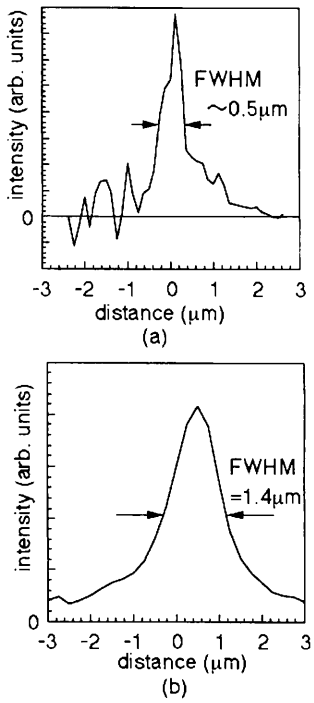

Fig.19 Focused beam profiles measured by edge-scanning. (a) A slit between the 1st crystal and the 2nd crystal is used as s pseudo-point source. (b) SR source is demagnified without the slit

source point was formed by the FZP, the focused beam size measured by edge-scanning was 1.4 μm in FWHM, as shown in Fig.19 b, and the flux density of the focused X-ray beam measured with the ionization chamber was about 1×10^6 photons/s/μm^2/10mA_stored_current. This beam intensity is sufficient for applying to the scanning microscopy experiment. However, the focal spot size (1.4 μm) is larger than that with a pseudo-point source (0.5 μm). Although, it seems to be probable that the blur is mainly due to ultra-small angle scattering by graphite filters and Be windows, a closer investigation is necessary for explaining the experimental result.

Y. Suzuki, Hitachi Ltd. and N.Kamijo, Osaka National Institute

References

1) Y. Suzuki and F. Uchida, Rev. Sci. Instrum. 63, 578-581 (1992)
2) J. H. Underwood, et al., Nucl. Instrum. and Meth. A266 (1988) 296-302.
3) W. Yun, et al., SPIE 1740, 117-129 (1992).
4) A. Snigirev, Rev. Sci. Instrum. 66, 2053-2058 (1995).
5) N. Kamijo, et al., Rev. Sci. Instrum. 66, 2132-2134 (1995).
6) N. Kamijo, et al., Rev. Sci. Instrum. 68, 14 (1997).

5.3 HIGH-RESOLUTION SMALL-ANGLE X-RAY DIFFRACTION OF SKELETAL MUSCLES

We report on the results of two small-angle X-ray diffraction experiments on skeletal muscle fibers using an undulator inserted in the Tristan main ring as an innovative source of intense and well-collimated synchrotron radiation.[1] One experiment was performed to study the ultra-structure of the thick filaments in the sarcomere from the X-ray diffraction with a high angular-resolution recorded on a storage-phosphor area detector (an imaging plate, IP). The other experiment aimed to prove cross-bridge behaviors in a striated muscle at the active state by collecting one-dimensional time-resolved X-ray diffraction data from chemically skinned muscle fibers using a rotating-drum IP system. In this experiment, a sinusoidal length oscillation was applied to a muscle during active contraction and in rigor to compare the time courses of the intensity changes of the 14.5-nm meridional reflection.

The Tristan main ring energy was set at 8.0 GeV. The beam currents were 1-8 mA (in static measurements) and ~15 mA (in time-resolved measurements) using either 8 or 32 bunches. Figure 20 shows the beamline layout for the present experiments. The monochromator crystals (Si (220)) were adjusted to pass the first harmonic of the undulator beam (8.4 keV). The large offset arrangement of two monochromators resulted in data with an extremely low background. Two optics were used, depending upon the experiments. The specimen-to-detector distance was 2 m in two experiments described below. For static measurements, optics with only two pairs of slits systems was employed (Fig. 20a). For recording a high spatial-resolution X-ray pattern, the first pair of slits were placed just behind the second crystal, limiting the beam size to 0.14(V) × 0.57 mm(H). The second pair were used as guard slits to reduce any parasitic scatter. The beam size after the second slits was 0.16 × 0.60

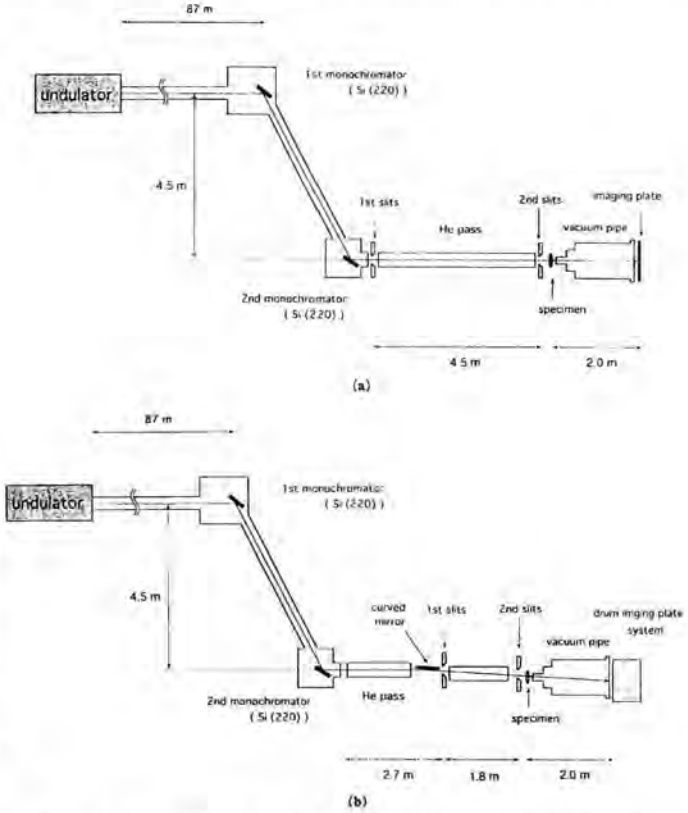

Fig. 20 Beamline layout for the diffraction experiments on muscle. (a) For the high-spatial resolution measurements and (b) for the time-resolved measurements. The crystals were adjusted to pass the first harmonic of the undulator beam. In (b) a 20 cm-long platinum-coated bent glass-mirror is inserted to focus the X-ray beam vertically to ~0.3 mm at the specimen.

mm, showing that the vertical beam increased by only 20μm over the travelling distance of 4.5 m. The flux was ~15×10^8 photons s^{-1} at a ring current of 5 mA. The diffraction patterns were recorded on the IP. In the time-resolved experiments a 20 cm-long platinum-coated cylindrically bent glass-mirror was inserted horizontally at ~95 m from the source and 2 m upstream of the sample position (Fig. 20b). The mirror was able to intercept about 40% of the beam and made it focus vertically to a line ~0.3 mm at the specimen position. The beam was collimated to 0.3(V) × 2.0 mm(H) on the specimen by the first slits placed behind the mirror. The flux was ~1×10^{11} s^{-1} at ~15 mA, which is one order of magnitude higher flux than that for a similarly sized beam from the BL15A bending-magnet line at PF. One-dimensional streak patterns were recorded using the rotating-drum IP system.

5.3.1 Static experiments on muscle

Figure 21 shows the diffraction pattern taken from a frog live sartorius (whole) muscle resting in a Ringer's solution. The small beam size ensured sharp reflection peaks, making patterns with high spatial resolution in both the meridional and equatorial directions.

The patterns also have high contrast because the background is very low. The most notable feature of the diffraction pattern in Fig. 21 is the number of fine peaks (over 100) along the meridian (the central vertical axis of the pattern) in the 0.015-0.25 nm^{-1} region. Figure 22 depicts the intensity tracing on the meridian after subtraction of the background intensity. These fine peaks, which would have a peak-to-peak separation of 700-1000 nm, arise from the protein arrangements in the two symmetrical halves of the thick and thin filaments across the M-line and Z-band, respectively. A precise measurement of the peak-to-peak separation on the thick filament-based meridional reflections (denoted by M in the left-hand side of Fig. 21) gave a 704 nm Bragg spacing (i.e., the angular separation of ~2×10^{-4} rad), proving the highly collimated nature of the undulator beam. Most of the fine fringes come from the protein arrangements in the two symmetrical halves (0.8μm long) of the thick filaments across the M-line located at the center of the sarcomere.

In each half of the thick filament of a frog muscle, the thick filament has a three-stranded helical structure (each strand having a 91 (9 residues/1 turn) helix) and

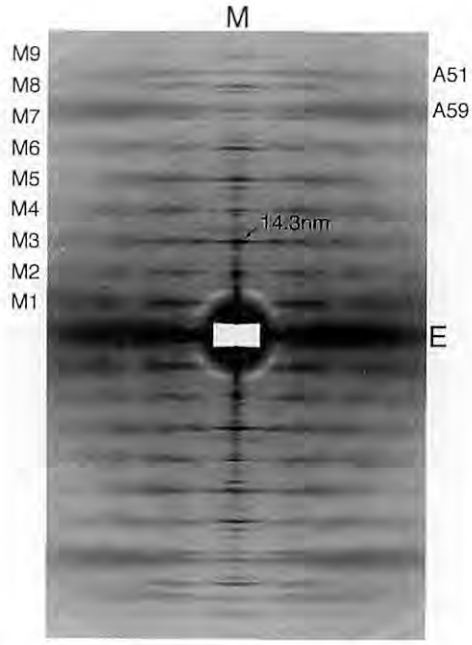

Fig. 21 X-ray diffraction pattern taken from a frog skeletal muscle in the living relaxed state. The pattern was recorded on an imaging plate for an exposure time of about 30 min at a camera length of 2 m with a ring current of 4 mA. The fiber axis of the muscle is vertical. M is the meridional axis and E is the equatorial axis. M1-M9 denote the thick filament-based reflections with a basic repeat of 43 nm and A59 and A51 denote the thin filament-based reflections. The arrow indicates the 14.3-nm thick filament-based meridional reflection. The spacing of this reflection changes to 14.5 nm when the muscle is activated or put into rigor.

the myosin projections are protruding from the backbone surface at 14.3-nm intervals axially. Since the thick filament has a three-fold rotational symmetry, the crystallographic repeat of the whole filament is 43 nm (=14.3 nm × 9/3). These projections from the thick filaments are called cross-bridges, which interact with actin during muscle contraction. Such a regular thick filament structure only gives meridional reflections at three integral orders of 43 nm. However, there are the presence of 'forbidden' reflections on the meridian (see Fig. 21), indicating that the axial cross-bridge repeat is not the regular 14.3 nm, but, rather, that successive periods are systematically perturbed with retaining the basic repeat of 43 nm. C-proteins are bound with an axial interval of 44 nm to a certain region in the thick filament backbone, giving meridional reflections with a repeat of 44 nm. Thus, interference effects between the

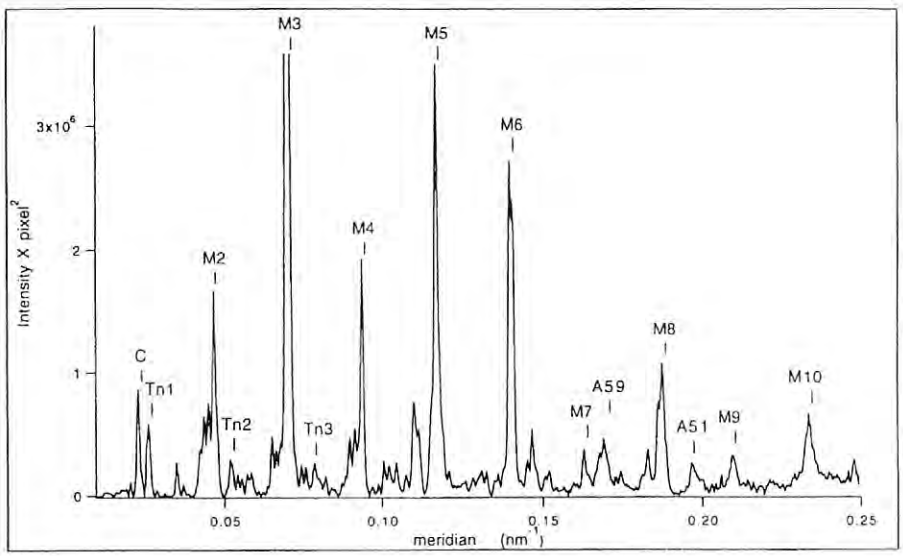

Fig. 22 Intensity distribution on the meridian in the X-ray pattern from a live frog skeletal muscle in Fig. 20. The intensities after subtraction of the background are shown by multiplying the square of the axial coordinate. M2-M10 denote the thick filament-based meridional reflections with a basic repeat of 43 nm and C denotes a 44-nm reflection from C-proteins bound to the thick filaments. Tn1-Tn3 depict the reflections with a repeat of 38 nm from troponin molecules bound on the thin filaments.

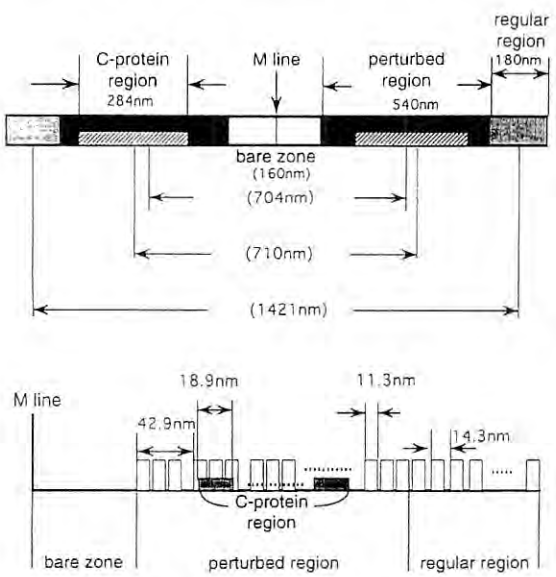

Fig. 23 Model of the thick filament structure projected onto the fiber axis. The upper shows the distribution of the perturbed and regular regions of cross-bridge periods and the C-protein regions along the thick filament. The lower depicts the mass density distribution of the cross-bridges (denoted by the white squares) in the two regions and the C-proteins (denoted by the hatched squares).

two symmetrical halves of the thick filaments (containing C-proteins) across the M-line give rise to the fine fringes on the thick filament-based meridional reflections.

A precise measurement of the peak-to-peak separations on the thick filament-based reflections determined the center-to-center distances between the perturbed regions of the cross-bridge arrangements and those between the C-protein regions together with the lengths of their respective regions (see Fig. 23). Using these data, we calculated the meridional intensities from the assumed mass density distribution projected onto the filament by modeling the structures of a cross-bridge and a C-protein and the successive periods of cross-bridges within their basic repeat in the perturbed regions so as to get the best fit with the observed intensities.[2] Figure 23 shows the best-fit model of the projected structure of the thick filament, and the calculated intensities from the model is compared with the observed one in Fig. 24. The goodness of the fit was evaluated by the R factor, being ~0.1. The result reveals that the perturbed regions of the cross-bridge periods started at a distance of 80 nm apart from the M-line and terminated at a distance of 180 nm from the filament end, in which the successive periods of cross-bridges are 12.9 nm, 12.9 nm and 17.2 nm in an axial periodicity of 43 nm. In the terminal region of 180 nm long the cross-bridges are arranged with a regular 14.3 nm period. C-proteins are existing over the region of about 300 nm long in the perturbed regions of cross-bridges.

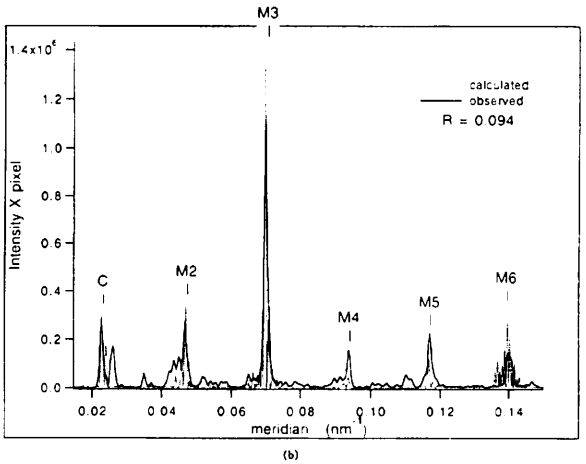

Fig. 24 Comparison of the calculated meridional intensities from the best-fit model and the observed one. The discrepancy factor (R) between them was ~0.1.

5.3.2 Time-resolved experiments

In time-resolved experiments the rotating-drum IP system was used as a one-dimensional detector (Fig. 25). A drum with a circumference of 1080 mm rotated at 20 rotation s^{-1}. The vertical aperture of the entrance slit placed just in front of the drum was set at 4 mm so that the time resolution of measurements was

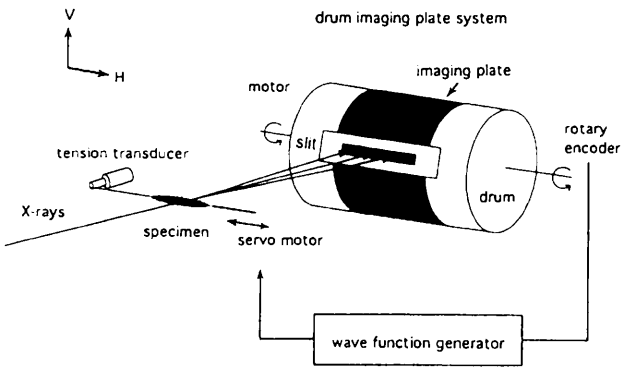

Fig. 25 Rotating-drum imaging plate (IP) system used for the time-resolved X-ray experiments during the length oscillation of the muscle fibers. The IP (200 × 1000 mm) is attached on a drum. A one-dimensional X-ray pattern which passes through the receiving slit is recorded on the IP along the drum axis while intensity changes of the pattern as a function of time are recorded along the circumference. The length of the muscle fiber was oscillated by a fast-moving servo motor in synchronism with the rotation of the drum using a rotary encoder. Tension changes of the muscle were measured by a force transducer.

0.185 ms (50 ms × 4 mm/1080 mm). A small bundle containing less than ten fibers from a chemically skinned rabbit skeletal muscle was used in this experiment. The length of the muscle bundle at the full filament overlap was oscillated at 500 Hz by a fast-moving servo motor synchronously with the rotation of the drum (Fig. 25). The amplitude of oscillation was ~0.3% of the muscle length. The drum circumference could accommodate the streak diffraction image of 25 complete 2-ms oscillations. In a typical total exposure time of 3 min, each of the 25 diffraction images represented the sum of the diffraction from 3600 oscillations. The 25 images were summed to provide an averaged diffraction pattern with a high S/N ratio. An investigation of the intensity changes was made on only the 14.5-nm meridional reflection indicated by the arrow in Fig. 21, one of the most intense in the axial pattern. The experiments were performed at 8 °C

When small oscillatory length changes were applied to either active fibers or rigor fibers, the tension revealed a simple response in synchronism with length changes. Fig. 26 shows the results of a length change of the muscle fibers (a) and intensity changes of the 14.5-nm reflection in the active state (b) and in rigor (c) in one oscillation cycle, which were derived from the streak images recorded on the IP. In the active state the intensity of the 14.5-nm reflection decreased during the stretching phase and increased during the releasing phase synchronously with the tension change. Thus, the intensity change occurred out of phase against the tension change (Fig. 26b). Similar results were obtained from fibers contracting during the addition of inorganic phosphate (Pi) corresponding to a product of ATP hydrolysis. The effect of added Pi was to decrease the amount of tension change and the magnitude of the intensity change (data not shown) due possibly to a reduction of the number of cross-bridges in the force-generating state by shifting the equilibrium of a phosphate-releasing step in the ATP hydrolysis reaction. In contrast, when the fibers were in a rigor state, strong oscillations occurred in this reflection intensity in phase with the tension, i.e., increased tension during the stretch resulted in an increase in intensity and vice versa (Fig. 26c). In a rigor muscle the myosin heads are all firmly attached to actin in the same chemical state, which may correspond to the end of states in the ATP hydrolysis cycle. A control experiment using relaxed fibers showed only very small oscillations in this intensity, which can be attributed to a variation in

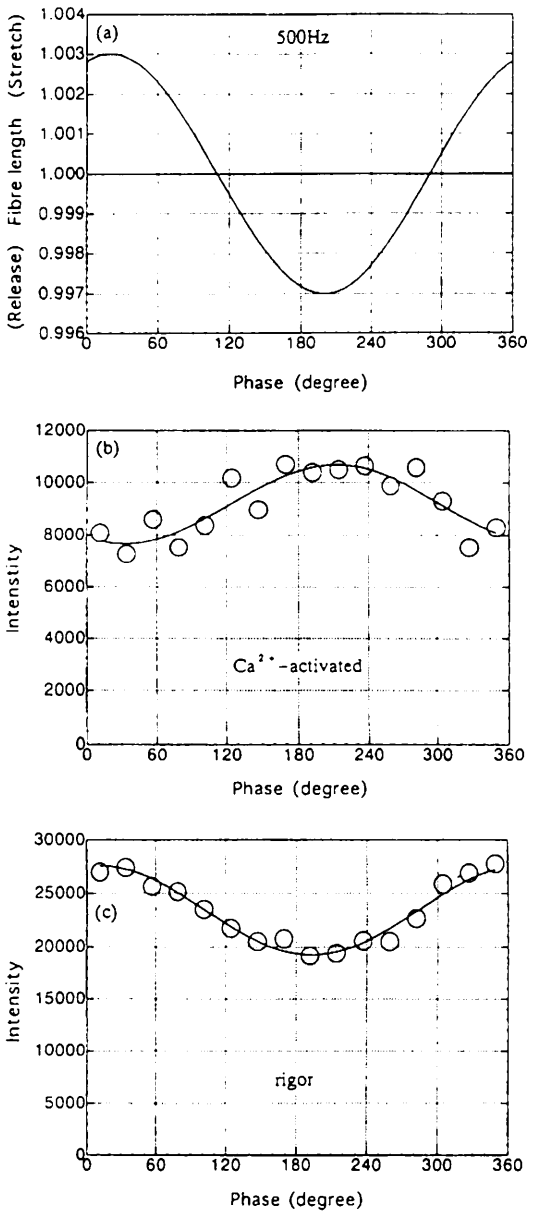

Fig. 26 Length change of the muscle fibers and intensity changes of the 14.5-nm meridional reflection in one oscillation cycle. (a) Oscillatory length change from either active fibers or rigor fibers. (b) A change of the 14.5-nm intensity in the active state, and (c) a change of that in the rigor state. In (b) and (c) the data points were taken from the sum of ~ 90000 oscillations in a total exposure.

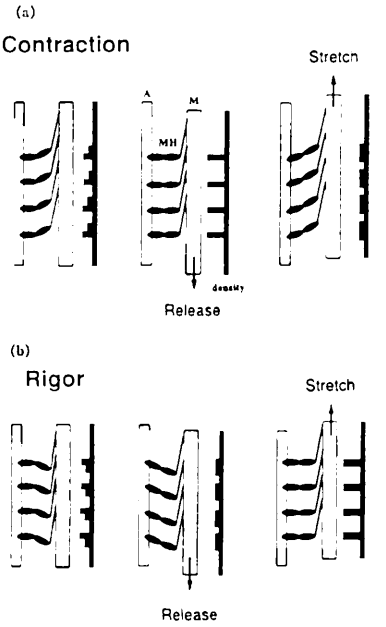

Fig. 27 Schematic views of the possible behaviors of the myosin cross-bridges in response to sinusoidal length oscillation and of their mass projection along the fiber axis. (a) In the active muscle, and (b) in the rigor muscle. M-line located at the center of the sarcomere is upward. A: thin filament, M: thick filament and MH: myosin head.

the muscle thickness with stretch and release.

Although most of the myosin heads in an active muscle are at different stages of their working stroke, the application of a rapid length oscillation to the active muscle fibers may allow the partial synchronization of the behaviors of the myosin heads on a sub-millisecond timescale. The observed intensity changes of the 14.5-nm meridional reflection are likely to be due to an alteration of the projection of the mass of the population of myosin heads along the filament axis. These could be caused by a change in the conformation of the heads attached to the actin filaments. Since there is no net shortening during the oscillation, the structural change produced in the releasing phase would be reversed in the subsequent stretching phase. In a simplified model shown in Fig. 27a, the intensity increase during the releasing phase could be accommodated by altering the orientation of the attached heads (possibly the proximal portion of the myosin heads) to almost perpendicular to the fiber axis so that their mass projection is more sharply localized on the 14.5-nm planes. The intensity decrease during the stretching phase could be due to a further tilting away from the isometric orientation, resulting in a spreading out of their mass projection along the filament axis. In contrast, in the rigor fibers the intensity changes of this reflection occurred in a reverse manner to those in the active fibers. If we explain this reverse response in terms of a similar mechanism by assuming that this reflection in rigor also comes from attached heads, the average orientation of attached heads in the rigor state is on opposite sides

of the plane perpendicular to the filament axis, as in the active state (Fig. 27b).

Although Fig. 27 seems to be simple and plausible models describing the behaviors of the cross-bridges during length oscillations in the both states, for a precise interpretation of the observed changes it would be necessary to consider various factors, such as the two-headed nature of the myosin heads, interference of the diffraction from attached heads and free heads and elastic changes in the structure of the thick filament backbone.

In summary, our results reported here demonstrate the excellent nature of the highly collimated undulator beam from the Tristan main ring. Although the expected flux was not attained in this short experimental period, the present low emittance and relatively high flux made it possible to perform not only a high spatial-resolution study, but also high time-resolved studies. The high spatial-resolution study helped provide an important clue into the architechtural principle of the myofilaments in muscle and the high time-resolved experiments yield an insight into the relationship between conformational changes and force generation by actomyosin in muscle. These studies show a preview of the expected gains for studies of small biological samples as well as single muscle fibers from more widespread use of undulator radiation at third-generation synchrotron sources.

K. Wakabayashi, Osaka University and N. Yagi, Tohoku University

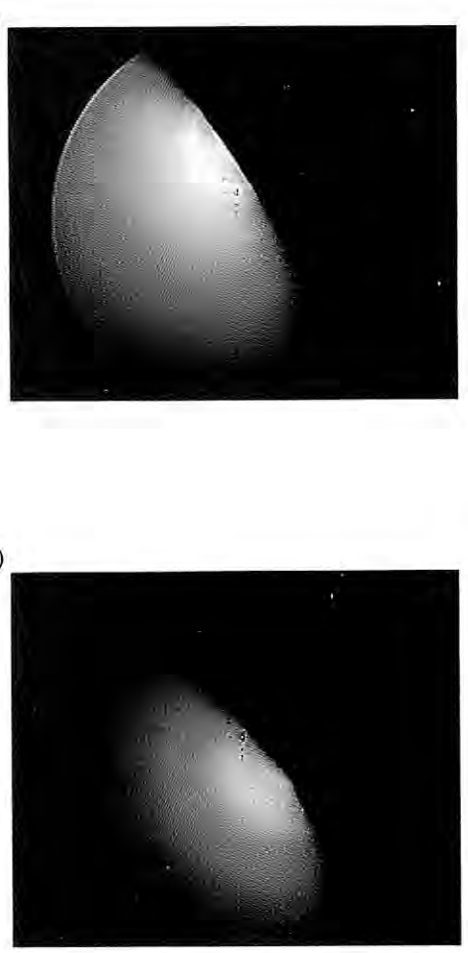

Fig. 28 RHEED patterns after Si growth at 700°C come from the non-irradiation area (a) and the irradiation area (b).

References
1) N.Yagi, et al., J. Synchrotron Rad. 3, 306 (1996).
2) K. Wakabayashi & N. Yagi, J. Japan. Soc. Synchrotron Rad. Res. 10, 200 (1997).

5.4 GROWTH CONTROL OF THIN FILMS BY X-RAY STANDING-WAVE FIELDS

An X-ray standing wave has been used to analyze the surface and interface structure. However, intense X-ray standing-wave fields could be lattice-aligned energy totally different from specially uniform energy, such as heat or light. In this study, intense X-ray standing-wave fields formed by Si substrate were utilized in film growth control. Si or Ag film has been grown on amorphous SiO_2 films on a Si substrate1).

We used a double-crystal monochromator of Si 400 reflection. The X-ray energy was about 11.5 keV. The reflection plane of the sample was the 400 plane of the Si(111) wafer, which gives an X-ray standing-wave field on the amorphous SiO_2 films on the Si substrate.

For Si-film growth, Fig. 28 shows RHEED patterns after Si growth at 700°C coming from the non-irradiation area (a) and the irradiation area (b). While the RHEED pattern of Fig. 28(a) shows the growth of Si, the pattern of Fig. 28(b) shows that the surface of the irradiation area is SiO_2. These results mean that photo-assisted Si desorption has been observed at 700°C of the substrate temperature in the hard X-ray wavelength region.

For Ag-film growth, the intensity ratio of the 111 and 200 reflections of Ag in-plane diffraction was measured using energy-dispersive grazing-incidence X-

ray diffraction techniques. The intensity ratio of the Ag-growth sample with X-ray standing-wave fields was found to be different between the Å from that without X-ray standing-wave fields. This suggests that the X-ray standing-wave fields slightly change the preferred orientation of Ag films from free-energy changes of nucleation.

K.Akimoto, Nagoya University and A.Tanikawa, NEC Corporation

Reference

1) K.Akimoto and A.Tanikawa, J. Jpn. Soc. Synchrotron Radiation Research, 10 (1997) 133.

5.5 TWO-PHOTON CORRELATIONS IN X-RAYS FROM A SYNCHROTRON RADIATION SOURCE

5.5.1 Introduction

An intensity-correlation experiment with visible light was first demonstrated by Hanbury Brown and Twiss.[1] They observed that photons in a monochromatic light beam from a thermal source did not arrive completely at random, but arrived in bunches. Further, this technique was applied to an optical stellar intensity interferometer and the angular diameter of visible stars was determined.[2] About twenty years after their pioneering work, the observation of two-photon correlations at synchrotron radiation (SR) was proposed.[3] Actually, the difference in the visible photon counting statistics between SR from a wiggler and that from a bending magnet was observed.[4] However for the observation of such a phenomenon in X-rays one had to wait for the realization of high-brilliance SR sources. This is because the temporal and spatial coherence conditions in the X-ray region are much more difficult to fulfill than those in visible light. This experiment may be applied to the determination of the transverse SR source size of the third-generation ring, which is approaching the diffraction limit. Intensity correlation experiments are planned for such purposes in the third-generation SR facilities.[5-7]

5.5.2 Experiments

The experiment was carried out at a test SR beamline temporarily constructed in the TRISTAN

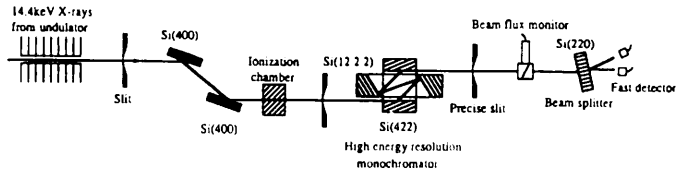

Fig. 29 Schematic side view of the experimental setup.

Main Ring (MR). The MR was operated at an energy of 10 GeV in the 8-bunch mode. The ring current was kept at between 9 mA and 5 mA during the experiment. The brilliance of SR from the undulator was about 10^{18} photons s^{-1} mm^{-2} $mrad^{-2}$ $(0.1\%bw)^{-1}$. The experimental setup is shown in Fig. 29. X-rays from the undulator were roughly monochromatized at 14.4keV by a Si(400) double-crystal monochromator. Next, a high-energy resolution four-crystal Si monochromator was arranged. It comprises two channel-cut Si crystals nested with each other, in which 422 asymmetric reflections served as the first and fourth reflection and 12 2 2 symmetric reflections served as the second and third reflections. Highly monochromatic X-rays with an energy width of 6.4meV were obtained. This energy width determined the temporal coherence of the X-ray beam. The coherence time was estimated to be 0.66ps.

After the four-crystal Si monochromator a precise slit was arranged, which determined the spatial coherence of the beam. The intensity distribution of the source was assumed to be Gaussian. The nominal source sizes in the horizontal and vertical directions were 169μm and 53μm, respectively. The transverse coherence widths of X-rays in the horizontal and vertical directions at a detector position located 100m from the SR source were calculated as 14μm and 46μm, respectively. The optimum condition for the slit size is that it is nearly the same as the transverse coherence width. The vertical slit width was fixed at 40mm, while the horizontal slit width was varied from 20μm to 1mm. The blades of slits made of tantalum metal were driven by stepping motors and their positions were read by linear encoders. The slit width was set to an accuracy of 1μm .

The Si 220 Laue case diffraction served as the beam splitter. The thickness of the crystal plate was 4mm. The diffracted and transmitted beams were incident on avalanche photo-diode detectors. A beam splitter was necessary to make coincidence measurements, since the time resolution of the detector was longer than the pulse width of SR. We now consider

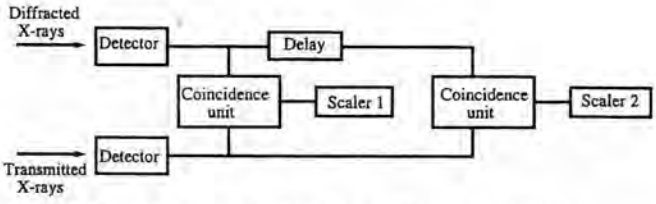

Fig. 30 Block diagram of the photon counting system. Actually, three sets of a delay circuit, a coincidence unit and a scaler were additionally connected in series.

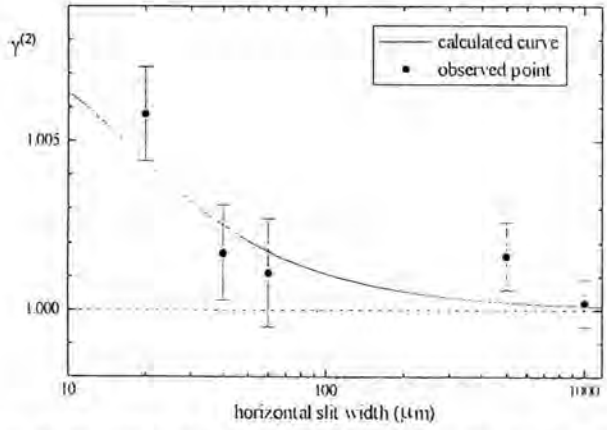

Fig. 31 Variation of the integrated second-order degree of coherence, ($\gamma^{(2)}$) with the horizontal slit width. The error bars show the statistical errors.

the case that two photons relevant to the measurement are included in a SR pulse. Only when two photons in the same pulse are separated from each other by the splitter, is a coincidence event counted. If both photons are diffracted or transmitted in the splitter, no coincidence event is counted.

A block diagram of the photon counting system is shown in Fig. 30. Output pulses from two detectors were fed into the coincidence unit, and then scaler 1 counted the number of coincidences. In the delay circuit the delay time for the output pulse from one detector was set at the circulation period of electrons, 10μs. Random-coincidence events between one photon emitted from a certain electron bunch and another photon emitted from the same electron bunch after making one revolution were counted at the scaler 2. It is essential to use the same electron bunch, because each bunch has a different number of electrons. Coincidence counts measured at scalers 1 and 2 were denoted by R and R_0, respectively. R was normalized by using R_0. To reduce statistical uncertainty of the random coincidence rate, it was counted between two photons separated at the intervals of 20, 30 and 40μs as well as 10μs .

5.5.3 Results and Discussion

The total coincidence counts (R) and random coincidence counts (R_0) were measured for the measurement times at five horizontal slit widths, and the values of the integrated second-order degree of coherence $\gamma^{(2)}$ were obtained as the ratio R / R_0. Here, R_0 is an averaged value of four random coincidence counts measured between two photons separated at intervals of 10, 20, 30 and 40μs.

Figure 31 shows the variation in the integrated second-order degree of coherence $\gamma^{(2)}$ as a function of the horizontal slit width. The experimental results are plotted as points with their associated statistical errors. The full line is the theoretical curve, which was calculated by using the nominal source sizes. The dotted straight line $\gamma^{(2)} = 1$ shows the random coincidence level. The region above this level is considered as contribution from the excess coincidence rate. At a slit size of 20μm × 40μm the excess part is about four times as large as the associated statistical error. As the slit size increases, the value of $\gamma^{(2)}$ decreases, approaching 1. At a slit size of 1mm × 40μm $\gamma^{(2)}$ is very close to 1. The data and expected curves agree relatively well, giving clear evidence for the bunching effect of X-ray photons.

When we calculated the theoretical value of $\gamma^{(2)}$, we treated SR as thermal light. Considering an agreement between the experiment and the theory, we can say that this assumption is valid.

In summary the observation of two-photon correlations is made successfully for the first time in the X-ray region using high-brilliance SR source[8]. The unique method of obtaining $\gamma^{(2)}$ is developed, in which the total coincidence count R is normalized by the random coincidence count R_0 using a circulating electron bunch.

If a high-energy resolution monochromator with sub-milli eV becomes available, a more remarkable correlation effect will be observed. In this case, it may be possible to make the following applications. This technique will be useful for characterizing the source size of third-generation SR sources, just as Hanbury Brown and Twiss determined the angular diameter of visible stars. Further in studies of X-ray laser action

beam diagnosis concerning the coherence at the transition from an incoherent state to a coherent state may be made.

S.Kikuta, Univ. Tokyo

References

1) R.Hanbury Brown and R.Q.Twiss, Nature, 177 (1956) 27.
2) R.Hanbury Brown and R.Q.Twiss, Nature, 178 (1956) 1046.
3) E.V.Shuryak, Sov. Phys. JETP 40 (1975) 30.
4) T.Tanabe, M.C.Teich and T.C.Marshall, Nuclear Instrum. & Methods A304(1991) 77.
5) E.Ikonen, Phys. Rev. Lett. 68 (1992) 2759.
6) E.Ikonen and R.Rüffer, Hyperfine Interactions, 92 (1994) 1089.
7) E. Gluskin, et al., Nuclear Instrum. & Methods A319 (1992) 213.
8) Y.Kunimune, et al., J.Synchrotron Rad., to be published.

B. PF-AR (ADVANCED RING FOR PULSE X-RAYS) PROJECT

1. INTRODUCTION

The purpose of the PF-AR (Advanced Ring for pulse X-rays) project is establishment of a new scientific facility utilizing "single bunch and high flux synchrotron radiation in X-ray region" which is realized by the reconstruction of the former TRISTAN accumulation ring (AR). The project includes a renewal of the accelerator (lattice, vacuum system, RF and monitor systems etc.), construction of new experimental halls, and beamlines.

The scientific program based on synchrotron radiation has spread over large field; material science, chemistry, biology, engineering, medical application etc., and these studies are realized by using following distinctive characteristics of synchrotron radiation;

(a) High intensity
(b) Availability of wide energy range
(c) High Brilliance
(d) Linear or circular polarization
(e) Pulsed time structure

The characteristics (a), (b), and (c) have been used by various experiments (XAFS, topography, small angle scattering, structural analysis etc.) since the initial operation of PF (1982). The polarization nature (d) has been also recognized as an important characteristics for experiments such as polarized XAFS, magnetic Bragg and Compton scattering, magnetic circular dichroism. Recently, the pulsed time structure (e) has played an essential role in advanced SR experiments. For example, Mössbauer spectroscopy has made a great advance by the time-domain technique. The time of flight spectroscopy of ions or electrons created by pulse X-ray photons has been applied to studies such as the photo-chemical reaction or high resolution measurement of 3-dimensional electron momentum density by using Compton scattering process. On the other hand, time-resolved structural analysis of protein crystal during a photo-induced reaction was also performed by the Laue method. The time resolution was in the milli-second range in a moment. If we use the high intense pulse X-rays at PF-AR (the pulse width is about 100 psec and the interval of each pulse is 1.26 msec), it will be possible to investigate the dynamics with the nano-second time resolution. Such investigation of a dynamics will be done by XAFS and small angle X-ray scattering to clarify what kind of the electronic state and structure at the intermediate state of the reaction. In order to advance these activities further, we are eager to establish a new scientific facility based on "single bunch and high flux synchrotron radiation in X-ray region".

The designed PF-AR accelerator is a single bunch and high flux synchrotron light source; a dedicated machine for single bunch operations with a high stored beam current (6-6.5 GeV, 200 mA, single bunch). Third-generation machines (ALS, ESRF, APS, and SPring-8) have been already operating. These machines are designed as a low emittance ring to get a high quality of (c) High Brilliance characteristics. On the other hand, the present PF-AR project is designed to emphasize (e) Pulsed time structure and (a) High intensity.

Figure 32(a) shows flux spectra on a single pulse from the PF-AR (200mA) and Photon Factory (50mA). The PF-AR will provide 10^8 photons/pulse at a sample position (the focused beam size is about 0.5×0.3 mm^2) with the energy resolution of 10^{-4} at 10keV. The intensity of the above pulse X-rays would be sufficient to clarify what kind of the electronic state and structure at the intermediate state of the reaction by using X-ray

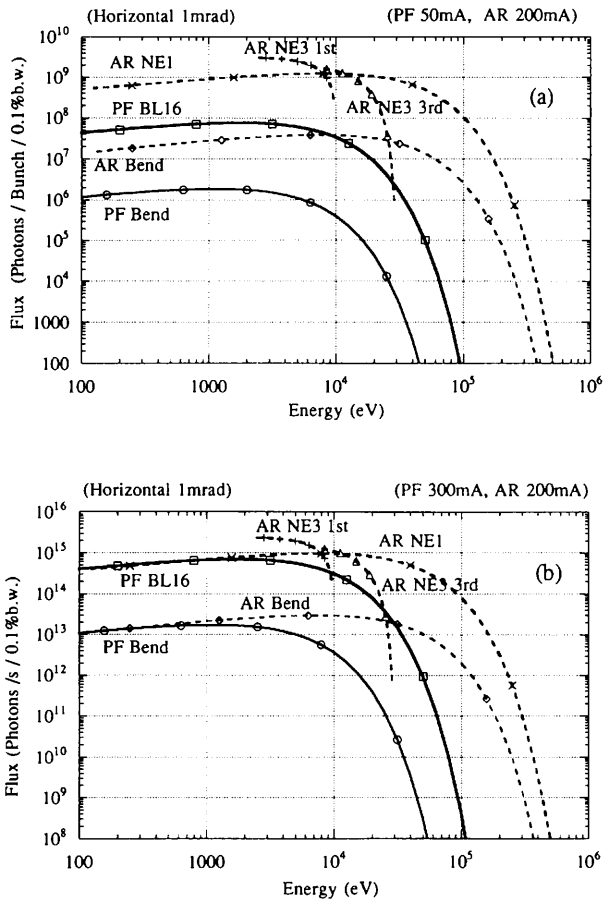

Fig. 32 (a) Solid (dotted) lines correspond to flux spectra on a single pulse from the insertion device beam lines and bending magnet beamlines at the Photon Factory (50mA) and the PF-AR (200mA). (b) Flux spectra from the PF-AR (200mA) (dotted lines) and Photon Factory (300mA) (solid lines).

scattering and/or XAFS experiments even in a single shot, because the typical value of the reflectivity of X-ray diffraction from the sample would be ~10^{-4}. The PF-AR light source also would be attractive for studies based on time domain measurements like Mössbauer spectroscopy and time of flight spectroscopy of ions and electrons created by pulse X-ray photons.

The PF-AR will bring not only a single bunch X-ray source but also a high flux hard X-ray source. Figure 32(b) shows usual flux spectra from the PF-AR (200mA) and Photon Factory (300mA) at natural operation conditions. As shown in this figure, the PF-AR will provide almost one order of magnitude (or more) higher flux than those from Photon Factory at a hard X-ray region (>10 keV). The high flux enables us to measure an weak X-ray scattering phenomena like a magnetic scattering, structural analysis under extreme conditions (like a high pressure, surface etc.), and also to establish a medical application like "Coronary Angiography".

2. SCIENTIFIC PROGRAMS

The beam lines proposed for the PF-AR project are listed in Table 6. Among these some of the experiments are mentioned briefly.

Table 6 List of proposed beam lines in PF-AR project

Time-resolved protein crystallography
Time-resolved XAFS
Time-resolved small-angle scattering
Photochemistry and Photobiology
Nuclear resonant scattering/spectroscopy using pulsed X-rays
Compton sattering
Medical imaging
X-ray diffraction under high pressure and high temperature
Charge, spin and orbital structure analysis by X-ray diffraction
Inelastic X-ray scattering
Magnetic circular dichroism in soft X-ray
XAFS in high-energy region
X-ray diffraction with high-energy photons
X-ray optics
Development and characterization for detectors

Time-resolved protein crystallography

Biological activity is invariably accompanied by changes in structure in which atoms, groups of atoms or domains which move very rapidly under near-physiological conditions. But macromolecular crystallography provides space- and time-averaged structure alone. Here, time-resolved crystallography in less than a micro second is planned in order to clarify the mechanism of reaction of biological macromolecules by combining time-structure of PF-AR and Laue diffraction.

The design of the beam line is progressing now, whose preliminary design is shown in Fig.33. Here not only the Laue diffraction but also monochromatic large angle oscillation techniques(LOT) are used according to the research aim.

Time-resolved XAFS

Chemical reaction is always accompanied by changes in structure and electronic state. Many chemical reactions, including biological one, have been

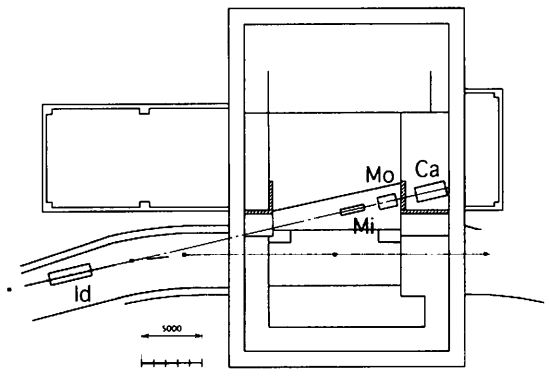

Fig. 33 Preliminary design of the beamline for Time-resolved protein crystallography

studied by using many physicochemical methods. But their information is rather indirect or speculation derived from the initial and final structure, thus the direct structural information on reaction intermediates is very limited. Here time-resolved XAFS experiment is planned in order to clarify the structural and electronic change of molecules in the time-resolution of less than micro second. The experimental result will indicate the reaction mechanism, which will suggest the new reaction routes.

Time-resolved small angle scattering

Small angle X-ray scattering (SAXS) is used to study the nano-scale structure of materials such as macromolecules, polymers, alloys, and liquid crystals, as it gives the information on electron-density distribution of the materials in a scale of nano-meter to micro-meter. By using the high intensities of synchrotron X-ray radiation, the dynamics of the nano-scale structure can be studied with a time resolution of a few milliseconds by the method of time-resolved SAXS. When the single bunch property of PF-AR is utilized, time resolution can be improved further to the order of microseconds, which is quick enough to pursue the structural change of enzymes in solution during the reaction and of proteins under folding and re-folding in real time mode. This will enable us to reach the better understanding of the "mystery of life". The structural changes not only of the macromolecules, but also of metallic alloys and polymers under phase transitions can be studied with time-resolved SAXS.

Nuclear resonant scattering/ spectroscopy by using pulsed X-rays

Nuclear resonant scattering process can be separated from the scattering by atomic charge, when the time gate technique is used. This is due to that the X-ray pulse width (~100 ps) is quite shorter than the lifetime of Mössbauer levels (~10 ns), and the charge scattering is instantaneous with the SR flash. Such experimental method has been developed in the Photon Factory by using the single-bunch machine-AR. The quality of experiment will be much improved by the increase of beam current, lifetime and stability in this project. Some applications which cannot be studied with conventional Mössbauer spectroscopy, such as small samples, linear or circular polarized gamma rays, nuclear excitation in gaseous or liquid states, will be also studied in this beam line.

Compton scattering

It is possible to obtain the information on the three dimensional momentum distribution of electrons in solid by measuring the energies and directions of both Compton scattered X-ray photon and the recoil electron simultaneously. The energy of the electron can be measured by using a time-of-flight technique, which can be realized by single bunch property of PF-AR. Studies on the minute electronic state variation accompanied by the phase transition, determination of Fermi surface of complex or disordered system can be realized.

Medical imaging

A two-dimensional imaging system for intravenous coronary angiography is developed in the Photon Factory. First patient examinations were done in 1996 at AR NE1, a MPW beamline, and got many useful clinical information on the patients. It will be possible to do more practical examinations using SR from the high-current AR, and a dedicated station to medical applications. It is strongly demanded by the medical community. Also the clinical application of intra-arterial angiography to evaluate small vessels for cancer and high resolution monochromatic X-ray CT is to be developed.

3. NEW EXPERIMENTAL HALL

The construction of new experimental halls is an essential point of the PF-AR project. Figure 34 shows the plan view of the PF-AR. The shaded areas correspond to present buildings of an experimental hall (North-East part of the ring; NE-experimental hall) or

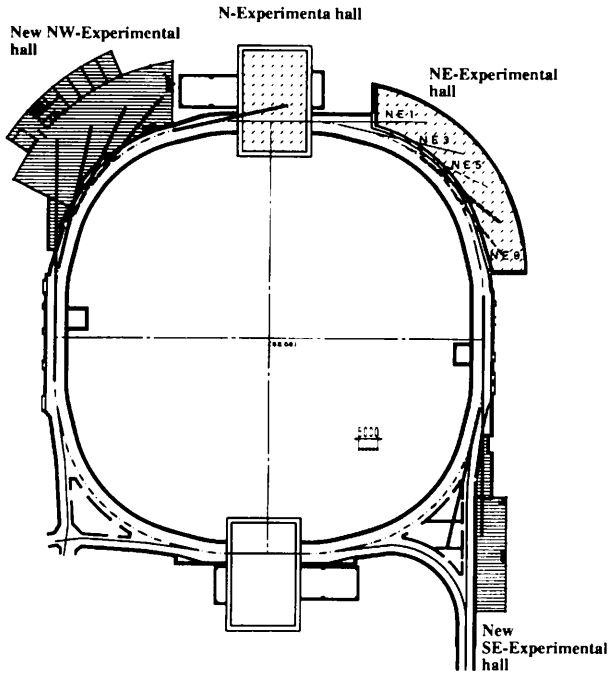

Fig. 34 Plan view of the PF-AR. The shaded part corresponds to present buildings, and the hatched part corresponds to new experimental halls. The thin (thick) lines are those which are already constructed (under planning). The solid (dotted) beamlines are insertion device (bending magnet) beamlines.

that which can be reconstructed to an experimental hall (North part of the ring; N-experimental hall). The hatched areas correspond to new experimental halls (North-West and South-East parts of ring; NW and SE-experimental halls). As shown in this figure, two insertion device and two bending magnet beamlines have been already constructed in the NE-experimental hall, and there remains just one bending magnet beamline to be constructed. Even after the N-experimental hall is reconstructed, just one insertion device beamline can be installed. It is impossible to realize so many scientific programs as mentioned at the preceding section without constructing new experimental halls. As shown in this figure, two insertion device and two bending magnet beamlines will be constructed in the NW-experimental hall. There are several preparation rooms for the sample, detectors, and electronics etc.. In the SE-experimental hall, at least one insertion device beamline will be constructed. This hall also makes it possible to access to a small room (triangular shape one) which has been already constructed in a ring tunnel. One more insertion device beamline can be constructed in this area.

4. LIGHT SOURCE

The AR was built as a booster of the TRISTAN main ring in 1984, and its application for synchrotron radiation experiments started in 1987 using interval time between injections for the main ring. At present, the TRISTAN project has come to completion, and construction of the new B-factory project has started. Since the beams of the B-factory rings will be injected directly from the upgraded linear accelerator, we are planning to use the AR as a dedicated machine for the synchrotron radiation experiments.

In the original design, an electron energy of 6.5GeV and a beam current of 200mA in the single bunch mode were proposed, however, several problems were found by the task force. In the project, resources of the present AR have to be used as much as possible considering the available manpower and budget. However, the lattice and the vacuum system including the beam monitor system should be optimized to a dedicated light source. Furthermore it is difficult to change the lattice or the vacuum system after commissioning, therefore, it is desirable to renew them in the first phase of the project. On the other hand, since renewal of the RF acceleration system and the injection system is relatively easy, improvement of these systems may be done in the second phase. The electron beam is accelerated by 8 APS cavities in the present AR. If the intense single bunch is accelerated by them, the higher order mode (HOM) loss becomes comparable to the radiation loss, therefore, the number of the cavities have to be minimize. We will use 4-6 APS cavities compromising the required RF voltage with the HOM loss as shown in RF system. Since it is insufficient to accelerate a single-bunched electron beam with 6.5GeV and 200mA with the new RF system with the reduced number of cavities, we decided to decrease the electron energy down to 6GeV considering that the required photon energy range is covered with improved insertion devices. The energy and the beam current of the original design would be realized in the second phase of the project with damped or superconducting cavities that we have been developing at KEK.

Injection of the beam into the ring will be done with the present 2.5GeV injection line for electrons and

Table 7 Parameters of PF-AR

Energy	E=6.0Gev	Radiation damping time	
Lattice type	FODO	Hor.	τ_x=2.345ms
Circumference	C=377.26m	Ver.	τ_y=2.348ms
Bending radius	ρ=17.825m	Long.	τ_ε=1.175ms
Bending strength	B=1.122T	RF frequency	f_{RF}=508.58MHz
Revolution frequency	f_r=0.794657MHz	Harmonic number	h=640
Energy loss per turn	U_0=6.34MeV	RF voltage	V_{RF}=15MV
Emittance	ε=159nm	Synchrotron tune	ν_s=0.041
Momentum compaction		RF bucket height	$(\Delta p/p)_{RF}$=0.0122
factor	α=0.007	Bunch length	σ_z=12.73mm
Betatron tune		Energy spread	σ_ε=0.00122
Hor.	ν_x=12.72		
Ver.	ν_y=6.45		

the beam will be accelerated to 6GeV. According to preliminary investigation, instabilities are not severe and the Touschek lifetime is sufficient at the injection energy of 2.5GeV.

The main parameters of PF-AR are shown in Table 7.

Lattice

We have been investigating feasibility of several lattice configurations. We concluded that the following improvements are optimum to our purpose.

i) 15m long free spaces for insertion devices will be secured in the east and west long straight sections changing the arrangement of quadrupole magnets in these sections. Symmetry of the lattice from the mirror symmetry suitable for a collider will be changed to the rotational one which is adequate to a light source.

ii) The bending magnets will be shortened in order to make a space for vacuum components and beam monitor electrodes. Each bending magnet can be divided into two pieces; a pole-piece with an upper yoke and a pole-piece with lower yoke, in order to make maintenance of beamlines easy.

iii) We make use of dipole windings on sextupoles in stead of present vertical steerers in order to make free spaces in short straight sections.

These improvements ensure free spaces between magnets, give freedom into design of the vacuum system and the beam diagnostic devices and improve their maintenancability. These advantages are quite important for a dedicated SR machine. The emittance

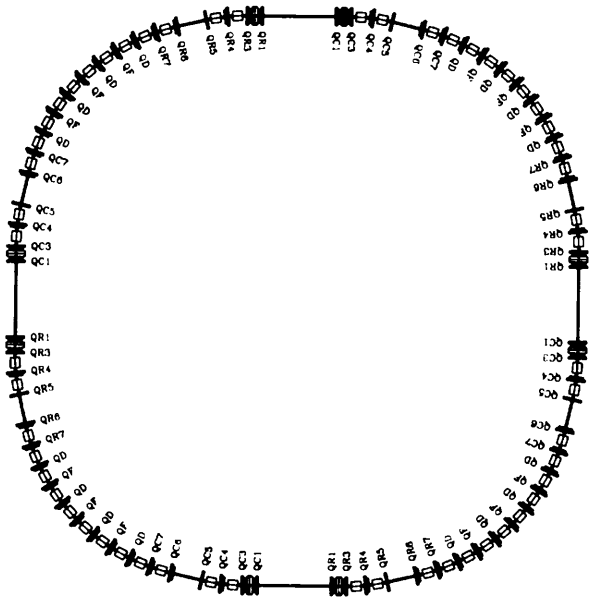

Fig. 35 Lattice of PF-AR

of 160nm of the lattice is not so large compared with that of the 2.5 GeV PF ring before the upgrade project underway.

The lattice of PF-AR and the normal cell are shown in Fig. 35 and Fig. 36, respectively.

Vacuum System

As mentioned before, the renewal of the vacuum system is essential for the project. Features of the system are:

i) The system can handle the single-bunched beam with 6GeV and 200mA or a beam with 6.5GeV and 100mA safely.

ii) It ensures a lifetime of 900min.(Touscheck

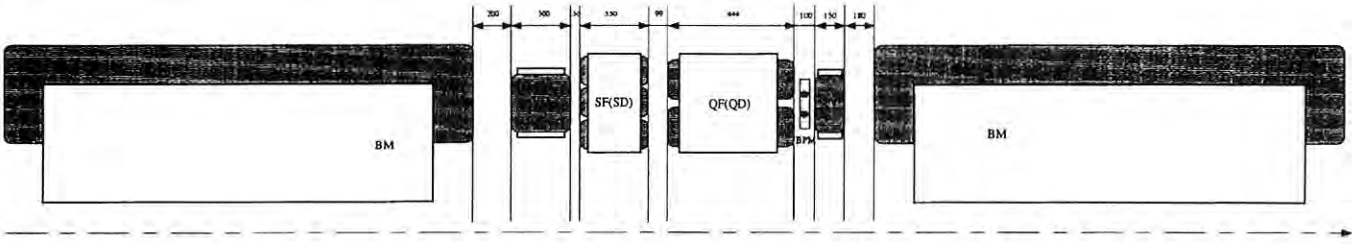

Fig. 36 Normal cell of PF-AR

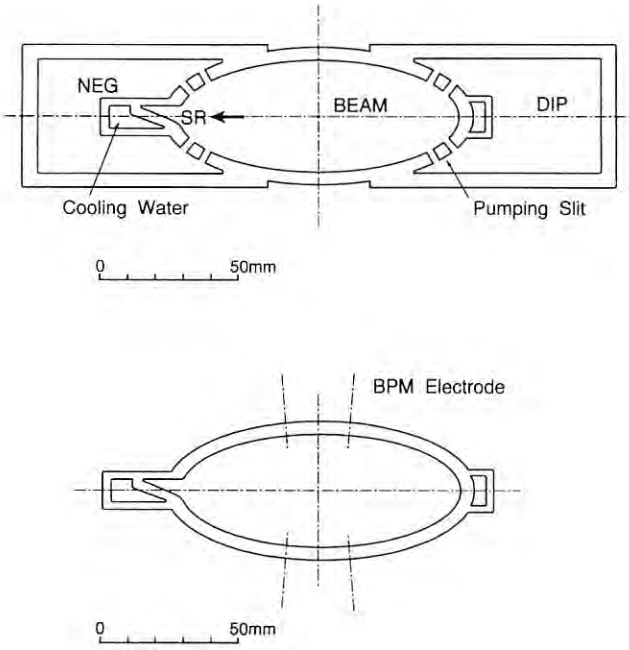

Fig. 37 Examples of the vacuum duct designs. Cross section of B-duct (top), and Q-duct (bottom).

lifetime is sufficiently long.)
We are now designing a beam duct with special cross section to absorb intense SR safely. An example of the duct design is shown in Fig. 37.

RF Acceleration System

In the first phase, we will install 2 or 4 cavities in the east and west long straight sections(total 4-6 cavities). These cavities are powered by 2 klystrons in the east and west support buildings (total 2 klystrons). It is impossible to improve the beam current increasing the number of the cavities. We will introduce a temperature controller for cooling water of the cavities in order to stabilize the beam. HOM dampers and input couplers might be improved in this phase.

Injection

We will divert the present 2.5GeV injection line for electrons in the south-east straight section and their power supplies. Though the present system handles the beam with the energy up to 3GeV, we have to accelerate the beam after injection, anyhow. It is possible to inject a 6GeV beam at the south-east straight section reinforcing the beamline magnets, however, it is not economical. The full-energy injection at the south-west straight section is a future subject.

5. TIME SCHEDULE

The PF-AR project will be done from 1998 to 2000 for 3 years as shown in Fig. 38. It consists of the renewal of the accelerator, constructions of the new experimental halls and the beamlines. It must be scheduled to minimize a shut down period as short as possible, in order to keep the present activities, so that the construction will be divided into two steps. As the first step, which corresponds to 1998-1999, the components of the accelerator will be designed and prepared. On the other hand, the N-experimental hall will be reconstructed and one insertion devise beamline will be installed at this period. At the second step, which corresponds to the end of 1999-2000, the components of the accelerator will be installed at the ring, and we have to stop the operation. At the same time, the new experimental halls; NW-, and SE-experimental halls, and three insertion device beamlines and one bending magnet beamline will be constructed.

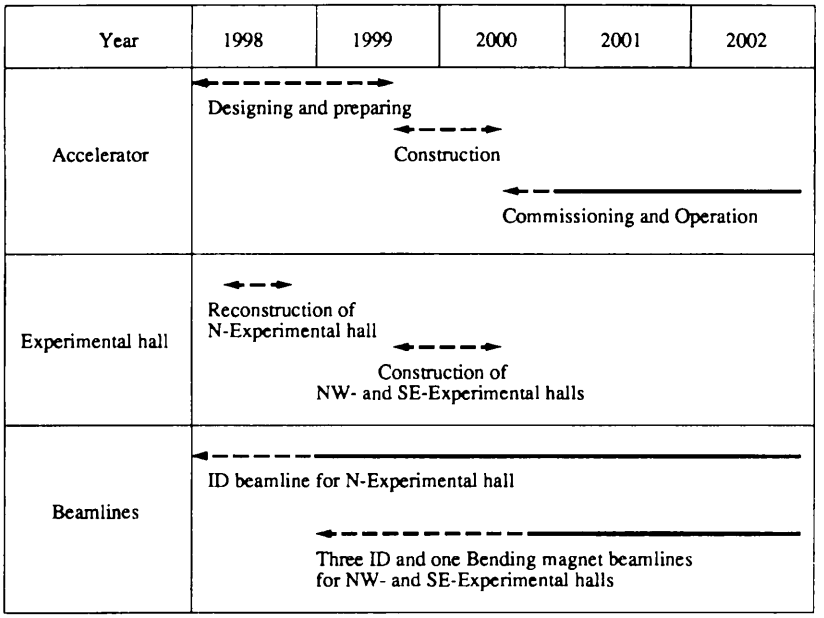

Fig. 38 Time schedule of PF-AR. Dotted line indicate the periods of the designing, preparing, and commissioning. Solid lines indicate normal operation.

C. SLOW-POSITRON SOURCE

A slow-positron dc beam was successfully obtained from a pulsed slow-positron beam utilizing Penning-trap electrodes. Each of the electrodes is a 50-mm-long cylinder with an inner diameter of 64 mm, which is slightly larger than that of a beam duct of 60 mm in order to avoid any beam loss during the trapping process. The necessary voltage waveforms for each of the electrodes were generated by programmable function generators with the aid of voltage amplifiers.

Several experiments were performed at the PF slow-positron source: energy-distribution measurements by the time-of-flight method (TOF) of the positronium (Ps) emitted from single-crystal insulators, rare-decay measurements of Ps for the verification of quantum electrodynamics (QED), and brightness-enhancement measurements of the slow-positron beam.

As an example of the obtained results at the PF slow-positron source, Fig. 39 shows the preliminary result of a Ps TOF spectrum from single-crystal quartz. Two energy peaks are clearly resolved, which correspond to Ps energies of 3.3 and 0.8 eV, respectively. Although the 3.3 eV peak had already been reported by Sferlazzo et al., the 0.8 eV peak was identified for the first time by the present measurements. This 0.8 eV peak might be due to a thermalization process of the Ps.

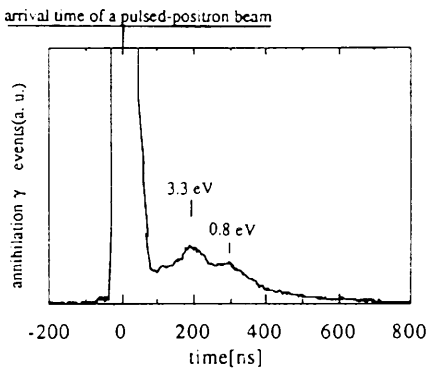

Fig. 39 Positronium (Ps) time-of-flight (TOF) spectrum measured at a distance between the sample surface and the annihilation γ-ray detector of 135 mm.

In accordance with the 2.5-GeV-linac upgrade plan relevant to the KEKB project, we must relocate our PF slow-positron source to the 1.5-GeV point of the upgraded linac. We shut down our facility at the end of 1996 and started to relocate it to a new place. Although this relocation will take more than eight months, we are also planning to install a dedicated linac for slow-positron utilizing only the remnants of the present 2.5-GeV linac smartly.

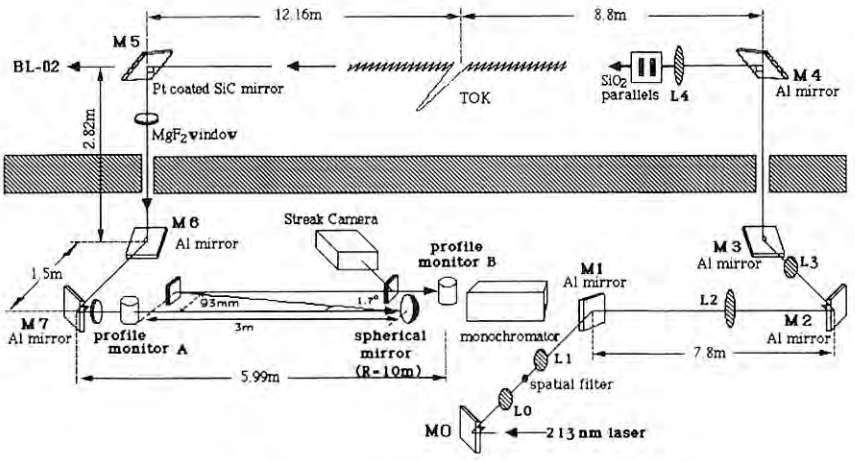

Fig. 40 Schematic layout of the FEL beam line.

D. VUV FEL

An FEL gain measurement at 213-nm wavelength is underway at the beamline BL-2. For the gain measurement, we need to make overlapping between the electron bunches and the laser-beam pulses in both the space and time domains. In order to adjust the spatial overlapping, we developed a special profile monitor which can watch both electron beams and laser pulses. It comprises a movable pinhole and a compact monochromator system. Since a long-wavelength component of the spontaneous emission has a large angular divergence, it scatters around the beam pipes. Such a component can be rejected by the monochromator system. Using this profile monitor, we measured both profiles of the spontaneous emission and the laser beams at two locations on the FEL beamline, 7m apart from each other. Figure 40 shows a schematic layout of the FEL beam line. A spherical mirror system was used to focus the light at the downstream profile monitor (referred as B) in order to improve the position resolution. The position of the laser light was adjusted to that of the spontaneous emission using mirrors and SiO_2 parallels. Figure 41 shows the thus-obtained profiles of the spontaneous emission and the laser light at the locations of A and B, respectively.

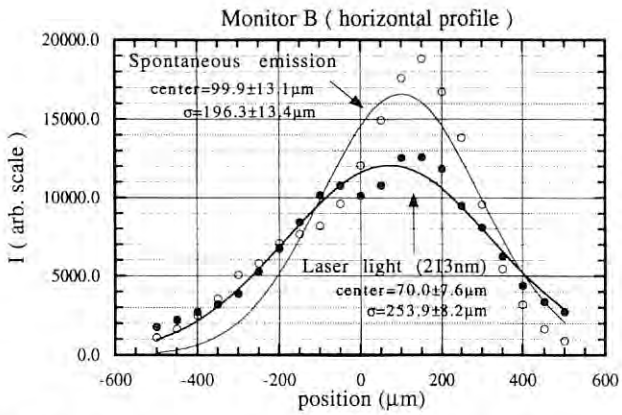

Fig. 41 Typical measured profiles of the spontaneous emission and the laser light.
(A) Vertical profile at the monitor B.
(B) Horizontal profile at the monitor B.

A timing system used to coincide the laser pulses with the electron bunch has been developed. Because the laser pulses and electron bunch are both short (about 100 ps), a streak camera was adopted for the system. A trigger signal for the laser pulses (repetition rate : 50 Hz) was synchronized with an rf frequency of the ring. The delay of the trigger was then adjusted so as to coincide the laser pulses with the electron-bunch passages. Figure 42 shows images from the streak camera during this experiment. At the present time, the accuracy of the timing adjustment is limited by an existing jitter of laser pulses, which would spoil the accuracy of the FEL gain measurements. A system which can reduce the timing jitter of the laser pulses is under development.

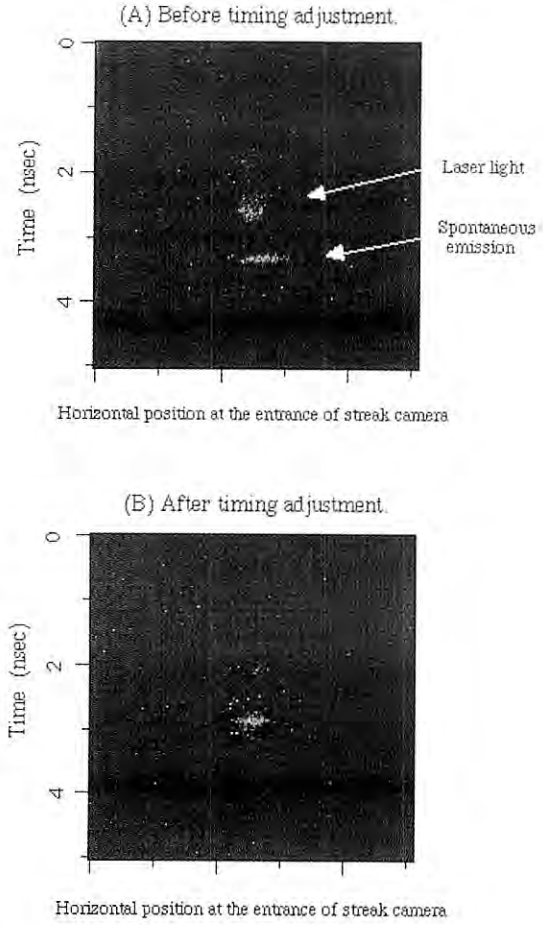

Fig. 42 Image from the streak camera.
(A) Before timing adjustment.
(B) After timing adjustment.

E. KEKB

1. PROGRESSIVE STATUS

Fiscal 1996 was the third year of the five-year reconstruction program of the KEKB injector. At the end of 1996 a new extension of the 2.5GeV-linac building was completed on schedule and installation of linac devices was started in a new building, which includes a new gun room and sectors A, B and C.

In sectors 1 through 5 all 38 accelerating units had their rf-compression system (SLED) attached and their klystrons and modulators upgraded by March, 1997. The rf drive system in sectors 1 through 5 was also upgraded using a newly developed sub-booster klystron. An energy gain of 160MeV/unit on the average has become possible.

An upgrade of the beam-transport system in sectors 3 through 5, corresponding to the beam-energy increase, was completed during this period. A trial use of the beam-position monitors was also started. A simulation study to improve the beam-transport is in progress.

Control-system improvements, including new hardware development and software renewal, are being continued.

The beam switchyard at the end of the linac was completely dismantled, except for the beam-transport system for the PF storage ring, followed by surveying and settling new base plates for the new KEKB beam lines.

2. PERFORMANCE OF THE SUB-BOOSTER KLYSTRON

The KEKB-project requires an energy upgrade of the PF-linac from 2.5GeV to 8.0GeV; the development of an rf source is a key issue in this project.

The 60 kW-pulsed driver klystrons (sub-booster klystron; SBK), which feed the rf driver power to 8 newly developed 50-MW klystrons under the SLED mode operation, had been designed and manufactured through a collaboration between KEK and MHI (Mitsubishi Heavy Industries), since no commercial tubes were available. Up to the end of the FY95, 5 SBKs had been manufactured, including the first prototype klystron. The design principle and specifications were reported in the previous Activity Report.

According to the manufacturers tests, an output power of 80 kW and an efficiency of about 40% were obtained at an applied beam voltage of 25kV. These test results satisfied our specifications. On the other hand, some discrepancies between the design and real performance were observed, especially the focusing-magnetic field profile greatly deviated from the designed value. This resulted in a very high gain of more than 70dB under this focusing field.

In an operation test of the SBKs from the beginning of 1996, unstable performances were found in some tubes. From the winter in 1997, prior to the SLED operation of the 2.5-GeV linac section, we started to re-test all of the SBK tubes in order to survey these unstable performances. All of tests were performed again in the test bench. The re-test comprised a power-waveform measurement and a phase measurement at the flat top of the pulse; in the SLED mode the phase of the drive pulse is shifted by

180 degrees in the flat top of the pulse. A summary of the re-test and operation results is as follows:

(1) It became easy to find the unstable operation point by observing the phase-detector output.

(2) It was shown that the most stable operation was realized with an applied magnetic field near to the designed value. The peak power and the gain at this condition were less than those at the previously tuned point, and the obtained output power was in the range of 60-70kW and the gain was about 60dB.

(3) It was found that in some tubes, even though the output power waveform was normal, the output phase showed an instability. Therefore, utilizing the phase detector was very useful for adjusting the tube performance at a proper operation point.

(4) Since a rather large VSWR (from 1.2 to 1.4) was observed in each output coaxial line in the klystron gallery, the test-bench results were not perfectly reproduced due to the load characteristics of the klystrons. It is necessary to measure this load dependence on the output power by measuring the Rieke-diagram experiment.

(5) It might be necessary to slightly change the design so as to eliminate the unstable operation point in the future.

(6) Operation (microwave processing operation) for the entire 2.5-GeV linac section with the SLED mode was conducted and the performances of the sub-booster klystrons after tuning were satisfactory.

Figure 43 shows the waveform of the applied voltage and the beam waveform of the sub-booster klystron. Figure 44 shows the power waveform and phase of the SBK output.

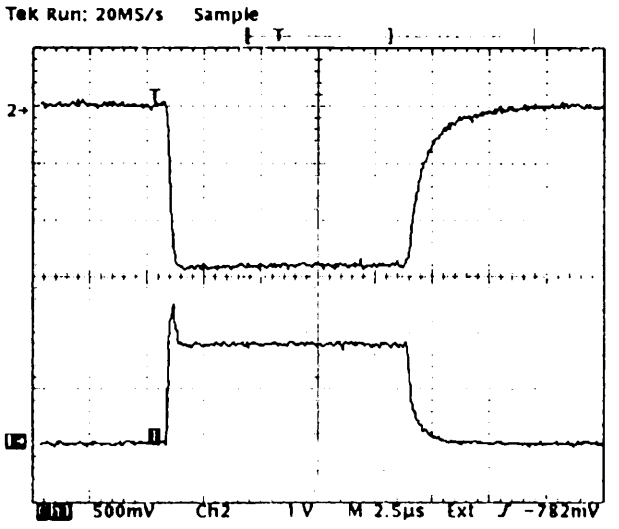

Fig. 43 Waveforms of the applied voltage pulse (top) and the current pulse (bottom) of the SBK.

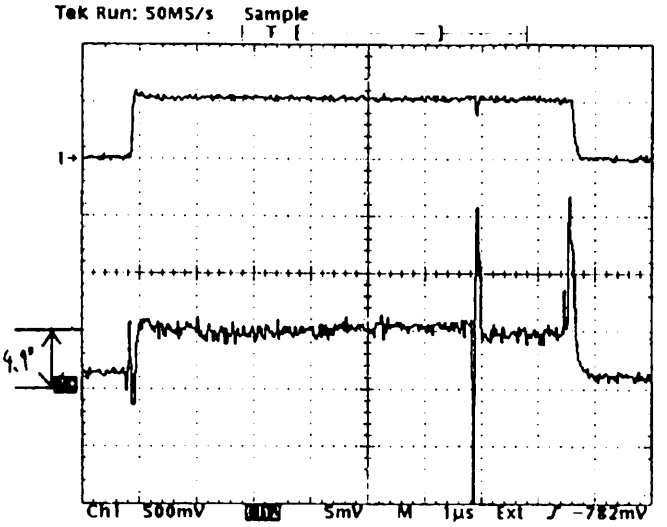

Fig. 44 Waveforms of the power (top) and phase (bottom) of the SBK output.

3. DEVELOPMENT OF A DUMMY LOAD

In KEKB, according to the rf source upgrade, high-power rf (5MW klystron output, 4µs pulse width, 50pps repetition rate and SLED mode) is fed to a dummy load at the end of the accelerator guide. Since the present dummy load is directly water-cooled, any cooling-water leak trouble due to damage to the SiCs is apprehended. Thus, a new high-power dummy load has been developed on the basis of a SiC brazing technique developed by the JLC group and Mitsubishi Heavy Industries. The JLC-type dummy load uses button-type SiCs that are brazed on the H plane of the waveguide at an interval of about a quarter wavelength, and are indirectly water-cooled. In order to save the length and production cost, the configuration of the SiCs was designed so that the total rf power can be absorbed, not by one way, but by going back and forth between the entrance and end of the dummy load. The cross sections of the dummy load are shown in Fig. 45.

The interval of SiCs and the distance between the end plate and the SiC (#9, see Fig. 45) were determined by a cold test so as to have a small reflection and a

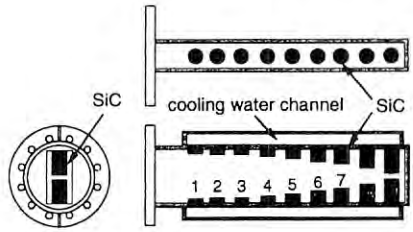

Fig. 45 Cross sections of the dummy load.

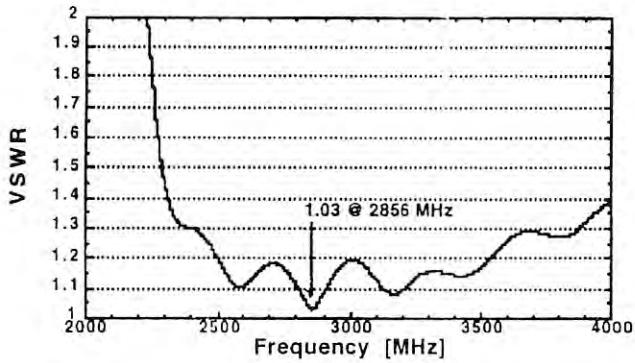

Fig. 46 Reflection characteristics of the dummy load.

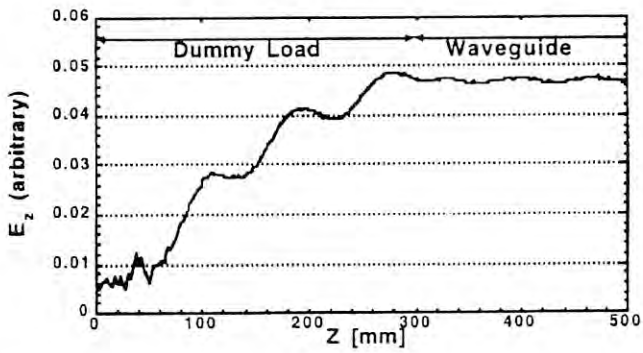

Fig. 47 Electric-field distribution in the dummy load measured by a bead pull method.

uniform decrease of the rf power. The reflection characteristics and electric-field distribution along the axis are shown in Figs. 46 and 47, respectively. In order to evaluate the effect of the scatter of the complex dielectric constant of SiC on the rf characteristics, ε and tan δ were measured by the reflection method for some samples. It was shown by cold tests that the effect is negligibly small. A high-power model has been fabricated (Fig. 48) and tested. The results show that the dummy load can stably absorb the high-power rf (13MW klystron output, 4μs pulse width, 50 pps repetition rate and SLED mode).

The dummy load which had been used for the rf

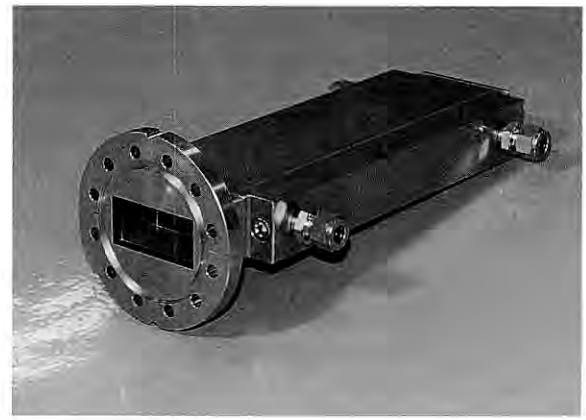

Fig. 48 Photograph of the high-power dummy load.

linac (direct water cooled) was also high-power tested, and a fine result was obtained. Thus, it will be used until new dummy loads have been fully installed.

4. SIMULATION STUDY FOR IMPROVING THE ENERGY-SPREAD OF THE POSITRON BEAM

The beam energy-spread at the end of the injector linac is required to fit the small energy acceptance of the KEKB linac-to-ring beam-transfer line; dE/E ≤ +/–0.25%, which is almost half the present value. The intrinsic energy spread of the positrons will be larger than the acceptance, due to a large phase spread in the rf acceleration for the following reasons: (1) the long bunch length of primary electrons due to the space-charge effect in the rf-bunching process and (2) bunch lengthening of the positrons in solenoidal focusing.

The first problem can be cured using the bunch-length compression system (BCS), which works as an emittance transformer in the bunch-length/energy-spread phase plane. Figure 49 shows a schematic view of the BCS. The bunch is compressed at the chicane, which lets the tail of the bunch catch up with the head. The path-length difference at the chicane is made with the energy gradient in the bunch by accelerating the

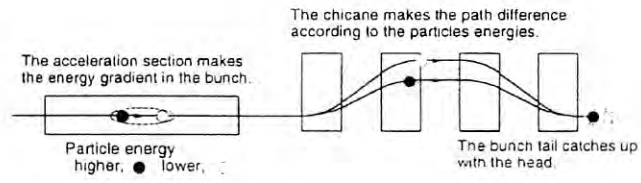

Fig. 49 Bunch-compression system layout.

beam slightly off the crest of the rf wave. Figure 50 shows the simulated phase-space transformation, which resulted in successful bunch compression. The details of the simulation will be described later. Even though the primary electrons will have a larger energy spread due to off-crest acceleration, it is acceptable as long as the focused spot size on the target is small enough, since the energy spread of the generated positrons is quite insensitive to the primary electron energies.

Even with successful bunching of the primary electrons, the final energy spread of the positrons will not be sufficiently small. To improve the spread, the energy-spread compression system (ECS) will be used at the end of the linac. The ECS makes the energy spread smaller by a phase-space transformation, as shown in the Fig. 51. The bunch is lengthened at the ECS chicane with its own energy spread. Subsidiary acceleration after the chicane compensates the energy gradient to make the energy spread smaller. Though the positron beam has a long bunch length, it is acceptable as long as it is less than the longitudinal acceptance of the storage ring.

To estimate the improvement of the energy spread

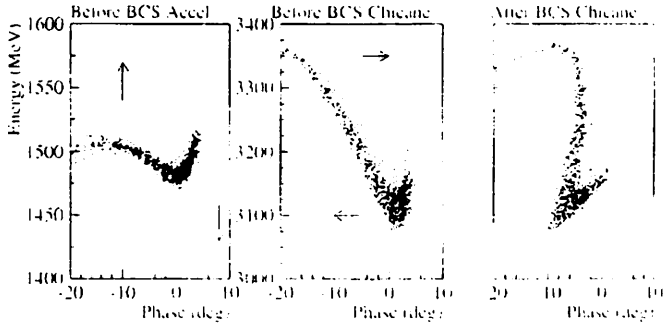

Fig. 50 Phase-space transformation by BCS.

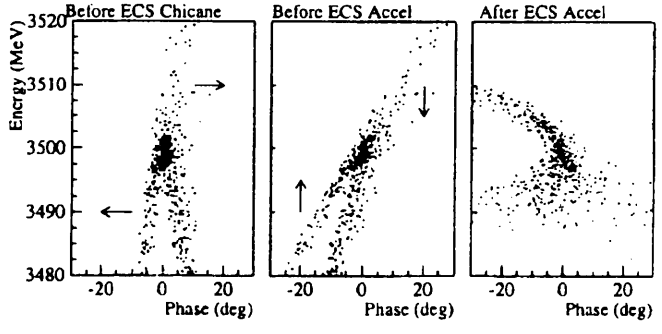

Fig. 51 Phase-space transformation by ECS.

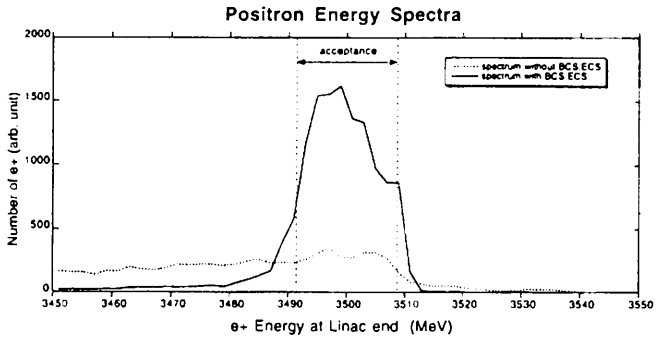

Fig. 52 Simulated energy spectra of positrons.

with these systems, we performed a detailed Monte-Carlo simulation of the particle motion in the bunch-length/energy-spread phase space, not only at the BCS and ECS, but all through the linac. In our simulation, the following items were taken into account: (1) the space-charge effect in the rf bunching of the electrons estimated with the PARMELA code; (2) the rf phase spread due to the particle distribution in the bunch; (3) the pulse-to-pulse jitters of the rf phases, the accelerating field strength and the injection timing from the pre-injector as well; (4) the phase-space deformation by the longitudinal wake field; (5) the positron-generation process in the target material with the EGS4 code; (6) the de-bunching effect in the solenoidal focusing and (7) the phase-space transformation by BCS and ECS with a precise path length calculation. Figure 52 shows the estimated energy spread of the positrons with and without BCS and ECS. The spread is expected to be improved so as to fit the required energy acceptance.

5. CONTROL SYSTEM

5.1 Overview

For the KEKB project, many components of the control system have been improved in order to make it reliable. Some of them are already used in normal operation.

Device controllers for accelerator equipment were also re-configured so as to support an increased number of devices and advanced control functions. Although a standard controller is not defined to cover all devices, an UDP connection capability over Ethernet is required for each controller. PLC, VME, VXI, CAMAC and old controllers are used to meet their equipment-dependent

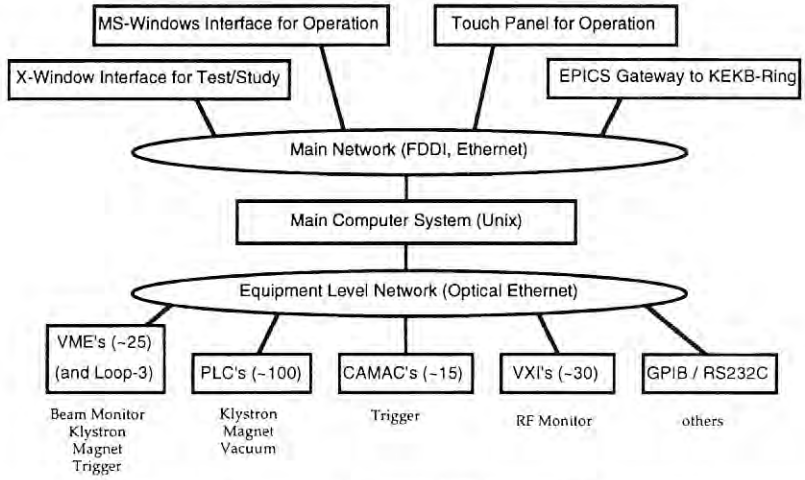

Fig. 53 Physical configuration of the control system. TCP and UDP based RPC protocols are used for distributed controls.

requirements as shown in Fig.53.

For the rf system, VXI-based measurement stations are being installed. Controllers based on PLC (programmable logic controller) were also developed for new klystron modulators. Most of the old modulators continue to use old controllers based on SBC (single-board computer).

For the new magnet power supplies and for all of the vacuum devices, PLC-based controllers are being installed. Some of them are already available and give satisfactory performance. Old magnet power supplies are served by old controllers.

VME-based measurement stations were employed for beam instrumentation, and CAMAC controllers are being installed at timing control stations. Advanced software is under development.

Since there exist several different controllers for the same purposes, server software for each equipment class has been developed and used to hide such unnecessary differences and to serve essential controls.

Those services are provided for the operator console system and other applications, through simple RPC (remote procedure call) on the TCP network. While this protocol serves client systems in the linac, KEKB ring requires the channel-access protocol, since EPICS was employed at the ring controls. Thus, a gateway, what is called the CA-server, for linac devices, is being developed to provide controls to EPICS clients.

5.2 The New Vacuum Control System

With the KEKB project, an increase in the number of vacuum components (ion pumps, gauges, valves, etc.) has been required, about 50 percent more than before. We need to rejuvenate the controller for them, so as to accept the increase and to adapt them to the linac control system, which is also being gradually upgraded. Maintenance is another reason for the renewal.

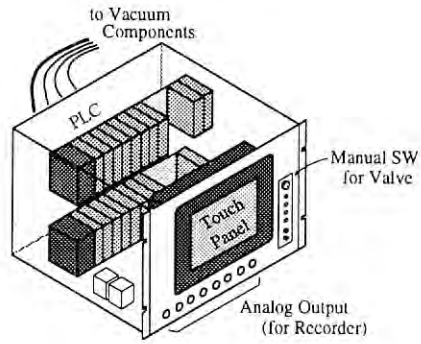

Fig. 54 Outline view of the new vacuum controller.

The new controller includes a Yokogawa programmable logic controller (PLC) as a main device (Fig. 54). Each set of PLC comprises a CPU module, ADC modules, digital I/O modules, and an Ethernet communication module. A touch panel is installed in front of the controller for local operation. For operating valves, manual switches have also been prepared. They are available even when the PLC is in trouble, since they are not related to the PLC. One controller is responsible for about 30 pieces of vacuum equipment (Table 8), which are distributed over four accelerating units.

Table 8 Number of vacuum parts connected at one controller.

	ordinary	max.
Ion-pump controller	12	12
Penning-gauge controller	2	5
Valve (pneumatic) controller	2	5
Valve (manual)	8	8

The vacuum controller is connected to the upper level of the linac control system via an Ethernet network. The Ethernet line is directly bound to the PLC module. Between the PLC and the linac control network, we set a computer (Windows NT PC), named "device manager (DM)". All of the vacuum data are accumulated there once, and are then arranged and served to the upper level of the control network (Fig. 55).

The new controllers will be applied for an extended part of the linac as well as for the existing part. The replacement of old ones was finished by March 1997. A total of 20 controllers will be operational at the final phase.

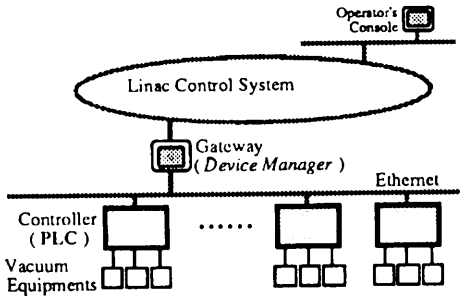

Fig. 55 Network layout around the vacuum control system.

6. STRIP-LINE-TYPE BEAM-POSITION MONITORS

In the KEKB project, non-destructive beam-position monitors are indispensable for providing stable, high-quality beams. This is especially important to suppress transverse wake fields in the accelerating structure, which can be strongly excited by high current beams. Thus, strip-line-type beam-position monitors were designed and are being installed.

During the summer shutdown in 1996, about twenty monitors were installed in the first two sectors. Originally, the read-out system was designed to employ shaping amplifiers and ADC's. However, because of a budget shortage it was planned to utilize digital oscilloscopes (Tektronix TDS680B) instead, which

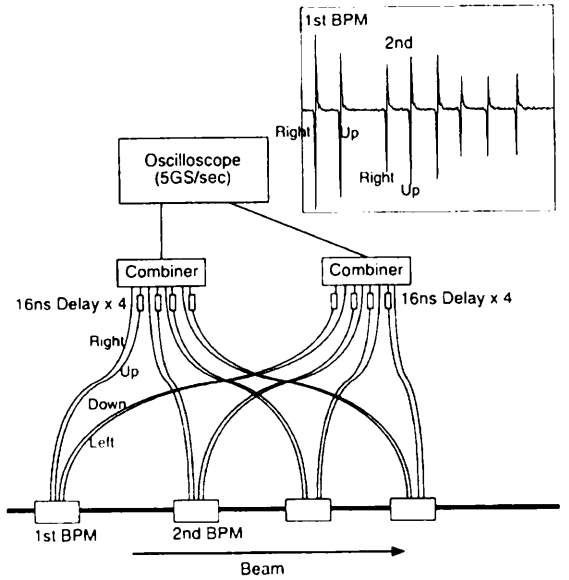

Fig. 56 Signals from the beam-position monitors are summed with rf combiners and fed to oscilloscopes.

were installed to observe the signals from wall-current monitors.

In order to read signals with limited oscilloscope channels we summed up several signals with rf combiners. The length of the cables from the monitors to four monitoring stations in these two sectors was carefully arranged to be equal, and appropriate delay cables were added to vertical-position signals. Those made signals from the monitors along the linac to be distributed along the time axis on oscilloscopes, as shown in Fig. 56.

The internal functions on the oscilloscopes were used to average the signals and to measure the peak-to-peak pulse-height values. VME computers at each station took data through the GPIB and transferred them to UNIX servers. A visualization tool was made with software called tcl/tk to display the positions and beam intensities, derived in UNIX.

This system helped beam studies during this period. It was found that this system gave reliable beam currents, as well as beam positions, compared to wall-current monitors, which show the position dependence. However, since it took ten seconds to read all of the positions, it is planned to calculate the values on VME computers, instead of utilizing oscilloscope functions, to improve the speed.

ISSN 0912-1803

PHOTON FACTORY ACTIVITY REPORT 1996

#14

PHOTON FACTORY ACTIVITY REPORT 1996

#14